Transactions of the ASME

FLUIDS ENGINEERING DIVISION
Technical Editor
FRANK M. WHITE (1984)
Executive Secretary
L. T. NELSON (1984)
Calendar Editor
M. F. ACKERSON

Associate Editors
Fluid Machinery
AWATEF A. HAMED (1985)
WILLIAM E. THOMPSON (1984)
Fluid Measurements
THEODORE R. HEIDRICK (1984)
Fluid Mechanics
SHLOMO CARMI (1984)
KIRTI N. GHIA (1984)
THOMAS J. MUELLER (1985)
HASSAN M. NAGIB (1986)
Fluid Transients
M. HANIF CHAUDHRY (1983)
Multiphase Flow
JOHN T. JUREWICZ (1985)
OKITSUGU FURUYA (1984)
Review Articles
RICHARD A. BAJURA (1985)

FOREIGN CORRESPONDENTS
Europe and Russia
JACQUES CHAUVIN
Europe and Russia
JOHN H. HORLOCK
India and Middle East
ARUN PRASAD
Japan and China
YASUTOSHI SENOO

BOARD ON COMMUNICATIONS
Chairman and Vice President
K. N. REID, Jr.

Members-at-Large
W. BEGELL, J. T. COKONIS, W. G. GOTTENBERG, D. KOENIG, M. KUTZ, F. LANDIS, R. E. NICKELL, J. ORTLOFF, C. PHILLIPS, H. C. REEDER

President, G. KOTNICK
Executive Director
PAUL ALLMENDINGER
Treasurer,
ROBERT A. BENNETT

PUBLISHING STAFF
Mng. Dir. Publ., J. J. FREY
Dep. Mng. Dir. Publ.,
JOS. SANSONE
Managing Editor,
CORNELIA MONAHAN
Editorial Production Assistant,
MARISOL ANDINO

The Journal of Fluids Engineering (ISSN 0098-2202) is published quarterly for $72 per year by The American Society of Mechanical Engineers, 345 East 47th Street, New York, NY 10017. Second class postage paid at New York, NY and additional mailing offices. POSTMASTER: Send address changes to The Journal of Fluids Engineering, c/o THE AMERICAN SOCIETY OF MECHANICAL ENGINEERS, P.O. Box 3199, Grand Central Station, New York, NY 10163.
CHANGES OF ADDRESS must be received at Society headquarters seven weeks before they are to be effective. Please send old label and new address.
PRICES: To members, $36.00, annually: to nonmembers, $72.00. Add $6.00 for postage to countries outside the United States and Canada.
STATEMENT from By-Laws. The Society shall not be responsible for statements or opinions advanced in papers or . . . printed in its publications (B7.1, Par. 3).

INDEXED by the Engineering Index, Inc.

Journal of Fluids Engineering

Published Quarterly by The American Society of Mechanical Engineers

VOLUME 106 • NUMBER 3 • SEPTEMBER 1984

Solid Particle Dynamic Behavior Through Twisted Blade Rows

A. Hamed
Department of Aerospace Engineering and Applied Mechanics, University of Cincinnati, Cincinnati, Ohio 45221

Particle trajectory calculations provide the essential information required for predicting the pattern and intensity of turbomachinery erosion. Consequently, accurate flow field and blade geometry representation in the trajectory computational model are required to evaluate machine performance deterioration due to erosion. A model is presented that is simple and efficient yet versatile and general, applicable to axial, radial and mixed flow machines, and to inlets, nozzles, return passages and separators. Computations are presented for particle trajectories through a row of twisted vanes in the inlet flow field. The effect of the particle size on trajectory blade impacts, and on particle redistribution and separation are discussed.

Introduction

The erosion of turbomachine blades, vanes, and shrouds represents a serious problem in many gas turbine applications. Sand, dust, or salt are the cause of erosion in aircraft and naval installations. Solid particles are also ingested by gas turbine engines in ground vehicles, auxiliary power units and tanks. The particles can be products of combustion such as coal ash or other components in advanced fuels. Continued operation under these conditions affects the life of these engines and adversely influences their performance.

The erosion rate of metals is known to be strongly dependent on the particle velocities and impact angles [1, 2]. In order to apply the erosion wind tunnel findings to turbomachines, it is necessary that particle impacting velocities relative to the various blades as well as the impacting locations and frequency of particle impacts be known. The particle trajectory calculations in turbomachines provides this essential information for the determination of the influence of these particles on the engine life and performance.

Many particle trajectory studies [3, 4, 5] were carried out in simple flow fields which were prescribed analytically, and did not include the effects of particle boundary impacts into the solution. In turbomachinery applications, the particles impact the successive rows of rotating and stationary blades as well as the hubs and shrouds. It is necessary to include the effects of these particle metal impacts in the trajectory calculations since the solid particle velocities change both magnitude and direction after each impact.

Hussein and Tabakoff [6, 7] developed a code for predicting three dimensional particle trajectories through rotating and stationary turbomachine blade rows which models the effect of particle boundary impacts. The results of the computations were verified experimentally in axial flow machines, and in tunnels and water tables simulating successive rotor and stator blades [8, 9, 10]. The method is suited for trajectory calculations in axial flow machines with large hub-tip ratio since its flow field representation at the cylindrical mean-radius stream surface is two dimensional. A second model was developed by Beacher et al. [11] to provide better representation of the flow field of axial flow machines with twisted blades. The computer storage required for flow field data is multiplied by the number of two dimensional flow field representatives at several radial locations, and expensive computer time is consumed in the complex interpolation procedures for the gas properties, which are required in the particles trajectory computation.

The present paper presents another approach for the three-dimensional flow field description to reduce the computer time and storage required for three-dimensional particle trajectories. The flow field is represented by the solution at the mean hub-to-tip stream surface [12] and a velocity gradient equation, to represent the blade-to-blade flow field variation, in the particle trajectory calculations. Axial, radial and blade-to-blade flow field variations through twisted blade rows in contoured annular passage are represented by this model at computer storage and time savings similar to Hussein and Tabakoff's code. It is applicable to axial, mixed and radial flow machines and includes the effects of blade, hub and shroud impacts. It can also be used for calculating particle trajectories in inlets, nozzles, return passages, separators, and in axisymmetric flow fields.

Analysis

The particle dynamics in a gas solid suspension are determined by the gas-particle interaction and particle-boundary impacts. For the small particle concentrations and ρ/ρ_p involved in turbomachinery applications, the gas flow field is not significantly altered by the presence of the solid particles. The particles travel in the flow field under the influence of the aerodynamic forces exerted on them by the gas flow field. In the trajectory calculations, the equations governing the particle motion in the gas flow field are integrated numerically and the location of their impacts with the

Contributed by the Fluids Engineering Division of THE AMERICAN SOCIETY OF MECHANICAL ENGINEERS and presented at the Fluids Engineering Conference, St. Louis, Mo., June 7-11. Manuscript received by the Fluids Engineering Division, May 10, 1983.

various boundaries are determined. The particle rebounding characteristics after each impact constitute the initial conditions for the rest of the particle trajectory calculations.

Particle Dynamics. The equations governing the particle motion as they travel through the flow field in a blade row are written with respect to a frame of reference which is fixed relative to the blades:

$$\ddot{r}=F_r+r(\dot{\theta}+\Omega)^2 \tag{1}$$

$$\ddot{\theta}=\frac{F_\theta}{r}-\frac{2\dot{r}}{r}(\dot{\theta}+\Omega) \tag{2}$$

$$\ddot{z}=F_z \tag{3}$$

where r, θ, and z define the particle relative location in cylindrical polar coordinates. The last terms on the right hand side of equations (1) and (2) represent centrifugal force and Coriolis acceleration. The first term on the right-hand side of equations (1) through (3) represent the force of interaction between the two phases, per unit mass of particles. It is dependent on the relative velocity between the particles and the gas flow, as well as the particle size and shape.

Gas Particle Interaction. In most turbomachinery applications the gas velocities and rotational speeds are high and particle concentrations are relatively low. Under these conditions, the aerodynamic forces on the particles due to the flow field pressure gradient, the magnus effect, and the forces to accelerate the apparent mass, are small compared to the friction and form drag. The forces of interaction between the two phases can therefore be expressed as follows:

$$F_r=G(V_r-\dot{r}) \tag{4}$$

$$F_\theta=G(V_\theta-r\dot{\theta}) \tag{5}$$

$$F_z=G(V_z-\dot{z}) \tag{6}$$

In the above equations V_r, V_θ, and V_z represent the components of the relative gas velocity and G the reciprocal of the characteristic relaxation time of the particle's translational motion

$$G=\frac{3}{4}\frac{\rho}{\rho_p}\frac{C_D}{d}[(V_r-\dot{r})^2+(V_\theta-r\dot{\theta})+(V_z-\dot{z})^2]^{1/2}$$

where ρ, ρ_p are the gas and solid particle densities, d the particle diameter, and C_D the drag coefficient.

Empirical correlations are used in the analysis for the drag force on a spherical particle in terms of the Reynolds number which is based on the particle diameter and the slip velocity of the particles in the gas flow field (7).

Particle Boundary Impacts. The equations of motion of the solid particles are integrated numerically in the specified flow field up to the point of blade, hub or tip impact. The impact location can be determined from the particle trajectory calculations and the configuration of the impacted surface. The magnitude and direction of the impact velocity relative to the surface, for a large number of particles constitute the essential data needed for the evaluation of the erosion of the various turbomachinery components. The particle rebounding velocity magnitude and direction after these impacts are dependent on the impacting conditions and the particular particle surface material combination under consideration. Empirical correlations of the restitution parameters are used to calculate the particle rebounding conditions in the calculation of particle trajectories. These correlations are based on the experimental data obtained using high speed photography and Laser Doppler Velocimetry for particle laden flows over metal samples at various incidence angles and flow velocities in a special tunnel (1). The correlations are determined for a given particle-sample material combination over a range of impinging angles and impinging velocities as shown by the curves in Figs. 1 and 2 for quartz particles impacting stainless steel. Two correlation parameters such as the velocity and angle restitution ratios describe the particle rebound characteristics in the two dimensionla tunnel. These ratios were found to be mainly dependent upon the impingement angle and not significantly influenced by the particle size and impact velocity. The impact and rebound velocities are measured through a glass window for a large number of particles at a certain incidence angle and results in a statistical distribution as that shown at 15° in Fig. 2. This distribution is due to particles not being identically spherical, sample surfaces not being geometrically smooth, and particle reflection in the third dimension.

Nomenclature

B = tangential space between blades
C_D = particle drag coefficient
C_p = specific heat at constant pressure
d = particle diameter
F = force of interaction between the gas and the particles per unit mass of particles
g = gas constant
H = stagnation enthalpy
m = distance along the meridional streamline
p = stagnation pressure
r = radial distance from the axis
r_c = radius of curvature of meridional streamline
s = distance along orthogonal mesh lines in through flow direction
t = distance along orthogonal mesh lines in direction across flow
u = normalized stream function
V = flow velocity
V_p = particle velocity
z = axial coordinate
α = angle between meridional streamline and axial direction
β = angle between flow velocity vector and meridional plane
β_1 = angle between impacting particle velocity and the surface
β_2 = angle between rebounding particle velocity and the surface
θ = angular coordinate
ρ = gas density
ρ_p = particle density
ϕ = angle between s-line and axial direction
Ω = rotor speed (radians/s)

Subscripts

i = inlet conditions
m = meridional streamline direction
p = particle
r = component in radial direction
z = component in axial direction
θ = component in circumferential direction

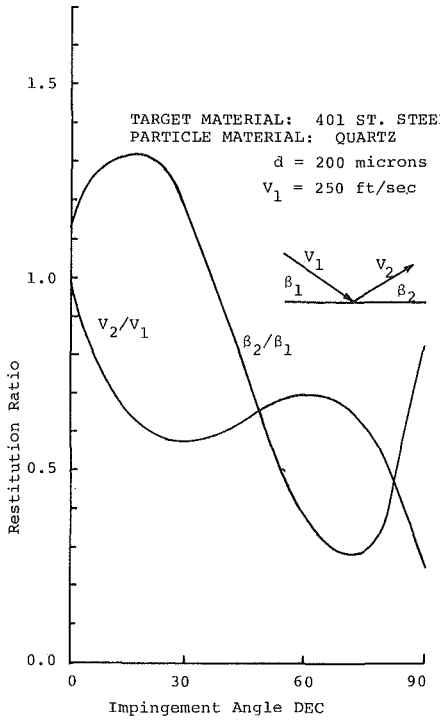

Fig. 1 Erosive particle restitution ratio

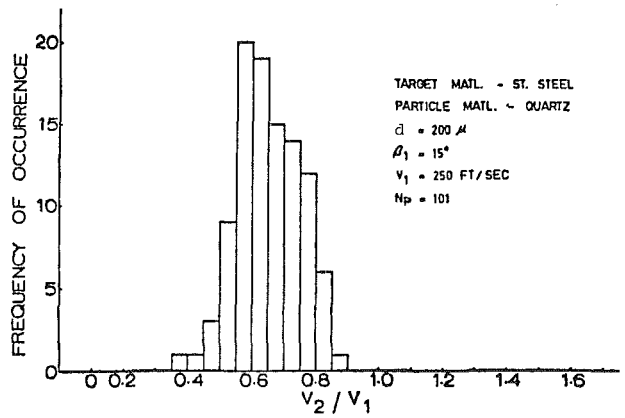

Fig. 2 Erosive particle velocity restitution ratio distribution

The velocities and angles of impact and rebound should be considered relative to the rotating blade in the case of rotor blade impacts. Furthermore, in order to use these two-dimensional correlations in the three dimensional particle trajectories, a knowledge of the geometry of the solid surface at the impact location is required. Geometrical data describing the blade, hub and tip configuration should be therefore available during the trajectory calculations to be used for the determination of the impact location and the impingement angle relative to the surface. The empirical correlations are applied in the plane of the unit normal to the surface at the point of impact, and the impacting particle velocity relative to the surface. The particle rebounding velocity V_{p_2} and rebound angle β_2, as determined by the empirical correlations, constitute the initial conditions for the following segment of particle motion through the gas flow field.

Flow Field Representation in Particle Trajectory Computation. Careful consideration must be given to the flow field representation in the particle trajectory calculations. The flow field solution must be chosen to represent the important flow field characteristics in any particular application.

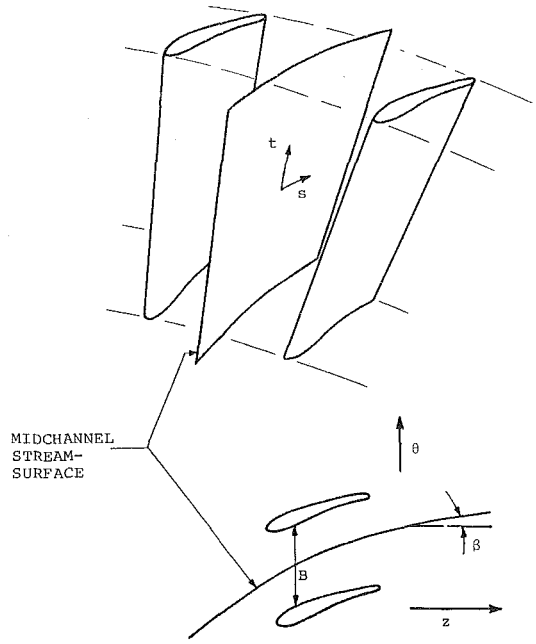

Fig. 3 Mean flow field representation on a midchannel hub-tip streamsurface

Further consideration must also be given to the computer storage required for this data and computer time for interpolating flow properties at each time step in the numerical integration of the particles equations of motion. In the present analysis, the solution is obtained on a midchannel hub-to-tip stream surface, using an orthogonal mesh with s in the streamwise direction, and t normal to it (Fig. 3).

The differential equation for the normalized stream function, u, on the hub to tip stream surface is given by:

$$\frac{\partial^2 u}{\partial s^2}+\frac{\partial^2 u}{\partial t^2}-\frac{\partial u}{\partial s}\left(\frac{\sin\phi}{r}+\frac{1}{B}\frac{\partial B}{\partial t}+\frac{1}{\rho}\frac{\partial \rho}{\partial s}+\frac{\partial \phi}{\partial t}\right)$$
$$-\frac{\partial u}{\partial t}\left(\frac{\cos\phi}{r}+\frac{1}{B}\frac{\partial B}{\partial t}+\frac{1}{\rho}\frac{\partial \rho}{\partial t}+\frac{\partial \phi}{\partial s}\right)$$
$$+\frac{rB\rho}{GV_s}\left[\frac{V_\theta}{r}\frac{\partial (rV_\theta)}{\partial t}+\xi V^2+\zeta+F_t\right]=0 \tag{8}$$

where

$$\xi=\frac{1}{2}\left(\frac{R}{C_p p}\frac{\partial p}{\partial t}-\frac{1}{H}\frac{\partial H}{\partial t}\right) \tag{9a}$$

$$\zeta=-\frac{HR}{pC_p}\frac{\partial p}{\partial t} \tag{9b}$$

and ϕ represents the angle between s and the axial direction. The force component, F_t, is caused by the hub-tip pressure gradient induced by the blades. It is therefore equal to zero outside the blade passage and is calculated from the following relation inside the blade passage:

$$F_t=-\frac{\partial \theta}{\partial t}V\frac{\partial V}{\partial \theta}. \tag{9c}$$

The flow field solution is obtained from the iterative solution of equation (8). The velocity components in the cylindrical polar coordinates, are calculated using the following relations:

$$V_z=\frac{G}{rB\rho}\left(\frac{\partial u}{\partial t}\cos\phi-\frac{\partial u}{\partial s}\sin\phi\right) \tag{10a}$$

$$V_r=\frac{G}{rB\rho}\left(\frac{\partial u}{\partial t}\sin\phi-\frac{\partial u}{\partial s}\cos\phi\right) \tag{10b}$$

$$V_\theta = \frac{G}{rB\rho}\tan\beta\left[\left(\frac{\partial u}{\partial t}\right)^2 + \left(\frac{\partial u}{\partial s}\right)^2\right]^{1/2} \tag{10c}$$

where B represents the stream-filament thickness, which is taken as the overall blade-to-blade spacing, G is the mass flow through one blade channel, and β is the angle between the flow velocity vector and the meridional plane (Fig. 3).

The flow computations were performed using the code of reference [12], which combines the subsonic flow solution, as obtained from the iterative solution of equation (9), with the velocity gradient method in the case of transonic flow fields. The transonic flow solutions are computed on the mean stream surface from the following velocity gradient equation:

$$\frac{dV}{dt} = V\left[\frac{\cos^2\beta + \cos(\alpha-\phi)}{r_c} - \frac{\sin^2\beta\cos\phi}{r} + \sin\alpha\sin\beta\cos\beta\frac{d\theta}{dt}\right] + \cos\beta\frac{dV_m}{dt}\sin(\alpha-\phi) + r\cos\beta\frac{dV_\theta}{dm}\frac{d\theta}{dt} + \frac{1}{V}\left[\frac{d(H_i-H)}{dt} - \zeta - V^2\xi\right] \tag{11}$$

where

$$V_m = \frac{G}{rB\rho}\left[\left(\frac{\partial u}{\partial s}\right)^2 + \left(\frac{\partial u}{\partial t}\right)^2\right]^{1/2} \tag{12}$$

The terms on the right-hand side of equation (11) are determined from the elliptic solution of the stream function equation at a reduced mass flow rate. Outside the blade channel, the angle β is not known and is therefore eliminated using the relation

$$\sin\beta = V_\theta / V. \tag{13}$$

The solution to equations (8) through (13) provides averaged blade-to-blade gas velocity components and the density at the orthogonal mesh grid points. In addition, the following velocity gradient equation is used to calculate the blade-to-blade variation in the flow velocity during the particle trajectory computations.

$$\frac{\partial V}{\partial\theta} = \cos\beta\frac{d(rV_\theta)}{dm} \tag{14}$$

where m is the direction of the meridional streamline. Katsanis [13] compared the calculated blade surface velocities using the above equation to those obtained from a subsequent blade-to-blade solution. The agreement between the two results is very satisfactory for the purpose of the trajectory calculation, and only the trajectories of extremely small particles will be sensitive to the large flow deceleration near the blade leading edge.

Results and Discussion

Some representative results of the particle trajectory computations are presented in the inlet flow field with 12 swirling vanes shown in Fig. 4. The hub ad tip annulus contours and the swirling vanes are designed to direct the ingested particles in the radial direction for separation. The annulus inlet area is equal to 0.6822 ft^2 (0.0634 m^2) and the total mass flow is 11.675 lb/s (5.296 kg/s) of which 10 lb/s (4.536 kg/s) go through the engine compressor and the rest is scavenged to separate the particles. The 2.73 in. (0.069 m) chord vanes with zero inlet angle and a linear variation in the exit angle from 43.46 deg at r = 4.455 in. (0.113 m) to 33 deg at r = 6.55 in. (0.166 m) are placed in a highly contoured hub section which is designed to reflect the particles in the radial direction. The large variations in the flow path due to hub and tip contouring combine with the twisted vanes to produce large radial and axial flow accelerations. The results of the trajectory computations are presented for different particle sizes to show the effect of these large accelerations, annulus contours and vane geometries. The location and frequency of particle vane impacts as well as the impact velocities and impact angles are presented for different particle sizes and the resulting vane erosion pattern discussed.

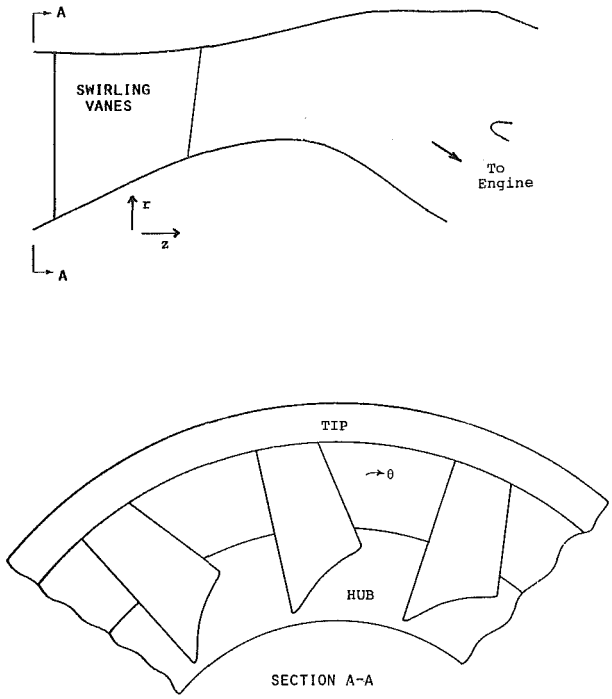

Fig. 4 Schematic inlet separator

The trajectories of several 100 micron particles entering at the same circumferential location are shown in Fig. 5. It can be seen from this figure that the hub impacts reflect the particles in the radial direction while the vane impacts reflect the particles in the circumferential direction. After the vane impacts, the particles travel in the radial direction under the effect of the centrifugal forces. In both cases, subsequent tip impacts reflect the particles in the radial inward direction towards the engine inlet. One can see in the figure, the big difference between the trajectories of the particles impacting the boundaries and those traversing the flow field without impacts. The latter proceed practically at constant velocity and are unaffected by the flow field. One can conclude that the larger particle trajectories are dominated by their boundary impacts which reduce their velocities, alter the direction of their motion, and cause their redistribution in the flow field.

The trajectories of the 10 micron diameter particles are shown in Fig. 6 from which one can see that the trajectories of these small particles are strongly influenced by the flow field. They tend to acquire the gas velocity and their trajectories are close to the flow streamlines. Fewer of these small particles impact the hub annulus and the vanes and the effect of these impacts on the particle trajectories is much less significant than the influence of the flow field. One can conclude from the presented results that the accurate three dimensional representation of the flow field and the blade geometry is essential in the particle trajectory calculations, with the former influencing the smaller particles and the latter the larger particles.

The effect of the particle size on the performance of this integrated inlet separator is shown in Fig. 7. One can see that, while it is highly effective in separating a wide range of in-

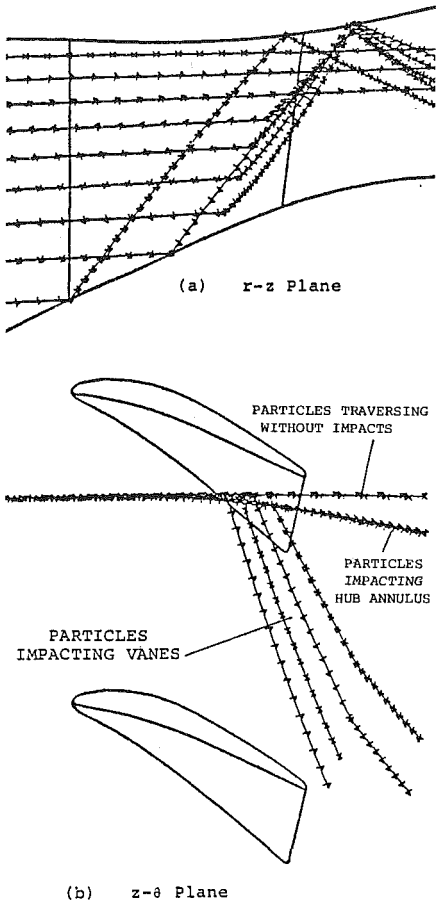

Fig. 5 Effect of initial location on the trajectories of 1000 micron particles through twisted blade row

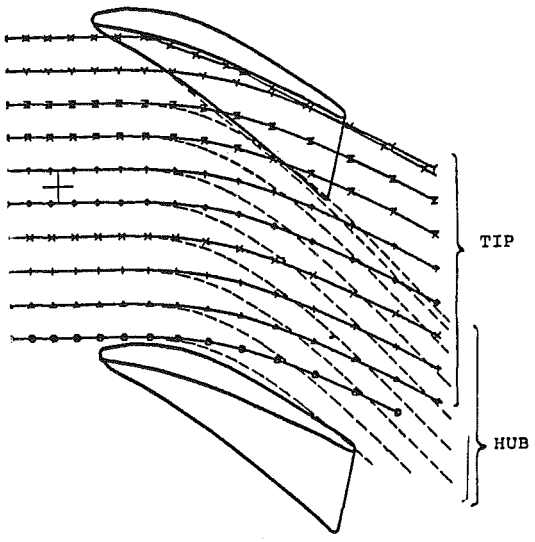

Fig. 6 Effect of initial location on the trajectories of 10 micron particles through twisted blade row

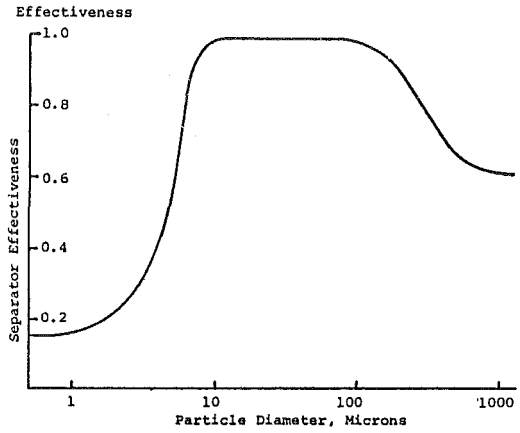

Fig. 7 Effect of particle size on separator effectiveness

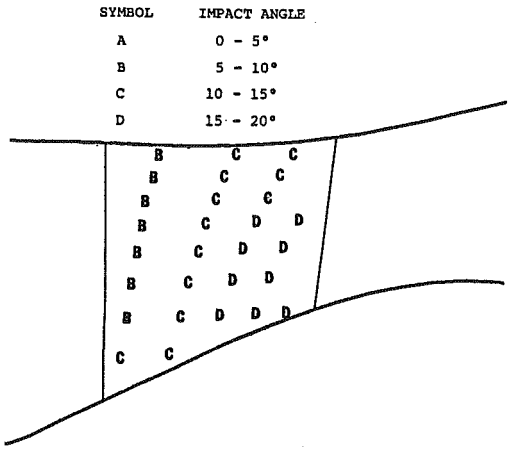

Fig. 8 1000 micron particle vane impact angles

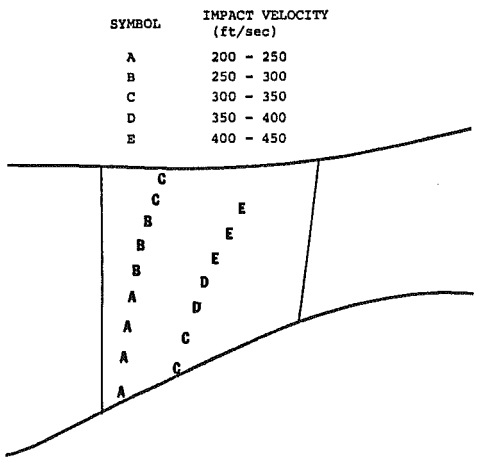

Fig. 9 10 micron particle van impact velocities

termediate size particles, the effectiveness diminishes for extremely small and extremely large particle sizes [14]. The drop in the separator effectiveness for the smaller particles is caused by their tendency to follow the bulk of air flow into the compressor. On the other hand, the drop in separator effectiveness for very large particles is caused by the tip impacts that reflect the particles in the inward radial direction and into the compressor.

The impact locations of the 1000 micron particles with the vanes are shown in Fig. 8. Different symbols are used to show the impact angle variation along the vane surface. The impacts are seen to be distributed over all of the vane concave surface, but the impact angles increase towards the trailing edge and the hub. The impact velocities are practically the same at all locations and equal to the initial particle velocity for these large particles. Since the maximum erosion of stainless steel occurs at impact angles around 25 deg, one can concude that the twisted vane geometry reulsts in increased vane erosion patterns toward the hub and trailing edge corner.

Figure 9 shows the vane impact location for the 10 micron particles with different symbols used to show the impact velocities. One can observe the large variation in the impact

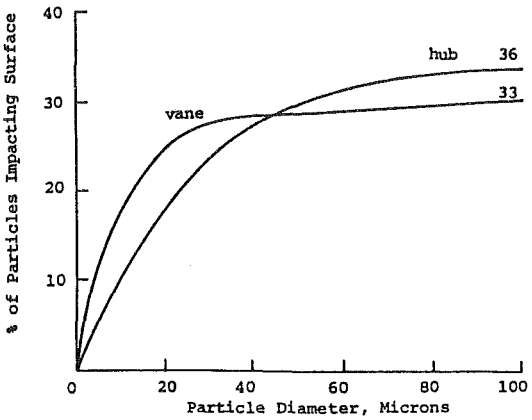

Fig. 10 Effect on particle size on frequency of impacts

velocities of these small particles as they change with the local gas velocities. The impact velocities are greater in the regions of higher flow velocities toward the tip. These small particles quickly recover their velocities after the initial vane impacts shown in Fig. 9. They later experience repeated impacts with the vanes at extremely small impingement angles which are not included in the figure. The vane erosion due to small particle impacts increases with the increased impact velocities near the pressure surface mid-chord toward the tip.

The frequency of particle vane impacts depends on the concentration of particles in the gas flow and on the percentage of particles that actually impact the vanes. Figure 10 shows the variation in the percentage of particles that impact the vane surface and hub annulus with the particle sizes. The percentage increases with increased particle size and asymptotically reaches fixed values for very large particle sizes that are generally dependent on the vane and hub geometry. The presented results were obtained using a 20 × 40 grid for flow field representation. The average CPU time was 0.025 second per particle trajectory, on AMDAHL 370.

Conclusions

The small and large particle trajectories display different characteristics in the same flow field. The smaller particles tend to follow the streamlines, acquire the local gas velocities, and have fewer impacts with the blades and annulus boundaries. As the size of particles increases, the influence of the flow field on their trajectories decreases. The larger particles have more tendency to impact the blade surface and hub and tip annulus, and their trajectories are dominated by these particle metal interactions. The presented results demonstrate the influence of the radial variation in vane shape and of hub and tip contours no the particle trajectories.

Acknowledgment

This research was sponsored by U.S. Army Research Office, Durham, North Carolina, under Grant No. DAAG29-82-K-0029.

References

1 Tabakoff, W., and Hamed, A., "Aerodynamic Effects on Erosion in Turbomachinery," JSME and ASME Paper No. 70, 1977 Joint Gas Turbine Congress, Tokyo, Japan, May 1977, pp. 574–581.

2 Tabakoff, W., Hamed, A., and Ramachandran, J., "Study of Metal Erosion in High Temperature Coal Gas Stream," ASME *Journal of Engineering for Power*, Vol. 102, Jan. 1980, pp. 148–152.

3 Kriebel, A. R., "Particle Trajectories in a Gas Centrifuge," ASME *Journal of Basic Engineering*, Vol. 83, Part 2, Sept. 1961, pp. 333–340.

4 Lapple, C. E., and Sheperd, C. B.,"Calculation of Particle Trajectories," *Industrial and Engineering Chemistry*, Vol. 32, No. 5, May 1940, pp. 605–617.

5 Fabian, J. M., and Oates, G. C., "Analysis of Flows Within Particles Separators," ASME Paper No. 77-WA/FE-21, 1977.

6 Hussein, M. F., and Takakoff, W., "Computation and Plotting of Solid Particle Flow in Rotating Cascades," *Computers and Fluids*, Vol. 2, 1974, pp. 1–15.

7 Hussein, M. F., and Tabakoff, W., "Dynamic Behavior of Solid Particles Suspended by Polluted Flow in a Turbine Stage," *Journal of Aircraft*, Vol. 10, No. 7, July 1973, pp. 434–440.

8 Tabakoff, W., Hamed, A., and Hussein, M. F., "Experimental Investigation of Gas Particle Flow Trajectories and Velocities in an Axial Flow Turbine Stage," ASME Paper No. 72-GT-57.

9 Tabakoff, W., Hamed, A., and Hussein, M. F., "Experimental Investigation of Gas Particle Flow in a Simulated Axial Flow Compressor Stage," University of Cincinnati, Project Themis Report No. 71-21, 1971.

10 Tabakoff, W., and Hussein, M. F., "Properties and Particle Trajectories of Gas Particle Flows in Cascades," AIAA Paper No. 70-712, 1970.

11 Beacher, B., Tabakoff, W., and Hamed, A., "Improved Particle Trajectory Calculations Through Turbomachinery Affected by Coal Ash Particles," ASME *Journal of Engineering for Power*, Vol. 140, 1982, pp. 64–68.

12 Katsanis, T., and McNally, W. D., "Revised Fortran Program for Calculating Velocities and Streamlines on the Hub-Shroud Mid-Channel Stream Surface of an Axial, Radial, or Mixed Flow Turbomachine or Annular Duct; Vols. 1 and 2," NASA TDN 8430 and NASA TND 8431, 1977.

13 Katsanis, T., "Fortran Program for Calculating Transonic Velocities on a Blade-to-Blade Stream Surface of a Turbomachine," NASA TND 2809, May 1965.

14 Hamed, A., "Particle Dynamics of Inlet Flow Fields with Swirling Vanes," *Journal of Aircraft*, Vol. 19, No. 9, 1982, pp. 707–712.

O. Kafri

A. Livnat

I. Glatt

Nuclear Research Center—Negev,
Beer-Sheva 84190
Israel

Temporally Stable Density Patterns in Liquids

By applying a new optical technique, moire deflectometry, we have observed complex density patterns in apparently homogeneous solutions, under ambient conditions. The density patterns of the liquids are attributed to cooling due to evaporation, precipitation caused by gravity, or dissolution.

Introduction

Liquids at equilibrium, like water in glass, are intuitively considered a homogeneous phase. The thermodynamic argumentation to this statement is, that at equilibrium, the most stable state is the one with maximum entropy, namely, that of uniform distribution.

In this communication we report on observations of temporally stable density structures in pure liquids and aqueous solutions under ambient conditions. In some of the liquids inspected the steady state density patterns are of a dynamic nature. The density patterns can be attributed to the various processes, taking place in the liquid, like evaporation, sedimentation due to gravity or dissolution.

In the observations reported a new optical technique for density gradient detection, moire deflectometry, has been applied. First we shall present the technique, and then we shall describe the observations made in the various liquids, and discuss their significance.

The Measuring System

When a collimated beam of light passes through a phase object, for example, a transparent liquid having density gradients along an axis, perpendicular to the direction of propagation of the light, the rays are deflected from their original course. A new method, moire deflectometry (1), has been developed for mapping of the ray deflections. The deflectometer is based on moire effect, which is demonstrated in Fig. 1.

When two identical transmission gratings are superimposed, creating a small mutual angle θ, a moire pattern is formed. Note that the direction of the fringes is perpendicular to the bisector of the grooves of the two gratings. For small θ's the density of the fringe pattern is proportional to θ, namely, $p' = p/\theta$, where p and p' denote the pitch of the gratings and of the moire pattern, respectively, and θ is expressed in radians. If the two gratings are put apart, at a distance Δ (see Fig. 2), then, a noncollimated beam traversing the pair of gratings will form a distorted moire pattern, known as "moire deflectogram." The fringe deviation from

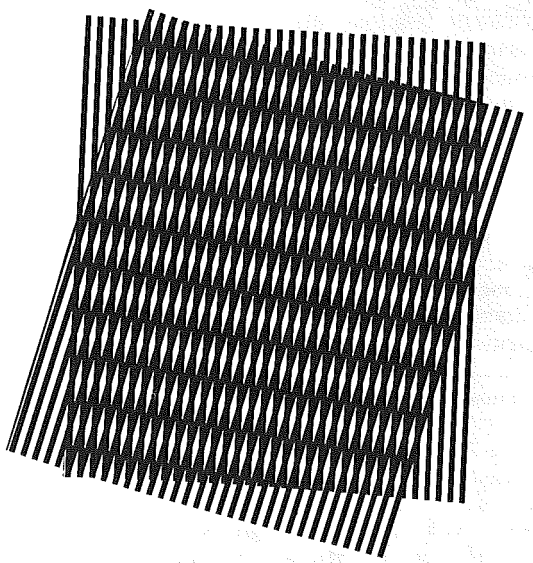

Fig. 1(*a*)

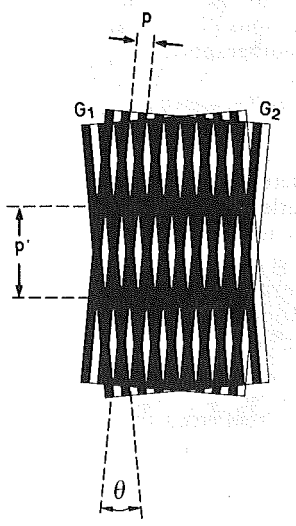

Fig. 1(*b*)

Fig. 1(*a*) Photograph of a moire pattern obtained by superposition of two gratings. (*b*) Fig. 1(*a*) enlarged. Legend: θ—mutual angle of rotation, p—pitch of the gratings, p'—pitch of the moire pattern.

Contributed by the Fluids Engineering Division for publication in the JOURNAL OF FLUIDS ENGINEERING. Manuscript received by the Fluids Engineering Division, June 7, 1983.

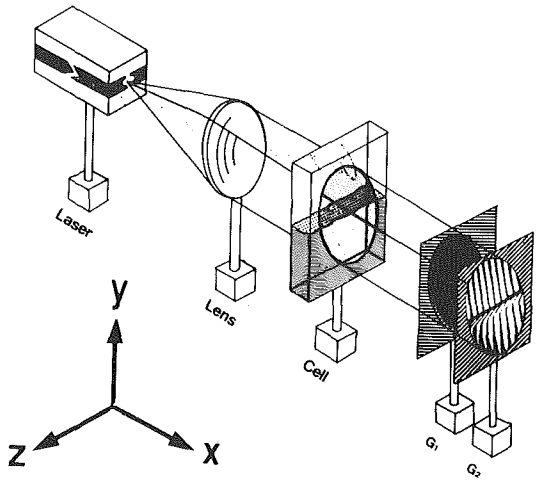

Fig. 2 Experimental setup

the undistorted position, h, is directly proportional to the angle of ray deflection ϕ (1):

$$h = \frac{\phi \Delta}{\theta} \tag{1}$$

ϕ is related to the gradient of the index of refraction, n, along the optical path, in the paraxial approximation (1), by:

$$\phi = \frac{1}{n_f} \int \frac{\partial n}{\partial y} dx, \tag{2}$$

where n_f is the refraction index at the exit from the phase object, and the integration is performed along the optical path. It was shown (1) that the sensitivity, obtained by moire deflectometry, may reach that achieved by interferometric techniques. However, since the distance between the gratings is variable, the sensitivity can be tuned to meet lower requirements, thus enabling work under considerably low mechanical stability. In interferometry, to compare with, the mechanical stability required is determined by λ, the wavelength of light, rather than by the sensitivity requested.

Figure 2 presents schematically the experimental setup. A collimated HeNe laser beam, expanded by a telescope, is passed through the sample cell. The cell is a rectangular glass container with an optical length of 74 mm. The distorted beam then enters the deflectometer, a pair of gratings, with a nearly horizontal groove alignment, to allow measuring of vertical ray deflections. The moire pattern is projected on a mat screen and photographed.

Results

Pure Liquids. The glass cell was filled with distilled water up to a point, where both the liquid phase and the air above it appear in the deflectogram. Fig. 3(*a*) is a deflectogram of water, obtained when the cell is covered. The straight parallel fringes in the upper part belong to the air phase. One can see a dark boundary layer, where the rays are strongly deflected, which is caused by wetting of the front and rear windows of the cell due to the adhesive force. The lower section of the picture shows the liquid phase. The non-uniformity of the fringe is attributed to imperfections in the cell.

If the cover is removed, then, within few seconds the continuity of the moire pattern at the upper layer of the water is broken, and the fringes rotate clockwise as shown in Fig. 3(*b*). In the experimental configuration, where the front grating, G_1, is rotated counter-clockwise relative to the rear grating, G_2, this means that the rays are deflected upwards, or, that the upper liquid layer (about 10 mm thick) has a higher density, compared to the bulk. When the cover is returned, or the liquid is stirred, the fringes straighten up again. The explanation to this phenomenon is rather simple. When the cover is removed the rate of evaporation increases,

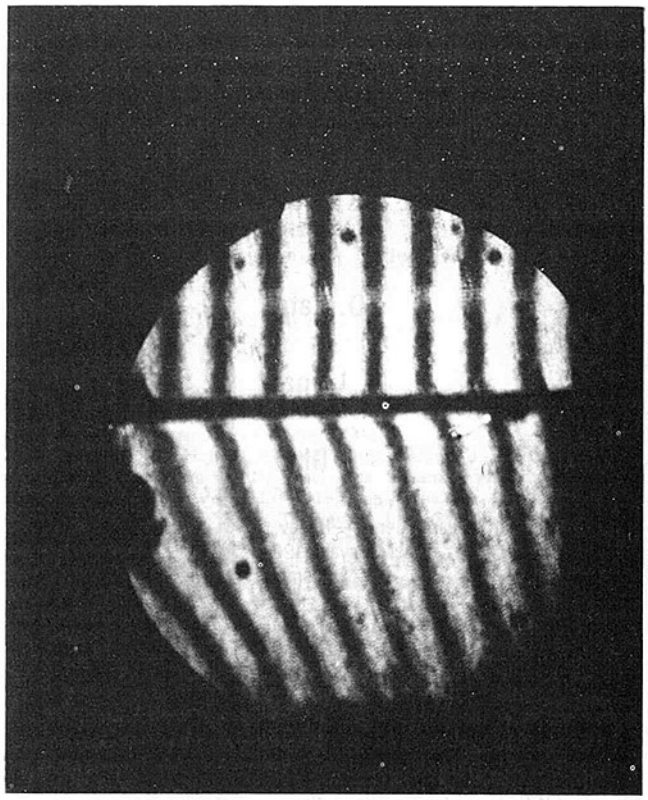

Fig. 3(*a*) Deflectogram of water in a covered cell

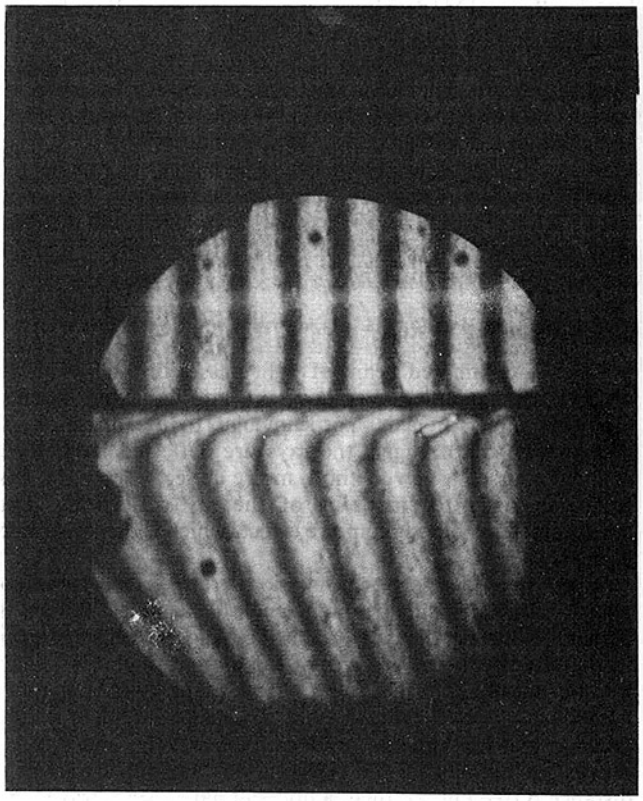

Fig. 3(*b*) Deflectogram of water in an open cell

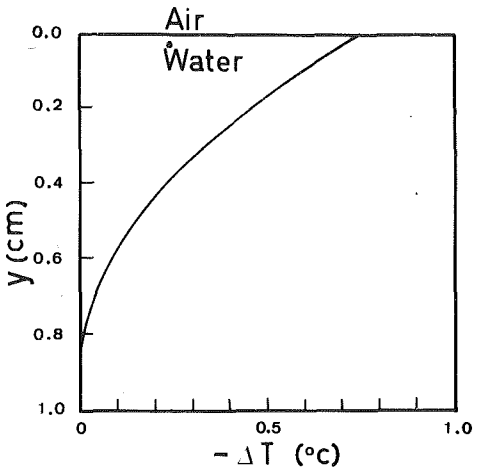

Fig. 4 The decrease in temperature of water near the air-water interface versus the distance from the interface

and the upper layer cools down. From the fringe shift, we can easily calculate the temperature profile of this layer.

The thermal expansion coefficient, γ, of water is 1.8×10^{-4} $°C^{-1}$ at 18°C (2), whereby:

$$\frac{\delta V}{V} = \gamma \delta T, \tag{3}$$

where δV is the change in the volume, V, as the temperature is varied by δT. Since $\delta V/V = -\Delta\rho/\rho$, where ρ is the specific gravity, and the index of refraction of water can be approximated, for small variations in ρ, to $n = 1 + 0.334\rho$ (3), we obtain:

$$\frac{\delta n}{n} = -\gamma \delta T. \tag{4}$$

Assuming that the changes in n are small, the temperature gradient can be related to the refractive index by:

$$\frac{\partial T}{\partial y} = -\frac{1}{n\gamma}\frac{\partial n}{\partial y}. \tag{5}$$

Further, we assume that the temperature gradient falls linearly with the distance from the interface, and obtain an expression:

$$\frac{\partial T}{\partial y} = \left(\frac{\partial T}{\partial y}\right)_{\max}\left(1 - \frac{y}{l}\right), \text{ for } y < l \text{ and zero otherwise,} \tag{6}$$

where l is the thickness of the cooler layer, and $(\partial T/\partial y)_{\max}$ is the temperature gradient calculated at the air-water interface. $\partial n/\partial y$ is calculated from equation (2). Assuming that $\partial n/\partial y$ does not depend on x it can be factored out of the integration. ϕ is calculated from the fringe deviation, using equation (1). θ is simply the ratio between p and p'. The temperature at any given point $y < l$ is obtained from the integration of equation (6), namely:

$$T = T0 + \int_l^y \frac{\partial T}{\partial y}\, dy = T_0 + \left(\frac{\partial T}{\partial y}\right)_{\max}\left(y - \frac{y^2}{2l}\right)\Bigg|_l^y, \tag{7}$$

where $T0$ is the bulk temperature.

In this measurement l = 9 mm, h = 13.4 mm, p = 0.17 mm, p' = 7 mm, and Δ = 140 mm. The maximum decrease of the temperature, at the interface, was 0.75 °C. Figure 4 shows the temperature variation along the cool layer.

The behavior of other liquids with higher vapor pressures, i.e., methanol, ethanol, hexane, acetone, has also been investigated. In an open container the liquid becomes very inhomogeneous and a speckle pattern appears, probably, due to vigorous evaporation. This is demonstrated in Fig. 5(*a*), which is a deflectogram of ethanol in an open container. Figure 5(*b*) is a deflectogram of methanol in a covered cell.

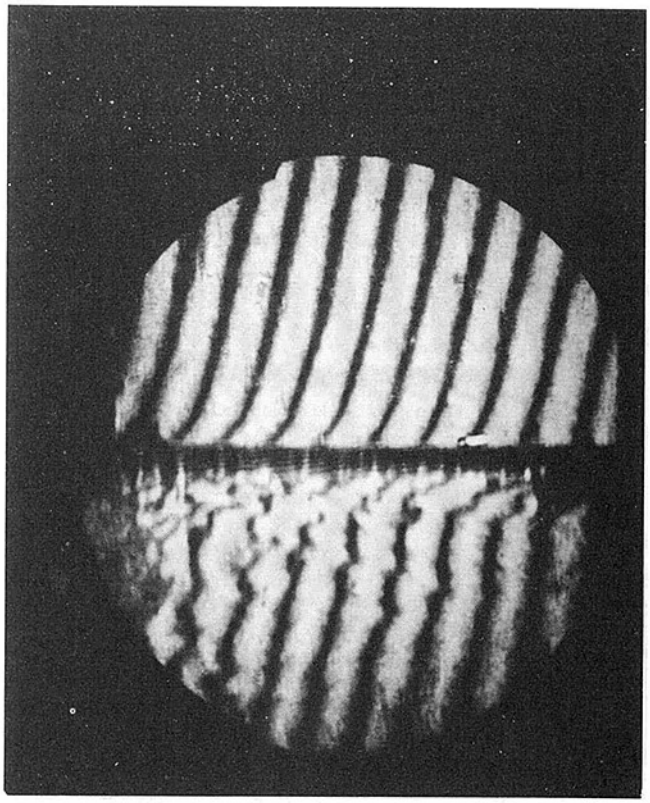

Fig. 5(*a*) Deflectogram of ethanol in an open cell

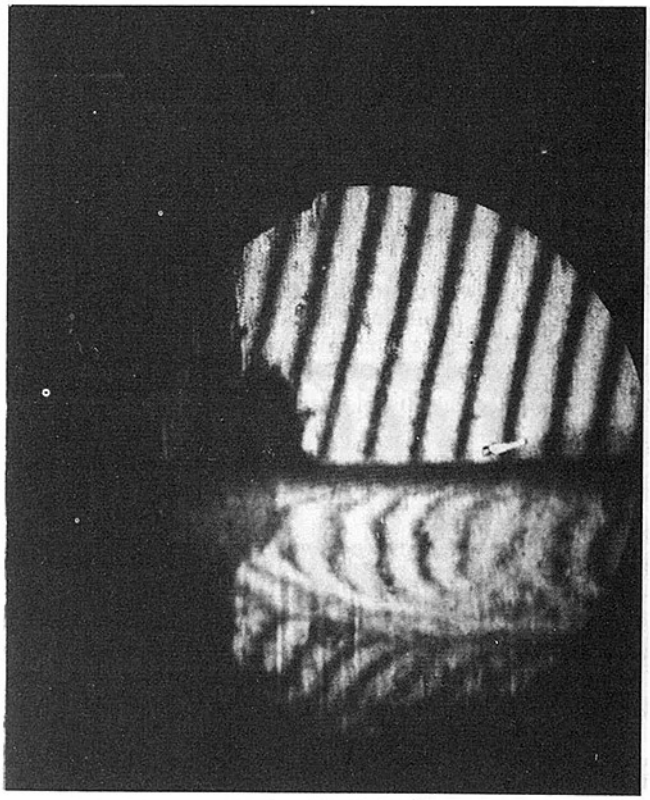

Fig. 5(*b*) Deflectogram of methanol in a covered cell

Besides the increase in the density at the upper layer as in water, a new phenomenon, formation of a boundary layer of higher density, about 20 mm below the surface, is observed. The behavior of the fringes in this zone is similar to that of

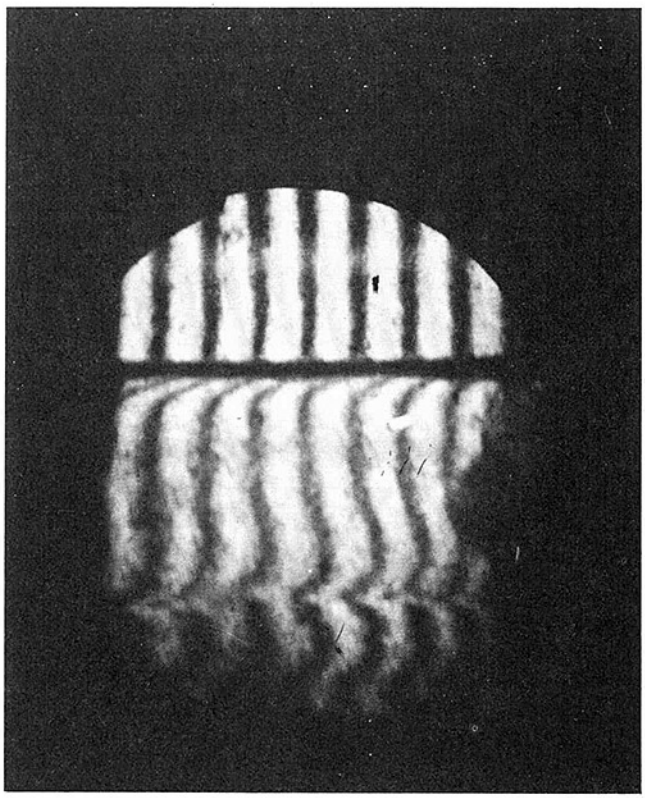

Fig. 6(*a*) Deflectogram of an aqueous solution of sodium sulfite 2 min after adding the salt

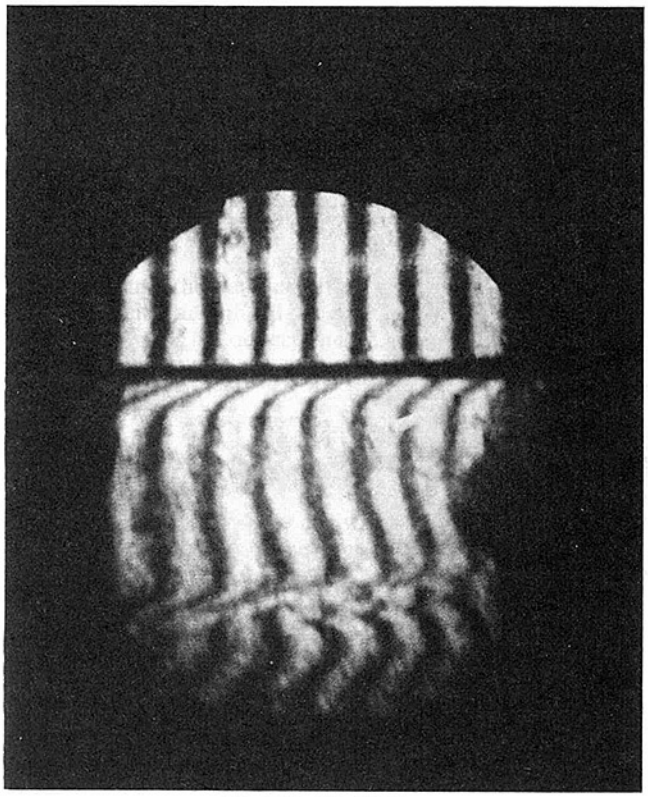

Fig. 6(*b*) 30 min later

fringes of a shock wave, seen in a wind tunnel (4). A possible explanation to this behavior is the effect of gravity on the higher density layer, which caused convective motion. Although it seems that this pattern is of dynamic nature, unless mixing is involved it is temporally stable.

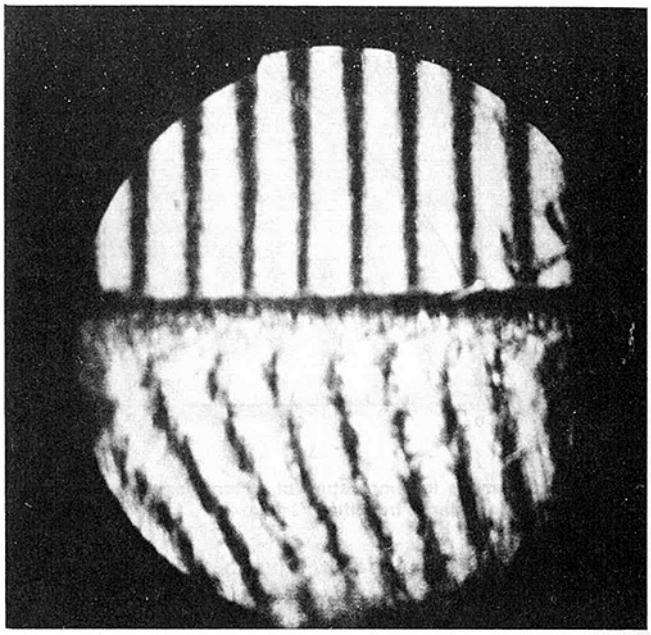

Fig. 7 Deflectogram of a 20 percent-weight solution of sodium sulfite in water, in an open cell

Solutions

Two types of density patterns have been observed in aqueous solutions. The first is seen in a solution in which the solute concentrates in excess at the bottom of the cell, and the second is typical to "homogeneous," well-stirred solutions. If the solute is in excess it does not always mean that the solution is saturated. This can also occur in spontaneous dissolution without stirring. Figures 6(*a*) and 6(*b*) are deflectograms of solutions of sodium sulfite in water. Figure 6(*a*) is the pattern formed few minutes after adding the salt, while Fig. 6(*b*) is the pattern half an hour later. In Fig. 6(*b*) we see a layer of sharp gradients, resembling a shock wave pattern, about 30 mm below surface, implying the existence of two well-defined layers of different concentrations. Again, this pattern is temporally stable. The concentration difference was calculated in a way, similar to the temperature calculation in water, and is about 0.1 percent-weight. We found that the index of refraction of the sodium sulfite solution obeys $n = 1.33 + 3.5 \times 10^{-3}c$, where c is the concentration in percent-weight.

The second effect was observed in saturated solutions, and we can only describe it qualitatively. For demonstration, a solution of 20 percent-weight of sodium sulfite in water has been prepared. When evaporation is avoided the moire fringes are straight, similar to those of water shown in Fig. 3(*a*). When the cover is removed, then, within about 10 sec the fringes rotate clockwise exactly as in Fig. 3(*b*), but a few seconds later, the pattern becomes grainy and a fallout of small speckles is observed (see Fig. 7). This phenomenon lasts as long as the cell remains uncovered. When the container is covered again the sharp straight fringe pattern is restored. A possible explanation to the effect is, that due to cooling of the solution near the surface, salting out takes place, and clusters of hydrated salt precipitate to the bottom of the cell (5).

Summary

Many chemical reactions of industrial or biological importance take place in the liquid phase. Chemists do often treat liquids as homogeneous media, while we have shown here, applying moire deflectometry, that this is seldom true. On the contrary, liquids in open containers, without stirring,

develop density gradients, due to cooling through evaporation, or precipitation caused by gravity.

A physical limitation of moire deflectometry which is common to all the optical techniques is absorption by the tested liquid. Turbulent motion of the fluid reduces the fringe contrast, but the pattern can be still discerned working at lower sensitivity (6). To avoid undesired ray deflection by the surroundings optical flats at highly parallel configuration are required. Finally, since the deflection is integrated over the optical path, the technique is insensitive to density fluctuations along the axis of light propagation.

Despite these limitations, this new technique may be of interest in studies of the formation of macroscopic patterns in chemical systems far from equilibrium (7), or the behavior of highly concentrated solutions in nonequilibrium (8, 9). It can find practical applications in solar pond study or ocean research.

Acknowledgment

We thank D. Avnir and M. Kagan for their useful comments.

References

1 Kafri, O., *Opt. Lett.*, Vol. 5, 1980, p. 555; *Phys. Bull.*, Vol. 33, 1982, p. 197.
2 Weast, R. C., Ed., *Handbook of Chemistry and Physics*, 48th Edition (The Chemical Rubber Co., Ohio, USA, 1967-1968) p. F-4.
3 ibid, p. E-159.
4 Stricker, J., and Kafri, O., *AIAA Journal*, Vol. 20, 1982, p. 820.
5 Shuker, R., and Gammon, R. W., *J. Chem. Phys.*, Vol. 55, 1971, p. 4784.
6 Glatt, I., and Kafri, O., "Analysis of the Turbulent Mixing of Liquids by Moire Deflectometry," *Chem. Eng. Sci.*, in press.
7 Kagan, M., Levi, A., and Avnir, D., *Naturwiss.*, Vol. 69, 1982, p. 548; D. Avnir, M. Kagan, and A. Levi, ibid, Vol. 70, 1983, p. 144.
8 Gambale, F., and Gliozzi, A., *J. Phys. Chem.*, Vol. 76, 1972, p. 783.
9 Crapper, P. F., *Nature*, Vol. 260, 1976, p. 308.

Hydrodynamics in Tubes Perturbed by Curvilinear Obstructions

A. K. Rastogi
A.S. Veritas Research,
Det norske Veritas,
Høvik, Norway;
present address:
Institut für Hydromechanik,
Universität Karlsruhe,
D-7500 Karlsruhe 1, FRG

A calculation procedure for two-dimensional separated flows over curved boundaries, e.g., flow in constricted tubes, is described. The method is based on the numerical solution with finite differences of the governing equations in orthogonal curvilinear coordinates. A body fitted curvilinear orthogonal numerical grid is generated first which is then employed for the solution of partial differential equations governing fluid flow. Results of calculations are presented for laminar and turbulent flows in constricted tubes. For turbulent flow calculations the k-ϵ turbulence model has been employed. Comparison between computed and measured values of flow quantities is also presented and is discussed in some detail. Although the present paper deals only with constricted pipes, the method developed is general and can be used without difficulty for two-dimensional flows over other curved boundaries.

1 Introduction

Motivation for the present work comes from safety aspects of offshore pipelines. It is often experienced in offshore practice that the regions of pipelines where the flow conditions are disturbed, e.g., in a teejoint or a bend or near a constriction, are more prone to internal corrosion attacks. Constrictions caused by welded joints in straight pipelines present serious corrosion problems, firstly due to microstructural changes and secondly due to altered flow conditions [1]. Usually the heat affected zone (within 25 mm of the weld) and the flow affected areas as a result of flow separation and high turbulence levels overlap which makes these regions critical. The present paper deals with the flow behavior in constricted tubes in detail (see Fig. 1). Work reported is limited to single-phase flows.

Flow characteristics in constricted tubes are studied theoretically with the help of partial differential equations governing mass and momentum conservation. A general calculation method is presented to solve numerically the two-dimensional form of these equations in curvilinear orthogonal coordinate system. The purpose of the present work is to provide a design method for optimizing the weld shape in pipelines so that the flow disturbance can be minimized. The method is capable of calculating both laminar and turbulent flow over various curved boundaries. It is, thus suitable for the above purpose as well as for many other flow problems in engineering practice.

The governing equations for mass and momentum conservation in curvilinear orthogonal coordinate system are presented in the next section. The solution procedure employing finite differences is also briefly discussed. This solution requires a curvilinear orthogonal numerical grid. The method of generating such a grid is described in Section 3. Calculations are carried out for two types of pipe contrictions. A geometry similar to welded joints (Fig. 1(*a*)) and a second one with a more gradual change in the cross-sectional area (Fig. 1(*b*)) which is typical of arterial stenosis, have been used to demonstrate the calculation method. With respect to area reduction, the constrictions shown in Fig. 1 are much more severe than those found in offshore practice. These geometries (Fig. 1) have been chosen for the present work because they have been studied experimentally and present suitable test cases for the calculation method. The results of the computations and their comparison with published experimental data are presented in Section 4. Concluding remarks are given in Section 5.

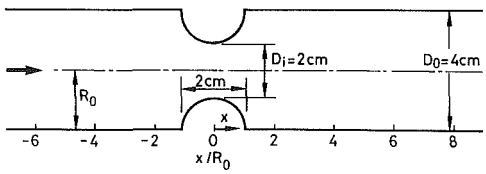

Fig. 1(*a*) Pipe with a weld constriction

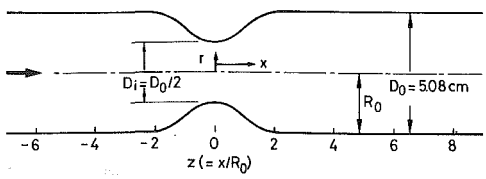

Fig. 1(*b*) Pipe with a stenosis constriction

Contributed by the Fluids Engineering Division for publication in the JOURNAL OF FLUIDS ENGINEERING. Manuscript received by the Fluids Engineering Division, April 19, 1982.

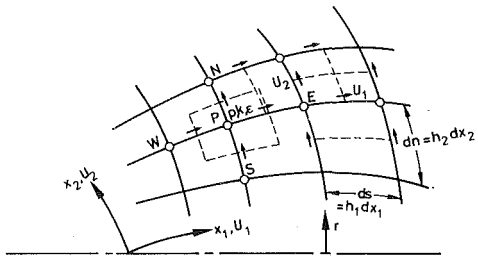

Fig. 2 Coordinate system and grid disposition

2 Governing Equations and Their Solution

The flow under consideration is axisymmetric and can be represented by conservation equations written in the cylindrical polar coordinate system. The numerical solution of these equations, however, presents difficulties in the specification of boundary conditions along curved boundaries which do not coincide with one of the coordinate directions. These difficulties are not unsurmountable; numerical calculations of flows over curved boundaries which employ the standard cartesian or cylindrical polar coordinate system have been carried out [2, 3]. Instead of using standard cartesian or cylindrical polar coordinates, the present work employs a body-fitted orthogonal coordinate system which completely avoids the above mentioned difficulties. The use of body-fitted coordinates provides a much more general method of solution. The curvilinear orthogonal coordinate system employed is shown in Fig. 2 where the metric coefficients are also defined. The partial differential equations governing steady viscous fluid flow have the following form in the coordinate system shown in Fig. 2:

Continuity:

$$\frac{1}{h_1 h_2 r}\left[\frac{\partial}{\partial x_1}(\rho h_2 r U_1) + \frac{\partial}{\partial x_2}(\rho h_1 r U_2)\right] = 0 \tag{1}$$

x_1-momentum conservation:

$$\frac{1}{h_1 h_2 r}\left[\frac{\partial}{\partial x_1}(\rho h_2 r U_1^2) + \frac{\partial}{\partial x_2}(\rho h_1 r U_1 U_2)\right]$$
$$= -\frac{1}{h_1}\frac{\partial P}{\partial x_1} + S_{U_1} + \frac{1}{h_1 h_2 r}\left[\frac{\partial}{\partial x_1}\left(\frac{\mu h_2 r}{h_1}\frac{\partial U_1}{\partial x_1}\right) + \frac{\partial}{\partial x_2}\left(\frac{\mu h_1 r}{h_2}\frac{\partial U_1}{\partial x_2}\right)\right] \tag{2}$$

x_2-momentum conservation:

$$\frac{1}{h_1 h_2 r}\left[\frac{\partial}{\partial x_1}(\rho h_2 r U_1 U_2) + \frac{\partial}{\partial x_2}(\rho h_1 r U_2^2)\right]$$
$$= -\frac{1}{h_2}\frac{\partial P}{\partial x_2} + S_{U_2} + \frac{1}{h_1 h_2 r}\left[\frac{\partial}{\partial x_1}\left(\frac{\mu h_2 r}{h_1}\frac{\partial U_2}{\partial x_1}\right) + \frac{\partial}{\partial x_2}\left(\frac{\mu h_1 r}{h_2}\frac{\partial U_2}{\partial x_2}\right)\right] \tag{3}$$

Equations (1) to (3) have the same form as the equations written in conventional coordinate systems except for the presence of metric coefficients and the source terms in the momentum equations. These source terms are:

$$S_{U_1} = \rho U_2^2 \frac{\partial h_2}{\partial x_1}/h_1 h_2 - \rho U_1 U_2 \frac{\partial h_1}{\partial x_2}/h_1 h_2$$
$$- \frac{1}{h_1 r}\frac{\partial r}{\partial x_1}\left[\frac{2\mu U_1}{h_1 r}\frac{\partial r}{\partial x_1} + \frac{2\mu U_2}{h_2 r}\partial r/\partial x_2\right]$$
$$+ \frac{1}{h_1 h_2 r}\left[\frac{\partial}{\partial x_1}\left(\frac{\mu h_2 r}{h_1}\frac{\partial U_1}{\partial x_1} + \frac{2\mu U_2 r h_2}{h_1 h_2}\frac{\partial h_1}{\partial x_2}\right)\right.$$
$$\left. + \frac{\partial}{\partial x_2}\left(\frac{\mu r h_1 h_2}{h_1}\frac{\partial}{\partial x_1}(U_2/h_2) - \frac{\mu h_1 r U_1}{h_1 h_2}\frac{\partial h_1}{\partial x_2}\right)\right]$$
$$- \frac{1}{h_1 h_2}\frac{\partial h_2}{\partial x_1}\left[\frac{2\mu}{h_2}\frac{\partial U_2}{\partial x_2} + \frac{2\mu U_1}{h_1 h_2}\frac{\partial h_2}{\partial x_1}\right]$$
$$+ \frac{1}{h_1 h_2}\frac{\partial h_1}{\partial x_2}\left[\frac{\mu h_2}{h_1}\frac{\partial}{\partial x_1}\left(\frac{U_2}{h_2}\right) + \frac{\mu h_1}{h_2}\frac{\partial}{\partial x_2}\left(\frac{U_1}{h_1}\right)\right] \tag{4}$$

S_{U_2} = Same as (4) by interchanging 1 and 2 (5)

Equations (1) to (5) can be formally derived employing conservation principles or more rigourously arrived at by using coordinate transformation. Rigorous derivations can be seen in reference [4] for two-dimensions and in reference [5] for three dimensions. A useful compilation of the conservation equations in orthogonal curvilinear coordinates is given in reference [6]. The above equations form a closed set for laminar flows. For turbulent flows the same set of equations can also be solved, taking U_1 and U_2 to represent the time averaged values of velocities and replacing μ by $(\mu + \mu_t)$ as a result of the eddy viscosity hypothesis. The k-ϵ model of turbulence has been employed to close the set of equations for turbulent flow, i.e.,

$$\mu_t = \rho c_\mu k^2/\epsilon \tag{6}$$

Nomenclature

C_1, C_2, C_μ = empirical constants
D_0 = pipe diameter
h_1, h_2 = metric coefficients
K = mass transfer coefficient
K_0 = K for smooth tube
$K_a = \frac{\nu}{U_G^2}\frac{dU_G}{dx}$ = acceleration parameter
k = turbulent kinetic energy
k_{cL} = k at center line
m = mass flow rate
P = pressure
P_r = production of turbulent kinetic energy
R_0 = pipe radius
$\mathrm{Re} = \frac{\bar{U} D_0}{\nu}$ = Reynolds number
r = radial direction
Sc = Schmidt number
$\mathrm{Sh} = \frac{K D_0 \mathrm{Sc}}{\nu}$ = Sherwood number
$U, \bar{U}_{\mathrm{in}}$ = axial velocity, at inlet
U_1, U_2 = velocities in x_1 and x_2 directions
U_G = free stream velocity
x_1, x_2 = orthogonal coordinate directions
x, z = axial direction, x/R_0
ρ = density
ϵ = dissipation rate of k
μ = laminar viscosity
μ_t = turbulent viscosity
ν = kinematic viscosity
$\sigma_k, \sigma_\epsilon$ = empirical constants
ψ, ψ_m = stream function, maximum value

and k are ϵ are obtained by solving their conservation equations:

$$\frac{\partial}{\partial x_1}(\rho h_2 r U_1 k) + \frac{\partial}{\partial x_2}(\rho h_1 r U_2 k) = \frac{\partial}{\partial x_1}\left(\frac{\mu_t h_2 r}{\sigma_k h_1}\frac{\partial k}{\partial x_1}\right) + \frac{\partial}{\partial x_2}\left(\frac{\mu_t h_1 r}{\sigma_k h_2}\frac{\partial k}{\partial x_2}\right) + S_k h_1 h_2 r \tag{7}$$

$$\frac{\partial}{\partial x_1}(\rho h_2 r U_1 \epsilon) + \frac{\partial}{\partial x_2}(\rho h_1 r U_2 \epsilon) = \frac{\partial}{\partial x_1}\left(\frac{\mu_t h_2 r}{\sigma_\epsilon h_1}\frac{\partial \epsilon}{\partial x_1}\right) + \frac{\partial}{\partial x_2}\left(\frac{\mu_t h_1 r}{\sigma_\epsilon h_2}\frac{\partial \epsilon}{\partial x_2}\right) + S_\epsilon h_1 h_2 r \tag{8}$$

where S_k and S_ϵ, in the present coordinate system, are:

$$S_k = P_r - \rho\epsilon \text{ with } P_r = \mu_t\left[2\left(\frac{\partial U_1}{\partial x_1} + U_2 H_1(2)\right)^2 + 2\left(\frac{\partial U_2}{\partial x_2} + U_1 H_2(1)\right)^2\right] + \mu_t\left[\frac{\partial U_1}{\partial x_2} + \frac{\partial U_2}{\partial x_1} - U_1 H_1(2) - U_2 H_2(1)\right]^2 + 2\mu_t\left[\frac{U_2}{r}\frac{\partial r}{\partial x_2} + \frac{U_1}{r}\frac{\partial r}{\partial x_1}\right]^2 \tag{9}$$

$$S_\epsilon = \frac{\epsilon}{k}[C_1 P_r - \rho C_2 \epsilon]$$

where

$$H_2(1) = (\partial h_2/\partial x_1)/h_1 h_2 \tag{10}$$

and

$$H_1(2) = (\partial h_1/\partial x_2)/h_1 h_2$$

Derivation of equations (7) and (8) in the curvilinear orthogonal coordinate system can be seen in reference [4].

The set of equations (1) to (10) can be solved numerically provided the boundary conditions are specified. Conditions at the inlet section upstream of the obstruction were known from experiments. These corresponded to fully developed pipe flow. At the exit section a zero gradient condition was employed for all the dependent variables. The exit section was chosen far downstream from the obstruction, so that the boundary condition employed there did not influence the calculations in the region of separated flow. The velocity U_1 parallel to the wall at the grid line next to the wall has been calculated from the law of the wall. The law of the wall is, of course, not ideal for turbulent flows with separation and should be replaced by a more appropriate law. At the grid points nearest to the walls the source terms in the equation for turbulence energy are evaluated from the local wall shear stresses and the law of the wall. The equation for ϵ was not solved at the points nearest to the walls. The ϵ values at these points were fixed using the condition of local equilibrium of turbulence [7].

The governing equations, prresented above, can be solved using finite differences in very much the same way as their counterparts in cylindrical polar coordinates, provided the metric coefficients and their gradients are known over the calculation domain. This is done by generating a body fitted orthogonal grid numerically and suitably calculating the grid parameters, e.g., line elements, etc. The grid generation procedure is described in the next section. For the moment, it is assumed that h_1, h_2, $\partial h_2/\partial x_1$ and $\partial h_1/\partial x_2$, all of which are needed for the solution of equations (1) to (10), are known.

The computer program TEACH [8] written for solvling equations in cartesian and cylindrical polar coordinates has been modified in the present work for solving the governing equations (1) to (10). The staggered grid employed in the present coordinate system is shown in Fig. 2. Modifications of the computer program TEACH relate mainly to the body fitted grid system. The hybrid differencing scheme, which has been retained, is expected to result in less false diffusion in calculating separated flows using the present coordinate system than when, for example, a cartesian coordinate system is employed. For convergence, it was found necessary to introduce the source terms in the momentum equations (4) and (5) slowly. The source terms were appropriately linearized. A typical turbulent flow calculation using 40 × 20 grid needed about 550 iterations to converge. On the UNIVAC 1108 machine such a calculation requires 47k words of storage and about 30 minutes of computing time.

3 Generation of Body-Fitted Orthogonal Numerical Grids

The generation of body-fitted orthogonal grids was achieved in the present work by solving numerically the Laplace equations which represent the physical coordinates of the grid required. The given calculation domain is prescribed by discrete points on its boundary and is represented by a rectangle in a transformed plane. The rectangle on the transformed plane is divided by a uniform grid in both directions. The physical coordinates of this grid are represented by Laplace equations which are solved by central differencing with appropriate boundary conditions. Basis and the details of the method can be found in references [4] and [9]. The method employed provides a fairly uniform grid density in both the directions, but this can be modified [10] to obtain a finer grid in certain regions, e.g., near a wall. This modification was not used in the present work, but the grid density was changed manually by specifying the grid lines to be used in the fluid flow solution.

The metric coefficients h_1 and h_2 and their gradients appearing in the differential equations governing fluid flow given in the previous section can be obtained from the line elements of the generated grid. These line elements are calculated using piecewise third order polynomials. Apart from the line elements or arc lengths, the fluid flow solution also requires the face areas and volumes related to the micro control volumes of the dependent variables. These parameters are calculated along with the calculation of the arc lengths and are stored on tapes or data files to be read by the fluid flow solver. Grid generation together with the calculation of the geometrical grid parameters require about 40k words (for 32 × 20 grid) of storage and 5 minutes of computing time on the UNIVAC 1108. Most of this time is required for the grid generation. It was found necessary to do 500 iterations on the Laplace equations to obtain the necessary accuracy for some of the grid parameters, e.g., the gradients of the metric coefficients.

For the geometries shown in Fig. 1, the curvilinear orthogonal grid could also be generated analytically, e.g. using conformal mapping [11]. For generality, however, numerical grid generation is favored in the present work over the more problem-specific analytical methods.

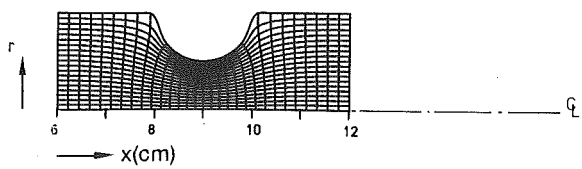

Fig. 3 Generated grids for the configurations shown in Fig. 1(*a*)

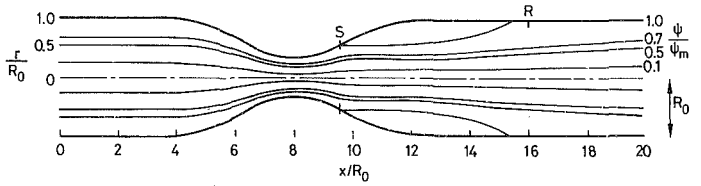

Fig. 4 Calculated steam lines for laminar flow (Re = 50) in a stenosis

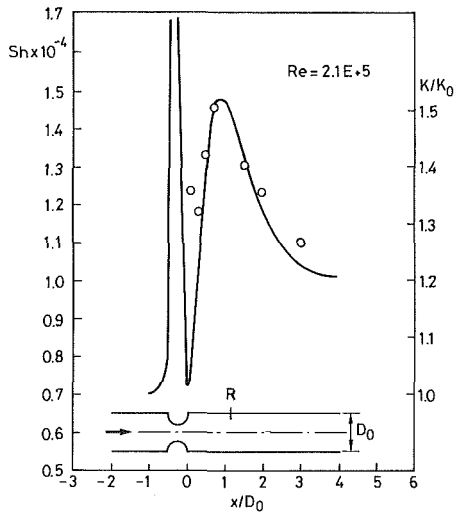

Fig. 5 Calculated (—) and measured (○) mass transfer coefficients

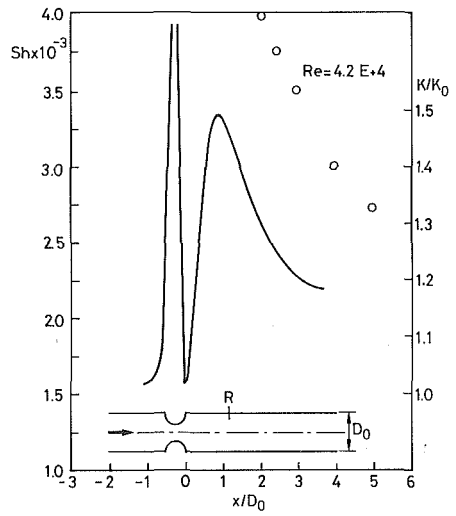

Fig. 6 Calculated (—) and measured (○) mass transfer coefficients

Figure 3 shows the grid generated for the constriction geometry shown in Fig. 1(*a*). This grid was extended on the downstream side by a cartesian grid to cover the region of interest from the fluid flow point of view. The grid generation program was also used to generate curvilinear orthogonal grids for other domains to confirm its viability, but these results will not be presented here.

4 Results of Computations

Three calculations were performed with the procedure described in the previous two sections:

1. Laminar flow in a model stenosis (Fig. 4)
2. Turbulent flow in a pipe perturbed by a ring obstruction of semicircular cross section similar to a weld geometry (Fig. 1(*a*))
3. Turbulent flow in a model stenosis (Fig. 1(*b*))

These three flow configurations have been studied experimentally and serve to test the calculation procedure. Results of these calculations compared with the respective experimental data will be presented and discussed below.

Laminar steady flow in models of arterial stenoses has been studied experimentally by Young and Tsai [12] in some detail. One of their measurements was chosen for a check on the numerics and the implementation of the curvilinear coordinate system in the TECH program. Figure 4 shows the calculated streamline pattern at a Reynolds number of 50 for the model M-2 of reference [12]. At the chosen Reynolds number the flow is well within the laminar range. The measured separation point *S*, downstream of the constriction throat and the measured reattachment point, *R*, are also shown in Fig. 4. The calculated locations compare satisfactorily with the measured data. The calculated reattachment point lies somewhat upstream of the measured one, but the difference is small. The agreement can be made better using finer grids in the calculations. The detailed pressure distribution is not measured at low Reynolds numbers in reference [12]. Overall pressure drops are also reported [12] at Reynolds number larger than 150. Therefore the computed pressure field will not be presented here.

The motivation for this work was chiefly the calculation of turbulent flow. The laminar case, as mentioned above, was employed to check the calculation procedure. The comparison shown in Fig. 4 was taken to be sufficient to show that implementation of the curvilinear coordinate system in the fluid flow solver was carried out correctly. Similar evidence was also provided from other laminar flow calculations carried out with the computer program developed in the present work. One flow situation is flow in a diffusor, which was set up as a test case in the Vth working group meeting on "Refined modelling of flows" organized by IAHR in Rome in June 1982. Results obtained by various calculation methods, including the present one, can be seen in reference [13].

Due to interest in internal corrosion of pipelines, the electro-chemical measurements in constricted pipes carried out in reference [14] were chosen to test the present turbulent flow calculations. The measurements of reference [14] are unfortunately restricted to mass-transfer and, therefore, the inferred hydrodynamic behavior from these measurements must be compared with the calculations. The measurements [14] of the mass-transfer coefficient at the pipe wall in a 40 mm diameter pipe were carried out downstream of a ring obstruction of semicircular cross section of 10mm radius as shown in Fig. 1(*a*). Local mass-transfer measurements were performed using locally active ring electrodes of 10mm length. The influence of electrode length on the mass-transfer is well known [15] and was confirmed in the measurements of reference [14], particularly at Reynolds numbers lower than 10^5. This influence was, however, compensated for in the measurements of reference [14] by using a polarized electrode upstream of the working electrode. Comparison of measurements of references [14] and [15] for a pipe-step indicates also that the Reynolds number influence on mass-transfer shown in reference [14] is definitely a function of electrode length. At high Reynolds numbers however this influence is small [15, 16]. The mass transfer measurements

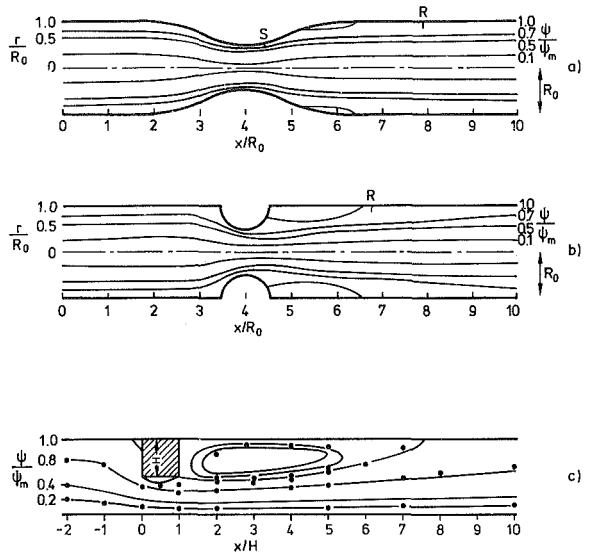

Fig. 7 Streamline pattern for turbulent flow in a tube with (*a*) stenosis, (*b*) weld constriction, (*c*) in a channel with square destruction [19]

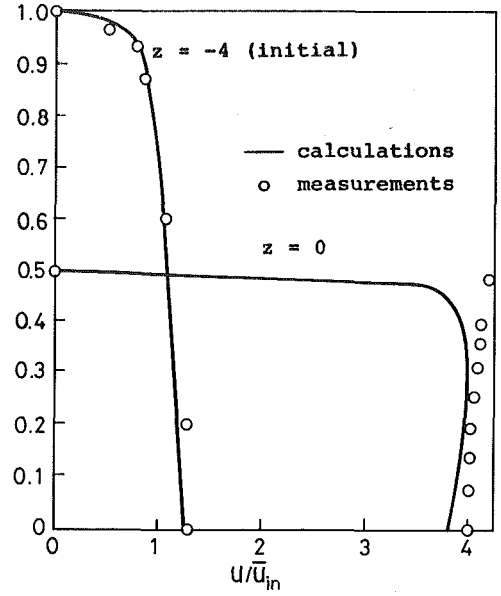

Fig. 8 Velocity profiles for turbulent flow in a stenosis corresponding to Fig. 7(*a*)

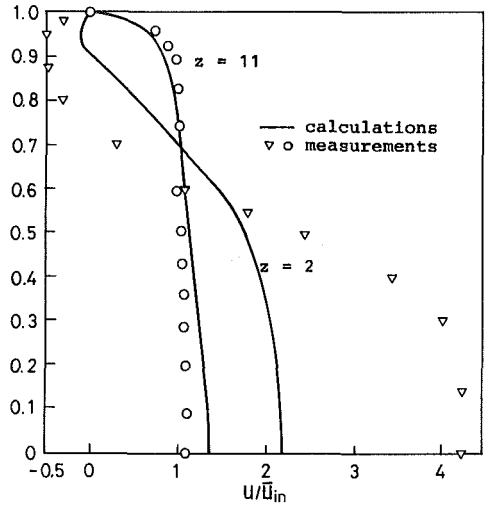

Fig. 8 (Cont.)

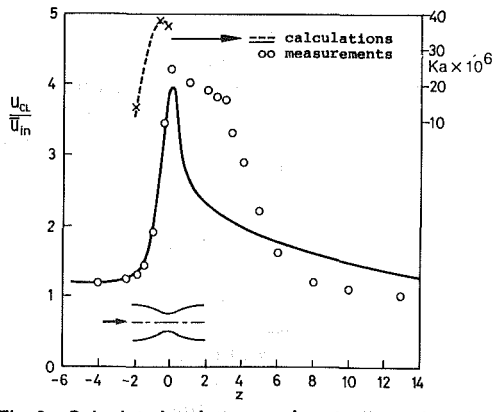

Fig. 9 Calculated and measured center line axial velocity

[14], therefore, should be considered more reliable at Reynolds numbers larger than 10^5. Mass transport calculations were also performed in the present work which will now be presented.

Calculated values of mass-transfer coefficients in the flow configuration of Fig. 1(*a*) are shown in Figs. 5 and 6 for two Reynolds numbers. Measured values [14] are also shown in these figures. Calculations were performed with zero values of concentration all along the pipe wall which corresponds to a long working electrode. Finite length electrodes cannot be simulated with the present calculations because the concentration layer is too thin (Schmidt number = 1460) to be resolved in the turbulent flow calculations [17]. For the reasons of accuracy in the measurements mentioned above, therefore, the comparison shown in Fig. 5 is more meaningful and looks very encouraging. Although measurements were available only downstream of the constriction, one can surmise the qualitative upstream behavior. The calculations show the expected trends upstream, as well as over the constriction. Due to flow acceleration in the throat region, mass-transfer increases significantly. Downstream of the constriction in the separated flow region mass-transfer reduces sharply and then increases, reaching a maximum near the flow reattachment. *R* in Figs. 5 and 6 indicates the calculated reattachment point which lies just upstream of the measured maxima in the mass-transfer at the wall, as expected [18]. The measurements of reference [14] show no influence of Reynolds number on the location of the maximum mass-transfer downstream of the obstruction and this is calculated correctly with the present method, as is shown in Figs. 5 and 6 by the location marked *R*. Although the fluid dynamic parameters have not been measured for the flow configuration shown in Fig. 1(*a*), the calculated reattachment point (indicated by *R* in Figs. 5 and 6) compares well with the region of flow reattachment deduced from mass transfer measurements.

Figure 7(*b*) presents the calculated streamline pattern for the geometry of Fig. 1(*a*), which looks as expected when compared with Fig. 7(*c*), taken from reference [19], showing the streamline pattern in a channel containing a square sectioned obstruction. Though Figs. 7(*b*) and 7(*c*) are not directly comparable, the calculated trend is correct, i.e., the separation region behind a rounded obstruction is less severe than the one behind a sharp edged one. The calculated streamline pattern shown in Fig. 7(*a*), corresponding to turbulent flow in a stenosis, to be discussed next, shows an even smaller region of separation. The reduced separation region is expected since the constriction of the stenosis is more gradual than the ones shown in Figs. 7(*b*) and 7(*c*). Flow patterns shown in Fig. 7 provide valuable information to

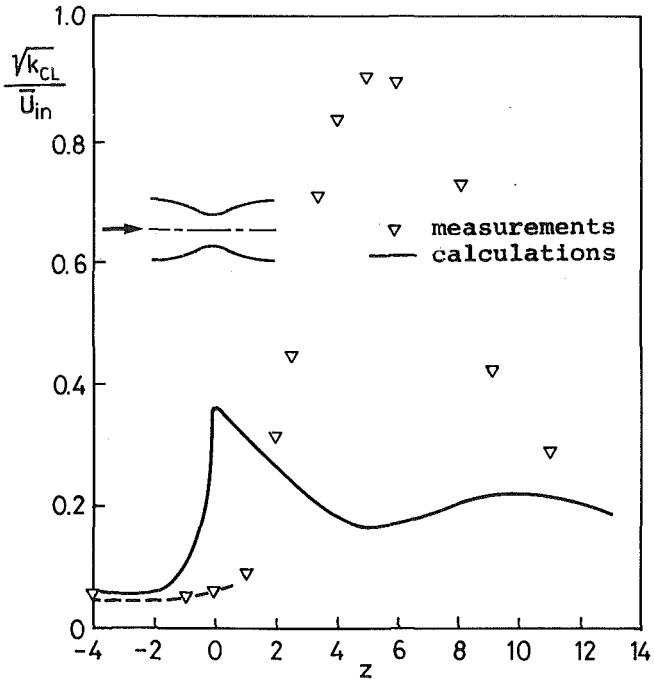

Fig. 10 Calculated and measured center line turbulent kinetic energy

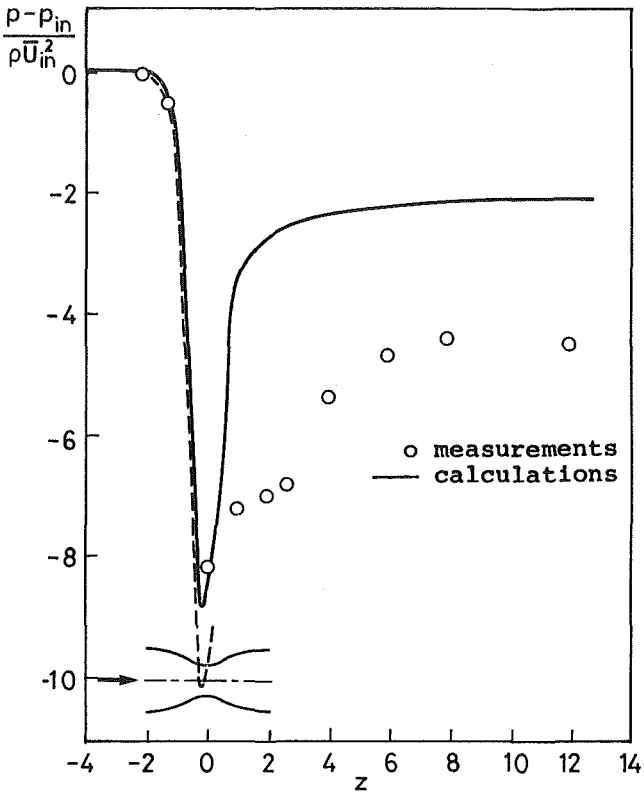

Fig. 11 Calculated and measured wall pressure distribution

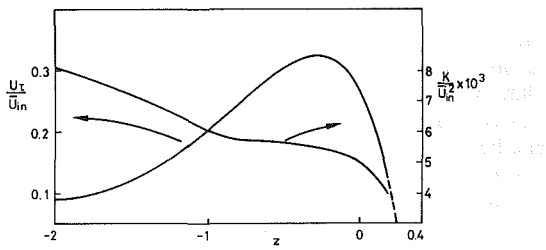

Fig. 12 Friction velocity and the wall near turbulent kinetic energy calculated with the low Reynolds number version of the k-ϵ-model

engineers who have to design optimum weld geometries in pipelines.

The third test calculation has been performed for the turbulent flow (Re = 1.5×10^4) in a constricted tube (Fig. 1(*b*), investigated experimentally by Deshpande and Giddens [20]. Detailed flow measurements are presented in reference [20] which may be compared with the calculations. Results of calculations for this geometry are shown in Figs. 7 to 12, along with the measured values. Figure 7(*a*) shows that the calculated point of separation appears significantly downstream than the measured one, denoted by *s* on Fig. 7(*a*) and the flow reattaches much before the measured point of reattachment represented by *R*. The detailed velocity profiles in Fig. 8 show that the computed negative velocities are much smaller than the measured ones. This results in calculated center line velocities smaller than measured downstream of the constriction throat, as shown in Fig. 9. This heavy under prediction of the separation zone looks curious at first glance. The calculated reattachment length in Fig. 7(*b*) is in agreement with the measured values based on mass-transfer measurements. The measurements for the geometry of Fig. 7(*a*), however, show a larger reattachment length than that of Fig. 7(*b*), contrary to the expectation of a lower value. The measured reattachment length with the gradual geometry [20] in Fig. 7(*a*) is comparable to the reattachment lengths observed with sharp obstructions and fences [17], again contrary to expectation. The large difference between the calculated and the measured values of the reattachment length shown in Fig. 7(*a*) requires the following considerations of the flow in question.

The configuration of reference [20] provides 75 percent reduction in the cross sectional area at the constriction throat resulting in high flow acceleration in the converging part. This acceleration is well predicted as can be seen from Fig. 9 and is simply governed by continuity. Figure 9 shows the acceleration parameter at a few discrete points in the converging section of the tube. The values of the acceleration parameter are much higher than necessary to relaminarize the flow. From accelerated boundary layer investigations it is known [21] that $K_a = 3 \times 10^{-6}$ is enough for relaminarizing a turbulent boundary layer. Looking at the K_a values shown in Fig. 9, one can surmise that the flow in the stenosis geometry (Fig. 7(*a*)) relaminarizes in the converging section and this results in a larger separation zone than for the case of a fully turbulent flow. The present turbulence model is, of course, unable to simulate the transition phenomenon and, therefore, the differences between calculations and the measurements shown in Figs. 8 to 11 are not surprising. The low Reynolds number version [21] of the k-ϵ model may be used for relaminarizing flows, but is not suitable for the present situation where separation takes place in the diverging section. Calculations with the low Reynolds number version of the k-ϵ model can, however, be performed in the converging part of the stenosis in order to determine if relaminarization can take place. This was done in the present work and results of these calculations are shown in Fig. 12.

Flow in the converging section of the stenosis geometry shown in Fig. 1(*b*) ($-2 \leq Z \leq 0$) was computed by solving the boundary layer form of the momentum equations. These equations are solved by the forward marching integration procedure of Patankar and Spalding [22]. The calculations are performed with the low Reynolds number version of the k-ϵ turbulence model [21]. Details of the equations solved and the numerical method can be seen in reference [23].

Flow at the inlet section ($Z = -2$) was taken to be fully

developed, in accordance with the experiments reported in reference [20]. 100 grid points were used in the radial direction between the axis and the nozzle wall and 800 forward steps were taken to cover the region up to the nozzle throat ($Z = 0$). The empirical constants used in the turbulence model were the same as given in reference [21]. Although these constants have been superceded, calculation of severely accelerated boundary layers in reference [21] has shown that they are suitable for this purpose. Figure 12 shows that the wall shear stress increases in the initial region as a result of flow acceleration, attains a maximum upstream of the throat at $Z = -0.3$ and decreases up to $Z = 0$, despite flow acceleration. Figure 12 also shows the turbulent kinetic energy calculated with the low Reynolds' number model and the boundary layer solution procedure at the wall near location where the grid line next to the wall ($20 < y+ < 60$) was placed in the elliptic calculations presented before. Turbulent energy decreases continuously at this location. The elliptic calculations, on the contrary, show large increase in the wall near value of the turbulent energy along the contraction, providing a maximum value at the throat which is an order of magnitude larger than the value shown in Fig. 12. The flow behavior shown in Fig. 12 demonstrates clearly that flow in the throat region relaminarizes at the wall and cannot be simulated by the wall function treatment used in the solution of equations (1) to (10) for the gradual constrictions.

After having found the above flow behavior and the importance of the wall near region, the boundary layer calculation was continued beyond the throat in order to locate the separation point. Since the boundary layer procedure breaks down at the separation point, the zero wall shear stress location is computed by extrapolating (dotted line in Fig. 12) The calculated wall shear stress in the diverging part of the stenosis. So obtained separation point lies a $Z = 0.24$ downstream of the throat and compares well with the measured location reported [20] to be between the throat ($Z = 0$) and $Z = 0.5$. As shown in Fig. 12 the wall near turbulent energy values continue to decrease sharply in the diverging part and strengthen the arguments presented already for flow relaminarization. The pressure coefficient computed in the boundary layer calculation is shown in Fig. 11 by the dotted line. The pressure coefficient in the separation region is much higher than necessary to separate a turbulent boundary layer [24]. In spite of such high adverse pressure gradient the elliptic calculations fail to predict flow separation early enough, due to the inappropriate wall treatment employed. Delayed separation as shown in Fig. 7(*a*) in the elliptic calculations makes the separation zone thin and too short.

Other than bringing out the importance of the near wall region, the boundary layer calculations also result in much better turbulence characteristics along the stenosis center line. The dotted line in Fig. 10 represents the center line turbulent energy as calculated by the boundary layer procedure and falls on the measured values. This is a consequence of the normal stress production terms in the turbulent energy equation. Using the cartesian coordinates here for simplicity these terms are

$$-\overline{u_1}^2 \frac{\partial U_1}{\partial x_1} - \overline{u_2}^2 \frac{\partial U_2}{\partial x_2} = -(\overline{u_1}^2 - \overline{u_2}^2) \frac{\partial U_1}{\partial x_1}$$

Now $\overline{u_1}^2$ and $\overline{u_2}^2$ are similar in magnitude in the central region and therefore their difference should give no (or a small) contribution to the turbulent energy. This is so in the boundary layer calculation since these terms are dropped. In the elliptic calculations, however, these terms are expressed via Boussinesq's hypothesis (see also equation (9)):

$$-\overline{u_1}^2 \frac{\partial U_1}{\partial x_1} - \overline{u_2}^2 \frac{\partial U_2}{\partial x_2} = 2\mu_t \left(\frac{\partial U_1}{\partial x_1}\right)^2 + 2\mu_t \left(\frac{\partial U_2}{\partial x_2}\right)^2 \quad (11)$$

with the result that instead of their difference, the normal stress production terms are added and overestimate the turbulent energy in regions of strong acceleration or retardation. In most of the separated flow calculations this consequence of the Boussinesq's hypothesis is not so important since the shear production term is much larger than the above terms. Along the center line of the stenosis geometry, the normal stresses are an order of magnitude larger than the shear stresses and result in the unrealistically large values of turbulent energy shown in Fig. 10. This behavior along the center line has little to do with the flow behavior near the wall which is of main significance in the present flow. Neglecting the normal stress production terms in the elliptic equations does bring the turbulent energy levels along the center line but hardly influences the separation behavior at the wall. Similar behavior of the elliptic calculations was found when performed only in the diverging part using the boundary layer solution as initial conditions at the throat. This confirms the significance of treatment near the wall.

The above results show that the gradual constriction of Fig. 1(*b*) presents a flow with rather complicated turbulent structure, including relaminarization in the throat region and transition in the diverging section. These influences can, of course, not be simulated by the standard k-ϵ-turbulence model employed. Beyond the separation region, however, the calculated values compare satisfactorily with the measurements as can be seen from the velocity profile at $Z = 11$ in Fig. 8 and the center line velocity in Fig. 9. This indicates that beyond flow reattachment, the turbulence redevelopes and the k-ϵ-model can be used successfully. The constriction in Fig. 7(*b*) also corresponds to an area reduction of 75 percent at the throat, but the constriction is sharper and shorter than the one in Fig. 7(*a*). The Reynolds numbers are also higher (see Figs. 5 and 6) for the flow in this constriction, requiring even higher accelerations to damp the turbulence. Moreover, unlike the gradual constriction of Fig. 7(*a*), the flow in FIg. 7(*b*) separates in the upstream corner of the obstruction (not shown in Fig. 7(*b*)). Turbulence produced in this region feeds the nozzle flow, helping flow in the converging section to remain turbulent.

From the above arguments it is seen that the reason for the large underprediction of the recirculation length in Fig. 7(*a*) is the flow relaminarization in the throat region. There may be, however, additional reasons for the above mentioned differences which will now be reviewed. The turbulence model employed is based on the concept of an effective viscosity which is isotropic. Isotropicity may be violated in the throat region and in the region of flow separation. Since, however, many computations of turbulent flows with separation have been successfully carried out [7, 17, 18] with the standard k-ϵ turbulence model, the error associated with the isotropic turbulence assumption in the k-ϵ model can be considered small.

Similarly, it is known that the wall treatment of the turbulence and the use of the law of the wall in the k-ϵ model are inappropriate for separated flows. They do provide, however, reasonable answers for the integral quantities such as the length of flow recirculation [19]. Refining the wall treatment of the turbulence quantities does influence the transport properties at the wall [18], but does not change the reattachment length considerably.

One may conclude, therefore, that despite the shortcomings in the two-equation model used in the present work, the large differences between the measured and calculated results shown in Fig. 7(*a*) are not stemming from the model.

Apart from the physical reasons discussed above, the failure of the calculations to accurately reproduce the measured data for the stenosis geometry may also stem from the numerical errors, e.g., false diffusion. The choice of the numerical grid employed was based on the author's previous

experience with computations of flows over rectangular obstructions with confined [19] and unconfined [7] boundaries. As expected, grid refinement is important for unconfined flow, particularly when upwind differencing is employed. For confined situations, however, a grid of 40 × 20 used in the present calculations is sufficiently fine to provide grid independent solutions. Out of 40 grid lines in the x-direction 32 lines were distributed uniformly between 8 obstruction heights upstream from the throat and 8 heights downstream. This grid is finer than the one employed in reference [19], where 50 grids were employed from 11 block heights upstream to 35 block heights downstream from the block. The calculations of reference [19] used 27 grids in the normal direction, compared with 20 in the present work. Moreover, use of body fitted coordinates reduces the angle between the stream lines and the coordinate lines which leads to a reduction in false diffusion. Considering that the calculations presented in reference [19] were grid independent, it is reasonable to believe that the present calculations do not suffer from false diffusion.

Conclusions

A calculation procedure has been presented which can calculate viscous fluid flow with heat and mass transfer over curved boundaries. The calculation procedure is based on the finite difference solution of the governing partial differential equations in curvilinear orthogonal coordinates which are generated numerically by solving the Laplace equations. The method is general for two dimensional flows but is applied in the present work only to flows in constricted tubes. Fluid flow, heat and mass transfer behavior can be reasonably well predicted for laminar as well as for turbulent flows with separation. For flow geometries, in which flow separation follows a region of possible relaminarization due to high acceleration resulting from a smooth, but rapid change in area, the flow field cannot be well calculated with the help of the standard k-ϵ turbulence model.

In the absence of flow separation the low Reynolds number version of k-ϵ model may be used. Flow in the converging part of the stenosis studied experimentally by Deshpande and Giddens [20], has been computed in the present work with this turbulence model and the results of the calculations show clearly, that the flow relaminarizes before the stenosis throat. The separation length in the diverging section of this stenosis is calculated to be shorter than the measured value. All possible reasons for this underprediction have been considered and, from among them, it is concluded that the main reason for the underprediction is the flow relaminarization in the physical flow.

Acknowledgments

The calculations presented in this paper were performed on the UNIVAC 1108 of the University of Karlsruhe. The author would like to thank Dr. R. J. R. Johns, presently at AVL Austria, for providing the grid generation method [9] which he developed at Imperial College, London. The assistance of Dr. C. Knisely of the Institut für Hydromechanik, University of Karlsruhe, in editing the paper is gratefully acknowledged.

References

1 Fisher, H. E., "Pipeline Operators Learning to Meet Offshore Challenges," *Pipeline Industry*, Apr. 1981, pp. 69–72.

2 Deshpande, M. D., Giddens, D. P., and Mabon, R. F., "Steady Laminar Flow Through Modelled Vascular Stenoses," *J. Biomechanics*, Vol. 9, 1976, pp. 165–174.

3 McGuirk, J. J., "Prediction of Turbulent Buoyant Jets in a Flowing Ambient Fluid," Ph.D. thesis, University of London, 1971.

4 Pope, S. B., "The Calculation of Turbulent Recirculating Flows in General Orthogonal Coordinates," *J. Computational Physics*, Vol. 26, 1978, p. 1987.

5 Bryant, D., and Humphrey, J. A. C., "Conservation Equations for Laminar and Turbulent Flows in General Three-Dimensional Curvilinear Coordinates," Mech. Eng. Dept., Imperial College Report.

6 Hughes, W. F., and Gaylord, E. W., *Basic Equations of Engineering Science. Schaum's Outline Series*, McGraw-Hill Book Company, New York.

7 Durst, F., and Rastogi, A. K., *"Turbulent Flow Over Two-Dimensional Fences," Turbulent Shear Flows 2*, ed. Bradbury et al., 1980, pp. 218–232.

8 Gosman, A. D., and Pun, W. M., Lecture Notes for Course Entitled—Calculation of Recirculating Flows, Imperial College Report HTS/74/2, 1973.

9 Gosman, A. D., and Johns, R. J. R., "A Simple Method for Generating Curvilinear Orthogonal Grids for Numerical Fluid Mechanics Calculations," Mech. Eng. Dept., Imperial College Report FS/79/23.

10 Mobley, C. D., and Stewart, R. J., "On the Numerical Generation of Boundary-Fitted Orthogonal Curvilinear Coordinate System," *J. Computational Physics*, Vol. 34, 1980.

11 O'Brien, V., "Conformal Mappings for Internal Viscous Flow Problems," *J. Computational Physics*, Vol. 44, 1981, pp. 220–226.

12 Young, D. F., and Tsai, F. Y., "Flow Characteristics in Models of Arterial Stenosis—I. Steady Flow," *J. Biomechanics*, Vol. 6, 1973, pp. 395–410.

13 Computational Results of the Test Cases Set Up for the Vth IAHR Working Group Meeting on Refined Modelling of Flows, compiled by B. Orlandi, Rome, 1982.

14 Sydberger, T., and Lotz, U., "Relation Between Mass Transfer and Corrosion in a Turbulent Pipe Flow," *Journal of the Electrochemical Society*, Vol. 129, No. 2, 1982.

15 Runchal, A. K., "Mass Transfer Investigation on Turbulent Flow Downstream of Sudden Enlargement of a Circular Pipe for Very High Schmidt Numbers," *Int. J. Heat and Mass Transfer*, Vol. 14, 1971, pp. 781–792.

16 Vanshaw, P., Philip, Reiss, L., and Hanratty, T. J., "Rates of Turbulent Transfer to a Pipe Wall in the Mass Transfer Entry Region," *A.I.Ch.E. J.*, Vol. 9, 1963, pp. 363–364.

17 Rastogi, A. K., Kvernvold, O., and Søntvedt, T., "Flow and Mass Transfer in a Perturbed Turbulent Pipe Flow," *Momentum and Heat Transfer Processes in Recirculating Flows*, ed. B. E. Launder and J.A. C. Humphrey, ASME HTD, Vol. 13, 1980.

18 Chieng, C. C., and Launder, B. E., "On the Calculation of Turbulent Heat Transport Downstream from an Abrupt Pipe Expansion," *Momentum and Heat Transfer Processes in Recirculating Flows*, ed. B. E. Launder and J. A. C. Humphrey, ASME, HTD, Vol. 13, 1980.

19 Durst, F., and Rastogi, A. K., "Theoretical and Experimental Investigations of Turbulent Flows With Separation," *Turbulent Shear Flows 1*, ed. Durst et al., Springer Verlag Heidelberg, 1979, p. 208.

20 Deshpande, M. D., and Giddens, D. P., "Turbulence Measurements in a Constricted Tube," *J. Fluid Mech.*, Vol. 97, Part 1, 1980, pp. 65–89.

21 Jones, W. P., and Launder, B. E., "The Prediction of Laminarization with a Two-Equation Model of Turbulence," *Int. J. Heat Mass Transfer*, Vol. 15, 1972, pp. 301–314.

22 Patanker, S. V., and Spalding, D. B., *Heat and Mass Transfer in Boundary Layers*, Intertext London 1970.

23 Durst, F., and Rastogi, A. K., "Calculations of Turbulent Boundary Layer Flows with Drag Reducing Polymer Additives," *The Physics of Fluids*, Vol. 20, No. 12, 1977, pp. 1975–1985.

24 Simpson, R. L., Chew, Y.-T., and Shivaprased, B. G., "The Structure of a Separating Turbulent Boundary Layer. Part I, Meanflow and Reynolds Stresses," *J. Fluid Mech.*, Vol. 113, 1981, pp. 23–51.

A. Haji-Sheikh
Mem. ASME

R. Lakshimanarayanan
Mem. ASME

David Y. S. Lou
Mem. ASME

Mechanical Engineering Department,
The University of Texas at Arlington,
Arlington, Texas 76019

Phil J. Ryan
Research Development,
Frito-Lay, Inc.
Irving, Texas 75061

Confined Flow in a Partially-Filled Rotating Horizontal Cylinder

Experimental and analytical studies are reported for a Newtonian fluid in a partially-filled cylinder rotating about its centerline axis at constant angular speeds. Two fluids, glycerin and water, are used in this study. The analytical results are in good agreement with the experimental data. This comparison is based on the profiles of the free surfaces and the streamlines experimentally obtained using a flow visualization technique and as predicted by the analytical model. When the rotational speed is not high enough to cause solid body rotation of the fluid, due to excessive centrifugal force, a recirculation region forms at the lower portion of the cylinder. The profile of the free surface in this region depends on the relative magnitude of the body force and the viscous force. In general, two distinct flow regions can be recognized for a cylinder of infinite extent; a recirculating flow and a boundary-layer-type flow along the cylindrical wall. In addition to the volume of the fluid in the cylinder, there are two other parameters governing this problem; the Reynolds number and the ratio, G, of the Reynolds number to the Froude number.

Introduction

A horizontal cylinder partially filled with liquid and rapidly rotating about its axis has been the subject of numerous investigations in the past [1-4]. However, little or no investigations have been cited in the literature dealing with a slowly rotating cylinder when a recirculation region of fluids exists at the lower portion of the cylinder.

When the rate of angular rotation is low, the acceleration terms in the momentum equation may be neglected. Under this assumption, a closed-form analytical solution is obtained for the fluid motion which is a function of the ratio of the Reynolds number to the Froude number, G. At higher angular speeds, especially in low viscosity fluids, e.g., water, the Reynolds number becomes significant and the acceleration terms must be retained. However, flow visualization confirms the existence of two distinct flow regions and the free surface for the recirculating region agrees with that calculated when acceleration terms are neglected. A boundary-layer-type flow along the rotating wall is observed which eventually becomes turbulent as the Reynolds number increases. The flow in this latter region is very complex and includes other flow characteristics not included in this study. In addition, since the experimental measurement of the profile of the free surface and streamlines are carried out in a finite cylinder, a secondary flow is also observed in the neighborhood of the end walls. The secondary flow problem is not included in this analytical model.

In the experimental investigation, a cylindrical enclosure, 15 cm in diameter, is constructed of plexiglas. Water and glycerin are the two fluids used. The profile of the free surface is obtained photographically. The streamlines in the recirculating region are made visible by adding dye to the flow. Since the dye had to be added before the beginning of rotation, it is found that, even at higher rotational speeds, the dye diffuses in water more quickly than it is carried away by the moving fluid. However, in glycerin, the dye diffuses much more slowly. Hence flow visualization and photography of the streamline becomes possible.

The analytical solution leads to closed-form solutions for v_r and v_ϕ, the components of the velocity vector in the r and ϕ directions, but the constants of integration in the solutions are computed numerically. They depend on the profile of the free surface which in turn depends on a nonlinear first-order differential equation. This differential equation is integrated numerically using the Runge-Kutta procedure. The results of integration are presented for various values of G and the volume of fluid in the cylinder. The profile of the free surface is computed and presented graphically. Additionally, graphs are prepared to illustrate the shape of the velocity profiles, v_r, and v_ϕ, each as a function of r and ϕ.

In the region beyond the recirculation region, the thickness of the fluid layer along the cylindrical wall is small. A boundary layer model is derived to describe the fluid behavior in this thin layer. This concept of two flow regions preempts the need for a cumbersome finite difference solution of the Navier-Stokes equation. Hence, a simple solution method is presented which can be accommodated even on a small desktop minicomputer.

This study is devoted to a situation when the Reynolds number is low. Visual observations of the boundary layer clearly indicate the different flow regimes in the boundary layer. When flow is laminar, the boundary layer is quite transparent. As the Reynolds number increases, a pronounced

Contributed by the Fluids Engineering Division of THE AMERICAN SOCIETY OF MECHANICAL ENGINEERS and presented at the Applied Mechanics, Bioengineering, and Fluids Engineering Conference, Houston, Texas, June 20-22, 1983. Manuscript received by the Fluids Engineering Division, February 8, 1983.

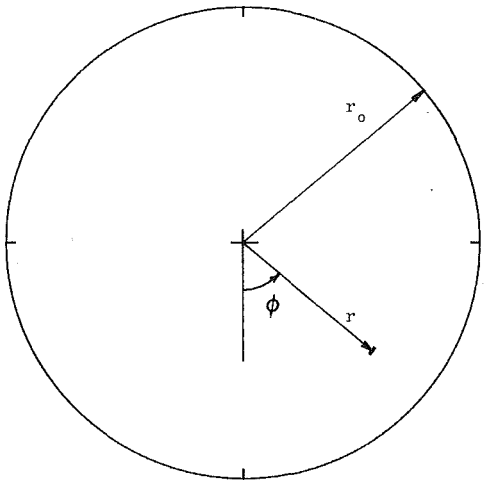

Fig. 1 Cylindrical coordinate for horizontal cylinder

change takes place in the boundary layer and the fluid is no longer transparent. The Reynolds number indicating the transition from the laminar to the turbulent regime is also measured.

Analysis

The study of flow behavior in a long horizontal cylinder rotating about its center-line axis requires the solution of the Navier-Stokes equation in a two-dimensional cylindrical coordinate system [5].

$$\mathrm{Re}\left[u\frac{\partial u}{\partial \eta}+\frac{v}{\eta}\left(\frac{\partial u}{\partial \phi}-v\right)\right]+\frac{\partial P}{\partial \eta}$$

$$=G\cos\phi+\nabla^2 u-\frac{1}{\eta^2}\left(u+2\frac{\partial v}{\partial \phi}\right) \tag{1a}$$

$$\mathrm{Re}\left[\frac{u}{\eta}\frac{\partial}{\partial \eta}(\eta v)+\frac{v}{\eta}\frac{\partial v}{\partial \phi}\right]+\frac{1}{\eta}\frac{\partial P}{\partial \phi}$$

$$=-G\sin\phi+\nabla^2 v+\frac{1}{\eta^2}\left(\frac{\partial u}{\partial \phi}-v\right) \tag{1b}$$

and the continuity equation

$$\frac{\partial(\eta u)}{\partial \eta}+\frac{\partial v}{\partial \phi}=0 \tag{2}$$

These equations are nondimensionalized by using $u = v_r/r_0\omega$, $v = v_\phi/r_0\omega$, $\eta = r/r_0$, $P = (p-p_a)/\mu\omega$, $G = \rho g r_0/\mu\omega$, and $\mathrm{Re} = \rho\omega r_0^2/\mu$ where r and ϕ are the radial and angular coordinates, Fig. 1, v_r and v_ϕ are the radial and angular velocity components, p and p_a are the local and atmospheric pressures, and ω is the angular speed.

The aim of this analytical study is directed toward the situations for which the Reynolds number is small; accordingly, the inertia terms are neglected. The values of G used in this study are, generally, larger than 100 while the terms corresponding to the viscous force in equation (1*a*) are of a much lower order. For $\phi < \pi/2$, $\cos\phi$ is of the order of unity, and the contribution of the viscous force in equation (1*a*) is negligible. In contrast, the term $G\sin\phi$ is zero at $\phi = 0$ and of the order of G at larger angles. Since the term $1/\eta\ \partial P/\partial\phi$ remains of the order of G at all angles and $G\sin\phi = 0$ at $\phi = 0$, then the contribution of shear force in ϕ-direction, equation (1*b*), is of the order of G. It was expected and then verified by the results of the computations that $\nabla^2 v$ is much larger than either $1/\eta^2\ \partial u/\partial\phi$ or v/η^2. The term v/η^2 is retained because it does not significantly complicate the analytical solution. However, the term $1/\eta^2\ \partial u/\partial\phi$ is discarded because it is small in comparison with the other terms (those of the order of G) and it would greatly complicate the analytical computations. Moreover, as discussed earlier, $\partial v/\partial\phi$ is of much lower order than G, hence $\partial^2 v/\partial\phi^2$ is not included in $\nabla^2 v$. The final form of the Navier-Stokes equations which approximately describe the problem under consideration is

$$G\cos\phi-\frac{\partial P}{\partial \eta}=0 \tag{3a}$$

$$-G\sin\phi-\frac{1}{\eta}\frac{\partial P}{\partial \phi}+\frac{\partial^2 v}{\partial \eta^2}+\frac{1}{\eta}\frac{\partial v}{\partial \eta}-\frac{v}{\eta^2}=0 \tag{3b}$$

The integration of equation (3*a*) is elementary and the result is

$$P=G\eta\cos\phi+f(\phi) \tag{4}$$

On the free surface, $P = 0$ and $\eta = \eta^*$, then $f(\phi) = G\eta^*\cos\phi$. In addition, equation (4) suggests that, as $\mu\omega\to 0$, $P\to\infty$ and $G\to\infty$, this equation reduces to $p-p_a=\rho g(r-r^*)\cos\phi$ which is the hydrostatic pressure distribution in the liquid region. The function P given by equation (4) can now be substituted into equation (3*b*), and the resulting equation is

$$\eta^2\frac{\partial^2 v}{\partial \eta^2}+\eta\frac{\partial v}{\partial \eta}-v=\eta f'(\phi) \tag{5}$$

which is a second-order linear differential equation with a standard solution

$$v=c_1\eta+c_2/\eta+\frac{1}{2}f'\eta\ln\eta \tag{6}$$

The variables c_1 and c_2 depend on angle ϕ. If the value of v is substituted into the continuity equation (2), the value of u can be obtained from the differential equation

$$\frac{\partial(\eta u)}{\partial \eta}=-\left(c_1'\eta+c_2'/\eta+\frac{1}{2}f''\eta\ln\eta\right) \tag{7}$$

Nomenclature

- c's = constants of integration
- f = function, equation (4)
- Fr = Froude number, $r_0\omega^2/g$
- g = gravitational acceleration
- G = dimensionless variable $gr_0\nu\omega$
- p = pressure
- P = dimensionless pressure
- p_a = atmospheric pressure
- Q_e = volumetric flow rate lifted per unit axial length
- r = radial coordinate
- r_0 = radius of cylinder
- Re = Reynolds number, $\rho\omega r_0^2/\mu$
- S_1, S_2 = parameters, equations (11*a*) and (11*b*)
- u = dimensionless radial velocity component, $v_r/r_0\omega$
- v = dimensionless angular velocity component, $v_\phi/r_0\omega$
- v_r = radial velocity component
- v_ϕ = angular velocity component
- $\mathbf{V}$ = velocity vector
- y = coordinate
- δ = boundary layer thickness
- η = dimensionless radial coordinate, r/r_0
- η^* = dimensionless radial coordinate to the shear-free surface
- λ = volume fraction
- μ = viscosity coefficient
- ν = kinematic viscosity
- ρ = density
- τ = shear stress
- τ_w = shear stress at the wall
- ϕ = angular coordinate
- ψ = stream function
- ω = angular speed

where $c_1' = dc_1/d\phi$ and $c_2' = dc_2/d\phi$. The integraiton of equation (7) results in

$$u = -\left[\frac{1}{2}c_1'\eta + \frac{1}{\eta}c_2'\ln\eta + \frac{1}{8}f''(2\eta\ln\eta - \eta)\right] + c_3/\eta \tag{8}$$

There are sufficient boundary conditions to calculate the constants c_1, c_2, c_3, and function f. The two readily available boundary conditions at the cylindrical wall are $v = 1$ and $u = 0$ when $\eta = 1$. The consideration of these two boundary conditions in conjunction with equations (6) and (8) results in

$$c_3 = \frac{1}{2}c_1' + f''/8 \tag{9a}$$

$$c_2 = 1 - c_1 \tag{9b}$$

The relation $\mathbf{V} \cdot \nabla P = 0$ is not used as the final boundary condition because it is identically satisfied. Instead, a most interesting boundary condition is derived from the consideration of net flow rate across any radius in the recirculation region between the free surface, $\eta = \eta^*$, and $\eta = 1$. This condition is described by the equation.

$$\int_{\eta^*}^{1} v d\eta = \bar{Q}_e \tag{10}$$

where $\bar{Q}_e = Q_e/r_0^2\omega$ and Q_e is the volumetric quantity of the fluid which is carried away by the cylinder wall from the main fluid bulk. This fluid rotates with the wall and then returns to the recirculation region. A casual examination of this problem may suggest that this quantity is small. It will be demonstrated later that, as the value of G decreases, the value of $\bar{Q}_e$ becomes a significantly larger fraction of the total fluid of the cylinder. Upon substitution of the dimensionless velocity, v, from equation (6), into equation (10) and following removal of c_2 in favor of $(1 - c_1)$ using equation (9b), the integration yields the value of c_1 as

$$c_1 = S_1 + S_2 f' \tag{11}$$

where,

$$S_1 = 2(\bar{Q}_e + \ln\eta^*)/(1 - \eta^{*2} + 2\ln\eta^*) \tag{11a}$$

$$S_2 = \frac{1}{4}(2\eta^{*2}\ln\eta^* - \eta^{*2} + 1)/(1 - \eta^{*2} + 2\ln\eta^*) \tag{11b}$$

The shear force in the liquid in the neighborhood of the free surface is negligibly small because the viscosity of the liquid is much larger than the viscosity of the gas which fills the rest of the cylinder. Also, the dimensionless pressure, P, is zero on the free surface. Since both P and the shear stress τ are zero on the surface, the total surface stress acting on the free surface is also zero. Accordingly, the components of the surface force along any direction is also zero. Then, the shear stress on the surface, which will be referred to as the shear-free surface, is

$$\tau_{\eta\phi} = \mu\left[\eta\frac{\partial}{\partial\eta}\left(\frac{v}{\eta}\right) + \frac{1}{\eta}\frac{\partial u}{\partial\phi}\right] = 0 \tag{12}$$

This relation can be further simplified since the value of $\nabla \times \mathbf{V}$ also becomes zero on this shear-free surface,

$$|\nabla \times \mathbf{V}| = \left|\frac{1}{\eta}\frac{\partial}{\partial\eta}(\eta v) - \frac{1}{\eta}\frac{\partial u}{\partial\phi}\right| = 0 \tag{13}$$

When equations (12) and (13) are combined, the following equation is obtained

$$\partial v/\partial\eta = 0 \text{ at } \eta = \eta^* \tag{14}$$

which will lead to the desired equation if v from equation (6) is substituted into this relation and equations (9b) and (11) are utilized to eliminate c_1 and c_2. Hence,

$$f' = \frac{1/\eta^{*2} - S_1(1 + 1/\eta^{*2})}{(1 + \ln\eta^*)/2 + S_2(1 + 1/\eta^{*2})} \tag{15}$$

Another relationship between f and η^* can be derived by setting $P = 0$, on the shear-free surface, in equation (4),

$$\eta^* = -f/G\cos\phi \tag{16}$$

The variables S_1 and S_2 depend upon η^*, equations (11a) and (11b). Equations (11a), (11b), (15) and (16) are sufficient for computation of f and η^*. Once η^* is on hand, all other quantities can be calculated. This is a remarkably lengthy nonlinear differential equation which must be integrated numerically.

When the value of G is large, the amount of fluid which is lifted from the bulk fluid is negligible, i.e., $\bar{Q}_e \approx 0$. However, for smaller values of G, especially when $G < 10{,}000$, the value of $\bar{Q}_e$ must be incorporated in the solution. Two approaches are considered. One is to guess a value of $\bar{Q}_e$, perform the integration, and then recalculate $\bar{Q}_e$ thereby leading to an iterative procedure. This idea is soon abandoned in favor of a more direct approach for evaluation of $\bar{Q}_e$. In the second approach, it is assumed that a fluid layer, δ, lifted from the bulk of the fluid is much smaller than the radius of the cylinder. Furthermore, the velocity in this thin layer using the momentum equation is described by a quadratic equation

$$v_\phi/(r_0\omega) = 1 - (\delta/r_0)^2 G\sin\phi[y/\delta - 0.5y^2/\delta^2] \tag{17}$$

where $y = r_0 - r$. This equation is derived following integration of the equation

$$\mu\frac{\partial^2 v_\phi}{\partial y^2} = \rho g\sin\phi$$

using boundary conditions $v_\phi = r_0\omega$ at the wall and $\partial v_\phi/\partial y = 0$ on the shear-free surface, and other appropriate substitutions. The volumetric flow rate, $\bar{Q}_e$ can now be computed utilizing equations (10) and (17)

$$\bar{Q}_e = (\delta/r_0) - \frac{1}{3}(\delta/r_0)^3 G\sin\phi \tag{18}$$

A logical hypothesis is introduced which is helpful in the computation of $\bar{Q}_e$. Whenever a continuous surface leaves a body of liquid, provided there is a sufficient supply of liquid, the surface will carry away the maximum amount of liquid that can be sustained by the shear force. Therefore, the maximizing parameter is the boundary layer thickness. Hence, the derivative of $\bar{Q}_e$ with respect to δ must be zero; that is,

$$\frac{d\bar{Q}_e}{d\delta} = \frac{\partial\bar{Q}_e}{\partial\delta} + \frac{\partial\bar{Q}_e}{\partial\phi}\cdot\frac{\partial\phi}{\partial\delta} = 0$$

Inasmuch as $\partial\bar{Q}_e/\partial\phi = 0$, then, following standard mathematical procedure and using equation (18), one obtains $\delta = r_0/\sqrt{G\sin\phi}$ and $\bar{Q}_e = 2/(3\sqrt{G\sin\phi})$. Cognizance should be taken that when $\phi > \pi/2$ there is not an adequate supply of liquid. When $\phi = \pi/2$, the least amount of liquid is lifted. This condition restricts the amount of fluid which will be carried away when $\phi < \pi/2$. Therefore, the volumetric flow rate of liquid lifted is obtainable by setting $\phi = \pi/2$, which is

$$\bar{Q}_e = \frac{2}{3}\sqrt{1/G} \tag{19}$$

This value of $\bar{Q}_e$ is necessary for calculating equation (11a) and subsequent computation of the flow parameters.

As a prelude to the evaluation of all flow parameters, the function, f, must be determined based on the mathematical model presented. The first-order, non-linear differential equation, equation (15), must be integrated. The initial condition for the function $f(\phi)$, that is, $f(0) = -G\,\eta_0^*$, is derived from equation (4) by setting $P = 0$ when $\eta = \eta_0^*$ and $\phi = 0$. Once the value of f is known, the velocity components u and v and shear stress, τ, in addition to the dimensionless pressure and profile of the streamlines, can be computed.

Analytical Results

A fourth-order Runge-Kutta-Gill routine is used for the

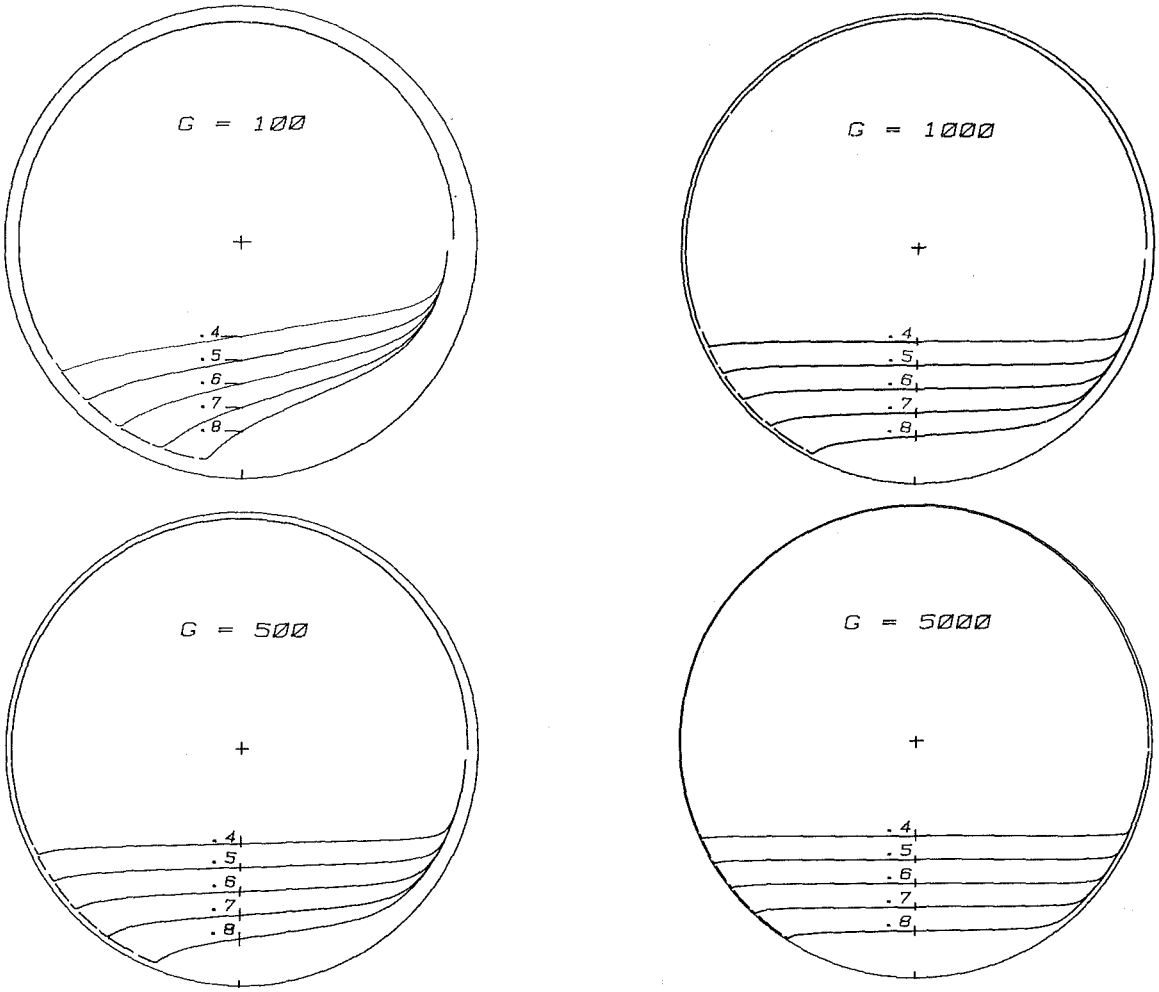

Fig. 2 Analytical values for the location of the shear-free surface η^*

Table 1 Value of liquid fraction λ for different η_0^* and G

G	η_0^*				
	0.4	0.5	0.6	0.7	0.8
100	.348	.296	.253	.219	.193
500	.296	.245	.194	.150	.114
1000	.284	.231	.179	.134	.097
5000	.269	.215	.161	.115	.074

numerical quadrature of equation (15) in which S_1 and S_2 are evaluated from equations (11*a*) and (11*b*), and η^* is replaced by f using equation (16). The entire computation is performed on a small desk-top computer, HP-85. An on-line plotter is used for graphical production of the computed results. The numerical integration begins at $\phi = 0$ with negative step size, $-\Delta\phi$, opposite to the direction of rotation. It continues until the profile of the shear-free surface, η^*, beyond the recirculation region, when $\phi < 0$, is computed. The results of the numerical computations show that integration can proceed beyond the recirculation region if the step size of integration, $-\Delta\phi$, is sufficiently small. The final angle ϕ used at the last step of the integration, designated by ϕ_e, is recorded for future use. The second part of the integration begins in a similar manner at $\phi = 0$ and proceeds toward positive ϕ. Therefore, the step size of the integration, $\Delta\phi$, is positive as the integration proceeds toward $\pi/2$.

The numerical computation performed in this manner is routine and well-behaved except when ϕ approaches $\pi/2$. A singularity of a high order (at least second) appears in the computation of η^* due to the existence of $\cos\phi$ in the denominator of equation (16). In addition, the integration for $\phi > \pi/2$ becomes sensitive to numerical errors. Accordingly, to circumvent this undesirable problem, the boundary layer approximation, described earlier, is used. The value of velocity, v_ϕ, at the outer edge of the boundary layer is $r_0\,\omega\,(1 - 1/2\,\sin\phi) > 0$. There is no down flow beyond angle $\phi = \pi/2$, in the direction of rotation. Therefore, the relation $\bar{Q}_e =$ constant is sufficient for calculation of η^* for all angles between $\pi/2$ and $2\pi + \phi_e$. The cubic equation

$$\frac{1}{3}(1-\eta^*)^3 G\sin\phi - (1-\eta^*) + \frac{2}{3}(1/G)^{1/2} = 0 \tag{20}$$

obtained by combining equations (18) and (19), is utilized for calculation of η^* when $\pi/2 < \phi < 2\pi + \phi_e$.

The computation of η^*, as described earlier, begins by assuming a value of η_0^*; which is η^* at $\phi = 0$. This quantity, in general, is an unknown. It is more realistic to compute the coordinates of the free surface for different parameters, G, and the fraction of the volume of the cylinder, λ, which is occupied by the liquid. The volumetric fraction, λ, is numerically obtainable from the equation

$$\lambda = 1 - \frac{1}{2\pi}\int_0^{2\pi} \eta^{*2} d\phi \tag{21}$$

Assuming the cylinder rotates in the positive (counterclockwise) direction, the value of η^* is computed and plotted in polar coordinates for different values of η_0^* and G, Fig. 2. It can be seen that for different values of η_0^* and G the value of λ is different. The values of λ, listed in Table 1,

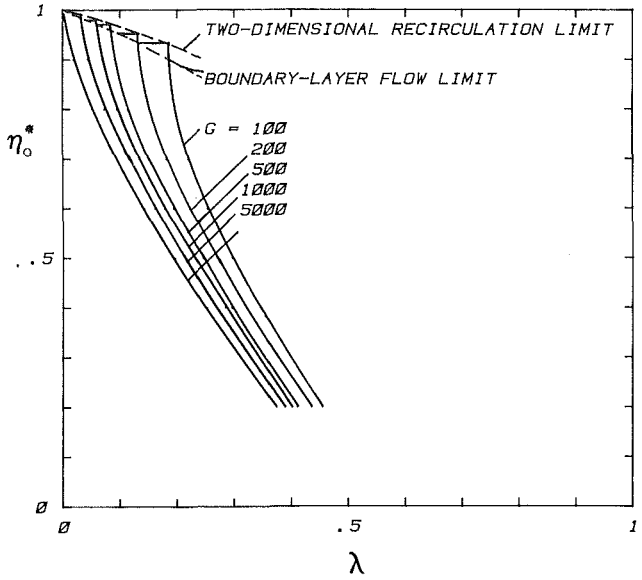

Fig. 3 Value of η_0^* for various fluid levels in the cylinder

correspond to the values η_0^* and G which appear in Fig. 2. The values of λ, for a larger range of η_0^* and G are plotted in Fig. 3. As shown in Fig. 3, for a given G, the value of η_0^* increases as λ decreases until a two-dimensional recirculation limit is reached. From that point on, the value of λ decreases while η_0^* remains constant until the boundary-layer limit is reached. The two-dimensional numerical solution becomes unstable when λ is between these two limiting values. The observation of fluid behavior between these two limits indicates that the flow is three-dimensional. When λ decreases beyond the boundary layer limit, the aforementioned maximum fluid lift hypothesis no longer holds.

The integration in the negative direction of ϕ may be continued beyond the recirculation region if the step size, $\Delta\phi$, is small. Figure 2 indicates that the coordinate of the free surface, η^* beyond the recirculation region matches perfectly the value of η^* computed using the cubic equation (20). A break in the line is intentionally provided to demonstrate the excellent agreement between the results of numerical integration of equations (15) and (20) in the thin layer located on the negative side of the recirculation region. A similar agreement, at $\phi = \pi/2$, exists only when $1-\eta^*$ is small. For smaller values of G, a slight difference exists at $\pi/2$ between the value of η^* obtained from equation (15) and that from equation (20). This is due to the inadequacy of the quadratic velocity profile approximation for the flow in this layer. However, the discrepancy is quite small and the agreement between the two solutions is satisfactory. It can be observed that the graphs representing η^* for different η_0^* asymptotically approach a single line which confirms that the boundary layer thickness at $\phi > \pi/2$ is independent of η_0^* when $\lambda < 0.5$. The value of $|\Delta\phi|$ used in numerical integration for all values of G begins at 0.02 radians, but its size is reduced considerably as the integration of f' continues beyond the recirculation region. When $G = 100$, the step size is reduced to -0.005 radians. A further reduction in step size to -0.001 radians is necessary when $G = 500$. Generally, the smaller the value of $1-\eta^*$ near the end of the recirculation region the finer the step size that must be selected. The situation is somewhat better when $\phi > 0$. The step size of 0.02 radians is satisfactory over the entire domain of $0 < \phi < \pi/2$. However, the value of $\Delta\phi = 0.005$ radians is used at larger values of G. Other step sizes were selected to verify the accuracy of the graphs presented; for instance, the difference between the step size of 0.005 and 0.01 radians attempted is graphically indistinguishable within $0 < \phi < \pi/2$.

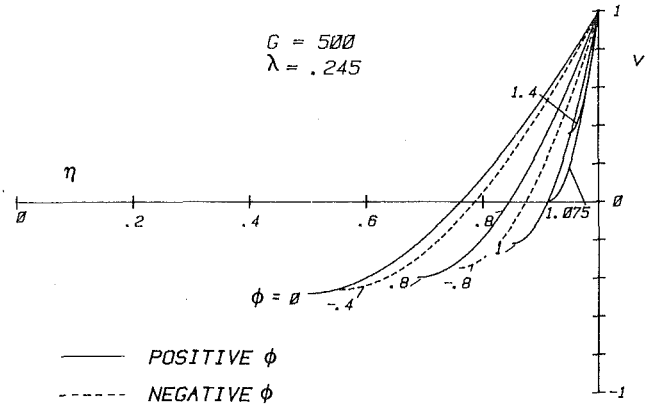

Fig. 4 Angular component of velocity for $G = 500$ and $\lambda = 0.245$

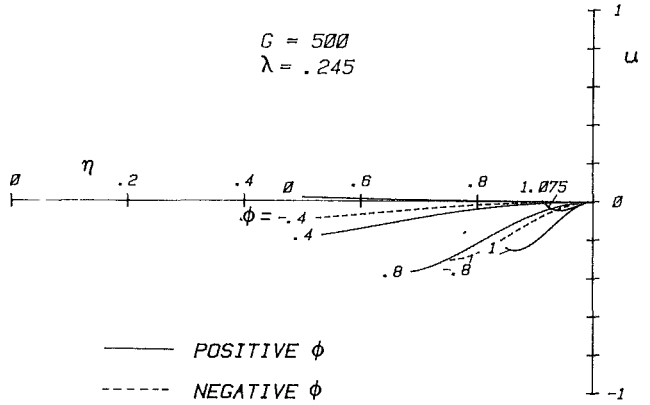

Fig. 5 Radial component of velocity for $G = 500$ and $\lambda = 0.245$

The velocity profile v is obtainable from equation (6) once η^* and consequently f', given by equation (15), is on hand. However, the calculation of u requires the calculation of f''. The value of f'' is computed by differentiating f' in equation (15).

$$f'' = -\frac{d\eta^*}{d\phi}\left\{\left[\frac{dS_1}{d\eta^*}(1+\eta^{*2}) + 2\eta^* S_1\right][(1+\ln\eta^*)\eta^{*2}/2 + S_2(1+\eta^{*2})] + [1 - S_1(1+\eta^{*2})]\left[\left(\frac{3}{2}+\ln\eta^*\right)\eta^* + \frac{dS_2}{d\eta^*}(1+\eta^{*2}) + 2\eta^* S_2\right]\right\}/[(1+\ln\eta^*)\eta^{*2}/2 + S_2(1+\eta^{*2})]^2 \quad (22)$$

$$\frac{dS_1}{d\eta^*} = 2[(1-\eta^{*2}+2\ln\eta^*)/\eta^* + (\ln\eta^* + \bar{Q}_e)(2\eta^* - 2/\eta^*)]/(1-\eta^{*2}+2\ln\eta^*)^2 \quad (22a)$$

$$\frac{dS_2}{d\eta^*} = \frac{1}{4}[4\eta^*(1-\eta^{*2}+2\ln\eta^*)\ln\eta^* + (2\eta^* - 2/\eta^*)(2\eta^{*2}\ln\eta^* - \eta^{*2}+1)]/(1-\eta^{*2}+2\ln\eta^*)^2 \quad (22b)$$

$$\frac{d\eta^*}{d\phi} = -[f'\cos\phi + f\sin\phi]/G\cos^2\phi \quad (22c)$$

Therefore, f'' is a function of η^* since f', $d\eta^*/d\phi$, and $df'/d\eta^*$ are explicit functions of η^*. The resulting values of v and u are plotted for selected values of G and λ, at different angles, ϕ, as a function of η in Figs. 4 and 5. Obviously, the purpose of these figures is to illustrate that the velocity components, as expected, exhibit no unusual behavior. The velocity component, v, at smaller angles ϕ reduces from unity

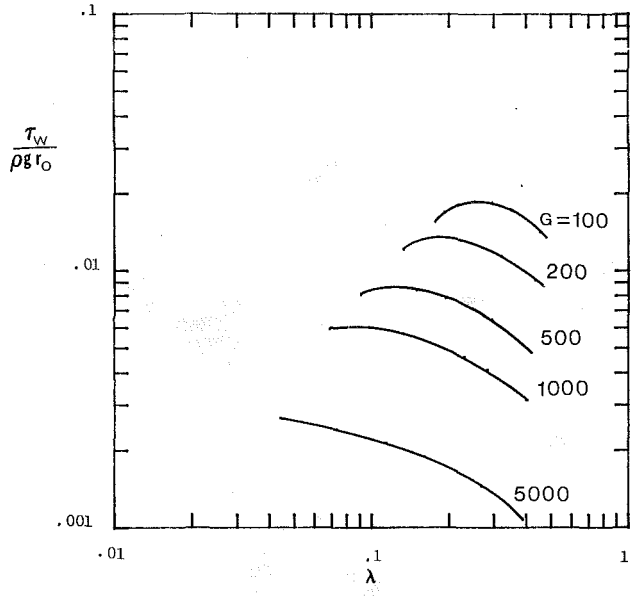

Fig. 6 Average wall shear stress for different values of G

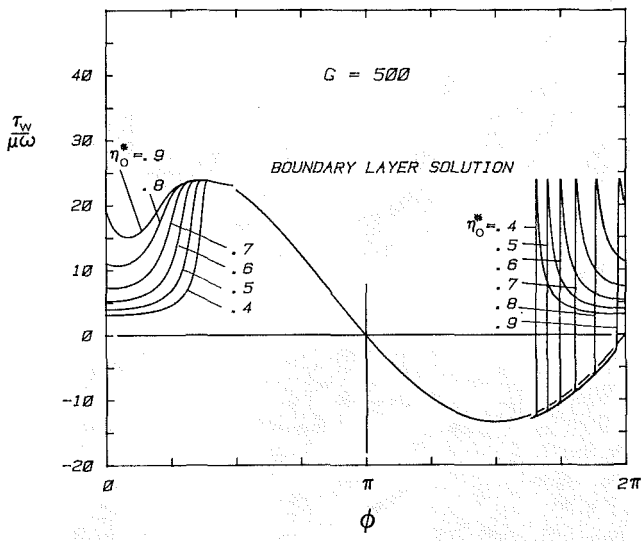

Fig. 7 Local wall shear stress for G = 500

to zero and then assumes negative values. As angle ϕ increases toward $\pi/2$, the point of zero velocity moves toward the shear-free surface. This indicates that the recirculation is followed by a total lifting of the boundary layer when $\phi >$ 1.075 radians, as shown in Fig. 4. Figures 4 and 5 also indicate that for $G = 500$ and $\lambda = 0.245$ both u and v have zero values on the shear-free surface when $\phi \approx 1.075$ radians.

Equation (12) at $\eta = 1$ is utilized to compute local and average shear stress along the cylindrical surface. The term $\partial u/\partial\phi$ in that equation identically vanishes since $u = 0$ when $\eta = 1$. The local shear stress is obtained from the relation

$$\tau_w/\mu\omega = -2c_2 + f'/2 \tag{23}$$

in the recirculation region. Also, in the boundary layer flow, the shear stress is obtainable from the relation

$$\tau_w/\mu\omega = (1-\eta^*)G\sin\phi \tag{24}$$

The shear force per unit length of the cylinder, F, is derived using the relation

$$F = \int_0^{2\pi} \tau_{r\phi} r_0 d\phi$$

which following some algebraic simplification results in a workable form

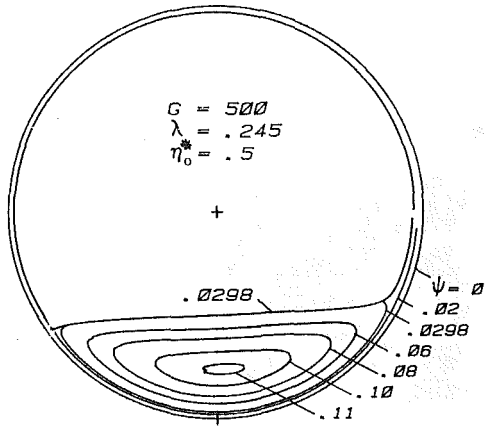

Fig. 8 Streamlines for G = 500, λ = 0.245

$$F/\mu\omega r_0 = \int_{\phi_e}^{\pi/2}(-2c_2 + f'/2)d\phi + \int_{\pi/2}^{2\pi+\phi_e}(1-\eta^*)G\sin\phi\, d\phi \tag{25}$$

in which $\phi_e < 0$. The value of $\tau_w/\rho g r_0 = F/2\pi G\mu\omega$ computed in this manner is plotted versus λ for different values of G, Fig. 6. The data indicate that the value of the average wall shear stress initially increases as λ decreases and it reaches a maximum before it begins to decrease. This can be explained by observing the variation of the local wall shear stress as a function of ϕ, Fig. 7. The value of local wall shear stress assumes its largest values in the vicinity of the recirculation region when $(1-\eta^*)$ is small. Figure 7 indicates that the shear stress in the first quadrant increases as λ decreases (or η_o^* increases) but the region of high shear stress decreases as λ decreases. Therefore, the magnitude of the shear stress and the size of the region of high local shear stress have opposite effects on the average shear stress. The local shear stress is zero when $\phi = \pi$ and near the end of the recirculation region in the fourth quadrant.

The fluid model defined in the foregoing is rotational; that is, $\nabla \times \mathbf{V} \neq 0$ except when $\eta = \eta^*$. However, the continuity equation can be utilized to define a stream function, ψ, so that

$$u\eta = \partial\psi/\partial\phi \text{ and } v = -\partial\psi/\partial\eta \tag{26}$$

This equation, in conjunction with equations (6) and (8) and following standard mathematical operations, yields the following stream function

$$-\psi = \frac{1}{2}c_1\eta^2 + c_2\ln\eta + \frac{1}{8}(1+2\eta^2\ln\eta - \eta^2)f' - \frac{1}{2}c_1 \tag{27}$$

The lines of constant ψ for one value of λ and $G = 500$ are plotted in Fig. 8. Additional graphs are presented when the analytical results are compared with the experimental data. The shape of the streamlines, Fig. 8, agrees well with all the assumptions described earlier, and indicates that a volumetric flow rate is lifted and then carried around with the cylindrical surface. In addition, the point at which the total lifting of the boundary layer begins is clearly indicated in the first guadrant of the graph. However, the fluid flow in the neighborhood of this total lift-off point is not studied experimentally. A comparison of streamlines calculated in this manner with experimental data appears in a later section. In calculating streamlines, the wall is selected as the zero streamline. The value of ψ for the streamline which includes the shear-free surface is 0.0298.

Experimental Setup

The experiment is conducted with a view to testing the validity of the analytical model for the shear-free surface developed earlier. In addition, the streamlines ae obtained photographically and compared with those from analysis.

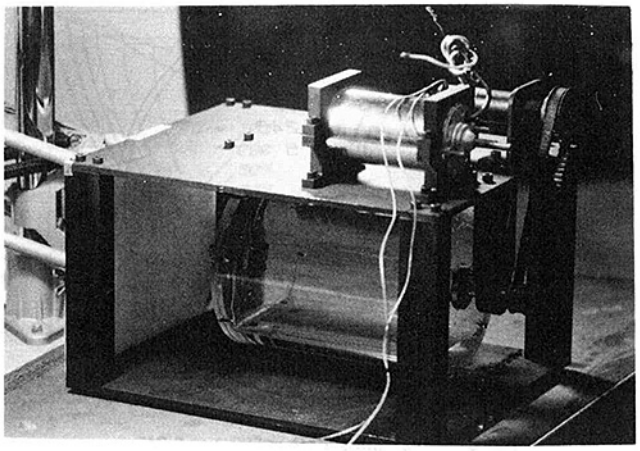

Fig. 9 Photograph of the apparatus

The experimental setup consists of a hollow cylinder made of plexiglas, 15.4 cm I.D. and 20 cm in length, with end walls also of plexiglas. It has two shafts, mounted on ball bearings, attached to the end walls. Each shaft is attached to an end wall and the end walls are mounted on the cylinder before the shafts are machined. This procedure minimizes the eccentricity of the cylinder. The whole assembly is suspended within a rigid frame and driven by D.C. motors with the transmission of power accomplished by a pulley-belt system. The power supply to the motors is provided by a variable D.C. power supply unit. A photograph of the setup is given in Fig. 9.

Experiments are conducted with two fluids (water and glycerin) at various rotational speeds so as to obtain data over a wide range of G and Reynolds numbers. The fluids can be put into the cylinder through a small port hole provided on one of the end walls. The water soluble dye needed to observe the streamlines can also be injected, by means of a syringe, through the same port hole.

The cylinder is first filled with the fluid to the desired level. The height of the free, undisturbed surface (measured on the vertical line passing through the center) is photographed. This will give the volume of the fluid in the system and subsequently the value of the volume fraction. The power supply is turned on and the voltage is set at the required level. The cylinder starts rotating and the flow inside the cylinder attains a steady state within a few minutes. The speed of the rotating cylinder is determined using a stop watch. A calibrated stroboscope is used when the rotational speed is high. A closeup photograph of the shear-free surface, formed due to flow inside the cylinder, is taken from the front end.

The second part of the experiment consists of injecting the dye when the cylinder is stationary and allowing the cylinder to rotate immediately after the syringe is withdrawn. Care is taken to prevent the injection of the dye into the secondary flow regions, prevalent near the end walls. The well-developed streamlines, which are made visible by the dye, are photographed for further analyses. The procedure is repeated for various speeds and volumes of fluid inside the cylinder.

The surface profiles from the photographs are retraced and stored in the form of digitized data, using a minicomputer, to be reproduced and compared with the analytical results.

Experimental Results

Numerous photographs are prepared which show the profiles of the shear-free surface for glycerin and water. Figure 10 contains three photographs selected for this paper. Red dye is added to the glycerin for a better photographic contrast. The profiles of the shear-free surfaces, Fig. 10, as expected, become steeper as the value of G decreases. The boundary layer created at the front plate must be identified and accounted for during data reduction. This causes some difficulty in accurate determination of the shear-free surface profiles. The coordinates of these profiles are determined by digitizing enlarged photographs using a desk-top computer and a plotter. The data obtained by this technique are plotted in Fig. 11. The analytical profiles of the shear-free surfaces are also computed for the same G values and plotted in the same figure. Despite some discrepancies between the analytical solution and experimental data, the agreement between results is satisfactory. The errors are caused by the

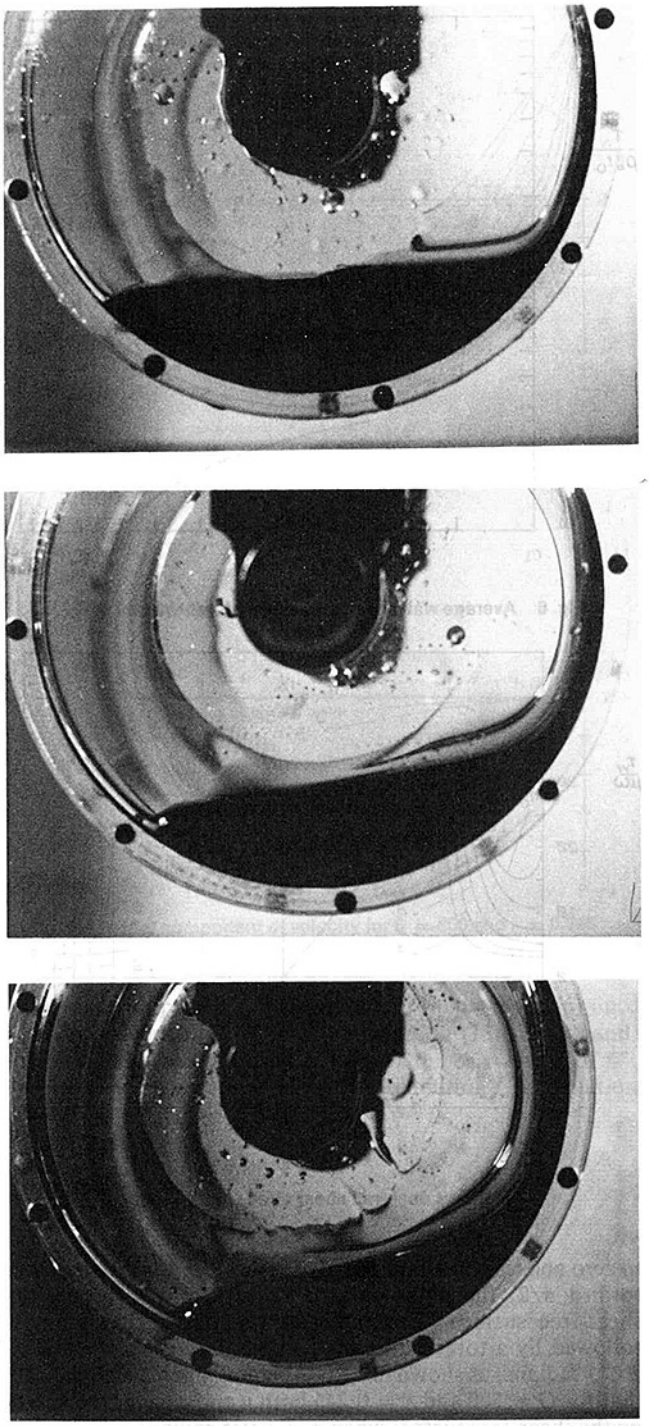

Fig. 10 Photographs of the shear-free surface for glycerin

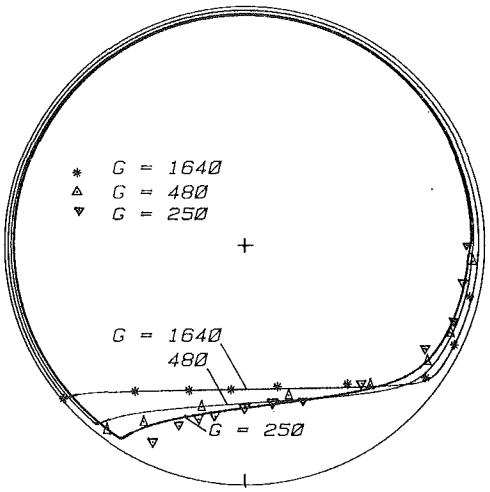

Fig. 11 A comparison between analytical and experimental values of shear-free surface profiles for glycerin, $\lambda = .175$. (Uncertainty in G is ± 15 percent and in η is ± .02 with 80 percent probability.)

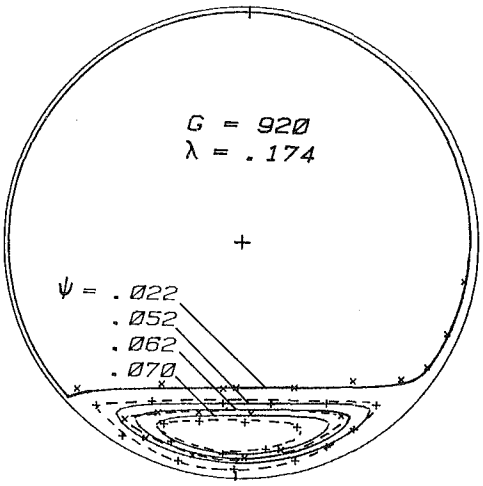

Fig. 13 A comparison between analytical (solid line) and experimental (dashed line) values of streamlines $G = 920$. (Uncertainty in G is ± 15 percent and in η is ± .02 with 80 percent probability.)

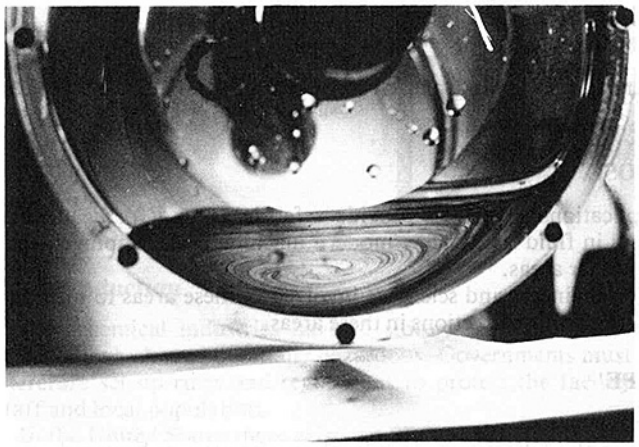

Fig. 12 Streaklines for glycerin, $G = 920$ and $\lambda = .174$

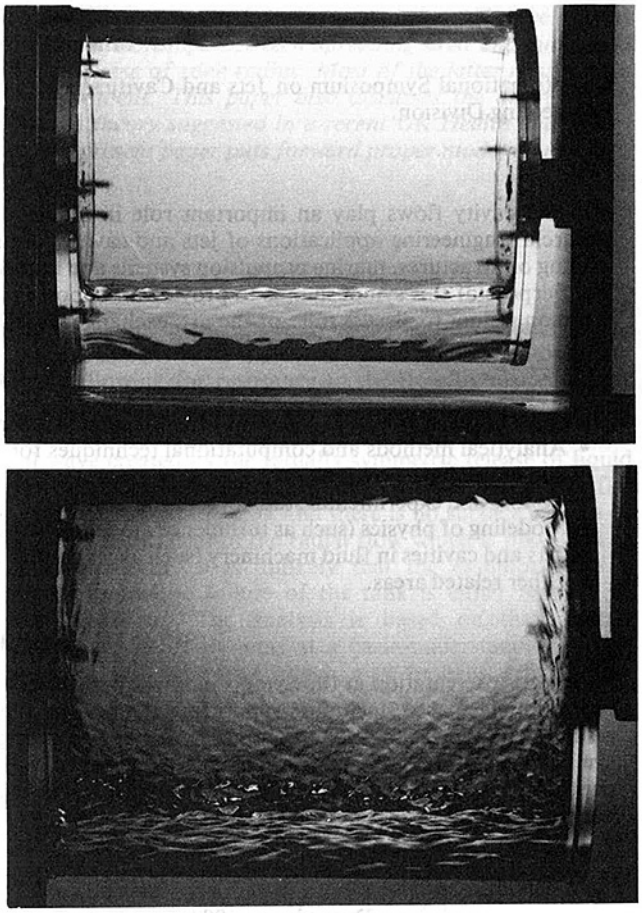

Fig. 14 Flow regimes for water in the rotating horizontal cylinder

visual effect of the boundary layer at the frontal plate, parallax error of the photography, the influence of the secondary flow, uncertainties in the value of the properties, approximations in the theoretical model, and surface tension. Similar photographs, not shown, with water as the working fluid, indicate that, at low Reynolds numbers, the profiles of the shear-free surface are very flat and their agreement with the analysis is assured. However, as will be discussed later, the flow in the recirculation region is significantly more complex.

A comparison is made between streamlines determined by flow visualization and those calculated analytically. The dye is introduced at a few points within the glycerin while the cylinder was not in motion. The traces of dye are really streaklines since each originates from a single point. It requires an infinite amount of time for the streaklines to become streamlines. Therefore, the streaklines appearing in the photograph, Fig. 12, approximate streamlines. The coordinates of the streaklines in this photograph are plotted in Fig. 13. The streamlines computed when $\eta_0^* = 0.63$ and $G = 920$ also appear in Fig. 13, and the agreement between the results is satisfactory. In addition, the pattern of streaklines in Fig. 12 is quite similar to the pattern of streamlines in Fig. 13.

Discussion

A simplified fluid model is developed which predicts the recirculation region in a rotating horizontal cylinder. This model applies to highly viscous fluids in slowly rotating cylinders. Except in the vicinity of the end plates, the flow is two-dimensional and well behaved. However, as the angular speed increases, the size of the recirculation region becomes smaller. At high angular speeds, all of the glycerin will be located in the boundary layer. Between the two-dimensional and boundary layer regimes, there is a third regime for which there is no two-dimensional solution and the flow is three-dimensional.

For low viscosity fluids, e.g., water, even at low angular speed, the Reynolds number is high. Small eddies are observed in the positive direction of the recirculation region and larger eddies on the negative side. The recirculation region is

located mostly in the first quadrant and the flow in the fourth quadrant is mainly controlled by the large eddies. The profile of the shear-free surface is nearly horizontal and the flow is three-dimensional. The boundary layer lifted is very thin and it moves toward the center of the cylinder forming droplets. As the angular speed increases, the flow in the boundary layer will become steady and eventually the boundary layer becomes turbulent. Two photographs in Fig. 14 show this transition from laminar to turbulent. The Reynolds number for the photographs are given in Fig. 14. Photograph (b) in Fig. 14 indicates an approximate starting Reynolds number for turbulent flow at Reynolds number, $r_0^2\,\omega/\nu = 120{,}000$.

Acknowledgment

This research work was supported by Frito-Lay, Inc. The authors wish to thank Dr. P. Desai for his many helpful discussions and Mrs. R. Haji-Sheikh for her photographic work.

References

1 Scott, W. E., "Free Surface Breakdown in a Rapidly Rotating Liquid," *J. Fluid Mechanics*, Vol. 86, June 1978, pp. 457–463.

2 Greenspan, H. P., "On a Rotational Flow Disturbed by Gravity," *J. Fluid Mechanics*, Vol. 74, Mar. 1976, pp. 335–352.

3 Gans, R. F., "On the Flow Around a Buoyant Cylinder Within a Rapidly Rotating Cylindrical Container," *J. Fluid Mechanics*, Vol. 93, Aug. 1979, pp. 529–548.

4 Gans, R. F., and Yalisove, S. M., "Observations and Measurements of Flow in a Partially-Filled Horizontally Rotating Cylinder," ASME JOURNAL OF FLUIDS ENGINEERING, Vol. 104, Sept. 1982, pp. 363–366.

5 Schlichting, H., *Boundary Layer Theory*, 6th Edition, McGraw-Hill, New York, 1968.

Asymptotic Behavior in Slumping From a Cylindrical Tank

Y. Bai[1]

W. Johnson

R. G. M. Low

S. K. Ghosh[2]

University of Engineering Department, Cambridge CB2 1PZ, England

When an oil tank collapses or ruptures any contained hazardous substance flows outwards and can damage nearby plant or people as well as lead to pollution of the local environment. In recent years, this and similar subjects have given rise to a new kind of engineering–spill prevention and control. However, theoretical background, backed by experiment, is lacking to work out reliable regulations. An intermediate-asymptotic analysis for late-stage spreading is carried out in this paper. This analysis reveals several characteristic features of the spill wave such as transition period and linear relationships between spreading area and time, and wave front velocity and the inverse of zone radius. Most of the latter results have been verified by model experiment. This paper also discusses the discrepancies between observations and the theory suggested in a recent UK Health and Safety Executive report. Finally, the present paper puts forward proper modeling rules for future work.

1 Introduction

Petrochemical industries have to store large amounts of materials which are potentially hazardous. Governments must therefore set up rules and regulations to protect the facility staff and local population.

In the United States there exists an SPCC plan [1] – a Spill Prevention Control and Countermeasure plan. The SPCC plan is carefully thought-out and prepared according to good engineering practice. For equipment failure (such as tank overflow, rupture or leakage), such a plan should include a prediction of the direction, rate of flow and the total quantity of oil which could be discharged from the facility as a result of each major type of failure. In the UK, the Health and Safety Executive investigated the hazards at the Canvey Island/Thurrock complex [2–4] with the intention of estimating the existing levels of risk and then proposing modifications to plant design and operation in order to reduce these risks to more acceptable levels. Obviously, predictions of flow characteristics such as area and height of flooded zone and roll wave front velocity are needed in the design of effective bunding arrangements for the storage vessels. Needless to say, it is desirable to have some theoretical guides in order to tackle such a complicated problem.

It is desirable to have some idea of the mechanical effect of a sudden release of a large quantity of hydrocarbon in liquid form. Kinkead [5] reported that the heights of the storage tanks for the Occidental Refinery vary from 14 to 22 metres and their diameters range from 20 to 70 metres. The largest tank has a diameter of 46.65 metres and a height of 14.63 metres. He suggested that the slumping of such a liquid source cylinder may be evaluated after assuming the surrounding flat land (as happens to be the case at Canvey) to be smooth and by not allowing for resistance to the flow by miscellaneous obstacles and irregularities on the ground surface.

The present paper confines itself to an investigation of the spill wave created by the radially symmetric release of liquid from a single vertical cylindrical tank. Smooth and flat surfaces surround the tank and there is no surface tension or any other resistances to the radial flow which is presumed to occur. Naturally, it is unlikely that the assumption of a radially symmetric failure of the tank is either realistic or most dangerous. The analysis is based on the simplest assumptions and only aims at a basic understanding of the nature of the spill wave which may be caused by a tank

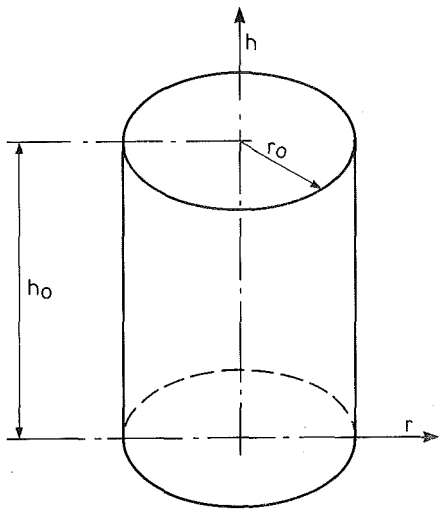

Fig. 1 Schematic diagram of initial liquid column and coordinates

[1] Now, Institute of Mechanics, Chinese Academy of Sciences, Beijing, People's Republic of China.

[2] Now, Brown Boveri Reaktor GmbH, 6800 Mannheim 31, West Germany.

Contributed by the Fluids Engineering Division for publication in the JOURNAL OF FLUIDS ENGINEERING. Manuscript received by the Fluids Engineering Division, May 24, 1982.

collapse. Because the central issue concerns the spreading area covered by the liquid, it is mainly the late stage behavior of this slumping process which is of interest. Therefore a technique of intermediate asymptotic analysis is adopted. Both flow patterns and the rules governing the wave front movement are given. A comparison between the analysis and some preliminary experimental observations confirms that asymptotic behavior controls slump spreading.

2 Asymptotic Analysis

Consider symmetrical radial flow from an initially stationary incompressible and inviscid liquid column of height h_0 and radius r_0, as shown in Fig. 1.

The system of equations governing the flow in cylindrical coordinates is as follows. The continuity equation is,

$$\frac{\partial(hr)}{\partial t}+\frac{\partial(vhr)}{\partial r}=0, \tag{2.1}$$

where h is the current height of the flow, v the velocity and r and t denote the radial coordinate and time, respectively. The momentum equation is,

$$\frac{\partial v}{\partial t}+v\frac{\partial v}{\partial r}+\frac{g}{2hr}\frac{\partial(h^2r)}{\partial r}=0. \tag{2.2}$$

The system of nonlinear partial differential equations (2.1) and (2.2) govern the flow under consideration. The initial conditions are,

$$\left.\begin{array}{lll}\text{At } t=0, & v=0, & \text{for all } h,\\ & h=h_0, & 0<r<r_0,\\ \text{and} & h=0 \text{ for } r_0<r<\infty.\end{array}\right\} \tag{2.3}$$

Because of the nonlinearity of the equations, there are no explicit solutions for such an initial value problem.

We wish to address the problem of liquid spreading, because it can have potentially harmful consequences to local environment. Since the local population and workforce, etc., generally will not be very close to the storage tanks, the crucial feature is late stage spreading rather than the early collapse of the liquid column or the early slumping. For this reason we can focus our attention on the behavior of the so-called intermediate asymptotic flow, which characterizes the late stage of the spill-wave even though it is unsteady.

Generally speaking, the flow is characterized by two variables: height h and velocity v, both of which are functions of the independent variables r and t and parameters h_0, r_0, and g, i.e.,

$$\left.\begin{array}{l}h=h(t,r,h_0,r_0,g)\\ v=v(t,r,h_0,r_0,g).\end{array}\right\} \tag{2.4}$$

Using dimensional analysis, the expressions (2.4) can be simplified to

$$\frac{h}{h_0}=\bar{h}\left(\frac{r}{h_0},\frac{h_0}{r_0},\frac{gt^2}{h_0}\right)$$

and

$$\frac{v}{\sqrt{gh_0}}=\bar{v}\left(\frac{r}{h_0},\frac{h_0}{r_0},\frac{gt^2}{h_0}\right). \tag{2.5}$$

It is easy to see that both flow velocity v and height h should tend to zero, as wave front r_f tends to infinity. Then, at a remote distance r or after a long time t, we can suppose the following form of asymptotic behavior to hold,

$$\left.\begin{array}{l}\left(\frac{h}{h_0}\right)\left(\frac{r}{h_0}\right)^{\beta}\sim 0(1),\\ \left(\frac{v}{\sqrt{gh_0}}\right)\left(\frac{r}{h_0}\right)^{\gamma}\sim 0(1),\\ \text{and } \left(\frac{gt^2}{h_0}\right)^{\alpha}\left(\frac{r}{h_0}\right)\sim 0(1).\end{array}\right\} \tag{2.6}$$

where β and γ should be positive (from physical considerations) whilst α is negative. In this circumstance, the dimensionless expressions (2.5) can be further simplified to functions of a single independent variable, thus

$$\left.\begin{array}{l}H\left(\xi,\frac{h_0}{r_0}\right)=\frac{h}{h_0}\left(\frac{r}{h_0}\right)^{\beta},\\ V\left(\xi,\frac{h_0}{r_0}\right)=\frac{v}{\sqrt{gh_0}}\left(\frac{r}{h_0}\right)^{\gamma},\\ \text{with } \xi=\left(\frac{gt^2}{h_0}\right)^{\alpha}\left(\frac{r}{h_0}\right),\end{array}\right\} \tag{2.7}$$

where all the variables ξ, H, and V are well-scaled. All partial differentiations in the governing equations (2.1) and (2.2) can be easily transferred to the ordinary differentiation of functions H and V with respect to ξ, as

$$\left.\begin{array}{l}\frac{\partial h}{\partial t}=h_t=2\alpha h_0 t^{-1}\left(\frac{r}{h_0}\right)^{-\beta}\xi H',\\ \frac{\partial v}{\partial t}=v_t=2\alpha\sqrt{gh_0}\left(\frac{r}{h_0}\right)^{-\gamma}t^{-1}\xi V',\\ \frac{\partial h}{\partial r}=h_r=(-\beta H+\xi H')\left(\frac{r}{h_0}\right)^{-\beta-1},\\ \text{and } \frac{\partial v}{\partial r}=v_r=(-\gamma V+\xi V')\frac{\sqrt{gh_0}}{h_0}\left(\frac{r}{h_0}\right)^{-\gamma-1}.\end{array}\right\} \tag{2.8}$$

Nomenclature

c = constant
g = gravitational acceleration
h = height of slump
p = pressure
r = radius of slump
t = time
v = flow velocity
C = wave speed with respect to fluid at rest
D = wave speed
H = dimensionless function of height
U = initial volume
V = dimensionless function of velocity
α,β,γ = constants
ρ = density
ξ = dimensionless independent variable

Subscripts

f = wave front, i.e., leading edge of flow
m = model
0 = initial condition

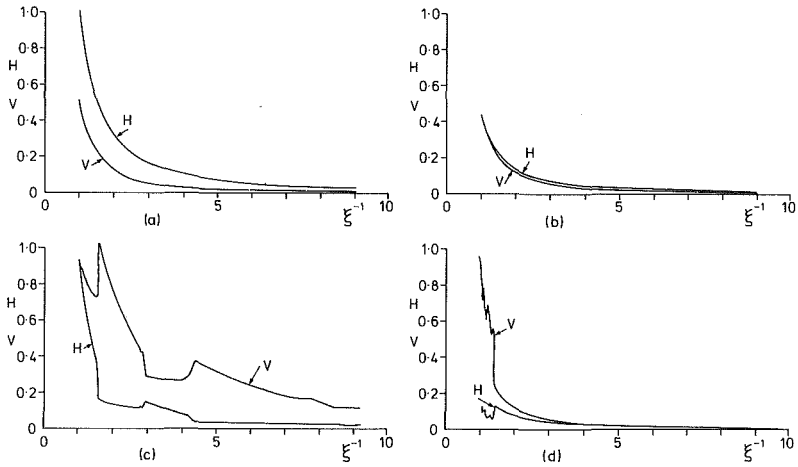

Fig. 2 The solution of H and V versus ξ^{-1} ($\Delta = 0.01$)

After substituting (2.8) into the continuity equation (2.1), it reduces to

$$H'\xi^{1-\frac{1}{2\alpha}}\left(\frac{r}{h_0}\right)^{\frac{1}{2\alpha}+\gamma+1}+\gamma[(1-\beta)H+\xi H']$$
$$+H(\xi V'-\gamma V)+HV=0. \tag{2.9}$$

All terms except the first are 0(1), with the first term implying some unsteady character of the flow.

Provided the unsteady behavior remains significant in the stage under consideration, the term must be 0(1). This requires

$$\frac{1}{2\alpha}+\gamma+1=0. \tag{2.10}$$

Turning to the momentum equation, in the same way we obtain the following equations

$$2\alpha\xi^{1-\frac{1}{2\alpha}}V'+V(-\gamma V+\xi V')+(\tfrac{1}{2}-\beta)H+\xi H'=0 \tag{2.11}$$

and

$$\beta=2\gamma. \tag{2.12}$$

One more equation is now needed for the determination of the parameters α, β, and γ and a pattern of very late spreading can provide an approximation for it.

According to dimensional analysis, the wave front parameter ξ_f must be a constant for a given case, therefore

$$\left(\frac{h_f}{h_0}\right)\left(\frac{r_f}{r_0}\right)^{\beta}=\left(\frac{h_0}{r_0}\right)^{\beta}H_f\left(\xi_f,\frac{h_0}{r_0}\right). \tag{2.13}$$

The latter, however, is of 0(1) and thus,

$$h_f r_f{}^{\beta}\sim h_0 r_0{}^{\beta}. \tag{2.14}$$

After long term spreading, the height of flow should be fairly flat. Based on the argument of mass conservation, as the wave front radius r_f tends to infinity, the index β should take the value of 2 in a cylindrical configuration, otherwise (2.14) is violated. Furthermore, from (2.10) and (2.12) we arrive at

$$\gamma=1, \tag{2.15}$$
$$\alpha=-\tfrac{1}{4},$$

and equations

$$\begin{cases}\left(V\xi-\dfrac{\xi^3}{2}\right)H'+\xi HV'-2HV=0\\[2ex] \xi H'+\left(V\xi-\dfrac{\xi^3}{2}\right)V'-V^2-\dfrac{3}{2}H=0.\end{cases} \tag{2.16}$$

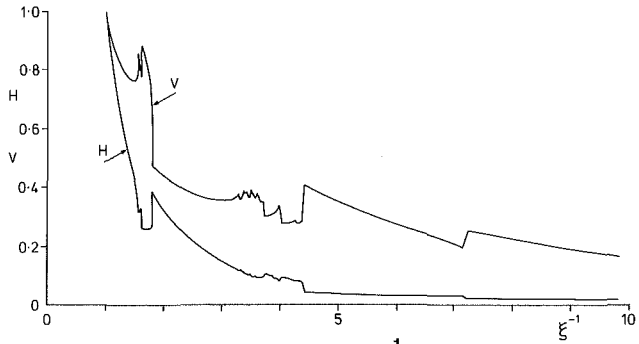

Fig. 3 The solution of H and V versus ξ^{-1} ($\Delta = 0.002$) with different parameters at $\epsilon^{-1} = 1$.

The system of nonlinear ordinary differential equations is easy to handle by means of numerical procedure. A program using the standard Runge-Kutta method was developed. It is well-known that the error due to remainders in the procedure is $0(\Delta^5)$, where Δ denotes difference and is taken as 0.01 in our computations. Computational examples are shown in Fig. 2(*a–d*). The ordinate represents function V or H and the abscissa is ξ^{-1}. Recalling definitions (2.7), the diagrams in Fig. 2 show variations of flow velocity or height with time at a fixed point r. It is interesting to note that the functions H and V are smooth for some values of H and V but they jump abruptly for others. For smooth ones, Fig. 2(*a–b*), the errors produced by the Runge-Kutta procedure are negligible, being based on the estimate $0(\Delta^5)$. The diagrams with jumps, i.e., Fig. 2(*c–d*) need further examination. Figure 3 shows the result with the same parameters as that in Fig. 2(*c*), but with a shrunken difference ($\Delta = 0.002$). It is seen that the main features, trends and major jumps, remain similar, though fine structures vary badly. We leave these for further discussion in the next section.

3 Implications of Spill Waves

Examine the propagation of a wave which is a surface of discontinuity, supposing the wave moves outward with a steady velocity D, see Fig. 4. In cylindrical coordinates the mass and momentum conservation laws take the following forms:

$$h_1 v_1{}' = h_2 v_2{}' \tag{3.1}$$

and

$$\left[v_1{}'^2+\frac{gh_1}{2}\right]h_1=\left[v_2{}'^2+\frac{gh_2}{2}\right]h_2, \tag{3.2}$$

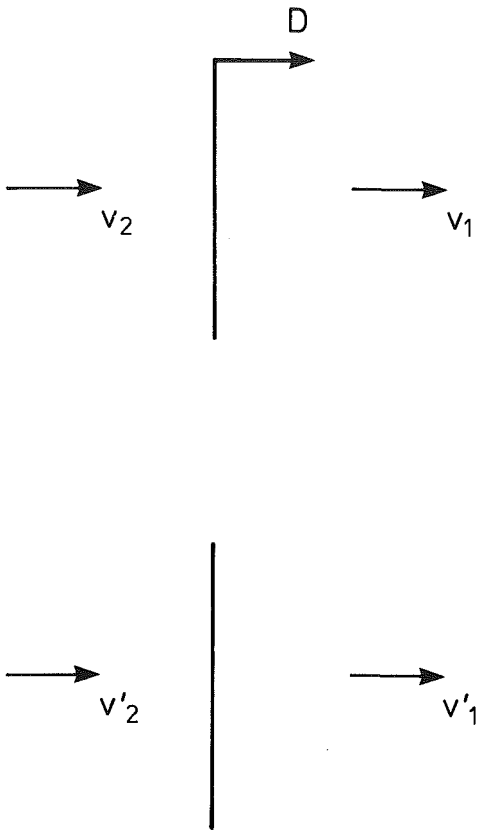

Fig. 4 A stationary jump

where $v_1' = v_1 - D$ and $v_2' = v_2 - D$.
Hence,

$$v_1' = \pm\sqrt{gh_2\left(1+\frac{h_2}{h_1}\right)\Big/2} \tag{3.3}$$

or

$$D = v_1 + C \quad \text{and} \quad C = v_1'. \tag{3.4}$$

If, $h_2 \sim h_1 = h_0$, then

$$C = \sqrt{gh_0}. \tag{3.5}$$

(3.1) and (3.2) describe a bore as given by Whithan [6] for a one-dimensional water wave. It is not surprising that there is a coincidence between planar and cylindrical flows, because there is a nearly zero-thickness of discontinuity. These are, as Whithan observed, "the turbulent bores familiar in water wave theory as 'hydraulic jump' or breakers on a beach." Both Whithan [6] and Lighthill [7] have given details about the structures of undulant and turbulent bores. It now appears clear that the jumping flow patterns shown in Fig. 2, (*c*–*d*) are a kind of turbulent bore or a hydraulic jump. To confirm this let us examine the values H and V.

From the definitions of H and V in (2.7), and with $\gamma = 1$, $\beta = 2$, V can be described by

$$V = \frac{v}{\sqrt{gh_0}}\left(\frac{r}{h_0}\right) = \frac{v\sqrt{H}}{\sqrt{gh}}. \tag{3.6}$$

The necessary condition for hydraulic jumps is that of so-called "supersonic flow" [7]. In accordance with (3.5), it requires that

$$v > \sqrt{gh}, \tag{3.7}$$

or

$$V > \sqrt{H}. \tag{3.8}$$

Figure 2(*a* and *b*) show smooth flows, in accordance with small values of V whereas abrupt jumps appear, in Fig. 2(*c* and *d*) owing to values of $V >> \sqrt{H}$. More interestingly, both V and H tend to become smooth, once V values decrease to a certain level, which seems to be somewhat similar to (3.8). It is apparent that computational jumps are due to the existence of hydraulic jumps. Because of the turbulent nature of bores, the details of computational jumps are quite sensitive to the

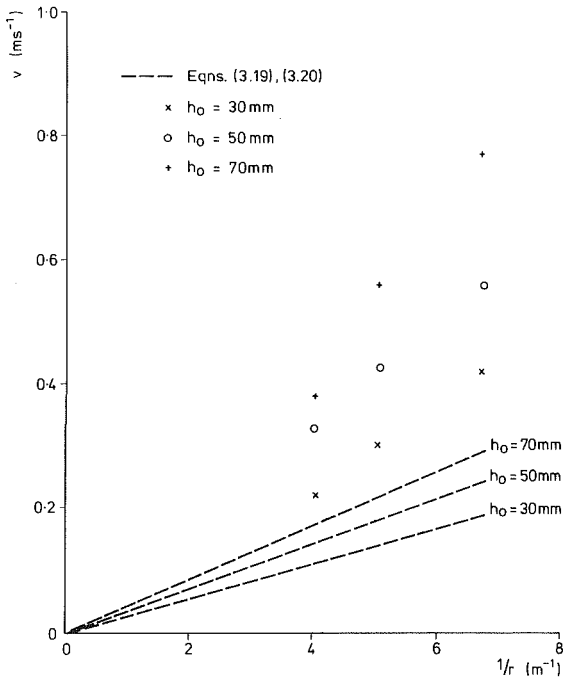

Fig. 5 Graph of the roll wave front velocity against the inverse of the radius of the slumped liquid zone

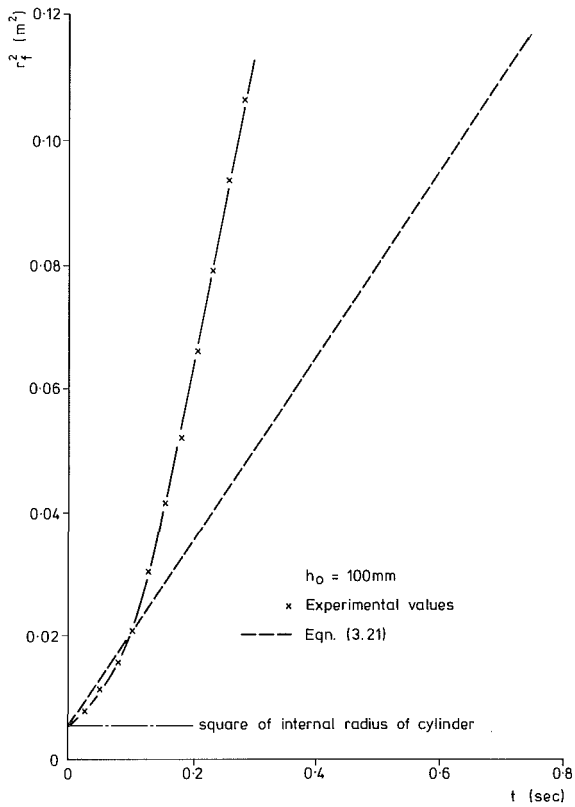

Fig. 6 Graph of the square of the slumped liquid radius against time for medium diameter cylinder

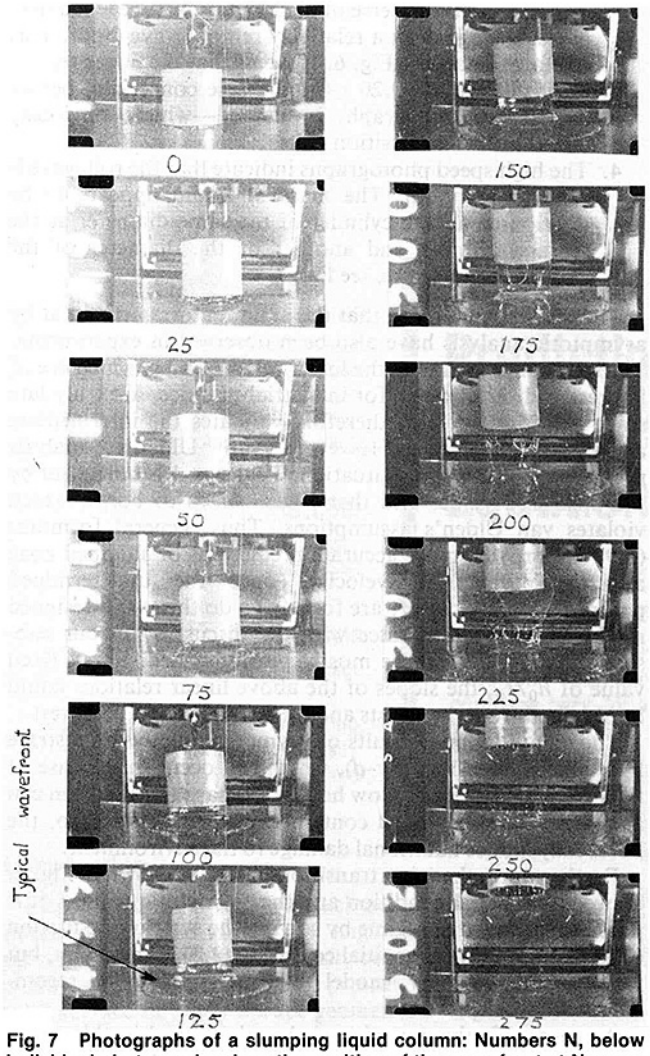

Fig. 7 Photographs of a slumping liquid column: Numbers N, below individual photographs show the position of the wave front at N m sec after the raising of the cylinder has commenced.

variation of Δ. It is unlikely that the fine features of bores can be predicted accurately by the present method.

Now we turn to the most significant practical feature of the spill wave, that is the movement of the wave front. As before we denote wave front quantities with a subscript f, and recall that for a certain case the parameter ξ_f must remain constant. Hence, from the definitions of (2.7) we can obtain several important relations:

$$h_f = h_0\left(\frac{h_0}{r_f}\right)^2 H_f\left(\xi_f, \frac{h_0}{r_0}\right) = h_0{}^3 r_f{}^{-2} f_1\left(\frac{h_0}{r_0}\right), \quad \text{(a)}$$

$$v_f = \sqrt{g h_0}\left(\frac{h_0}{r_f}\right) V_f\left(\xi_f, \frac{h_0}{r_0}\right) = \sqrt{g} h_0{}^{3/2} r_f{}^{-1} f_2\left(\frac{h_0}{r_0}\right) \quad \text{(b)}$$

and

$$r_f^2 = \sqrt{g\xi_f} h_0{}^{3/2} t_f = \sqrt{g} h_0{}^{3/2} f_3\left(\frac{h_0}{r_0}\right) t_f \quad \text{(c)}$$

(3.9)

where $f_1 = H_f, f_2 = V_f$ and $f_3 = \sqrt{\xi_f}$.

We can now draw some significant conclusions from (3.9).

(1) The Rules for Liquid Spreading. For a certain height h_0 and aspect ratio h_0/r_0, at the long term asymptotic stage the following rules may be established:

$$\left.\begin{aligned} h_f &\sim \frac{1}{r_f{}^2}, \\ v_f &\sim \frac{1}{r_f} \\ \text{and} \quad r_f{}^2 &\sim t_f. \end{aligned}\right\} \quad (3.10)$$

In other words, once an oil tank breaks symmetrically, the slumping will undergo a transition phase in which the flow does not follow the rules (3.10). However, the spill wave will gradually tend to spread according to the rules.

(2) Similarity Laws. All slopes in the linear relations $h_f \sim r_f{}^{-2}$, $v_f \sim r_f{}^{-1}$ and $r_f{}^2 \sim t_f$ are functions of the two variables, height h_0 and aspect ratio h_0/r_0. Thus for modeling, it is necessary to treat data using the following dimensionless expressions:

$$\left.\begin{aligned} \frac{h_f}{h_0} &= f_1\left(\frac{h_0}{r_0}\right)\cdot\left(\frac{r_f}{h_0}\right)^{-2} \quad \text{(a)} \\ \frac{v_f}{\sqrt{g h_0}} &= f_2\left(\frac{h_0}{r_0}\right)\left(\frac{r_f}{h_0}\right)^{-1} \quad \text{(b)} \\ \text{and} \quad \frac{r_f{}^2}{h_0{}^2} &= f_3\left(\frac{h_0}{r_0}\right)\frac{\sqrt{g} t_f}{\sqrt{h_0}}. \quad \text{(c)} \end{aligned}\right\} \quad (3.11)$$

(3) Modeling. In model testing, aspect ratio h_0/r_0 and the functions f_1, f_2, and f_3 in (3.9) remain unchanged although the dimensions change. For instance, the model height $h_{0,m} = kh_0$, where $k < 1$ and subscript m denotes model.

If we examine the phenomena with the unchanged time scale in both model and full scale test—then the spreading area $r_f{}^2$ will sustain the change as

$$r_{f,m}^2 = k^{3/2} r_f{}^2, \quad (3.12)$$

rather than $r_{f,m}^2 = k^2 r_f{}^2$, as might have been supposed at first sight. We also have

$$h_{f,m} = k^{3/2} h_f \quad (3.13)$$

and

$$v_{f,m} = k^{1/4} v_f. \quad (3.14)$$

We can examine this question from another viewpoint. Let the model test have the velocity $v_{f,m} = v_f$. In order to do so, we are obliged to change the time scale. From

$$1 = \frac{v_f}{v_{f,m}} = \left(\frac{(h_0)}{h_{0,m}}\right)^{1/4}\left(\frac{(t_{f,m})}{t_f}\right)^{1/2}, \quad (3.15)$$

it follows then that,

$$t_{f,m} = k^{3/2} t_f. \quad (3.16)$$

Under this condition,

$$r_{f,m}^2 = k^3 r_f{}^2 \quad (3.17)$$

and

$$h_{f,m} = h_f. \quad (3.18)$$

This means that a suitable change of time scale can lead to the same spill velocity and height at a much reduced area of spread.

It now becomes convenient to re-examine van Ulden's

approach [8]. His analysis is based on two fundamental assumptions, i.e.,

$$v_f = c\sqrt{gh_f} \tag{3.19}$$

and

$$h_f r_f^2 = \text{constant} = U, \tag{3.20}$$

where c is a constant and $U = h_0 r_0^2$. Substituting (3.20) into (3.19) and then integrating (3.19), we obtain

$$r_f^2 - r_0^2 = 2c\sqrt{\frac{gU}{\pi}}\, t_f$$

$$= 2c\sqrt{gh_0}.r_0 t_f. \tag{3.21}$$

Provided $c > 1$, then as discussed previously, a bore could occur and (3.20) would fail; thus c can hardly exceed unity. However, we shall see that the slope $2\sqrt{gh_0}.r_0$ is less than what experiments show. We will discuss this in detail in the next section.

Comparing (3.9, *b–c*) and (3.20), (3.21) gives special forms of function f_2 and f_3, thus

$$f_2 = c\frac{r_0}{h_0} \quad \text{and} \quad f_3 = 2c\frac{r_0}{h_0}. \tag{3.22}$$

This shows that van Ulden's formulas adopt very simple representations of wave front functions.

4 Some Comparison With Preliminary Experimental Results and Suggestions

Recently some model tests have been carried out, see reference [9], to study the effect of an unbunded spill from a tank. Even though they are of a preliminary nature they already provide helpful information.

The arrangement of the testing apparatus is as follows. A sheet of Tufnel was supported horizontally on a set of identical spacers in a catchment tray. The cylinders, containing water, of different diameters and heights were rapidly lifted vertically using stainless steel cord; sometimes a guide ring was used to ensure that the axis of a cylinder remained perpendicular to the sheet following lift-off. A counter-timer and a high-speed camera were used to monitor the process. Pairs of contact points projecting from the Tufnel sheet and set at pre-selected radial distances from the axis cylinder, provided the necessary signals for the counter-timer to record appropriate time intervals, which then allowed the roll wave front velocity to be calculated. Also a Hyspeed camera was used to take 16 mm film of the slumping liquid.

Some of the experimental results are shown in Figs. 5 and 6. The conclusions drawn from the tests are:

1. The experiments confirm that the relationships between the increase in slumped zone area and time and between the roll wave front velocity and the inverse of the zone radius are linear.
2. The choice of $c = 1$ in (3.21) would appear to be incorrect. The average value of c, using all the values obtained in tests with different diameters and heights is 1.72 with a standard deviation of 0.51. More accurately, the slope is dimension dependent, as Fig. 5 shows.
3. The linear relationship between the increase in slumped zone area and time and between the roll wave front velocity and the inverse of zone radius were reached only at a late stage or at a relatively remote wave front. This is shown clearly in Fig. 6. It seems that the linear regime begins at around 0.20 s for the case concerned; before that time the graph is curved—which obviously characterizes a transition phase.
4. The high speed photographs indicate that the roll wave is relatively smooth. The mass of liquid appears to be distributed as one cylinder of the same diameter as the storage cylinder and another of the diameter of the slumped liquid zone, see Fig. 7.

Thus far it can be seen that the main features arrived at by asymptotic analysis have also been observed in experiments. The tests confirm that all the linear relationships, which are of interest and significance for industrial practice, are truly late stage behavior and this therefore validates the intermediate asymptotic analysis. However, van Ulden's analysis represents a very special situation. That $c \neq 1$ is borne out by the measured values and that $c > 1$ leads to bores; which violates van Ulden's assumptions. Thus, general formulas (3.9) can provide more accurate predictions of slumped zone area and wavefront velocity, once the undetermined parameters f_1, f_2, and f_3 are found. To do this, well-designed model tests, in accordance with the discussion in our subsection on modeling, are mostly recommended. For a fixed value of h_0/r_0, the slopes of the above linear relations could be obtained from these tests and then used in a full scale test.

The computational results of asymptotic analysis illustrate hydraulic jumps, Fig. 2(*c–d*), which can occur in the case of flow of high velocity but low height. Perhaps the situation can also arise for pressurized containers and the like. If so, the bores may induce additional damage to the environment.

Furthermore, there is a transition phase, as shown in Fig. 6, between the initial condition and the asymptotic régime. It is possible to study the régime by solving the system of equation (2.1) and (2.2) with the initial condition (2.3) numerically, but from a practical view, model tests are more to be recommended.

A reasonable theoretical basis has developed in this paper for the study of spill prevention and control. However, it is a simple model and practical circumstances are much more complicated. Nevertheless, the present approach could benefit basic understanding of this complex slumping circumstance.

References

1 U.S. Environmental Protection Agency, "Oil Pollution, Non-Transportation Related On Shore and Off Shore Facilities," Federal Register 38, No. 237, Dec. 1973.

2 Health and Safety Executive, "Canvey: An Investigation of Potential Hazards from Operations in the Canvey Island/Thurrock Area," HMSO, 1978, Engineering Library DEE 62.

3 Cremer and Warner, "An Analysis of the Canvey Report," Oyez Intelligence Reports, 1980.

4 Slater, D. H., "Siting of Hazardous Plant," *Health and Safety at Work*, Jan. 1979.

5 Kinkead, A. N., "Effect of an Unbunded Spill of Hydrocarbon from a Refinery at Canvey Island."

6 Whitham, G. B., *Linear and Non-Linear Waves*, A Wiley Interscience Publication, New York, 1974.

7 Lighthill, M. J., *Waves in Fluids*, Cambridge University Press, Cambridge, 1978.

8 van Ulden, A. P., *On the Spreading of a Heavy Gas Released Near the Ground*, Elsevier, 1974, Loss Prevention Symposium, The Netherlands.

9 Low, R. G. M., "The Effect of an Unbunded Spill from a Tank," Project Report, Cambridge University, Engineering Department, Apr. 1981.

O. K. Kwon
Senior Project Engineer,
Allison Gas Turbine Operations,
General Motors Corporation,
Indianapolis, Ind.
Assoc. Mem. ASME

R. H. Pletcher
Professor.
Mem. ASME

J. P. Lewis
Research Assistant.

Department of Mechanical Engineering,
Iowa State University,
Ames, Iowa

Prediction of Sudden Expansion Flows Using the Boundary-Layer Equations

A finite-difference calculation method based on the boundary-layer equations is described for the prediction of laminar, developed channel flow undergoing a symmetric sudden expansion. The scheme requires only a fraction of the computational effort required for the numerical solution of the full Navier-Stokes equations that are usually employed for this flow. Predictions of the method compare very favorably with experimental data and solutions of the full Navier-Stokes equations.

Introduction

Flow separation and reattachment are important considerations in the design of engineering equipment. For subsonic flows, separation usually occurs either when the flow is subjected to a strong adverse pressure gradient on a smooth solid surface or when abrupt geometric changes occur in the solid surface, such as, for example, a forward or rearward facing step. It is of considerable interest to identify accurate prediction procedures for these flows, since separation and reattachment generally have a significant effect on performance.

This paper describes an economical prediction procedure for developed incompressible flow through a channel containing an abrupt symmetric expansion in flow cross-sectional area. The flow geometry is illustrated in Fig. 1. Such flows occur frequently in heat exchangers and other devices of practical importance. The computational concept is illustrated in the present paper for two-dimensional laminar sudden expansion flows. The approach is believed to be applicable as well to expansion flows in axisymmetric passages. An extension to fully-developed turbulent flow appears feasible, but the accuracy of such a calculation is likely to be very much dependent upon the choice of turbulence model.

An experimental and numerical study of a two-dimensional laminar symmetric expansion flow has been reported by Durst et al. [1]. Numerical predictions based on the full Navier-Stokes equations have also been reported by Hung [2], Morihara [3], and Agarwal [4]. The use of the Navier-Stokes equations apparently has been considered necessary in order to obtain accurate predictions because of the presence of flow recirculation. However, several investigators [5–10] recently have applied a simpler analysis, based on a form of the boundary-layer equations, to internal flows with separated regions. These analyses were successful for the regions where the streamwise length scale was the order of the Reynolds number, but difficulties, including singular behavior, were observed where the streamwise length scale was of order one, such as very near the step.

In the present paper a "once-through" calculation procedure based on the boundary layer equations is described for laminar developed flows undergoing a sudden expansion. The scheme appears to be free of the numerical difficulties associated with earlier methods based on these equations. The favorable numerical characteristics of the method are thought to be a result of solving the governing equations in a coupled manner and making use of the FLARE approximation [11] in regions of reversed flow. The computation time required for the scheme is at least an order of magnitude less than for the numerical solution of the Navier-Stokes equations. Details of the method are given and predictions are compared with experimental data and numerical solutions of the full Navier-Stokes equations.

Analysis

Governing Equations. The prediction scheme utilizes the two-dimensional boundary-layer equations. In addition, the streamwise convective derivative is assumed to be negligibly small in regions of reversed flow [11]. For an incompressible,

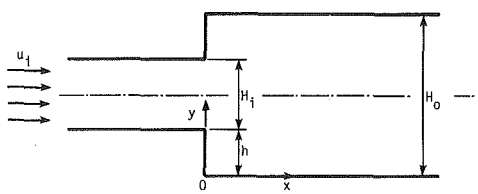

Fig. 1 Sudden expansion geometry

Contributed by the Fluids Engineering Division for publication in the JOURNAL OF FLUIDS ENGINEERING. Manuscript received by the Fluids Engineering Division, September 14, 1982.

steady, laminar flow, the equations are written in the Cartesian coordinate system as

Continuity Equation.

$$\frac{\partial u}{\partial x} + \frac{\partial v}{\partial y} = 0 \tag{1}$$

Momentum Equation.

$$Cu\frac{\partial u}{\partial x} + v\frac{\partial u}{\partial y} = -\frac{1}{\rho}\frac{dp}{dx} + \nu\frac{\partial^2 u}{\partial y^2} \tag{2}$$

where $C=1$ when $u>0$ and $C=0$ when $u\leq 0$. This treatment of the convective streamwise derivative has become known as the FLARE approximation and was introduced in [11].

Numerous numerical formulations of the boundary layer equations have been evaluated during the course of the present study in an attempt to obtain a stable and accurate solution scheme when recirculation was present. The numerical solutions of most of these gave rise to instabilities or unacceptable oscillations in the wall shear stress when large regions of recirculation were present. As the study progressed, it appeared crucial to solve the continuity and momentum equations simultaneously in a coupled manner to avoid the unacceptable behavior. To date, two satisfactory and efficient ways of accomplishing this have been identified. The first of these solves the finite-difference form of equations (1) and (2) in a coupled manner treating the pressure gradient as an unknown. This will be referred to as the u-v coupling procedure. The second scheme employs the stream function to satisfy the continuity equation. This latter formulation has proven to be more convenient when solving external flows by an inverse procedure because of the ease with which the displacement thickness, used as a boundary condition, can be introduced [12]. Because of this additional generality, the second scheme, referred to as the u-ψ coupling procedure, has been the preferred scheme in this study and will be described in detail. It should be noted, however, that both the u-v and u-ψ schemes will work equally well for the flows considered in the present paper.

The u-ψ scheme utilizes the stream function, defined as

$$u = \frac{\partial \psi}{\partial y} \tag{3}$$

$$v = -\frac{\partial \psi}{\partial x} \tag{4}$$

The continuity equation is satisfied by ψ, and equation (4) can be introduced into the momentum equation to eliminate v:

$$Cu\frac{\partial u}{\partial x} - \frac{\partial \psi}{\partial x}\frac{\partial u}{\partial y} = -\frac{1}{\rho}\frac{dp}{dx} + \nu\frac{\partial^2 u}{\partial y^2} \tag{5}$$

The system of equations to be solved numerically is composed of equations (3) and (5).

For a symmetric channel flow, the boundary layer equations are subjected to the following boundary conditions. Along the solid wall, including the face of the step, no slip boundary conditions are specified, i.e.,

$$u = v = \psi = 0 \tag{6}$$

and along the channel centerline, a symmetry condition for u is specified, i.e.,

$$\text{at } y = \frac{H}{2}, \quad \frac{\partial u}{\partial y} = 0 \tag{7}$$

In addition, the overall mass flow conservation requirement must be met, i.e.,

$$\dot{m} = \int_A \rho u dA = \text{constant} \tag{8}$$

throughout the channel.

For incompressible flow, equation (8) can be expressed in terms of the stream function as

$$\psi\left(x, \frac{H}{2}\right) = \frac{\psi_T}{2} \tag{9}$$

where

$$\psi_T \doteq \int_0^H u dy$$

The boundary conditions given by equations (6) and (7) are sufficient to permit the solution of the boundary-layer

Nomenclature

A = channel cross-sectional area
C = constant
c_f = skin-friction coefficient ($=2\tau_w/(\rho u_{i,\text{AVG}}^2)$)
H = channel height
h = step height
L_{REF} = reference length
l_e = distance from the step to the eye of the reversed flow vortex
l_R = reattachment length
M = nondimensional diffusion coefficient, ν/ν_r
$\dot{m}$ = mass flow rate
p = pressure
Re_{H_i} = Reynolds number based on the channel inlet height ($=u_{i,\text{AVG}}H_i/\nu$)
Re_h = Reynolds number based on the step height ($=u_{i,\text{AVG}}h/\nu$)
u = x component of velocity
U = nondimensional x component of velocity ($=u/u_r$)
δ_U = $U^{i+1} - \tilde{U}^{i+1}$
u_r = reference velocity
v = y component of velocity
V = nondimensional y component of velocity ($=v/u_r$)
x = coordinate along the surface measured from the step
X = nondimensional x coordinate ($=u_r x/\nu_r$)
ΔX_+ = $X^{i+1} - X^i$
y = coordinate normal to the surface
Y = nondimensional y coordinate ($=u_r y/\nu_r$)
ΔY_+ = $Y_{j+1} - Y_j$
ΔY_- = $Y_j - Y_{j-1}$
τ_w = wall shear stress
μ = viscosity
ν = kinematic viscosity
ρ = density
χ = nondimensional pressure gradient $\left(=-\frac{\mu}{\rho_r^2 u_r^3}\frac{dp}{dx}\right)$
Ψ = nondimensional stream function ($=\rho\psi/\mu$)
δ_Ψ = $\Psi^{i+1} - \tilde{\Psi}^{i+1}$
ψ = stream function defined by equations (3) and (4)
ψ_T = total flow rate per unit depth in a channel

Superscripts

i = mesh index corresponding to X
$\tilde{\ }$ = previous iteration level

Subscripts

AVG = averaged condition
CL = centerline
i = upstream of the sudden expansion
j = mesh index corresponding to Y
max = maximum condition
min = minimum condition
NJ = outer edge of the computational domain
0 = downstream of the sudden expansion
r = denotes reference value

equations if the pressure gradient is specified. The additional overall mass flow constraint given by equation (8) permits the pressure gradient to be determined as part of the solution. A distribution of u at a starting value of x must also be provided. The computation proceeds from the initial profile and continues downstream beyond the reattachment point. Only one streamwise pass is required.

Method of Solution. In terms of the nondimensional variables defined in the Nomenclature, the finite-difference representations of equations (3) and (5) are written for a variable y-grid as

$$\frac{U_j^{i+1} + U_{j-1}^{i+1}}{2} = \frac{\Psi_j^{i+1} - \Psi_{j-1}^{i+1}}{\Delta Y_-} \tag{10}$$

$$CU_j^{i+1}\frac{(U_j^{i+1} - U_j^i)}{\Delta X_+} - \frac{(\Psi_j^{i+1} - \Psi_j^i)}{\Delta X_+}\frac{(U_{j+1}^{i+1} - U_{j-1}^{i+1})}{(\Delta Y_+ + \Delta Y_-)} = \chi + \frac{2}{(\Delta Y_+ + \Delta Y_-)}\left[M_{j+1/2}^i\left(\frac{U_{j+1}^{i+1} - U_j^{i+1}}{\Delta Y_+}\right) - M_{j-1/2}^i\left(\frac{U_j^{i+1} - U_{j-1}^{i+1}}{\Delta Y_-}\right)\right] \tag{11}$$

The solution is to be advanced from the i to the $i+1$ level. The pressure gradient at the $i+1$ station, χ, is treated as an unknown in equation (11). The nondimensional diffusion coefficients specified for $j+1/2$ and $j-1/2$ are evaluated as arithmetic averages of these quantities at neighboring integer grid points:

$$M_{j+1/2}^i = \frac{M_{j+1}^i + M_j^i}{2}$$

$$M_{j-1/2}^i = \frac{M_j^i + M_{j-1}^i}{2}$$

For the particular constant property laminar results to be presented in this paper, M was constant throughout the flow.

The momentum equation is algebraically nonlinear in the unknowns (U_j^{i+1} and Ψ_j^{i+1}) in the form given by equation (11). A linear representation is obtained through the iterative application of Newton linearization. In this linearization procedure, the dependent variables on the left-hand side of equation (11) are first represented by

$$U_j^{i+1} = \tilde{U}_j^{i+1} + \delta_U$$

and

$$\Psi_j^{i+1} = \tilde{\Psi}_j^{i+1} + \delta_\Psi$$

where

$$\delta_U = U_j^{i+1} - \tilde{U}_j^{i+1} \text{ and } \delta_\Psi = \Psi_j^{i+1} - \tilde{\Psi}_j^{i+1}$$

In the above, $\tilde{U}_j^{i+1}$ and $\tilde{\Psi}_j^{i+1}$ represent values from a previous iteration. Terms representing products of δ's are dropped from the equations. To start the iterative procedure, $\tilde{U}_j^{i+1}$ and $\tilde{\Psi}_j^{i+1}$ are assigned values from the i level. Typically, only 2 or 3 iterations were required.

The system of algebraic equations for the unknowns can be written in the form

$$\begin{bmatrix} B_j & 0 \\ b_j & 1 \end{bmatrix}\begin{Bmatrix} U_{j-1}^{i+1} \\ \Psi_{j-1}^{i+1} \end{Bmatrix} + \begin{bmatrix} D_j & E_j \\ d_j & -1 \end{bmatrix}\begin{Bmatrix} U_j^{i+1} \\ \Psi_j^{i+1} \end{Bmatrix} + \begin{bmatrix} A_j & 0 \\ 0 & 0 \end{bmatrix}\begin{Bmatrix} U_{j+1}^{i+1} \\ \Psi_{j+1}^{i+1} \end{Bmatrix} = \begin{Bmatrix} H_j\chi + C_j \\ 0 \end{Bmatrix} \tag{12}$$

The coefficients A_j, B_j, C_j, D_j, E_j, H_j, b_j, and d_j are defined in the Appendix.

Because of the appearance of the unknown χ in the position usually reserved for the vector of "knowns," equation (12) cannot be solved as written by standard procedures for a 2 × 2 block tridiagonal system. However, the main steps in a 2 × 2 block tridiagonal solution procedure can be followed if χ is evaluated from information contained in the boundary conditions prior to the back substiution step. Further details on the solution procedure are given in the Appendix. The method used for solving the algebraic equations in the present work shares some points in common with the inverse boundary layer procedures of Cebeci [13] and Carter [14].

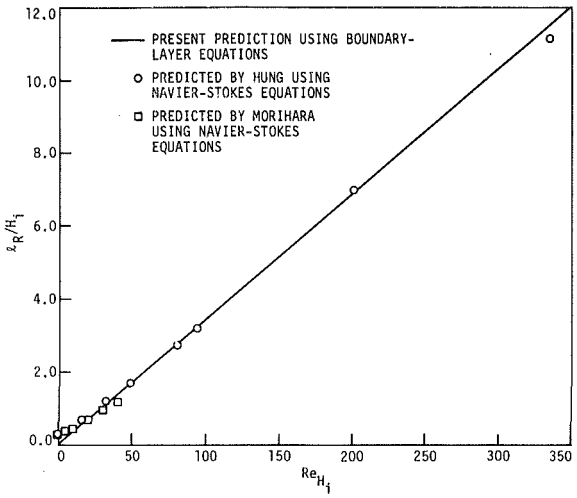

Fig. 2 Prediction of the reattachment length for laminar flow in channel with a symmetric sudden expansion, $h/H_i = 0.5$

Results

Most calculations were started upstream of the step. For fully developed flows undergoing a sudden expansion, the profiles are independent of streamwise position upstream of the step, and calculations for some of these flows were started with initial profiles at the step. The discontinuity in geometry at the step caused no numerical difficulties and required no special treatment in the analysis. Typical grid sizes used in the separate flow region were $\Delta x/h = 0.0625$ and $\Delta y/h = 0.025$ except as noted below in the grid refinement studies. In general, each calculation requires 3-5 seconds of CPU time on the NAS AS/6 computer.

Predictions have been obtained over a range of Reynolds numbers (based on channel inlet height) from 1 to 320 for two-dimensional, incompressible, fully-developed laminar flow undergoing a sudden 2:1 expansion.

The predicted reattachment lengths are plotted in Fig. 2 and are compared with the Navier-Stokes predictions of Hung [2] and Morihara [3]. The predictions are all in good agreement except for very low Reynolds numbers (below $Re_{H_i} = 20$). It is noted that Morihara's prediction lies below that of Hung, and the difference between the two predictions increases as Reynolds number increases. The reason for the difference is not clear. However, recent calculations by Kumar and Yajnik [5] using a form of the boundary-layer equations and Agarwal [4] using the Navier-Stokes equations for the same flow at $Re_{H_i} = 93.2$ provided good agreement with the predictions of Hung [2]. Agarwal solved the Navier-Stokes equations for

Table 1 Comparison of the present prediction with other predictions for laminar flow undergoing a 2:1 symmetric expansion in a two-dimensional channel.

Investigator	Equations solved	Predictions $l_R/(h\mathrm{Re}_h)$	Predictions $l_e/(h\mathrm{Re}_h)$	Predictions $\Psi_{\min}/\Psi_T$	Reynolds number $\mathrm{Re}_h = \frac{u_{i,\mathrm{AVG}}h}{\nu}$
Present calculations	Boundary-layer equations	0.138	0.026	−0.025	50.0
Hung	Navier-Stokes equations	0.132	0.032	−0.0215	46.6
Agarwal	Navier-Stokes equations	0.136	0.032	−0.0222	46.6
Kumar and Yajnik	Boundary-layer equations (integral method)	0.128	0.028	−0.0225	46.6

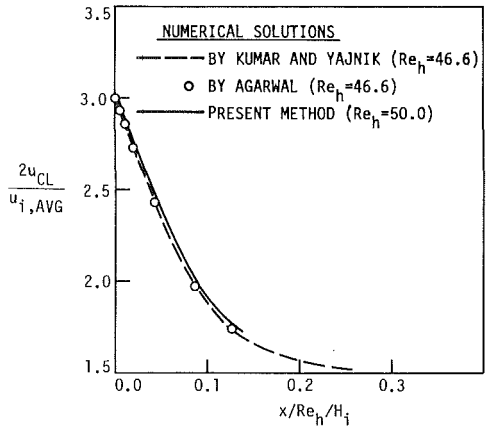

Fig. 3 Centerline velocity distribution for laminar flow in a channel with a symmetric sudden expansion, $h/H_i = 0.5$

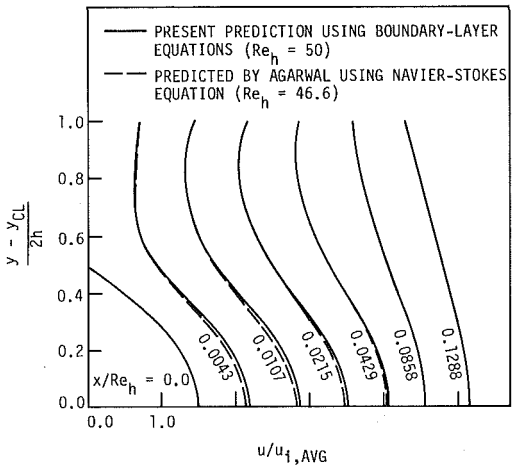

Fig. 4 Velocity profiles for laminar flow in a channel with a symmetric sudden expansion, $h/H_i = 0.5$

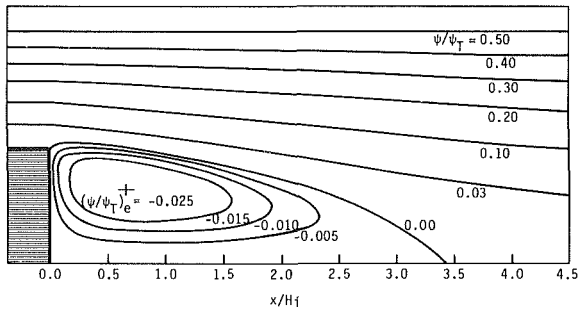

Fig. 5 Streamline contours for laminar flow in a channel with a symmetric sudden expansion, $\mathrm{Re}_h = 50$, $h/H_i = 0.5$

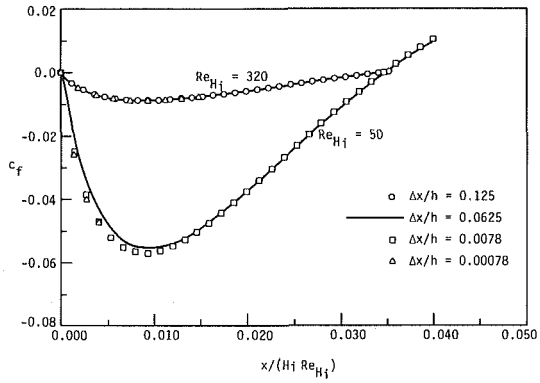

Fig. 6 Skin-friction coefficient for laminar flow in a channel with a symmetric sudden expansion, $h/H_i = 0.5$

stream function and vorticity with a third-order accurate scheme.

More recently, Madavan [15] also provided the same flow using the partially parabolized Navier-Stokes equations, resulting in good agreement with these results as well as with the present solution. The present prediction at $\mathrm{Re}_h = 50$ ($\mathrm{Re}_{H_i} = 100$) is compared in detail with the results obtained by other investigators in Table 1. All the solutions are found to be in good agreement for the normalized reattachment length. More variation was observed in the predicted normalized distance between the step and the eye of the vortex and the value of stream function at the eye of the vortex.

The centerline velocity distribution obtained by the present boundary-layer solution is compared with the predictions by Kumar and Yajnik [5], and Agarwal [4] in Fig. 3. Although the present predictions lie slightly above the latter, overall agreement is good. Velocity profiles obtained from the boundary-layer solutions also provide good agreement with those obtained from the Navier-Stokes solutions as shown in Fig. 4.

A typical streamline pattern, predicted using the boundary-layer equations, is shown in Fig. 5. Qualitatively, the pattern appears quite reasonable. However, the dividing streamline predicted by the boundary-layer equations does not appear to depart tangentially from the step as it does for solutions to the Navier-Stokes equations.

The 2:1 expansion case was also predicted by the u-v coupling procedure for Reynolds numbers (Re_{H_i}) of 50 and 320. The results were identical to those obtained by the u-ψ procedure to 3 significant figures. Grid refinement studies were also made for both methods at Reynolds numbers (Re_{H_i}) of 50 and 320. Reducing the Δy mesh by a factor of two

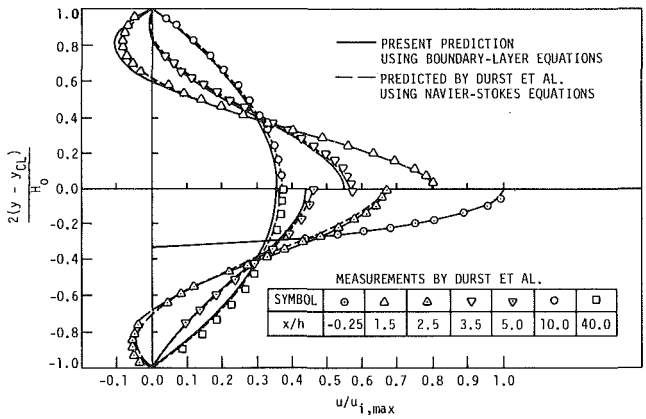

Fig. 7 Velocity profiles for laminar flow in a channel with a symmetric sudden expansion, $hu_{i,\max}/\nu = 56$, $h/H_i = 1.0$

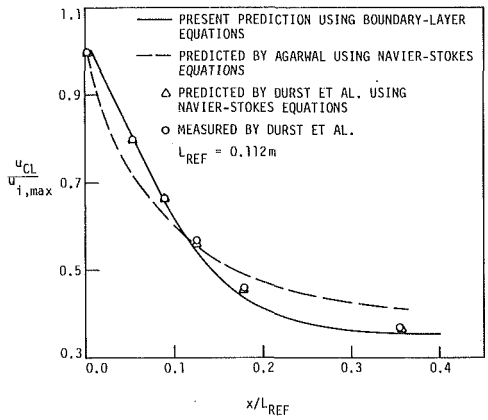

Fig. 8 Centerline velocity distribution for a laminar flow in a channel with a symmetric sudden expansion, $hu_{i,\max}/\nu = 56$, $h/H_i = 1.0$

caused no plottable change in the results. For $\mathrm{Re}_{H_i} = 50$, calculations were made for streamwise step sizes of $\Delta x/h = 0.0625$, 0.0078, and 0.00078, which provided reductions in step sizes by factors of 8 and 80. The resulting distributions in skin-friction coefficient are shown in Fig. 6. The trend indicates convergence. No tendency for the solution to be unstable near the step was detected. For $\mathrm{Re}_{H_i} = 320$, calculations were made for streamwise step sizes of $\Delta x/h = 0.125$, 0.0625, and 0.00078, representing reductions by factors of 2 and 160. These results are also shown in Fig. 6. Even less change was noted with grid refinement for the $\mathrm{Re}_{H_i} = 320$ case. The maximum predicted reversed flow velocity was 8 percent of the centerline velocity for the 2:1 expansion cases.

Comparisons were also made with the laser anemometer measurements of Durst et al. [1]. The Reynolds number based on the step height and the maximum inlet velocity for this case was 56, and the channel expansion ratio, 3:1. The velocity profile at $x/h = -0.25$ was in the nearly developed state. Far downstream from the step ($x/h = 40$), the flow was fully developed. Calculations by the present method were started at $x/h = -0.25$ using both a fully developed profile and a match to the experimental measurements. The results for both starting conditions were identical to plotting accuracy. The predicted mean velocity profiles and centerline velocity distribution are in good agreement with the measurements and with the solutions to the Navier-Stokes equations also reported by Durst et al. [1] (see Figs. 7 and 8). Agarwal [4] also predicted this flow using a fully developed inlet velocity profile, rather than the measured profile, as a boundary condition in the predictions. Surprisingly, Agarwal's predicted centerline velocity distribution and the reattachment length were found to be very different from the measurements. The centerline velocity distributions are compared in Fig. 8. The reason for the poor predictions by Agarwal [4] is not clear. The maximum predicted reversed flow velocity was 14 percent of the centerline velocity for the 3:1 expansion case.

Conclusions

The FLARE-modified boundary-layer equations were found to be a reasonably good approximate mathematical model for symmetric channel expansion flows with developed inlet velocity profiles for Reynolds numbers based on channel inlet height and inlet mean velocity greater than 20. The predicted reattachment length for such flows was found to vary nearly linearly with the Reynolds number as observed in solutions to the full Navier-Stokes equations. Most flow details predicted by the present boundary-layer method are in excellent agreement with Navier-Stokes predictions and experimental data. A minor exception is the dividing streamline near the step, which does not depart tangentially from the step as it does for solutions to the Navier-Stokes equations.

In the present study it was found necessary to solve the boundary-layer momentum and continuity equations simultaneously in a coupled manner when large regions of reversed flow were present. Two formulations, one using u-v variables and the other using u-ψ variables, were found to work successfully . The solutions appeared convergent under grid refinement in that changes in the solution were observed to become smaller with each successive refinement. No evidence of singular behavior was observed near the step.

Most previous calculations of sudden expansion flows have employed the full Navier-Stokes equations. The fact that the present boundary-layer solution procedure provides a very good approximate solution for symmetric sudden expansion flows with fully developed inlet velocity profiles should be of practical interest since the present method requires only a small fraction of the computer time required for solutions to the full Navier-Stokes equations. However, for internal flows in which an inviscid core can be identified (i.e., not fully developed) the results in [12] indicate that the analysis should provide for interaction between the boundary layer and the inviscid flow so that elliptic flow effects can be properly modeled.

Acknowledgment

This work was supported by the Engineering Research Institute, Iowa State University, through funds provided by the National Science Foundation under grants ENG-7812901 and MEA-8211713. Partial support from the National Aeronautics and Space Administration under Grant NGT-016-002-801 is also gratefully acknowledged.

References

1 Durst, F., Melling, A., and Whitelaw, J. H., "Low Reynolds Number Flow over a Plane Symmetric Sudden Expansion," *J. Fluid Mechanics*, Vol. 64, 1974, pp. 111-128.

2 Hung, T.-K., "Laminar Flow in Conduit Expansions," Ph.D. dissertation, University of Iowa, Iowa City, 1966.

3 Morihara, H., "Numerical Integration of the Navier-Stokes Equations," Ph.D. dissertation, State University of New York at Buffalo, 1972.

4 Agarwal, R. K., "A Third-Order-Accurate Upwind Scheme for Navier-Stokes Solutions at High Reynolds Numbers," AIAA Paper No. AIAA-81-0112, 1981.

5 Kumar, A., and Yajnik, K. S., "Internal Separated Flows at Large Reynolds Numbers," *J. Fluid Mechanics*, Vol. 97, 1980, pp. 27-51.

6 Eagles, P. M., and Smith, F. T., "The Influence of Nonparallelism in

Channel Flow Stability," *J. Engineering Mathematics*, Vol. 14, No. 3, 1980, pp. 219–237.

7 Plotkin, A., "Development of Confined Laminar Wakes at Large Reynolds Numbers," *AIAA Journal*, Vol. 20, No. 2, 1982, pp. 211–217.

8 Brady, J. F., and Acrivos, A., "Closed-cavity Laminar Flows at Moderate Reynolds Numbers," *J. Fluid Mechanics*, Vol. 115, 1982, pp. 427–442.

9 Acrivos, A., and Schrader, M. L., "Steady Flow in a Sudden Expansion at High Reynolds Numbers," *Physics of Fluids*, Vol. 25, No. 6, 1982, pp. 923–930.

10 Plotkin, A., "Spectral Method Solutions for Some Laminar Channel Flows with Separation," *AIAA Journal*, Vol. 20, No. 12, 1982, pp. 1713–1719.

11 Reyhner, T. A., and Flügge-Lotz, I., "The Interaction of a Shock Wave with a Laminar Boundary Layer," *Int. J. Nonlinear Mechanics*, Vol. 3, 1968, pp. 173–199.

12 Kwon, O. K., and Pletcher, R. H., "Prediction of the Incompressible Flow Over a Rearward-Facing Step," Technical Report HTL-26, CFD-4, ISU-ERI-Ames-82019, Engineering Research Institute, Iowa State University, 1981.

13 Cebeci, T., "Separated Flows and Their Representation by Boundary-Layer Equations," Mech. Engr. Report ONR-CR-215-234-2, California State University at Long Beach, 1976.

14 Carter, J. E., "Inverse Boundary-Layer Theory and Comparison with Experiment," NASA TP 1208, 1978.

15 Madavan, N. K., "Prediction of Incompressible Laminar Separated Flows Using the Partially-Parabolized Navier-Stokes Equations," M.S. thesis, Iowa State University, Ames, 1981.

APPENDIX

The coefficients appearing in equation (12) are evaluated as:

$$A_j = -\frac{\tilde{\Psi}_j^{i+1} - \Psi_j^i}{\Delta X_+ \Delta Y_- (K+1)} - \frac{2M_{j+1/2}^i}{(\Delta Y_-)^2 K(K+1)}$$

$$B_j = \frac{\tilde{\Psi}_j^{i+1} - \Psi_j^i}{\Delta X_+ \Delta Y_- (K+1)} - \frac{2M_{j-1/2}^i}{(\Delta Y_-)^2 (K+1)}$$

$$C_j = C\frac{(\tilde{U}_j^{i+1})^2}{\Delta X_+} - \frac{\tilde{\Psi}_j^{i+1}(\tilde{U}_{j+1}^{i+1} - \tilde{U}_{j-1}^{i+1})}{\Delta X_+ \Delta Y_- (K+1)}$$

$$D_j = C\frac{2\tilde{U}_j^{i+1} - U_j^i}{\Delta X_+} + \frac{2}{(\Delta Y_-)^2 (K+1)}\left(\frac{M_{j+1/2}^i}{K} + M_{j-1/2}^i\right)$$

$$E_j = -\frac{\tilde{U}_{j+1}^{i+1} - \tilde{U}_{j-1}^{i+1}}{\Delta X_+ \Delta Y_- (K+1)}$$

$$H_j = 1$$

$$b_j = \frac{\Delta Y_-}{2}$$

$$d_j = \frac{\Delta Y_-}{2}$$

where

$$K = \frac{\Delta Y_+}{\Delta Y_-}$$

The unknowns can be computed from

$$U_j^{i+1} = A_j' U_{j+1}^{i+1} + H_j' \chi + C_j' \tag{13}$$

and

$$\Psi_j^{i+1} = B_j' U_{j+1}^{i+1} + D_j' \chi + E_j' \tag{14}$$

providing the coefficients A_j', H_j', C_j', B_j', D_j', E_j' and the quantities U_{j+1}^{i+1} and χ are known a priori. The coefficients are given by

$$A_j' = -\frac{A_j}{q_1}$$

$$B_j' = A_j' q_2$$

$$C_j' = \frac{1}{q_1}[C_j - B_j C_{j-1}' - E_j(b_j C_{j-1}' + E_{j-1}')]$$

$$D_j' = b_j H_{j-1}' + D_{j-1}' + q_2 H_j'$$

$$E_j' = b_j C_{j-1}' + E_{j-1}' + C_j' q_2$$

$$H_j' = \frac{1}{q_1}[H_j - B_j H_{j-1}' - E_j(b_j H_{j-1}' + D_{j-1}')]$$

$$q_1 = D_j + A_{j-1}'(b_j E_j + B_j) + E_j(B_{j-1}' + d_j)$$

and

$$q_2 = d_j + b_j A_{j-1}' + B_{j-1}'$$

Since the inner boundary conditions are all homogeneous, i.e., U_1^{i+1} and $\Psi_1^{i+1} = 0$, the coefficients are initialized at $j = 1$ by letting

$$A_1' = B_1' = C_1' = D_1' = E_1' = H_1' = 0$$

Therefore, the coefficients A_j', B_j', C_j', D_j', E_j', and H_j' can be computed from the wall to the outer edge of the computation domain.

It now remains to compute χ and U_{NJ}^{i+1} so that equations (13) and (14) can be used to determine the solution throughout the flow. In the above NJ represents the value of j at outer edge of the computational domain. The boundary conditions at the channel centerline, equations (7) and (9), result in the following equations for the unknown centerline velocity, U_{NJ}, and pressure gradient, χ, [12]

$$U_{NJ}^{i+1} = \frac{l_2}{l_1}\left(\frac{l_1 m_3 - l_3 m_1}{l_2 m_1 - l_1 m_2}\right) + \frac{l_3}{l_1} \tag{15}$$

$$\chi = \frac{l_1 m_3 - l_3 m_1}{l_2 m_1 - l_1 m_2} \tag{16}$$

where

$$l_1 = 1 - A_{NJ-1}'(c_1 - c_2 A_{NJ-2}')$$

$$l_2 = (c_1 - c_2 A_{NJ-2}')H_{NJ-1}' - c_2 H_{NJ-2}'$$

$$l_3 = (c_1 - c_2 A_{NJ-2}')C_{NJ-1}' - c_2 C_{NJ-2}'$$

$$m_1 = 1 + \frac{2}{\Delta Y_-} B_{NJ-1}' + A_{NJ-1}'$$

$$m_2 = -\left(H_{NJ-1}' + \frac{2}{\Delta Y_-} D_{NJ-1}'\right)$$

$$m_3 = \frac{\Psi_T}{\Delta Y_-} - \frac{2}{\Delta Y_-} E_{NJ-1}' - C_{NJ-1}'$$

$$c_1 = \frac{4}{4-K}$$

$$c_2 = \frac{K}{4-K}$$

and

$$K = \frac{Y_{NJ} - Y_{NJ-1}}{Y_{NJ-1} - Y_{NJ-2}}$$

With the centerline velocity and pressure gradient obtained from equations (15) and (16), the back substitution process is initiated to solve for all the U's and Ψ's across the computational domain, from the centerline ($j = NJ$) down to the wall ($J = 1$), by using equations (13) and (14).

Since the present solution method is iterative at each streamwise station, the solutions obtained from equations

(13) and (14) must be compared with those obtained at the previous iteration. The iterative process at each streamwise location is continued until the maximum change in U's and Ψ's between two successive iterations, i.e.,

$$\text{Max. of } (|\delta_U|, |\delta_\Psi|)$$

is less than or equal to a convergence criterion that was set equal to 1.0×10^{-4} for the present calculations. The iterative calculation is initiated using the solutions obtained at the previous streamwise station as the initial assumed values for $\tilde{U}_j^{i+1}$ and $\tilde{\Psi}_j^{i+1}$ for the present station. Only two or three iterations are typically required at each streamwise station.

Forces Caused by the Radial Out-Flow Between Parallel Disks

C. E. Wark
Graduate Assistant.

J. F. Foss
Professor.

Department of Mechanical Engineering,
Michigan State University,
East Lansing, MI 48824

An experimental program, to determine the magnitude of the force on the impact disk for the radial out-flow between parallel disks, has been carried out for moderate Reynolds numbers. The present results are compared with a previously published, ad hoc, analytical formulation whose coefficients were established for low Reynolds numbers. Acceptable agreement exists for the low Reynolds number range of the present study; progressively significant disagreement is observed as the Reynolds number is increased. The present force data, when combined with previous observations and interpreted via appropriate theoretical considerations, reveal a complex blending of flow phenomena for the Reynolds number, diameter ratio, and plate separation values of the present study.

1 Introduction

The radial outflow, between stationary and parallel plates, serves as the pristine flow state for several technologically important flow fields. For example, radial diffusers, an air bearing, a nozzle-flapper valve or a VTOL aircraft in close proximity to the ground are representatives of the motivation problems that would stimulate an investigation of the subject flow. The specific features of the geometry and the pertinent Reynolds number value for a given investigation follow from the motivating application.

The radial outflow of air between the parallel plates will cause either an attracting or a repelling force to exist between the plates. For a given Reynolds number (V_1D_1/ν), repelling forces exist for small and large values of the distance between the plates whereas an attracting force results for intermediate values of this separation distance.[1]

The motivation for the present investigation was the development of a lifting device. Air, from a pressurized plenum ($\lesssim 100$ N/m^2), and with a maximum flow rate of nominally 1.1×10^{-3} m^3/s, was to be used to support a weight. Jet nozzle diameters of: $6.35 \leq D_1 \leq 12.7$ mm were used and the resulting Reynolds numbers: $10^3 < V_1D_1/\nu \leq 7 \times 10^3$ were substantially larger than those which were utilized in previous experimental and/or analytical studies [1, 2, 4].

It is the purpose of this study to clarify the physical mechanisms which are responsible for these flow phenomena and to provide quantitative results for the above noted geometric configurations and flow conditions. The experimental data, which are presented in this communication, therefore extend the data base which exists for the radial outflow geometry. Theoretical considerations are used to interpret the trends exhibited by the experimental results. These considerations are presented to aid in the interpolation and extrapolation of the observations and to clarify the important features of any analytical model that would be proposed to represent this flow field.

The principal results of the present study are the (appropriately nondimensionalized) measured forces which are expressed as functions of the independent variable: h^* ($=h/D_1$), and the relevant parameters; Re and D_2/D_1. A secondary body of results is provided by the (nondimensional) plenum pressures that are required to achieve a given Reynolds number for a given h^* and D_2/D_1 condition. Note that the $(p-q)$ relationship is the information which would be required by a flow-system designer.

The extant literature on this general subject is used, in the next section, to set the context for the present study. Specific comparisons with previous data and analytical formulations are provided in the results section. The Discussion of Results section also contains numerous observations regarding the distinctive fluid dynamic phenomena that occur in this flow problem. These phenomena are inferred from the trends of the force and pressure data and from the relevant theoretical and numerical results from the prior studies.

2 Problem Statement and Background Information

The existence of an attracting force between the plates is sometimes made rational by appeal to inviscid flow considerations; it is instructive that this explanation is incorrect for a source flow that *enters the gap region with momentum that is directed toward the lower plate.*

Figure 1(*c*) has been prepared to emphasize this point; the dashed surface represents a source plate that may be added or removed from the thin wall tube that delivers the source flow. In the absence of the source plate, the flow is characterized as shown with the consequent ambient pressure condition along the free streamline and the positive pressures along the impact surface. The jet flow continually "thins" as it progresses to larger radii. If the fluid were inviscid, then the addition of the source plate would have no influence on the flow pattern. In contrast, a viscous fluid will result in the entrainment of ambient fluid between the source plate and the separating streamline which, for appropriate geometric and Reynolds

[1] Note, the symbol list in the present paper is taken, where possible, from the paper by Hayashi et al. [1]. The present symbols are defined in the nomenclature list.

Contributed by the Fluids Engineering Division for publication in the JOURNAL OF FLUIDS ENGINEERING. Manuscript received by the Fluids Engineering Division, May 9, 1983.

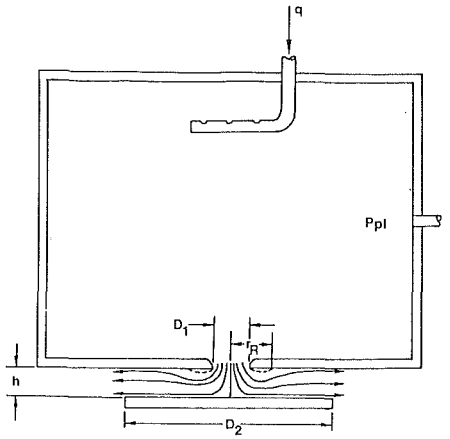

Fig. 1(*a*) Schematic of lifting device

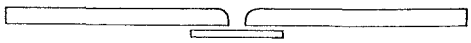

Fig. 1(*b*) Scale dwg of source and impact plate for D_2/D_1 = 5.33 and h^* = 0.25

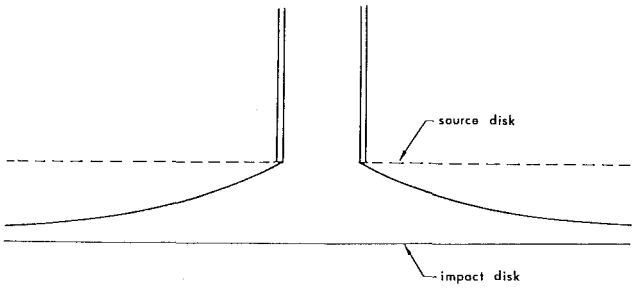

Fig. 1(*c*) Inviscid flow characterization

Fig. 1 The subject flow field

number conditions, will lead to reattachment of the separating streamline. Hence, the presence or absence of reattachment will exert a pronounced effect on the qualitative aspect of the flow field and it is reasonable to expect that the parameters which influence the reattachment location will be important for the description of the nondimensional force (F^*).

Separation at the salient edge between the source flow nozzle or conduit and the gap region is expected for all but relatively small Reynolds numbers. The analytical results of Raal [2] provide a quantitative expression of this for low Reynolds number values:

$$\mathrm{Re}]_s = 480h^* \text{(from Raal [2])} \qquad (1)$$

where $\mathrm{Re}]_s$ is the minimum Reynolds number for separation at the juncture of the source plate and the approach tube.

The qualitative feature, that the reattachment radius is increased as the Reynolds number is increased, is supported by analytical and experimental observations; see, e.g., Raal, Hayashi et al. and Moller [3]. For sufficiently large Reynolds number and D_2/D_1 values, the reattachment length approaches a constant value for a given h. For example,[2]

$$\frac{r_R}{D_1} = 2 \text{ for } \mathrm{Re} \gtrsim 1.2 \times 10^5 \text{ at } h^* = 0.25 \qquad (2)$$

The interplay between h^*, Re, and D_2/D_1 can be quite dramatic if an increase in the Re value leads to a nonreattachment condition; namely, a sudden change in the force from attracting to repelling is observed: Hyashi et al [1].

An important factor, in the specification of the geometry, is whether or not both disks have the same diameter. The diameter of the source disk, for the present study, was constant (D = 254 mm) in contrast with the more standard condition wherein the source and impact disks have the same diameter.

The importance of the reattachment condition suggests that three subcategories of performance be identified: (i) $D_2/D_1 \rightarrow 1$ and/or $h^* \rightarrow \infty$ for which no reattachment occurs, (ii) $h^* \rightarrow 0$ and/or $D_2/D_1 \rightarrow \infty$ for which reattachment always occurs and (iii) intermediate values of h^* and D_2/D_1 for which the Reynolds number plays an important role in the qualitative aspects of the flow field.

The influence of the D_2/D_1 parameter is not readily inferred from the prior studies. Welanetz [4] provides computed results from an ad hoc control volume formulation that suggest a decrease in F^* as D_2/D_1 decreases for given h^* and Re values. (This trend is, of course, only valid for sufficiently large D_2/D_1 values as noted above.) The limited experimental data in the Welanetz paper gives qualified support to the model for one D_2/D_1 condition.

3 Experimental Equipment and Procedure

A schematic representation of the experimental equipment is shown in Fig. 2. The plenum was 254 mm in diameter and 178 mm high. Three values for the jet nozzle diameter (D_1) were used; 6.35 mm, 9.53 mm, and 12.7 mm. Impact disk diameters (D_2) of 50.8 mm, 76.12 mm, and 152.4 mm were used to obtain the D_2/D_1 ratios of 4, 5.33, 8, and 24. The nondimensional gap height (h^*) was investigated for the range of $.013 \leq h^* \leq .560$. The minimum and maximum Reynolds numbers were 1004 and 6931.

The procedure employed in this investigation was as follows. The counterweights on the beam balance were adjusted to counterbalance the weight of the impact disk. In this condition, the surface of the impact disk was horizontal and

[2] Results due to Moller.

Nomenclature

D_1, D_2 = jet nozzle and impact disk diameters
F^* = nondimensional force on the impact disk, $F/(\rho V_1{}^2 D_1{}^2)$ (Note: a repelling force between the source and impact disks is defined to be a positive force)
h^* = nondimensional separation distance between the impact and source disks (h/D_1)
p^* = nondimensional pressure on the impact disk, $p/(\rho V_1{}^2)$
$P_{p1}{}^*$ = nondimensional plenum pressure, $P_{p1}/(\rho V_1{}^2)$
q = volume flow rate
Re = jet Reynolds number, $V_1/D_1/\nu$
r_R = radius at which reattachment occurs
r^* = nondimensional radius, r/D_1
V_1 = average velocity at jet nozzle, $q/(\pi D_1{}^2/4)$
V = average velocity between the parallel disks, $q/(2\pi rh)$
V^* = nondimensional velocity between the parallel disks, V/V_1
ρ = fluid density
ν = fluid kinematic viscosity
Re_s = minimum Reynolds number for separtion

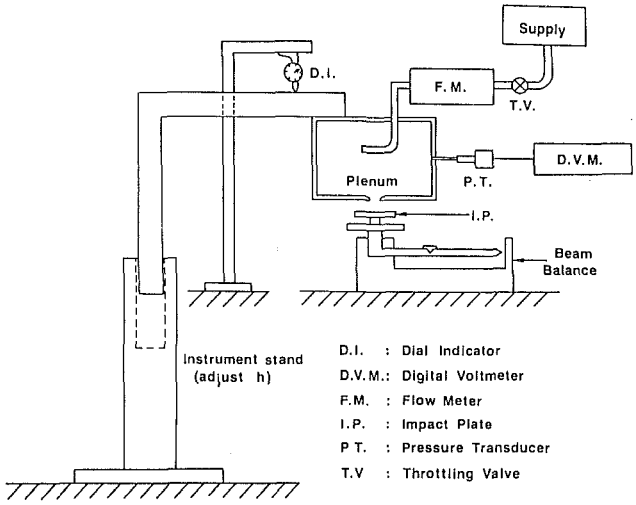

Fig. 2 Schematic representation of experimental setup

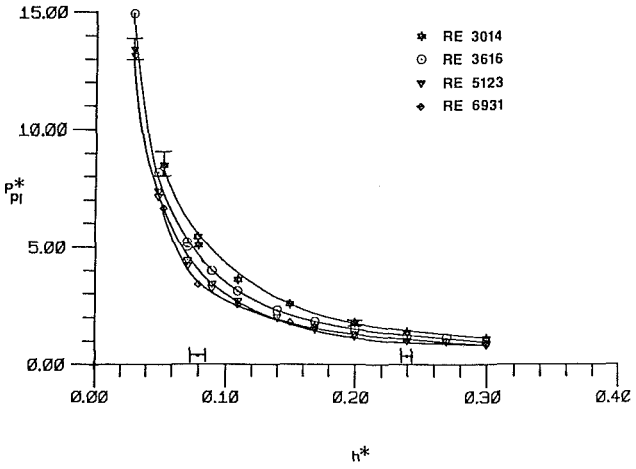

Fig. 3 Nondimensional plenum pressure distribution for $D_2/D_1 = 4$. Note: solid curves added for visual reference only in Fig. 3-12.

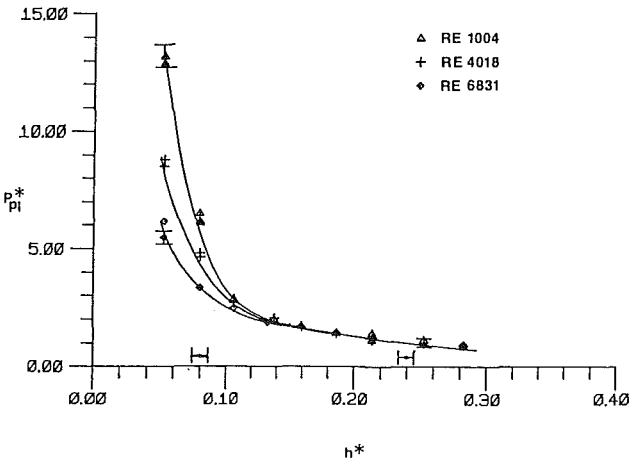

Fig. 4 Nondimensional plenum pressure distribution for $D_2/D_1 = 5.33$

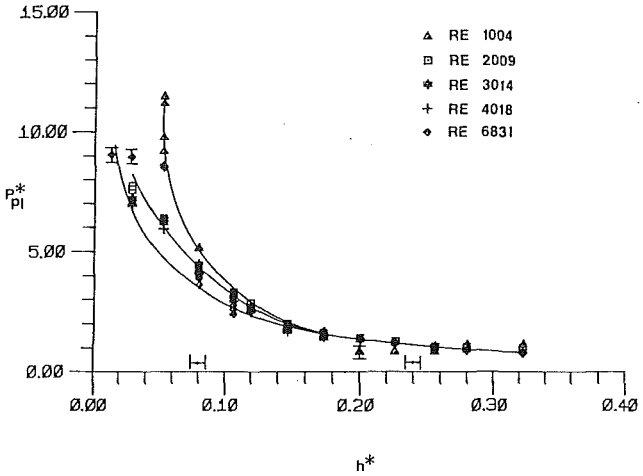

Fig. 5 Nondimensional plenum pressure distribution for $D_2/D_1 = 3/.375 = 8$

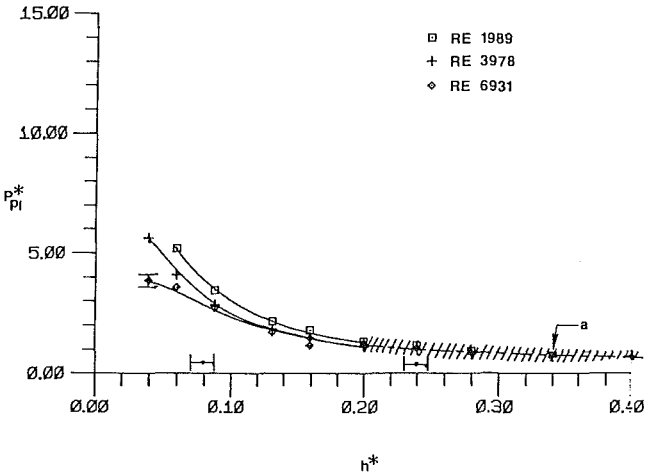

Fig. 6 Nondimensional plenum pressure distribution for $D_2/D_1 = 2/.25 = 8$.
Notes: (*a*) estimated error is ± .058 for Re = 3978

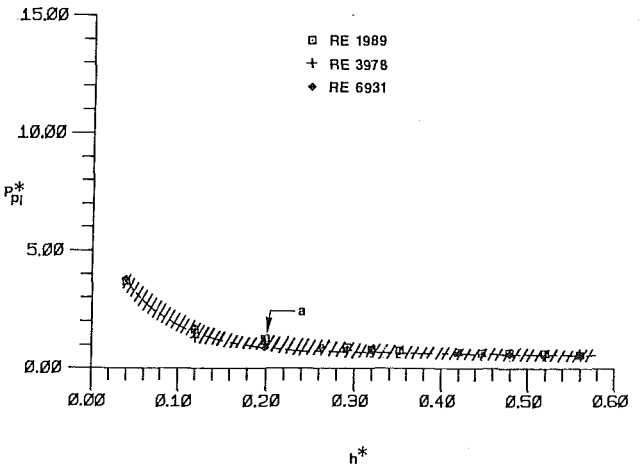

Fig. 7 Nondimensional plenum pressure distribution for $D_2/D_1 = 24$.
Notes: (*a*) estimated error is ± .058 for Re = 1989

the "pointer" identifies the null condition for both the applied force and the displacement. The plenum, and the attached disk/nozzle element, were then lowered toward the impact disk. Fine adjustments in the beam balance supports were made to ensure a parallel condition between the two disks and the dial indicator was positioned to zero when the two surfaces "first made" contact. It was estimated that the precision of this adjustment was of the order ± .1 mm for the h position. The corresponding precision of the parallel condition was ± 1.0 degrees. The position of the instrument

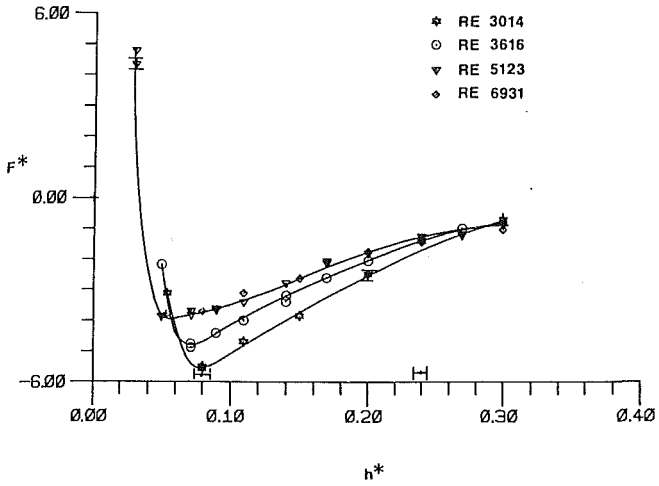

Fig. 8 Nondimensional force distribution for $D_2/D_1 = 4$

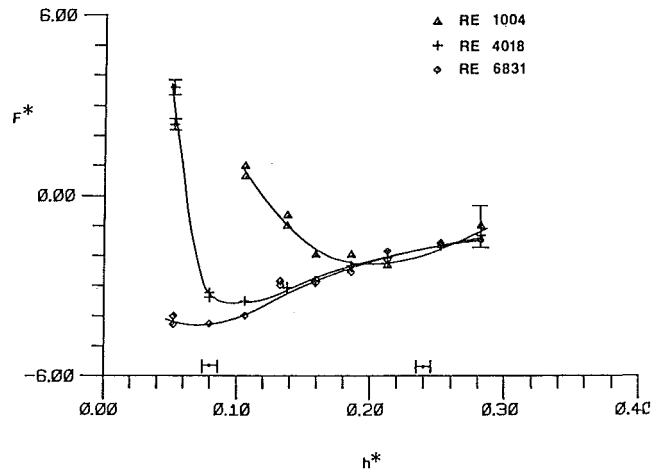

Fig. 9 Nondimensional force distribution for $D_2/D_1 = 5.33$

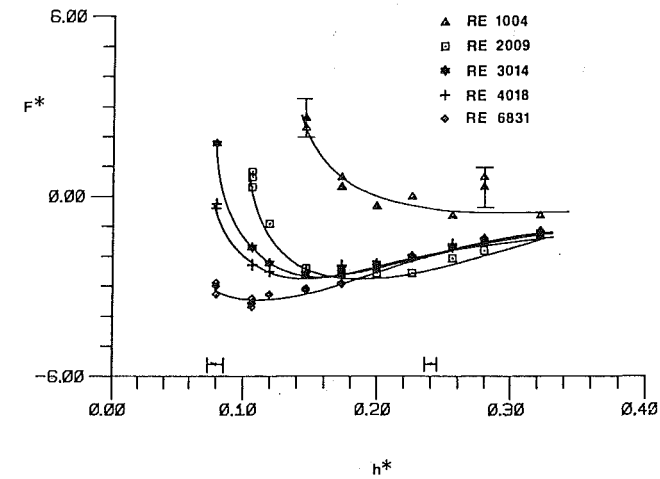

Fig. 10 Nondimensional force distribution for $D_2/D_1 = 3/.375 = 8$

stand was then adjusted (± 0.05 mm) to establish the desired h value.

Two "float-element" flow meters were used to record the volume flow rate. These units were calibrated for the ranges: 0.1-1.0 and 1.0-10.0 SCFM (where 1 SCFM = 4.72E−04 m^3/s). The repeatability of a given measurement was based

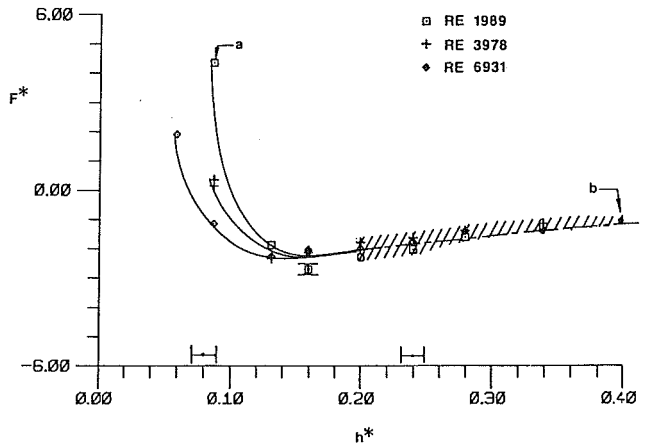

Fig. 11 Nondimensional force distribution for $D_2/D_1 = 2/.25 = 8$.
Notes: (*a*) estimated error is ± .198
(*b*) estimated error is ± .058

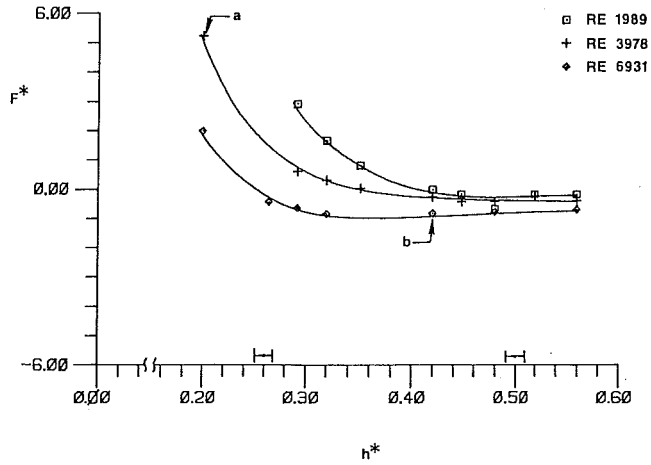

Fig. 12 Nondimensional force distribution for $D_2/D_1 = 24$.
Notes: (*a*) estimated error is ± .105
(*b*) estimated error is ± .046 for Re = 6931

on the precision with which the float position could be read, this value was estimated to be 0.3 percent of full scale. The absolute accuracy of the flow rate measurement was determined by using a sharp-edge orifice to determine the flow rate from the plenum to the atmosphere; an inaccuracy of < 2 percent, was inferred from this test.

In general, the air flow altered the net force on the beam balance and the "pointer" was displaced from the null condition. The counter-weights were then used to recover the null condition and the desired force could be read directly from the counterweight displacement. The uncertainty in this measurement was the same as the uncertainty in establishing the initial zero; this value was estimated to be ± 0.02 gms.

4 Discussion of Results

Plenum pressure values, appropriately nondimensionalized and expressed as a function of h^*, are presented in Figs. 3 through 7. These nondimensional pressure values ($P_{p1}{}^*$) show a systematic variation with Reynolds number for relatively low h^* values ($h^* \lesssim 0.15$). However for $0.15 \lesssim h^* \lesssim .6$ the $P_{p1}{}^*$ values were found to be insensitive to the Reynolds numbers and the D_2/D_1, values of this investigation.

The experimental force results; $F^*(h^*;\ \mathrm{Re},\ D_2/D_1)$ are shown in Figs. 8 through 12. A thorough examination of these results reveals a complex pattern of trends between the

dependent (F^*) and independent (h^*) variables for the Re and D_2/D_1 values of the present study. Correspondingly, the present discussion of results will be subdivided into sections of similar physical behavior for F^* (h^*).

A major subdivision is suggested by the Reynolds number influence on F^* at a given h^* as a function of the D_2/D_1 value; specifically, F^* ($h^* \lesssim .2$) decreases with increasing Reynolds number for $D_2/D_1 \geq 5.33$ whereas the opposite trend is encountered for $D_2/D_1 = 4$. The results for $D_2/D_1 \geq 5.33$ will be discussed first.

For small h^* values ($\lesssim 0.2$) it is observed that F^* decreases at a given h^* as the Reynolds number is increased; see Figs. 9 through 12. This trend is the same as that exhibited by the $P_{p1}{}^*(h^*)$ distributions (Figs. 4 through 8). Andersen [5] has measured the pressures along the impact disk: $p^*(r^* < .5\ D_2/D_1)$ for a relatively large D_2/D_1 value (i.e., 24); his data show that $p^*(r^*)$ monotonically decrease with increasing Reynolds number.

It is concluded that the basic flow pattern is qualitatively unchanged and that the pressures are decreased with increasing Reynolds number for this subset of the experimental conditions ($h^* \lesssim 0.2$, $D_2/D_1 \geq 5.33$).

The second subset of experimental conditions is provided by: $5.53 \lesssim D_2/D_1 \lesssim 8$ and $h^* \gtrsim 0.2$. With the exception of the lowest Reynolds number (1004), the $F^*(h^*)$ distributions exhibit no systematic dependence upon the Reynolds number for this range of parameters. Similarly, the $D_2/D_1 = 24$ results suggest the possible convergence of the $F^*(h^*)$ distributions for large h^* ($\gtrsim 0.48$) values. Superficially, this result could be explained by a similar independence that is observed between $P_{p1}{}^*(h^*)$ and the Reynolds number. However the reattachment radius (r_R/D_2) results of Moller show that r_R increases with Reynolds number and that r_R is a significant fraction of $D_2/2$ for the conditions of the present study. This suggests that a combination of separate physical effects result in the above mentioned F^*(Re) independence. It is concluded that an attempt to analytically model the flow field for these conditions would have to be relatively sophisticated and that any extrapolation beyond the direct observations should be executed with appropriate caution.

Hayashi et al. [1] provide an analytical formulation for the force on the impact disk. An ad hoc representation for the velocity was used in a control volume formulation and an expression relating the force to the geometric flow parameters was derived: their equation (47). A maximum Reynolds number value of 1000 was used for their experimental work.

Their equation (47) has been used to compute $F^*(h^*, \text{Re}, D_2/D_1)$ for the conditions of the present study, that is, for $1000 < \text{Re} < 7000$ and for the D_2/D_1 values; 4, 5.33, 8, and 24. The agreement between their formulation and the present experimental results is shown in Fig. 13 for the low (1004) and moderate (4018) Reynolds number conditions of the $D_2/D_1 = 5.33$ case. The agreement for $\text{Re} = 1004$ is relatively good. However the two distributions show increasing disagreement as the Reynolds number is increased; note the comparison for $\text{Re} = 4018$. The same trend was observed when the model was used to compute the other conditions that were examined in the present study. The empirical information of the length and thickness of the separation zone, that is required in the model and that is apparently increasingly invalid as the Reynolds number is increased, is at least one factor that contributes to this disagreement. The required empirical information was taken directly from [1] and no attempt was made to alter the length and thickness parameters in order to provide better agreement between the present data and their equation.

A distinctive characteristic of the Hayashi et al. analysis is that it becomes numerically unreliable for $h^* \approx 0.3$; namely, as h^* increases, the attracting force suddenly and dramatically increases. (It is probable that this numerical feature of the equation was not realized by these authors since they did not evaluate their equation for such large h^* values.)

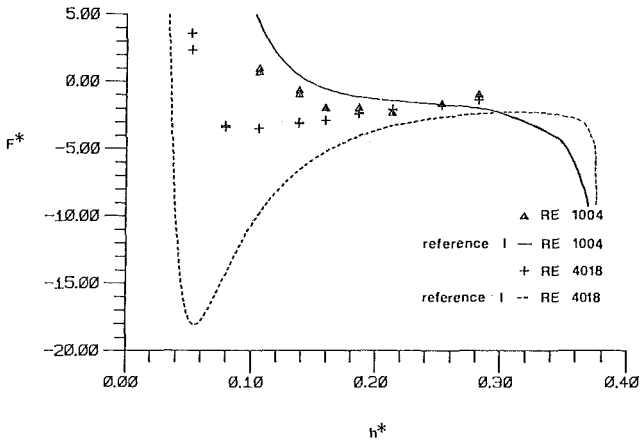

Fig. 13 Comparisons of Hayashi, et al. analysis with present experimental results for $D_2/D_1 = 5.33$

It is concluded that the specific form of Hayashi et al. analysis provided in [1] should only be used for relatively low Reynolds numbers ($\lesssim 1000$) and for $h^* \lesssim 0.3$.

For the experimental conditions discussed above ($D_2/D_1 \geq 5.33$), the force between the two disks is decreased as the Reynolds number is increased for $h^* \lesssim 0.2$; this trend is reversed for $D_2/D_1 = 4$. Apparently, the physical reasons for this reversal are grounded in the interaction between the geometric parameter: D_2/D_1, and the Reynolds number and it is best described in the context of three salient features of the flow field:

(i) the large source disk and the adequately large impact disk ($D_2/D_1 = 4$) ensure that the separation stream surface will reattach to the source disk.

(ii) the pressure distribution on the impact disk is constrained by the boundary conditions: $p(r=D_2/2) = 0$ and $p(r=0) = P_{p1}$.

(iii) the intermediate pressures, $p(r)$, on the impact disk will show a minimum value in the neighborhood of the minimum flow passage defined by the trajectory of the separation stream surface.

In addition to these salient features, it is useful to explicitly describe the F^* value as:

$$F^* = 2\pi\left[\underbrace{\int_0^{r_0{}^*} r^*p^*dr^*}_{I_1} + \underbrace{\int_{r_0{}^*}^{D_2/2D_1} r^*p^*dr^*}_{I_2}\right]$$

where r_0 is the radius at which the pressure (on the impact disk) is equal to the atmospheric value (see Fig. 1(*a*)).

From these observations, it is inferred that when the reattachment radius is comparable in magnitude with the radius of the impact disk, the relative magnitudes of I_1 and I_2 are governed by the Reynolds number dependence of the reattachment radius and the coupling between the two radii r_R and r_0.

A dramatic example of the interaction between r_R and the geometric properties of the flow system was noted in the Hayashi et al. study. The source and impact disk diameters were the same for this investigation and a dramatic increase in the force was noted when r_R exceeded ($D_2/2$). The presence of the large source-disk diameter, for the present study, prohibits a similarly dramatic change in the F^* (Re) behavior for a given D_2/D_1 and h^*.

An important conclusion, that is drawn from this reasoning, is that an optimum D_2/D_1 exists, for a given h^*

and Re, if a maximum force of attraction is desired between the two surfaces. Specifically, if lower Re values were investigated for $D_2/D_1 = 4$, or if larger Re values were included in the $D_2/D_1 = 5.33$ study, it is predicted that a minimum F^* would be observed at a given h^*.

5 Conclusions

Plenum pressure and impact surface data have been acquired for the flow between radial disks. The former data are insensitive to the Reynolds number and diameter ratio (D_2/D_1) for $h^* > 0.1$ and for the conditions of this study. A weak Reynolds number dependence is observed for the smaller h^* values.

The force data are more interesting and they suggest a quite complex mix of flow phenomena. The direct observations have been used to infer that a maximum "force of attraction" will exist for Reynolds numbers above ($D_2/D_1 \geq 5.33$) and below ($D_2/D_1 = 4$) those of the present study. The present results support the validity, and clarify the applicable range, of the Hayashi et al. analytical formulation. The present results provide design information for a "lifting device" wherein the subatmospheric pressure between the disks results in a "force of attraction." The optimal h^* value for a lifting device (i.e., $dF^*/dh^* < 0$ and $F^* < 0$) for a given D_2/D_1 value in the range: $4 \leq D_2/D_1 \leq 24$ and a Reynolds number in the range: $1 \times 10^3 \leq V_1 D_1/\nu \leq 7000$, may be inferred from the present results.

References

1 Hayashi, S., Matsui, T., Ito, T., "Study of Flow and Thrust in Nozzle-Flapper Valves," ASME JOURNAL OF FLUIDS ENGINEERING, Vol. 97, 1975, pp. 39–50.

2 Raal, J. D., "Radial Source Flow Between Parallel Disks," *Journal of Fluid Mechanics*, Vol. 85, Part 3, pp. 401–416.

3 Moller, P. S., "Radial Flow Without Swirl Between Parallel Discs," *Aeronautical Quarterly*, Vol. 14, May 1963, pp. 163–186.

4 Welanetz, L. F., "A Suction Device Using Air Under Pressure," ASME *Journal of Applied Mechanics*, Vol. 23, No. 2, June 1956, pp. 269–272.

5 Andersen, N., "Viscous Dominated Versus Inertial Dominated Fluid Flow," An unpublished report, Michigan State University, 1972.

Effects of Free Stream Turbulence on Low Reynolds Number Boundary Layers

I. P. Castro
Department of Mechanical Engineering,
University of Surrey,
Guildford Surrey, England

This paper documents some of the effects of free stream turbulence on the mean flow properties of turbulent boundary layers in zero pressure gradients. Attention is concentrated on flows for which the momentum thickness Reynolds number is less than about 2000. Direct Reynolds number effects are therefore significant and it is shown that such effects reduce as the level of free stream turbulence rises. A modification to Hancock's [1] empirical correlation relating the fractional increase in skin friction at constant Reynolds number to a free stream turbulence parameter containing a dependence on both intensity and length scale is proposed. While this modification has the necessary characteristic of being a function of the free stream turbulence parameters as well as the Reynolds number, it is argued that the relative importance of intensity and length scale changes at low Reynolds numbers; the data are not inconsistent with this idea. The experiments cover the range $500 \lesssim Re_\theta \lesssim 2500$, $u'/U_e \lesssim 0.07$, $0.8 \lesssim L_e/\delta \lesssim 2.9$, *where* u'/U_e *is the free stream turbulence intensity and* L_e/δ *is the ratio of the dissipation length scale of the free stream turbulence to the 99 percent thickness of the boundary layer.*

1 Introduction

It is well known that turbulent boundary layers are influenced by changes in the character of the external flow. In particular, the presence of free stream turbulence whose length scales are of the same order as the boundary layer thickness, generally causes increased boundary layer growth with associated increases in surface skin friction. The existence of the universal logarithmic "law of the wall" is not affected, but the outer region of the velocity profile can be substantially changed. Recently Hancock* [1] reviewed the fairly extensive literature and undertook some particulary careful experiments designed to extend the previously rather limited range of turbulence length scale ratios (i.e., the ratio of a typical turbulence length scale in the free stream to the boundary layer thickness). His results showed that "the effect of (nearly isotropic) free-stream turbulence depends significantly on both the free-stream intensity and the length scale ratio." Previous work was not effective in delineating the separate influences of these parameters because of the strong correlation between the two – special effort is required to set up flows which cover large ranges of both intensity and length scale ratio *separately*.

Hancock's data clearly demonstrated that not only does the effect of free stream turbulence increase with increasing turbulent intensity, as previously found by many workers (e.g., Robertson and Holt [2], Charnay et al. [3], Meier [4]) but also that the effect decreases with increasing length scale ratio, at least in the range $0.7 < L_e/\delta < 5.5$. Here, L_e is the external flow dissipation length parameter (defined in Section 2) and δ is the boundary layer thickness, measured to the point where the mean velocity is 0.995 times its free-stream value. A simple empirical correlation was found that relates the increase in skin friction $\Delta C_f/C_{f0}$ at constant Reynolds number, Re_θ, to a free-stream turbulence parameter, $(u'/U_e)/(L_e/\delta+2)$. u'/U_e is the free stream turbulence intensity. When this parameter, hereafter called FSTP, exceeds about 0.01, the data suggested that persistence of the "log-law" begins to restrict further change in the mean flow properties, so that $\Delta C_f/C_{f0}$ begins to "saturate."

Now, in order to avoid serious Reynolds number effects, Hancock limited his study to values of Re_θ in excess of 2000 (except for one data point). The single low Re_θ point did suggest, however, that this saturation in C_f is stronger than it is at high Reynolds numbers. Blair [5] has recently suggested that FSTP should be modified by the factor $(1+3\exp(-Re_\theta/400))$ to account for low Reynolds number effects. In the light of recent work on the structure of low Reynolds number boundary layers in the absence of free steam turbulence (Murlis et al. [6], Head and Bandyopadhyay [7], Antonia et al. [8]) it is certainly reasonable that changes in, say, C_f (at constant Re_θ) caused by free-stream turbulence, should be less at low than at high values of Re_θ. These authors all, in various ways, confirm the hypothesis of Huffman and Bradshaw [9] that Reynolds number effects are essentially associated with the "viscous superlayer." The surface area of the highly contorted viscous superlayer, per unit streamwise fetch, increases as the Reynolds number falls. If the external fluid is, in fact, turbulent, the super-layer will have a somewhat different character so that, arguably, the energy-containing motion will be less susceptible to viscous effects. One might therefore also anticipate that the magnitude of any Reynolds

Contributed by the Fluids Engineering Division for publication in the JOURNAL OF FLUIDS ENGINEERING. Manuscript received by the Fluids Engineering Division, June 13, 1983.

*Note added in proof. Hancock's mean flow data has recently been presented in reference [18] and his thesis is available on microfiche from Professor P. Bradshaw, Dept. of Aeronautics, Imperial College.

number effects will depend on the level of free stream turbulence – a feature not contained in Blair's modification to FSTP. Further there is no "a priori" reason to suppose that the relative importance of free stream intensity and length scale ratio implied by FSTP will be maintained at low Reynolds numbers. Indeed, since the range of length scales in the boundary layer significantly decreases with decreasing Reynolds number, the larger scales becoming increasingly emphasized, it would, perhaps, be surprising if the relative importance of u'/U_e and L_e/δ did *not* change.

The experiments described in this paper were designed to investigate the effects of free-stream turbulence on boundary layers in the low Reynolds number range ($Re_\theta < 2000$) not covered by previous workers – except for "occasional" data points like that of Hancock [1] mentioned earlier. (Robertson and Holts' [2] data are in the $Re_\theta < 2000$ range, but they appear not to have recognized the importance of Reynolds number effects so that their data, as presented, is of limited value. Some comparisons are possible, however (see Section 4.) Free-stream intensities were in the range $0.023 \lesssim u'/U_e \lesssim 0.07$ and length scale ratios covered $0.8 \lesssim L_e/\delta \lesssim 2.9$. These do not represent quite as wide a variation as Hancock achieved, but as the results will demonstrate, they were adequate to give a fairly clear indication of the differences in boundary layer response to that which occurs at high Reynolds numbers.

We have not made any direct measurements of turbulence structure. While the mean flow and also the turbulence energy data can be used to deduce some of the structural changes that lead to the observed response, more sophisticated techniques would obviously be required to confirm such deductions. In particular, the whole question of *how* one turbulence field (be it isotropic and homogeneous or not) interacts with a separate and essentially different shear layer warrants considerable study; it may be, paradoxically, that studies (like this one) of the interaction of a flow susceptible to viscous effects with another one that is not, will help in understanding the way the turbulence structure of each interacts.

The next section briefly describes the experimental technique and the major results are presented and discussed in Sections 3 and 4.

2 Experimental Details

All the experiments were done in the 0.6 × 0.75 × 4m wind tunnel in the Department of Mechanical Engineering. In the absence of turbulence generating grids the mean velocity variation across the working section did not exceed 1/4 percent and the turbulence intensity was less than about 0.05 percent. All the boundary layers studied were generated on a false floor mounted about 15 cm from the tunnel floor and 1.5 m from the contraction exit. This was fitted with an elliptical leading edge and a flap at the rear which was used in conjunction with static tappings on either side of the nose section to maintain zero circulation around the false floor. The whole assembly could also be tilted slightly and it was therefore possible to maintain a zero longitudinal pressure gradient, within experimental accuracy, except near the trailing edge flap. A strip of "Dyno" tape, stamped with a series of "V"s (pointing upstream) was used to trip the boundary layer at 40 mm from the leading edge.

Skin friction measurements were made either by using a surface mounted Pitot tube (Preston tube) of outside diameter 1.42 mm in conjunction with Patel's [10] calibration, or by fitting mean velocity profiles in the logarithmic region to the usual log-law

$$U/U_\tau = 1/k \ln(U_\tau z/\nu) + A.$$

Von Karman's constant, k, and A were taken as 0.41 and 5.2, respectively, in line with recommendations of Brederode and Bradshaw [11].

All velocity and turbulence measurements were made with standard hot-wire anemometry, operated on-line via 10-bit Analogue-to-Digital converters (ADC) to a Commodore PET microcomputer. Probes were calibrated in uniform flow against a standard pitot-static tube. The software allowed sampling at rates in excess of 2KHz and sampling times ranged up to 60 seconds, depending on the Reynolds number. Linearization of the bridge output was performed in the computer, thereby minimizing the quantity of electronic hardware. Accuracy was maintained by adjustment of a calibrated DC offset and gain built into the ADC module, so that the full range of the ADC was used in the regions of highest turbulence intensity. Free-stream velocities were measured before and after each traverse and if these differed by more than ½ percent the profile was rejected.

The probes were mounted on a traverse gear (outside the tunnel) whose positional accuracy was better than 0.1 mm. Reference heights of the hot wire above the surface were set visually using a fine-scale metal rule; zero error was therefore reckoned to be better than 0.25 mm. Small corrections to probe height were sometimes necessary to give good log-law fits at the lower heights but these never exceeded 0.2 mm. The traverse gear was not originally designed for boundary layer studies and would not be good enough for accurate work in the viscous sublayer and buffer layer. However, it was adequate for the present measurements, which concentrate on the log-layer and outer regions of the flow.

Two-dimensionality of the flow was checked by traversing a hot-wire laterally at a location near the end of the false floor and in the boundary layer where the velocity was about 0.8 times the free stream value. Variations of mean velocity did not exceed + 1.25 percent over the central 400 mm of span – i.e., over 0(10) times the boundary layer thickness. Spanwise skin-friction measurements obtained with the Preston tube showed variations no greater than those usually found (e.g.,

Nomenclature

C_f = skin friction coefficient
F = $100\,(u'/U_e)/(0.5L_e/\delta + 2.5)$; free stream turbulence parameter
H = shape factor of boundary layer = δ^*/θ
L_e = dissipation length scale of free stream turbulence
= $(\overline{u^2})^{3/2}/U\dfrac{d\overline{u^2}}{dx}$
M = mesh spacing of turbulence generating grid
Re_θ = Reynolds number = $U_e\theta/\nu$
U_e = free stream velocity
u_τ = shear velocity = $(\tau_0/\rho)^{1/2}$
u',v',w' = fluctuating velocities
x,y,z = Cartesian coordinates: x downstream, z vertical
δ = boundary layer thickness
δ^* = boundary layer displacement thickness
θ = boundary layer momentum thickness
ΔC_f = fractional change in skin friction
ΔH = fractional change in shape factor
ΔU = wake component velocity difference
τ_0 = wall shear stress
ρ = density
ν = kinematic viscosity

Subscript

0 = value in absence of free stream turbulence

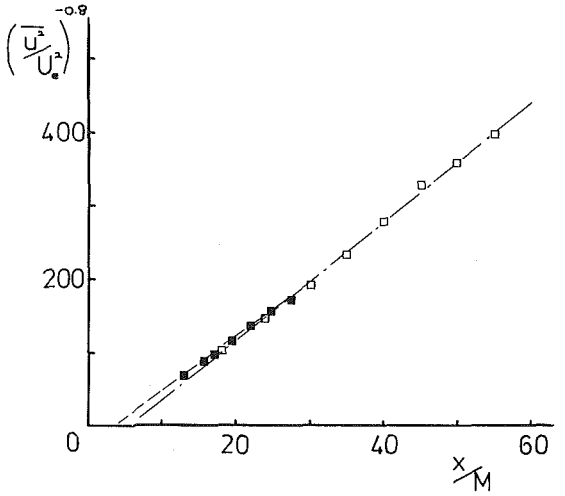

Fig. 1 Decay of longitudinal turbulence energy. □, 50 mm mesh; ■, 100 mm mesh.

Fernholz [12]). While exact two-dimensionality could not be expected because of the side-wall boundary layer growth, these results demonstrated the adequacy of the flow in this respect, particularly as the maximum axial distance from the leading edge trip was only about 1.5 m.

Two biplanar square mesh grids were used to generate free-stream turbulence. These had a nominal mesh/bar width ratio of 4 with mesh widths (M) of 50 mm and 100 mm. They could be positioned at various locations upstream of the false floor, but to ensure reasonable flow homogeneity at the leading edge the minimum distance was 6M. Figure 1 shows that the longitudinal turbulence energy decayed according to:

$$(\overline{u^2}/U^2)^{-0.8} = C((x-x_0)/M) \qquad (2.1)$$

for both grids, with x_0/M and C being given, respectively, by 5.8 and 8.1 for the 50 mm grid and 3.6 and 7.8 for the 100 mm grid. Crossed hot-wire measurements behind the larger grid showed that $\overline{u^2}/\overline{v^2}$ decayed slowly from about 1.11 at x/M = 12 to 1.08 at x/m = 25, whereas $\overline{u^2}/\overline{w^2}$ remained constant at about 1.04. These results are remarkably similar to Hancock's [1] and the degree of anisotropy is within the typical ranges found by other workers for this type of grid (e.g., Comte-Bellot and Corrsin, [13]).

The dissipation length scale, L_e, defined by

$$U(\overline{du^2}/dx) = -(\overline{u^2})^{3/2}/L_e$$

was deduced from equation 2.1 i.e.,

$$L_e/M = 0.8C((x-x_0)/M)^{0.375}$$

3 Results and Discussion

3.1 Mean Flow Data, No Grid. In view of the great number of profiles obtained it would be inappropriate to present all the raw data here; we concentrate on the more important results derived from them. Figure 2, however, presents typical profiles in the usual $U+$, $Z+$ coordinates for the no free-stream turbulence, "baseline" case and also (Fig. 2(b) for some cases for which the free-stream turbulence parameter, $(u'/U_e)/(L_e/\delta+2)$, was about 0.008. These give some indication of the typical scatter in the raw data; this was satisfactorily low except, as anticipated, very close to the wall.

Figure 3 presents the skin friction data for the baseline case, as a function of momentum thickness Reynolds number, Re_θ, and compared with other recent data. The hot-wire and Preston tube results generally differed by less than 1½ percent and were also very close to the data of Head and Bandyopadhyay [7], Murlis et al. [6] and Hancock [1]. They lie rather lower than the data of Purtell et al. [14] and Antonia et al. [8]. However, both these latter sets of authors used slightly different constants in the log-law (close to Coles' [15]) values, with C_f values correspondingly close to his values). This accounts for practically all the difference, that which is left being explainable by experimental error. For the present purpose, since most of the skin friction data obtained for the free-stream turbulence cases were derived from log-law fits, the smooth line drawn through the experimental points in Fig. 3 is biased toward the hot-wire data.

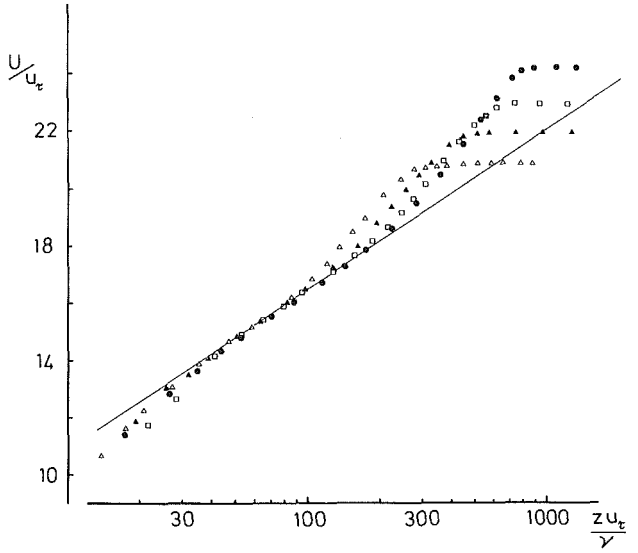

Fig. 2(a)

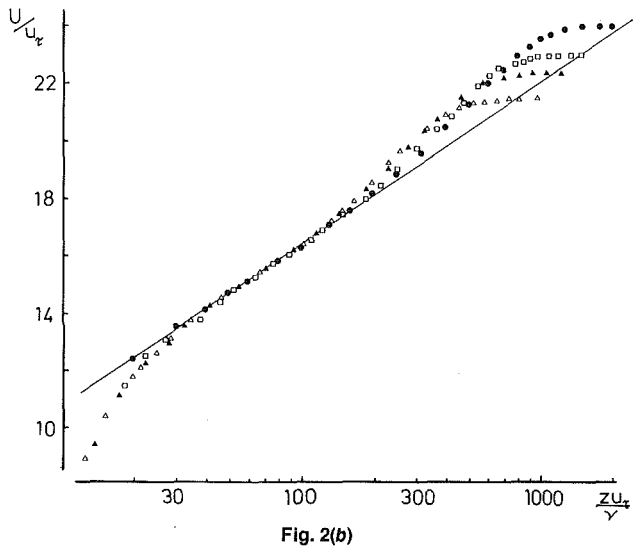

Fig. 2(b)

Fig. 2 Boundary layer profiles, —, u/u_τ = 1/0.41 ln(zu_τ/ν) + 5.2 (*a*) No Grid. Re_θ: ●, 2287; □, 1537; ▲, 1095; △, 705. *b*) FSTP = 0.008. Re_θ: •, 2628; □, 1826; ▲, 1359; △, 995.

Figure 4 shows the variation of shape factor H, the ratio of displacement thickness to momentum thickness, with Reynolds number. Although H is quite sensitive to the probes' positional accuracy, the data exhibit scatter of less than 1 percent and are within 2 percent of the values given by Murlis [16] and Head and Bandyopadhyay [7]. Except at either end of the Reynolds number range, Purtell et al.'s [14] data lie a little higher, but still within 3 percent of the present results.

It is important to know whether, at the lowest values of Re_θ, the boundary layers have achieved full development. Coles [15] and Purtell et al. have shown that this is most easily determined by inspecting values of the outer layer wake

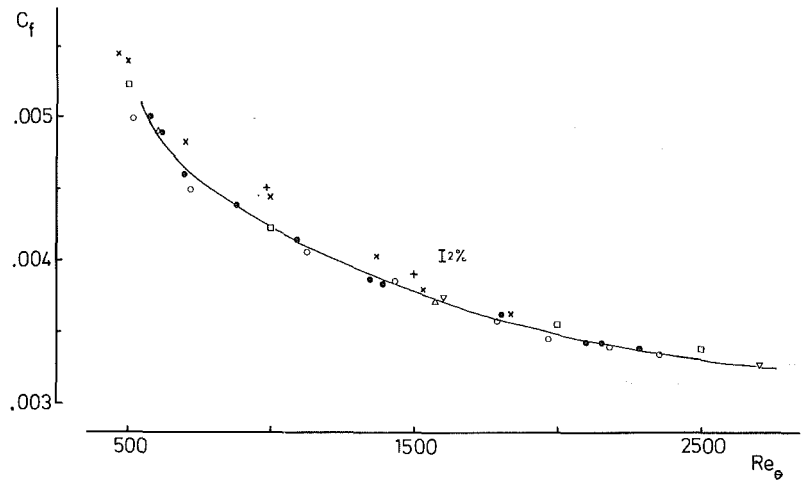

Fig. 3 Skin friction versus Re_θ; no grid. ●, log-law fits; ○, Preston tube. □, Murlis et al. [6]; △, Head and Bandyopadhyay [7]; ▽, Hancock [1]; ×, Purtell et al. [14]; +, Antonio et al. [8].

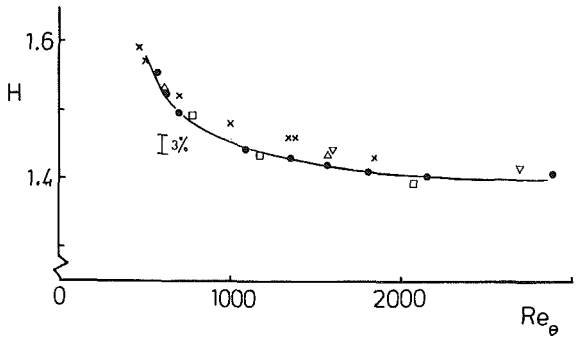

Fig. 4 Shape factor versus Re_θ. ●, present data. Other symbols as for Fig. 3.

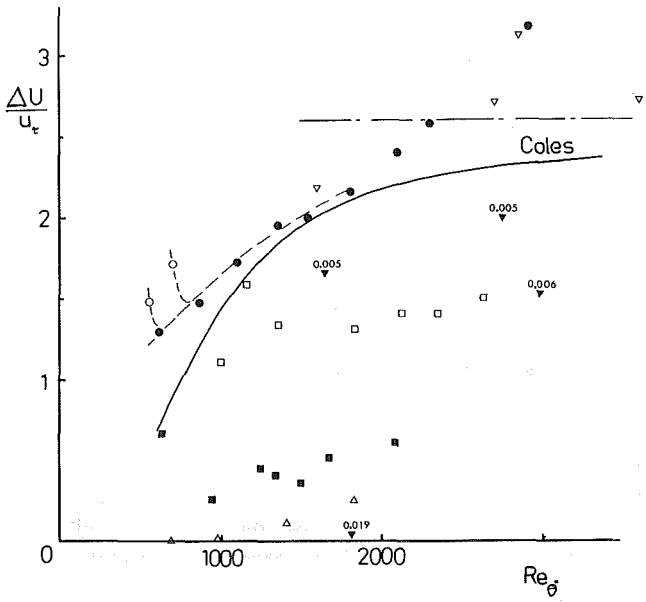

Fig. 5 Variation of Wake Component with Re_θ. ●, present data; (0, underdeveloped profiles). ▽, Hancock [1]; no grid cases. With grids, FSTP: □, 0.008; ■, 0.013; △, 0.02; ▼, Hancock, values of FSTP as shown.

component, $\Delta U/U_\tau$, underdeveloped layers being typified by abnormally high values of this parameter. Figure 5 shows that two of the present profiles were certainly not fully developed,

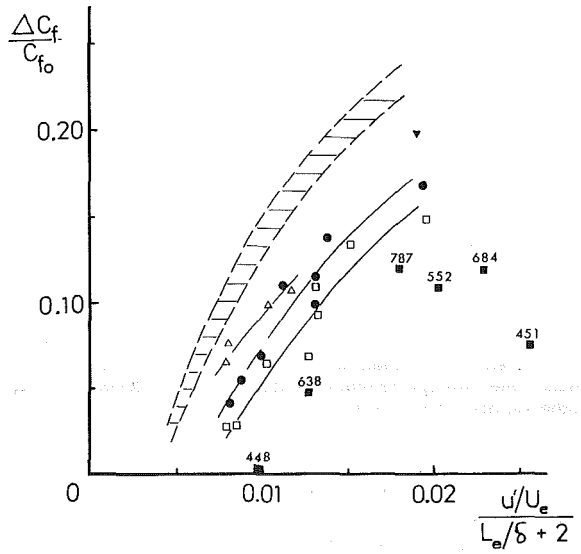

Fig. 6 Fractional increase in skin friction versus Hancock's "Free stream turbulence parameter." Shaded region is Hancock's data, with ▼ showing his Re_θ = 1830 result. Re_θ ± 5 percent: △, 2400; ●, 1350; □, 920. Other points (■) with Re_θ shown.

although it must be noted that the lack of full development is most noticeable in the outer region of the boundary layer, so that skin friction values are not necessarily affected. Apart from those two cases, the data are very close to those of Purtell et al. and support those authors' contention that the wake component does not decrease as rapidly as Coles suggested. It is also worth stating that the extent of the logarithmic region, expression as a fraction of the total boundary layer thickness, remains in excess of 20 percent for all the present no-grid cases, independent of Re. Although the results are not presented here, there is even evidence that this fraction increases slightly with decreasing Re_θ so that, as Purtell et al. stated, "the logarithmic region thus seems to be an inherent characteristic of the turbulent boundary layer."

3.2 Mean Flow Data, With Free Stream Turbulence. Although, as discussed earlier, we do not necessarily expect the FSTP of Hancock to be an adequate correlating parameter at low values of Re_θ, the data are first presented as if it were. Figure 6 shows the fractional increase in skin friction at constant Re_θ, $\Delta C_f/C_{f0}$, plotted against FSTP. C_{f0} values were

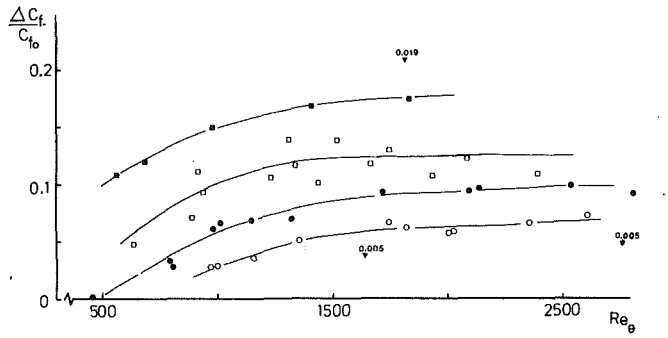

Fig. 7 Increase in skin friction versus Re_θ at constant (±5 percent) 'FSTP': ■, 0.02; □, 0.013; ●, 0.01; ○, 0.008. Hancock's data with FSTP values as shown.

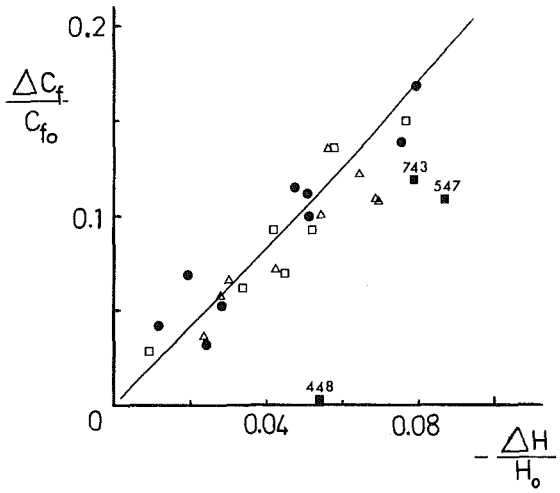

Fig. 8 Correlation between skin friction and shape factor changes. —, mean line through Hancock's data. Re_θ: △, > 2000; ●, 1350; □, 950; other points (■) as shown.

obtained from the smooth line in Fig. 3. Obtaining many results at exactly equal Reynolds numbers would be an exceedingly daunting task, but sufficient profiles were obtained to enable the data to be banded into a few groups of *roughly* constant Re_θ, with a reasonable spread of FSTP values in each band. Some isolated points at other Reynolds numbers are included in Fig. 6. While the scatter is not insignificant, and may in part be caused by small (±5 percent) variations in Re_θ within each band, the overall trend is clear. As Re_θ decreases, C_f is increased less and less by the addition of free-stream turbulence. Figure 7 shows the variation of ΔC_f with Re_θ at (roughly) constant values of FSTP, again clearly demonstrating the decreasing effect of free-stream turbulence as Re_θ falls. It should be noted that the use of standard log law constants again gave quite satisfactory fits to the mean flow data in all cases. The extent of the logarithmic region seemed similar to that in the no-grid cases.

Comparison of Figs. 2(*a*) and 2(*b*) shows that the outer layer wake component is reduced not only by Re_θ reductions, but also, as expected, with the addition of free-stream turbulence. Figure 5 includes some of the wake component results where, as in Fig. 7, the data have been selected to show the variation of $\Delta U/U_\tau$ with Re_θ for various roughly constant values of FSTP. Also plotted in both figures are the points obtained by Hancock [1] for $Re_\theta < 3000$; they demonstrate the same trend as that shown by the present data. In particular, the practical disappearance of the wake component for the highest values of FSTP (about 0.02) and $Re_\theta < 2000$ is confirmed by both the present data and Hancock's single point in

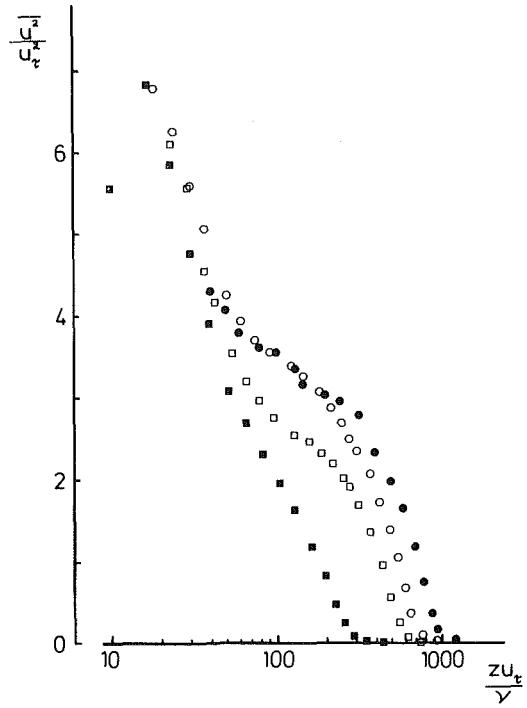

Fig. 9(*a*)

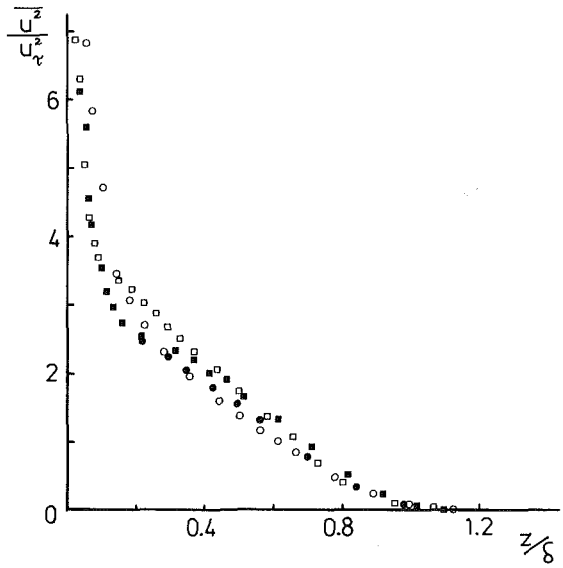

Fig. 9(*b*)

Fig. 9 Longitudinal turbulent energy profiles. No grid. (*a*) Re_θ: ●, 2901; ○, 2099; □, 1537; ■, 605. (*b*) Re_θ: □, 2099, ■, 1537; ●, 1095; ○, 605.

that range, and the latter's results for FSTP = 0.005 lie nicely between the present band of FSTP = 0.008 data and the no-grid results. It should be noted that $\Delta U/U_\tau$ results are generally only obtainable to an accuracy corresponding to about $0.1-0.2$ on $\Delta U/U_\tau$.

Now Hancock argued that in the presence of free-stream turbulence the wake strength will disappear earlier at low Reynolds numbers, "unless the reduction in wake strength due to free stream turbulence is itself Reynolds number dependent in an exactly compensatory manner." The fact that the value of $\Delta C_f/C_{fo}$ for his one low Re_θ data point lay below the correlation obtained for the higher Reynolds number data (see Fig. 6) suggested that such a compensation does not

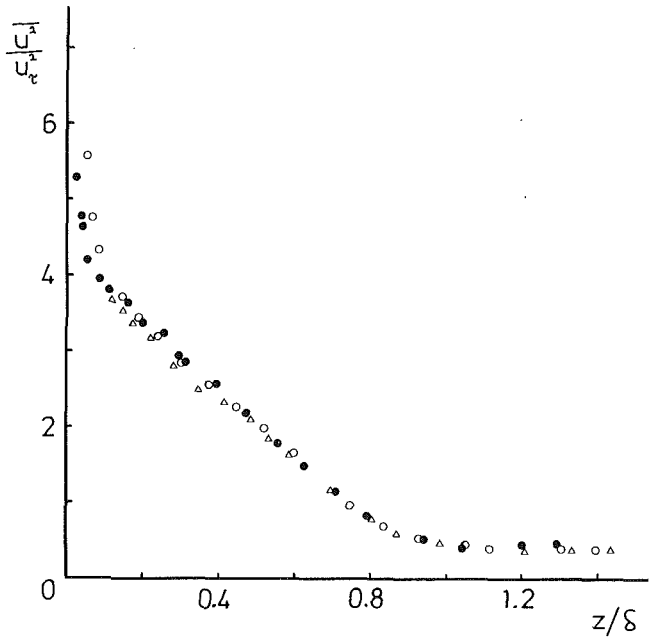

Fig. 10(a)

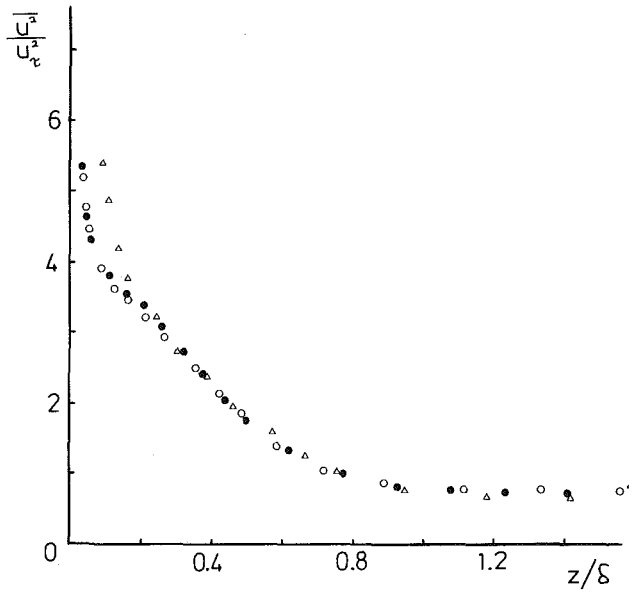

Fig. 10(b)

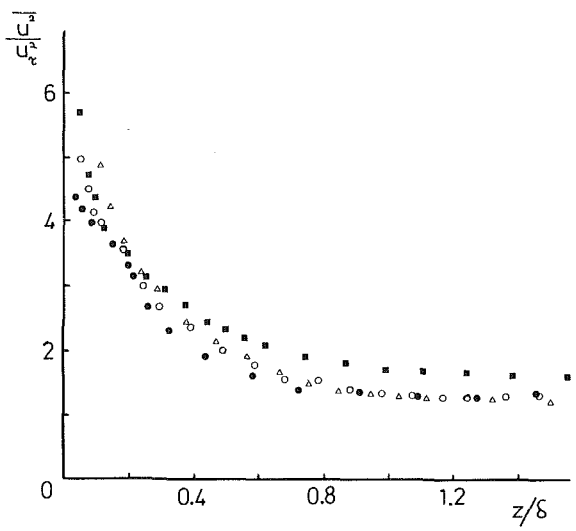

Fig. 10(c)

Fig. 10 *Longitudinal turbulent energy profiles in the presence of free-stream turbulence.*
(a) FSTP = 0.008. Re_θ = : ●, 2356; ○, 1359; △, 965 *(b)* FSTP = 0.013. Re_θ = : ●, 2081; ○, 1440; △, 638 *(c)* FSTP = 0.020. Re_θ = : ●, 1829; ○, 973; △, 553; ■, 684 (note the significantly higher free-stream intensity in this case).

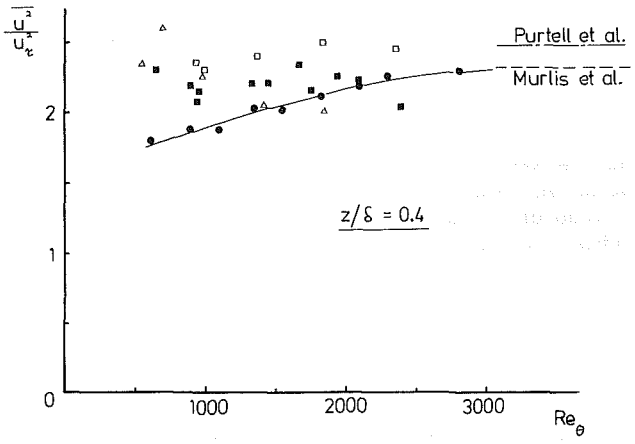

Fig. 11 Longitudinal energy variation with Re_θ at constant 'FSTP'. No grid: —, Murlis et al. [6]; ●, present data. FSTP = : □, 0.008; ■, 0.013; △, 0.020

occur. This single point of Hancock's is at least qualitatively consistent with the trends of the present data, lying between the Re_θ = 1350 results and Hancock's high Re results. Further discussion is deferred to Section 4.

Hancock found a strong correlation between the increase in skin friction and decrease in shape factor, which seemed to be largely independent of free-stream intensity and length scale ratio. $\Delta C_f/C_{fo}$ is plotted against $-\Delta H/H_0$ in Fig. 8, comparing the present results with the smooth line through Hancock's (less scattered) high Re_θ data. While there is no obvious Reynolds number trend for $Re_\theta > 1000$, the points measured at lower Re_θ generally show a rather greater effect of free stream turbulence on H than on C_f. This is consistent with the fact that C_f changes become limited by the slow disappearance of the wake component, which occurs earlier at low Re_θ. Even after C_f has "saturated," further increases in free stream turbulence levels will cause continual changes in H. Now in the absence of free-stream turbulence the Clauser Shape Parameter, G, is not a function of Re_θ and it seems likely that this would also be true with free-stream turbulence. So, as Hancock argues, the relationship between $\Delta C_f/C_{f0}$ and $\Delta H/H_0$ must, in fact, be dependent on Re_θ, for otherwise it can be shown that G must be a function of Re_θ. However, neither Hancock's nor the present data demonstrate any clear trend for $Re_\theta > 1000$.

3.2 Turbulence Data. Figure 9 presents the longitudinal turbulence energy plotted against z in both inner (Fig. 9(*a*)) and outer (Fig. 9(*b*)) layer units, at various values of Re_θ for the baseline, no grid case. Clearly Reynolds number effects penetrate much deeper into the boundary layer than they do in the case of the mean velocity. Even in outer layer variables, $\overline{u^2}/u_\tau^2$ is still noticeably Reynolds number dependent (Fig. 9(*b*)). These results are similar to those of Purtell et al. [14] and Murlis et al. [6]. The latter authors showed the dependence with Reynolds number of $\overline{u^2}/u_\tau^2$ at constant z/δ directly and Fig. 11 compares the mean line through their data with the present (less scattered) results, for z/δ = 0.4. The agreement

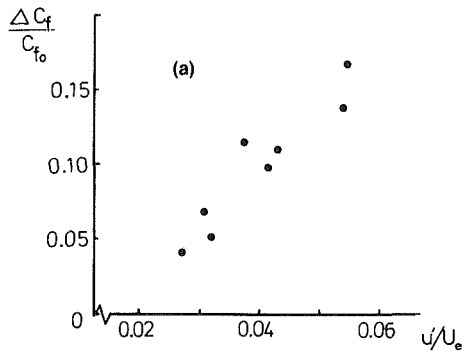

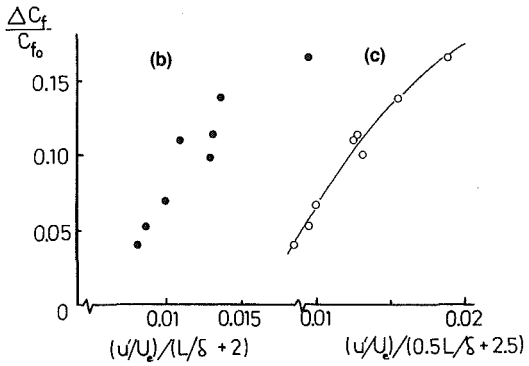

Fig. 12 Increase in skin friction at $Re_\theta \simeq 1350$ versus (*a*) free-stream turbulence intensity. (*b*) Hancock's FSTP. (*c*) An 'adjusted' FSTP.

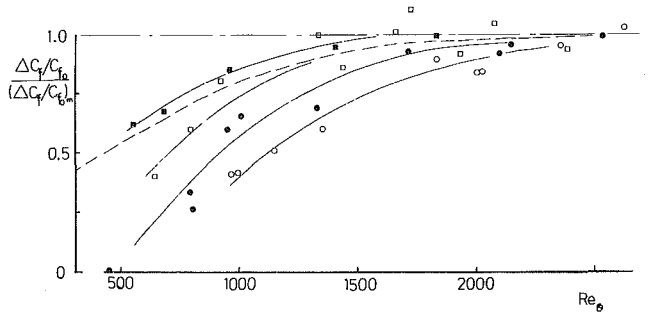

Fig. 13 Skin friction increase normalized by its asymptotic value at high Re_θ at constant values of 'FSTP': o, 0.008; •, 0.010; □, 0.013; ■, 0.020. —, Blair [5]

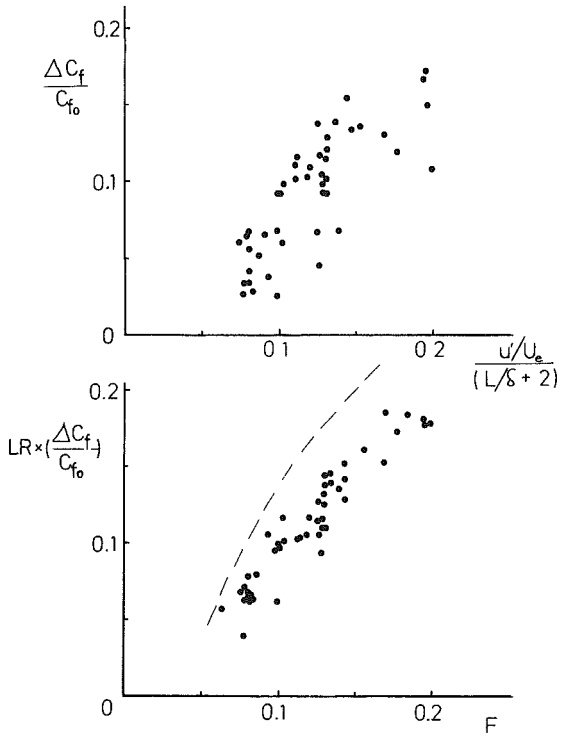

Fig. 14 Increase in skin friction – all data points. (*a*) Using Hancock's correlation. (*b*) With low Reynolds number modification: $LR = (1 + 10/F^2 . e^{-Re_\theta/400})$; ---, from Hancock [1]

is good and supports the increasingly well substantiated idea that low Reynolds number effects are a result primarily of an increasing influence of the viscous superlayer, with a suppression of all but the largest scales – Falco's [17] "typical eddies," which scale on ν/U_τ, become relatively large (as a fraction of δ) and closer in size to the large eddies as Re_θ falls (Huffman and Bradshaw [9], Murlis et al. [6], Antonia et al. [8]).

Figure 10 shows the variation of u^2/u_τ^2 with z/δ at various Reynolds numbers for three different values of FSTP. Interpolated data at $z/\delta = 0.4$ from these and other profiles are included in Fig. 11. It appears that the addition of free-stream turbulence significantly reduces the Reynolds number effects on $\overline{u^2}$ and there is even a suggestion that at the highest value of FSTP (0.02, Fig. 10(*c*)) the effect is reversed. The former is not, perhaps a surprising result since one would expect the influence of the viscous superlayer to be less pronounced if the outer, normally irrotational flow were turbulent. The latter can be explained by the fact that the increase in u_τ^2 is limited at low Reynolds numbers (see previous sections) whereas $\overline{u^2}$ will not be so limited. Indeed, even at $z/\delta = 0.4$, the turbulence energy will eventually be dominated by contributions from the external flow. It will be noted that although the data shown in Fig. 10 were selected to have constant FSTP (for each figure) the length scale variation was very small for the profiles shown, so that constant FSTP is equivalent, in this case, to constant free-stream intensity. The one exception is in Fig. 10(*c*), where the $Re_\theta = 684$ case had a significantly higher free stream intensity (and correspondingly higher L_e/δ). The rather higher value of $\overline{u^2}/U_\tau^2$ at $z/\delta = 0.4$ than would be suggested by the trend in the other results for the same FSTP (see also Fig. 11) is almost certainly a result of this higher free-stream intensity. Clearly FSTP is not really an appropriate parameter for assessing the influence of the free stream turbulence on the outer layer turbulence structure. We do not have sufficient data to determine how the Reynolds number effects change for constant free stream intensity but varying length scale ratio, but would anticipate a rather weaker effect than that seen for constant L_e/δ but varying u'/U_e, at least for $L_e/\delta = 0(1)$.

4 Final Discussion

In the presentation of results thus far it has been tacitly assumed that the free-stream turbulence parameter which Hancock found to be successful in correlating mean flow data would be adequate at low Reynolds numbers also. However, as indicated in Section 1, it could be argued that the changes in relative importance of the various eddy scales and the increasing importance of the viscous superlayer which occurs at low Reynolds numbers will lead to changes in the response of the boundary layer to free stream turbulence. For example, since the range of dominant eddy scales is smaller at low Reynolds numbers, the influence of *changes* in length scale of the free stream turbulence might, perhaps, be lower at least for $L_e = 0(\delta)$. Figure 12 shows that although attempting to correlate C_f with u'/U_e alone is no more successful than it is at high Reynolds number (Fig. 12(*a*)), the parameter used by

Hancock is not really much better (Fig. 12(*b*)). A rather more satisfactory collapse is achieved by using an "adjusted" FSTP, $(u'/U_e)/(0.5L_e/\delta+2.5)$. For $L_e/\delta = 1$ this is equivalent to Hancock's parameter, but it varies less with L_e/δ than does the latter. While this appears to be in line with the preceding argument, the correlation at other Reynolds numbers did not always seem to be so neatly affected by similar "twiddling" of FSTP. Since, in addition, the variation of L_e/δ in the present work is rather smaller than that achieved by Hancock (ranging from 0.8 to 2.0 in Fig. 12) no definitive conclusions on this point can be reached. The probability remains, however, that a good part of the scatter in Figs. 6 and 7 is attributable to changes in the relative importance of intensity and length scale at low Reynolds numbers. It is significant, in this regard, that the greatest scatter in Fig. 7 occurs for the FSTP = 0.013 data, for which the range of length scale ratio was twice that of the other constant FSTP bands ($0.8<L_e/\delta<2$).

What the present data *do* clearly show is that the effects of Reynolds number variations are increasingly less significant as the free stream turbulence levels rise. It was noted in Section 3.2 that the rate of reduction of the wake component is reduced with increasing values of FSTP, (Fig. 5) and in Section 3.3 that Reynolds number effects on $\overline{u^2}/u_\tau^2$ reduced similarly (Fig. 11). In Fig. 13 $\Delta C_f/C_{fo}$, normalized by its aysmptotic value at high Reynolds number (estimated from Fig. 7), is plotted as a function of Reynolds number for the various values of FSTP. The most rapid variations occur for the lowest values of FSTP. It is interesting that the modification proposed by Blair [5] to account for low Reynolds number effects is quite good for the highest values of FSTP (0.02) but clearly underestimates the effects at lower levels of free-stream turbulence. An alternative empirical factor:

$[1+10/F^2 \exp(-\mathrm{Re}/400)]$, correlates the present data rather better. F is the modified Hancock turbulence parameter, $(u'/U_e)\times 100/(0.5\ L_e/\delta + 2.5)$, mentioned above, so this low Reynolds number factor has the required feature of depending on the free-stream turbulence level as well as the Reynolds number itself. It was chosen entirely empirically, recognizing that it should approach unity as Re_θ tends to about 2000, but that the difference from unity should increase (at constant Reynolds number) for decreasing F (see Fig. 13). In Fig. 14, all the data are plotted on the basis, first, of Hancock's original correlation and, second, using the above modifications. The few data points which corresponded either to "fully-saturated" cases where the wake component had entirely disappeared, or to clearly transitional cases, have been omitted. Figure 14(*b*) shows a clear improvement in the degree of data correlation over the results of Fig. 14(*a*). It must be emphasized, however, that while this correlation does seem to collapse the data reasonably well, it implies no change in the relative effects of intensity and length scale. As discussed earlier, this may not be physically realistic, although any change may be sufficiently minor to make the above correlation, in practice, quite adequate.

The asymptotic values of $\Delta C_f/C_{f0}$ apparently implied by the results in Fig. 7 are somewhat lower than those given by the high Reynolds number data of Hancock. Using the latter to normalize the data of Figs. 13 and 14 does not alter the qualitative trend, although it would imply that Blair's [5] correlation is only adequate for values of FSTP considerably greater than 0.02. It also would imply that changes from the asymptotic value of $\Delta C_f/C_{f0}$ of the order of 30 percent occur by the time Re_θ has fallen to 2000. This is possible but since the few Hancock points for $2000 < \mathrm{Re} < 3000$ do not suggest such behavior and the present few data points for $\mathrm{Re}>2000$ lie noticeably below Hancock's curve (see Fig. 6) there does seem to be a consistent difference between the two data sets. The asympotitic values for $\Delta C_f/C_{f0}$ implied by the present data lie within the scatter of other workers results and are, in fact, very close to the data of Charnay et al. [3], as analyzed by Hancock. It is possible that the various differences, which anyway correspond to measured differences in C_f of only about 2 percent at most, are caused by small differences in three-dimensional effects. Hancock's boundary layers generally had a greater "spanwise aspect ratio" – tunnel width to boundary layer thickness – than that of most other workers, including the present author. No firm explanation for the differences is offered, but we do not believe that they have masked any of the important Reynolds number effects.[1]

A final point concerns the data of Robertson and Holt [2], all of which was obtained for $400 < \mathrm{Re}_\theta < 2000$. While they do not include values of Re_θ for any of their data points, careful scrutiny of the results for $\Delta C_f/C_{f0}$, which they plot against u'/U_e, indicates that the Reynolds number effects are similar to those demonstrated in the present work. C_f was found to vary less at high values of u'/U_e because these were largely obtained from profiles near the leading edge of the plate and hence at the lowest Reynolds numbers. The authors did not distinguish between general measurement scatter and Reynolds number effects, although trends are just apparent in their rather limited data.

5 Conclusions

The major conclusions of the present work can be summarized as follows:

1) In the absence of free-stream turbulence, the measured changes in mean flow variables and the longitudinal turbulence energy as the momentum thickness Reynolds number decreases are similar to those of other recent workers. To that extent at least, they are not inconsistent with the view that most of the Reynolds number effects are due to an increasing influence of the viscous superlayer. The boundary layer becomes relatively more dominated by large scale motions which can be directly linked to the typical ("Falco") eddies near the wall (Antonia et al. [8], Head and Bandyopadhyay [7]).

2) In common with the conclusions of Purtell et al. [14] the outer layer wake component does not decrease as rapidly with decreasing Re_θ as Coles [15] originally suggested. Incomplete development of the boundary layer is reflected in an abnormally high value of the wake component.

3) With the addition of free stream turbulence whose typical length scale is not too dissimilar from the boundary layer thickness, increases in skin friction are lower than those that would occur at higher Reynolds number and the outer layer wake component does not fall so rapidly with decreasing Re_θ. Similarly, Reynolds number effects on outer layer turbulence energy become weaker.

4) The magnitude of these changes depends not only on the Reynolds number itself, but also on the actual level of free stream turbulence. For low levels of the latter, Reynolds number effects are substantial, as they are in the absence of free-stream turbulence. As the level rises, however, the increase in skin friction, the decrease in wake component and the turbulence energy at constant z/δ, all became significantly less dependent on Reynolds number, though never entirely independent, at least within the range of free stream turbulence levels covered in the present experiment.

5) Although the range of length scale ratio covered is quite small ($0.8<L_e/\delta<2.9$), there is some evidence that the relative influences of this ratio and the free-stream intensity

[1] A referee has suggested that the method of tripping the boundary layer may have been a contributory factor to this difference between the two experiments. This is certainly possible but, again, as the same referee acknowledges, the differences are not large enough to obviate our conclusions.

Table 1 Uncertainty estimates for the experimental data

U/U_e,	±0.5 percent	L_e/δ,	±5 percent
$\overline{u^2}/U_e^2$,	±3 percent	H,	±5 percent
u_τ^2/U_e^2,	(α C_f), ±1½ percent	$\Delta C_f/C_{f_0}$,	±15 percent (at $\Delta C_f/C_{f_0}=0.1$)
	$u'/_{U_e}/(0.5L_{e/\delta}+2.5)$, ±3 percent		

changes at low Reynolds numbers. However, the data can be correlated reasonably well on the basis that this is not so.

6) Blairs' [5] modification of Hancocks' [1] free-stream turbulence parameter to take account of low Reynolds number effects appears to work reasonably well for $(u'/U_e)/(L_e/\delta+2) = 0.02$, but certainly does not at lower values. To be consistent with the present data and with the idea that viscous effects in the outer region of the boundary layer must become increasingly less important as the free stream turbulence level rises, any modification to Hancock's parameter must contain an explicit dependence on the free stream turbulence level as well as the Reynolds number. It has been found that the correlation:

$$\Delta C_{f0}/C_{f0}.[1+10/F^2\mathrm{Exp}(-\mathrm{Re}_\theta/400]=f(F),$$

with $F=100\,(u'/U_e)/(0.5L_e/\delta+2.5)$, works quite well for

$$600<\mathrm{Re}_\theta<2000,\ 0.8<L_e/\delta<2.9,\ u'/U_e<0.07.$$

Finally, while these conclusions are, we believe, fully justified on the basis of the present experimental results, it is not yet very profitable to attempt to concoct a more complex correlation parameter to cover the possible effects of changes in the relative importance of free stream intensity and length scale at low Reynolds numbers. Further work, specifically to try to separate the differing influences of intensity and length scale ratio, is required, and conditional sampling techniques could be usefully employed to investigate the way that the low Reynolds number large eddy structures are influenced by free-stream turbulence.

6 Acknowledgments

Helpful discussions with Prof. H. Fernholz and P. Inman are acknowledged, as are the useful comments of Professor P. Bradshaw on a first draft of this paper, and of the referees on the submitted version. The technical expertise of Mr. W. Langley and others in the Department Workshop, without whom the experiements would not have been possible, was invaluable and is also gratefully acknowledged.

References

1 Hancock, P. E., "The Effect of Free Stream Turbulence on Turbulent Boundary Layers," Ph.D. thesis, Imperial College, London, 1980.

2 Robertson, J. M., and Holt, C. F., "Stream Turbulence Effects on Turbulent Boundary Layers," *Proc. ASCE*, Vol. 98, HY6, 1972, p. 1095.

3 Charney, G., Compte-Bellot, G., and Mathieu, J., "Development of a Turbulent Boundary Layer on a Flat Plate in an External Turbulent Flow," AGARD CP 93, Paper No. 27, 1971.

4 Meier, H. U., "The Effects of Velocity Fluctuations and Non-Uniformities in the Free Stream on the Turbulent Layer Development," In *Turbulent Shear Flows*, I. ed. Durst et al., Springer-Verlag, 1977.

5 Blair, "Influence of Free-Stream Turbulence on Boundary Layer Heat Transfer and Mean Profile Development," ASME *Journal of Heat Transfer*, Vol. 105, 1983, p. 41.

6 Murlis, J., Tsai, H. M., and Bradshaw, P., "The Structure of Turbulent Boundary Layers at Low Reynolds Numbers," *J. Fluid Mech.*, Vol. 122, 1982, p. 13.

7 Head, M. R., and Bandyopadhyay, P., "New Aspects of Turbulent Boundary Layer Structure," *J. Fluid Mech.*, Vol. 107, 1981, p. 297.

8 Antonia, R. A., Rajagopalan, S., Subramanian, C. S., and Chambers, A. J., "Reynolds Number Dependence of the Structure of a Turbulent Boundary Layer," *J. Fluid Mech.*, Vol. 121, 1982, p. 123.

9 Huffman, G. D., and Bradshaw, P., "A Note on Von Karman's Constant in Low Speed Turbulent Boundary Layers," *J. Fluid Mech.*, Vol. 53, 1972, p. 45.

10 Patel, V. C., "Calibration of the Preston Tube and Limitations on its Use in Pressure Gradients," *J. Fluid Mech.*, Vol. 23, 1965, p. 185.

11 Brederode, V., and Bradshaw, P., "Influence of the Side Walls on the Turbulent Centre Plane," ASME JOURNAL OF FLUIDS ENGINEERING, Vol. 100, 1978, p. 91.

12 Fernholz, H. H., "Three-Dimensional Disturbances in a Two-Dimensional Incompressible Turbulent Boundary Layer," ARC R&M, 1964, p. 3368.

13 Compte-Bellot, G., and Corrsin, S., "The Use of a Contraction to Improve the Isotropy of Grid-Generated Turbulence," *J. Fluid Mech.*, Vol. 25, 1966, p. 657.

14 Purtell, L. P., Klebanoff, P. S., and Buckley, F. T., "Turbulent Boundary Layer at Low Reynolds Number," *Phys. Fluids*, Vol. 24, 1981, (S), p. 802.

15 Coles, D. E., "The Turbulent Boundary Layer in a Compressible Fluid," Rand Rep. R403-PR, ARC 24473, 1962.

16 Murlis, J., "The Structure of a Turbulent Boundary Layer at Low Reynolds Numbers," Ph.D. thesis, Imperial College London, 1975.

17 Falco, R. E., "Coherent Motions in the Outer Regions of Turbulent Boundary Layers," *Phys. Fluids Suppl.*, Vol. 20, 1977, p. 5124.

18 Hancock, P. E., and Bradshaw, P., "The Effect of Free-Stream Turbulence on Turbulent Boundary Layers," ASME JOURNAL OF FLUIDS ENGINEERING, Vol. 105, 1983, p. 284.

E. Benjamin Wylie
Professor of Civil Engineering,
University of Michigan,
Ann Arbor, MI 48109
Fellow ASME

Simulation of Vaporous and Gaseous Cavitation

A discrete free gas model is presented for numerical simulation of transients in liquids containing free gas. The model is also able to simulate vapor column separation during liquid transient flows in pipelines. The latter application may be the most significant attribute of the model.

Introduction

Free gas distribution throughout liquid in a homogeneous mix in a pipeline yields a wave propagation velocity that is strongly pressure dependent. Lumped pockets of free gas, or free gas trapped along the pipe wall, in pipe joints, in surface roughness, crevices, etc., provide a similar response. Naturally the influence is most significant at low pressures.

Various investigators have modeled this distributed parameter problem by lumping the mass of free gas at computational sections. Each isolated small volume of gas expands and contracts as the pressure varies, in accordance with the perfect gas law. In the same model pure liquid is assumed to exist in the pipeline between each computing section. The model has not been broadly used since, with small quantities of free gas, it provides unrealistic numerical oscillations during positive pressure waves. During the existence of negative waves and small perturbations on the system the procedure generally results in an effective wave speed that matches closely the actual wave speed in the distributed parameter mix.

This paper re-examines this same model and provides a numerical algorithm that yields practical results. The model is effective in treating relatively large gas volumes at low pressures as long as the gas volume is significantly less than the liquid volume between computing sections. At the other extreme, vapor column separation in pipelines may be successfully simulated using this model by utilizing very small quantities of free gas. The latter application may be the most significant attribute of the model.

Initially a discussion is presented of a homogeneous mix of free gas in liquids, the pressure dependent wave speed, and the general dynamic equations. The discrete free gas model is then introduced and applied to examples involving pressure-dependent wave speeds, with the attendant dispersion of the wave front during rarefaction waves, and steepening of the wave front on positive waves. The same model, with low free gas volumes, is then used to simulate vapor column separation. Examples and comparisons are included.

Contributed by the Fluids Engineering Division of THE AMERICAN SOCIETY OF MECHANICAL ENGINEERS and presented at the Applied Mechanics, Bioengineering and Fluids Engineering Conference, Houston, Texas, June 20–22, 1983. Manuscript received by the Fluids Engineering Division, July 25, 1983.

Free Gas in Liquids

Liquids carrying free gas, even in very small volumetric proportions, have a significantly reduced wave-propagation velocity. The fact that this reduced magnitude influences system response during a transient is well documented [4, 9, 11]. As a simplification in modeling, the free gas is assumed to be distributed throughout the pipe as a homogeneous bubbly-fluid mixture with gas bubbles and liquid moving at the same velocity. A void fraction, α, is used to describe the ratio of volume of free gas, V_g, to the mixture volume, V, and, for a given mass of free gas, it is pressure dependent.

$$\alpha = V_g / V \tag{1}$$

Herein only small void fractions at standard conditions are considered.

A review of Dalton's Law and the variables that influence the wave-propagation velocity are first presented, along with the one-dimensional equations to describe the dynamic behavior of the bubbly mixture.

Dalton's Law states that the total pressure exerted by a mixture of gases is equal to the sum of the partial pressures of the various components. If air were the free gas distributed in water in a pipeline the bubbles would contain a mixture of air and water vapor. The total volume occupied by the air would be the same volume as occupied by the water vapor. Dalton's Law is expressed:

$$P^* = P_g^* + P_v^* \tag{2}$$

in which P^* = total absolute pressure, P_g^* = absolute partial pressure of air, and P_v^* = absolute vapor pressure. The partial pressure of the air may be obtained for a given total pressure in equation (2), by subtracting the value of vapor pressure of water at the given temperature, obtained from tabulations in standard references.

For small void fractions isothermal behavior of the free gas is a reasonable assumption. With a given mass of free gas, M_g, and use of the perfect gas law:

$$P_g^* V_g = M_g R_g T \tag{3}$$

and

$$P_v^* V_v = M_v R_v T \tag{4}$$

in which V_g = gas volume, R_g = gas constant, T = absolute temperature, V_v = vapor volume and is equal to the free gas volume, M_v = mass of vapor, and R_v = vapor gas constant. For a constant M_g, equation (3) shows an inverse relationship between the two variables, gas partial pressure and the gas

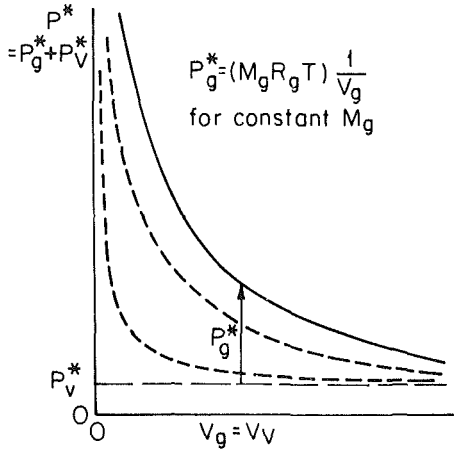

Fig. 1 Gas volume versus absolute pressure

volume. This relationship is shown in Fig. 1 for different values of constant mass of free gas. Also, at a constant temperature, P_v^* is a constant, and the two variables in equation (4), M_v and V_v, are linearly related, i.e., as the gas volume changes so does the mass of vapor.

The wave propagation velocity in a fluid in a pipeline, including the effects of pipe wall elasticity, is given by

$$a' = \left(\frac{K/\rho}{1+KD/Ee}\right)^{1/2} \tag{5}$$

in which K = bulk modulus of elasticity of the fluid, ρ = mass density of the fluid, D = pipe inside diameter, e = pipe wall thickness, and E = modulus of elasticity of the pipe wall material (14). The evaluate the wave speed as a function of mass of free gas or void fraction, and pressure, it is necessary to consider K and ρ. By defining $m = M_g/V$, the mass of free gas per unit volume of mixture, equation (3) may be rearranged to show the void fraction to vary inversely with the absolute partial pressure of the gas.

$$\alpha = mR_gT/P_g^* \tag{6}$$

The dependence of K on void fraction and pressure (14) is given by:

$$K = K_l/[1+\alpha(K_l/P_g^*-1)] \tag{7}$$

The subscript l refers to the liquid component of the mixture. With the isothermal assumption $K_g = P_g^*$. For practical transient problems $K_l/P_g^* >> 1$ so the denominator of equation (7) becomes $1 + \alpha K_l/P_g^*$. The mass density of the mixture can be assumed the same as that of the liquid ($\rho \sim \rho_l$) since small void fractions are being considered. With these assumptions equation (5) may be expressed (10, 14)

$$a' = a/(1+C_2m/P_g^{*2})^{1/2} \tag{8}$$

in which a is the wavespeed in the liquid without free gas in the pipe, and

$$C_2 = R_gTK_l/(1+K_lD/Ee) \tag{9}$$

Graphical representations of equation (8) have been presented elsewhere [12, 14]. Although the equation is developed for small void fractions, $\alpha < 2$ percent, it is known to be reasonably accurate for much higher void fractions [5].

In dealing with free air in water, use of the hydraulic grade line is convenient.

$$P_g^* = \rho g(H-Z-H_v) \tag{10}$$

The hydraulic grade line elevation, H, and the elevation of the pipeline, Z, are measured from the same reference datum, and H_v is the gage vapor pressure, $H_v = P_v^*/\rho g - H_b$, H_b = barometric pressure. Equation (10) may be substituted into equation (8).

The one-dimensional equations to describe the dynamic behavior of the bubbly mixture are the Equations of Motion and Continuity (14).

$$Q_t + gAH_x + fQ^2/2DA = 0 \tag{11}$$

$$H_t + a'^2Q_x/gA = 0 \tag{12}$$

In these equations Q = volumetric flow rate, f = Darcy Weisbach friction factor, A = pipeline area, and subscripts x and t denote partial differentiation with respect to the independent variables, position and time.

The method of characteristics may be used to transform the equations to four ordinary differential equations, without approximation.

$$\pm\frac{gA}{a'}\frac{dH}{dt} + \frac{dQ}{dt} + \frac{fQ^2}{2DA} = 0 \tag{13}$$

$$\frac{dx}{dt} = \pm a' \tag{14}$$

An exact integration of these equations is not possible due to the strong dependence of the wave speed on the variable hydraulic grade line elevation [12, 14]. Therefore, utilizing these equations in a numerical solution involves approximations that could lead to inaccurate results.

Discrete Free Gas Volumes

An alternative to modeling free gas distributed throughout

Nomenclature

A = pipeline area
a = wave propagation velocity
a' = wave propagation velocity in two-phase mixture
B = pipeline impedance, a/gA
B_1 = constant
C_1, C_2 = constants
C_3, C_4 = constants
C_M, C_P = constants in compatibility equations
D = pipeline diameter
E = modulus of elasticity of pipe material
e = pipe wall thickness
f = Darcy Weisbach friction factor
g = acceleration due to gravity
H = piezometric head
L = pipeline length
M = mass
m = mass of free gas present per unit volume of mixture
N = number of reaches in pipeline
P^* = absolute pressure
Q = volumetric flow rate
R = gas constant
T = absolute temperature
t = time
V = volume
Z = pipeline elevation
α = void fraction
ρ = mass density
ψ = weighting factor

Subscripts

b = barometric pressure
g = gas
l = liquid
o = reference condition, or initial condition
t = time
v = vapor
x = distance

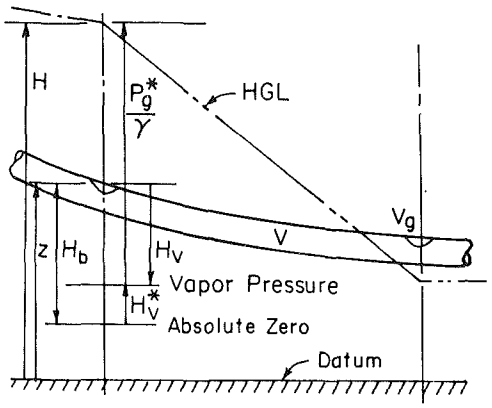

Fig. 2 Discrete free gas volume in pipeline

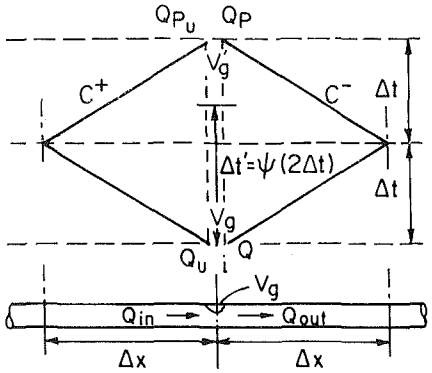

Fig. 3 Staggered grid of characteristics

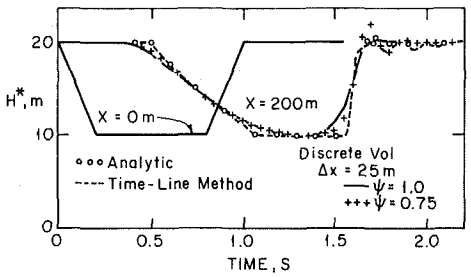

Fig. 4 Pressure head response in infinite pipeline. x = 200 m.

the liquid in a homogeneous mix can be achieved by lumping the mass of free gas at computing sections [1, 2, 7, 10]. Each isolated small volume of gas expands and contracts isothermally as the pressure varies, in accordance with the perfect gas law. Between each computing section, or concentrated gas volume, pure liquid is assumed without free gas. By lumping the same amount of free gas at discrete locations as is actually distributed in contiguous reaches, implementation of the procedure results in an effective wave propagation velocity that matches closely the actual wave speed in the distributed mix. Liquid mass conservation is preserved at each gas volume by applying a local continuity relationship. In inertia-dominated transient problems when the pressure is reduced to near vapor pressure, large gas volumes may exist at computing sections. As long as the gas volume is much less than the liquid volume between sections the model is reasonable, and varying degrees of success have been reported by different authors.

Numerical Model. Figure 2 shows a pipeline with concentrated gas volumes at computing sections. The amount of free gas concentrated at each section is determined by coalescing the distributed gas from the adjacent reach to a point. If α_0 is the void fraction at some reference pressure, P_0^*, for a constant mass of free gas, equation (3) may be used to express

$$M_g R_g T = P_g^* \alpha V = P_0^* \alpha_0 V \tag{15}$$

Since V, the volume of mix in the adjacent reach, is a constant equations (3) and (10) may be used to determine the volume of gas at each section for initial conditions, and at each time step:

$$V_g = \frac{C_1}{P_g^*} = \frac{C_3}{H - Z - H_v} \tag{16}$$

in which $C_1 = P_0^* \alpha_0 V$, and $C_3 = C_1/\rho g$.

Figure 3 shows a staggered grid of characteristics at the gas volume at an interior point in the pipeline. The equations needed to solve for the variables at each time step are: the C^+ compatibility equation

$$H = C_P - BQ_{Pu} \tag{17}$$

the C^- compatibility equation

$$H = C_M + BQ_P \tag{18}$$

and a continuity equation at the gas volume

$$\frac{dV_g}{dt} = Q_{\text{out}} - Q_{\text{in}} \tag{19}$$

Equation (19) must be integrated to be used in the numerical solution. A weighting factor is used in the time direction as shown in Fig. 3 and defined:

$$\psi = \frac{\Delta t'}{2\Delta t} \quad 0 < \psi \leq 1 \tag{20}$$

Integration of equation (19) yields

$$V_g' = V_g + [\psi(Q_P - Q_{Pu}) + (1-\psi)(Q - Q_u)]2\Delta t \tag{21}$$

in which V_g' and V_g = gas volumes at the current time and $2\Delta t$ earlier, respectively. The factor, $2\Delta t$, appears in this formulation as a result of the use of the staggered grid. The simultaneous solution of equations (16)–(18) and (21) gives

$$H = \frac{-B_1 + 2(Z + H_v) + \{[B_1 + 2(Z + H_v)]^2 + 8C_4\}^{1/2}}{4} \tag{22}$$

in which $C_4 = (C_3\ B)/(2\Delta t\psi)$ and $B_1 = -C_M - C_P + B[V/(2\Delta t) + (1-\psi)(Q - Q_u)]/\psi$. The compatibility equations and continuity equation should be used to find Q_{Pu}, Q_P, and V_g', respectively.

The weighting factor ψ is introduced to control the numerical oscillations that appear during simulation of transients that involve pressurization of the gas bubbles. Values of ψ between zero and 0.5 produce unstable results; at $\psi = 0.5$ some oscillations are likely to appear in the numerical results, particularly during positive waves on small gas volumes; as ψ approaches unity there is slightly more spreading of rarefaction waves and more than normal attenuation, however, at $\psi = 1$, there is no numerical oscillation. A value close to 0.5, that does not produce severe oscillations, is recommended for practical use.

These features are illustrated in the following examples.

Example 1. A frictionless pipeline example is used to demonstrate the wave speed variation with pressure in a liquid system with free gas, and to compare results from the discrete gas model with other methods. An imposed pressure history is used to excite an infinite pipeline of the following characteristics (12): $D = 0.61$m, $f = 0.0$, $Q_0 = 0.89$ m^3/s, $a = 1000$m/s, $\rho = 1000$ kg/m^3, $H_0^* = 20$ m, $\alpha_0 = 0.2$ percent at standard conditions, and $\Delta x = 25$ m. The forcing function at $x = 0$ is shown in Fig. 4 along with the response, by several methods, at $x = 200$ m. Results from the analytic and time-line methods were presented in an earlier publication [12]. The

spreading of the wave of pressure reduction is apparent at 200 m, as is the steepening of the positive wave. The analytic method is "exact" for the negative dispersive wave but is unable to handle the formation of the steep pressure front associated with the positive wave. The time-line interpolation method [12] yields a reasonably accurate response during the duration of the wave passage at 200 m, however it shows oscillation following the passage of the wave. The discrete gas model shows reasonable agreement with $\psi = 1$, although it yields greater dispersion than the other methods. With $\psi = 0.75$ slightly better agreement is obtained but a significant oscillation is introduced after passage of the positive wave.

Example 2. Numerical damping introduced by forward integration is illustrated in an example in a horizontal frictionless pipeline. The pipeline data are (7,12): $D = 0.61$ m, $L = 3000$ m, $f = 0.0$, $Q = 0.89$ m^3/s, $a = 981.4$ m/s, $\rho = 982$ kg/m^3, $H_0^* = 0.2$ percent free gas, $T = 288$ K, $R = 287$ mN/kgK. A reservoir exists at the downstream end of the pipeline. The transient is introduced by lowering the upstream head from 60 to 30 m instantaneously and holding it at that level for the duration of the transient [7]. Figure 5 shows results from analyses with three different values of the forward integration parameter, each with $\Delta x = 100$ m, $\psi = 0.51$, 0.75, and 1.0. The first shows evidence of a high frequency oscillation, which is completely dampened out in the other two cases. The numerical damping associated with forward integration is clear in the latter two cases.

Vapor Column Separation

When the pressure drops to vapor pressure in a liquid in a pipeline during transient flows, vaporization occurs. Vapor bubbles may be physically dispersed homogeneously, or collected into single or multiple void spaces, or a combination of the two. The result is referred to as vapor column separation, and gives rise to a reduction of the effective wave speed through the system, much as free gas influences wave speed. A standard analysis procedure [3, 8, 14] permits vapor cavities to form only at computing sections in the method of characteristics. Although the method is easily implemented, and faithfully reproduces many of the essential features of a physical event, it has a serious deficiency. Numerical oscillations are generated during the existence of multi-cavities in the pipeline. They tend to persist in a simulation and may result in unrealistic pressure spikes that discredit the overall value of results. Continuity and momentum principles are satisfied in the system however, and generally wave patterns are maintained if some averaging scheme is imposed; only high frequency numerical oscillations foul the numerical records. The source of the semi-random fluctuations is wave reflections off multi-cavities in the system, the latter effectively becoming fixed pressure boundaries. In this section the discrete gas model is presented as an alternative formulation to improve reliability of numerical modeling of vapor column separation. It is also suggested for cases of combined vaporous and gaseous cavitation.

Close examination of equation (8), or a graph of wave speed vs. absolute pressure at various void fractions [10, 12, 14], shows that if the void fraction, α_0, is less than 10^{-7}, there is little change in wave speed due to the presence of the free gas, even at low pressures. Therefore, if the discrete model, with α_0 less than 10^{-7}, were used to simulate a transient in a liquid the results should not be different from those that would be obtained by using a liquid without free gas. Such is the case. Moreover the discrete gas model can accommodate vaporous volumes as well, if the dynamics of the physical problem cause the liquid to vaporize. Thus vapor column separation can be modeled within the same simulation framework. Examples are used to illustrate.

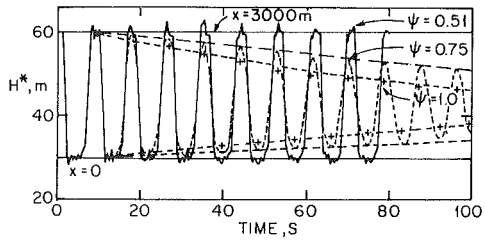

Fig. 5 Pressure head response in 3000 m pipeline. $x = 1200$ m.

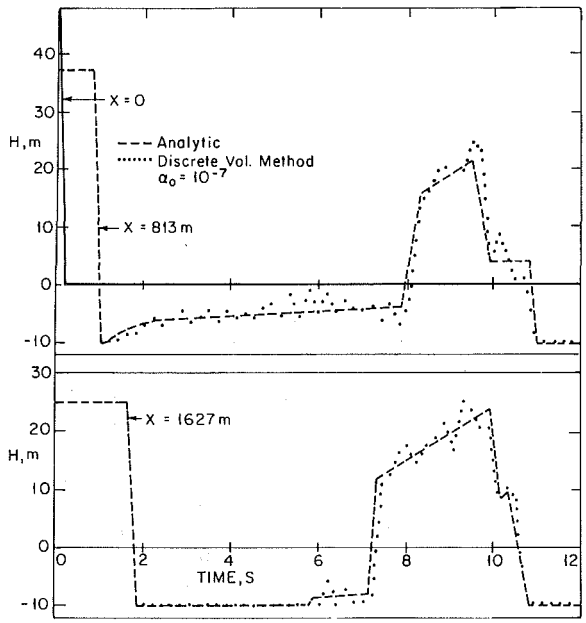

Fig. 6 Example 3, pressure head versus time at two locations

Example 3. A comparison is made with an analytical solution to a problem of vaporous cavitation in a horizontal pipeline [13]. The system data are: $D = 610$ mm, $L = 3048$ m, $f = 0.02$, $Q_0 = 0.89$ m^3/s, $a = 981$ m/s, $\rho = 1000$ kg/m^3, $H_v = -10.06$ m. At the upstream end the pressure is dropped linearly from the initial value of 50.38 m to zero in 0.20 s, and held at that level for the duration of the simulation. The rarefaction wave due to the pressure reduction, travels down the pipeline following the hydraulic gradeline until vapor pressure is reached; the wave then continues to the downstream reservoir where a positive reflection occurs. Behind the initial rarefaction wave vapor pressure exists and the fluid develops a void fraction filled with water vapor.

Figure 6 presents the analytical results as a function of time at two locations along the pipeline [13]. In addition, results from the discrete volume model, with $\alpha_0 = 10^{-7}$ at standard conditions, $N = 30$, $\psi = 1.0$, are presented. Although some oscillations are present, agreement in magnitude and timing of the transient events is apparent. Only minor modifications in these numerical results appeared with $\psi = 0.90$, or with $\psi = 0.75$, or with smaller void fractions. Numerical results from a discrete vapor cavity model do not provide as favorable comparison with the analytical results (13) as the discrete gas model in Fig. 6.

Example 4. Experimental results from the Delft Hydraulics Laboratory, simulating pump failure and restarting of the pump at the upstream end of a horizontal test pipeline, have been reported in the literature (4, 6). At the upstream end a pressure-time pattern is specified to simulate the pump behavior. A large pressure tank provides a constant downstream pressure. The system data includes: $D = 0.10$ m,

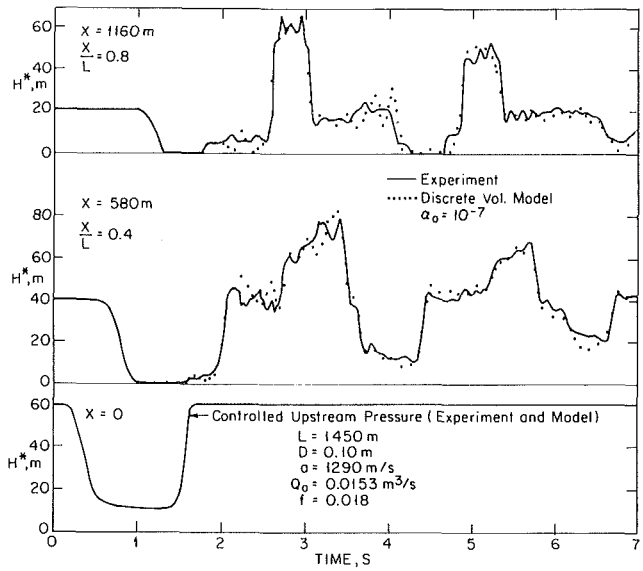

Fig. 7 Column separation in horizontal pipeline

$L = 1450$ m, $f = 0.018$, $Q_0 = 0.0158\ m^3/s$, $a = 1290$ m/s, $\rho = 1000\ kg/m^3$, $H_R^* = 60.2$ m, $Z = 0.0$ m, $H_v = -10.10$ m, $\alpha_0 = 10^{-7}$ at standard conditions, $N = 20$ with staggered grid.

Figure 7 shows the experimental record at $x = 0.4\ L$ and at $x = 0.8\ L$, as well as the upstream controlled pressure. In addition, the numerical results from the discrete gas volume model are presented with $\psi = 1.0$. Agreement is acceptable with only minor pressure oscillations. The same experimental results have been compared with numerical results from a vapor column separation model (no free gas other than water vapor) in the literature [14]. Although the timing of the positive and negative waves with the discrete vapor cavity model follow the experimental record quite closely, unrealistic pressure spikes dominate the response. Thus the presence of the small discrete gas volumes and the forward-weighting integration scheme, in the discrete gas model, Fig. 7, provide adequate numerical damping to reduce the random pressure excursions to a tolerable level while still maintaining the dominate features in the transient.

Conclusions

A discrete free gas model has been presented for improved modeling in the simulation of both vaporous and gaseous cavitation. Gaseous cavitation refers to situations in which free gas is either distributed throughout the liquid in a homogeneous mix, or is trapped at various positions in the system. Vaporous cavitation refers to cases in which the pressure level in portions of the system drops to vapor pressure of the liquid, causing the liquid to vaporize. The numerical model assumes discrete volumes of free gas at computing sections: in the case of gaseous cavitation the volumes are exactly equal to the actual free gas volume distributed in the physical system; in the case of vaporous cavitation only, void fractions of 10^{-7} or less are assumed. An effective wave speed is generated in the discrete gas model that closely matches the actual wave propagation velocity in the physical system.

The model is effective in treating relatively large gas volumes at low pressures. At the other extreme, vapor column separation in pipelines may be successfully simulated using this model by utilizing very small quantities of free gas. Again the model is effective in treating relatively large vapor cavities. The applications to vapor column separation may be the most significant attribute of the model.

Acknowledgment

The investigation described herein was supported by National Science Foundation Grant No. CEE 8120934 to The University of Michigan.

References

1 Brown, R. J., "Water-Column Separation at Two Pumping Plants," ASME *Journal of Basic Engineering*, Vol. 90, 1968, pp. 521-531.

2 Enever, K. J., "Surge Pressures in a Gas-Liquid Mixture with a Low Gas Content," *Proc. First Int. Conf. on Pressure Surges*, BHRA, Canterbury, Sept. 6-8, 1972, pp. 1-11.

3 Kot, C. A., and Youngdahl, C. K., "The Analysis of Fluid Transients in Piping Systems, Including the Effects of Cavitation," ASME, *Proc. Conf. on Fluid Transients and Acoustics in the Power Industry*, San Francisco, 1978, pp. 45-52.

4 Kranenburg, C., "Gas Release During Transient Cavitation in Pipes," *J. Hyd. Div.*, ASCE, Vol. 100, No. HY 10, Oct., 1974, pp. 1383-1398.

5 Martin, C. S., and Padmanabhan, M., "Pressure Pulse Propagation in Two-Component Slug Flow," ASME JOURNAL OF FLUIDS ENGINEERING, Vol. 101, Mar. 1979, pp. 44-52.

6 Provoost, G. A., "Investigation into Cavitation in a Prototype Pipeline Caused by Water-Hammer," *Proc. Second Int. Conf. on Pressure Surges*, BHRA, London, Sept. 22-24, 1976.

7 Provoost, G. A., and Wylie, E. B., "Discrete Gas Model to Represent Distributed Free Gas in Liquids," Fifth Int. Symp. on Column Separation, Obernach, Germany, Sept., 1981, 8 pp.

8 Streeter, V. L., "Unsteady Flow Calculations by Numerical Methods," ASME *Journal of Basic Engineering*, June, 1972, pp. 457-466.

9 Swaffield, J. A., "A Study of the Influence of Air Release on Column Separation in an Aviation Kerosene Pipeline," *Proc. Inst. of Mech. Eng.*, Vol. 186, 56/72, 1972, pp. 693-703.

10 Tullis, J. P., Streeter, V. L., and Wylie, E. B., "Waterhammer Analysis with Air Release," *Proc. Second Int. Conf. on Pressure Surges*, BHRA, Cranfield, Sept. 22-24, 1976.

11 Wiggert, D. C. and Sundquist, M. J., "The Effect of Gaseous Cavitation on Fluid Transients," ASME JOURNAL OF FLUIDS ENGINEERING, Vol. 101, Mar. 1979, pp. 79-86.

12 Wylie, E. B., "Free Air in Liquid Transient Flow," *Proc. Third Intern. Conf. on Pressure Surges*, BHRA, Cranfield, Mar. 1980, pp. 27-42; Closing Discussion, Vol. 2, pp. 519-524.

13 Wylie, E. B., and Streeter, V. L., "Column Separation in Horizontal Pipelines," *9th IAHR Symp. on Fluid Mechanics*, Fort Collins, CO, June 1978.

14 Wylie, E. B., and Streeter, V. L., *Fluid Transients*, FEB Press, Ann Arbor, MI, 1983.

Tetsuo Nishiyama
Professor,
Department of Mechanical Engineering,
Tohoku University,
Sendai, Japan

Hideya Nishiyama
Postgraduate,
Graduate School of Engineering,
Tohoku University,
Presently, Research Assistant,
Akita University,
Akita, Japan

Dynamic Responses of Partially Cavitated Hydrofoil Cascade to Axial Gust in Bubbly Water

A method for analysis by singularity representations is presented for dynamic responses of partially cavitated hydrofoil cascade to axial gust in bubbly water. Conservation laws of mass and momentum are applied to take account of the unsteady parts of cavity area, cavity termination thickness, and cavity pressure for unsteady partial cavity model. Also, the cavitation compliance and mass flow gain factor obtained from the cavity model determined are considered in relations to cavity length, reduced frequency, and air volume ratio. Comparisons of the mean unsteady pressure rise and unsteady discharge difference are also made with the available former results.

1 Introduction

With the notable increases of rotational speed and also remarkable improvements of suction performance for rocket pumps with inducer and industrial turbo-pumps, it is desirable to clarify the instability mechanism and also the dynamic responses of a closed pipeline system including pumps under cavitation. Former analytical treatments on dynamic responses may be categorized to two standpoints of view: One by Kim [1] and Brennen [2] examined the dynamic responses of the cavitated hydrofoil cascade to purely time varying axial gust. However, since neglecting the unsteady part of cavity area and beside treating the chord length as semi-infinite, there still remain further careful reexaminations for their analytical results. The other by Brennen [3] and Kolesnikov [4] examined the dynamic transfer characteristics of the cavitated hydrofoil cascade in bubbly water, particularly the compressibility effects. Since assuming the perturbed flows as one dimensional, they cannot fully consider the unsteady two dimensional compressibility effects in cascade.

Against these backgrounds, the present paper aims to propose a more reliable analytical method for frequency responses and dynamic transfer characteristics of the partially cavitated hydrofoil cascade to axial gust in bubbly water. Thus the serious effects of air contents are clarified through some concrete numerical examples on the cavitation compliance and mass flow gain factor, both of which constitute important elements of transfer matrix, and also comparisons are made with the former analysis and available measured data on mean unsteady pressure rise.

2 Governing Equation

Since the real bubbly flow is of very complicated nature, we introduce here some assumptions which are at least amenable to dynamic analysis:

(i) The air is mixed homogeneously with the water and distributed uniformly in dispersed form of infinitely small bubbles.

(ii) The air within the infinitely small bubbles is regarded as a free gas and also there is no slip velocity and no thermal exchange between two phases.

Then the averaged local density of bubbly water is given by

$$\rho = \frac{1+\mu}{1+\theta}\rho_w ; \mu = \frac{m_a}{m_w}, \theta = \frac{V_a}{V_w} \tag{1}$$

in which μ and θ denote the mass and volume ratio, respectively, and the suffix a and w show the corresponding ones in pure air and water. The relation between the local pressure and averaged local air volume ratio is given by [5]

$$p\theta^{1+\epsilon} = \text{constant} \ ; \ 1+\epsilon = \frac{C_w + \mu C_p}{C_w + \mu C_v} \tag{2}$$

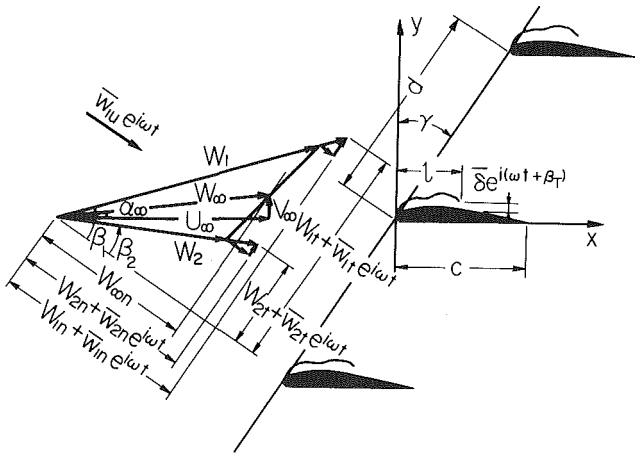

Fig. 1 Partially cavitated hydrofoil cascade in bubbly water of axial gust

Contributed by the Fluids Engineering Division for publication in the JOURNAL OF FLUIDS ENGINEERING. Manuscript received by the Fluids Engineering Division, January 30, 1981.

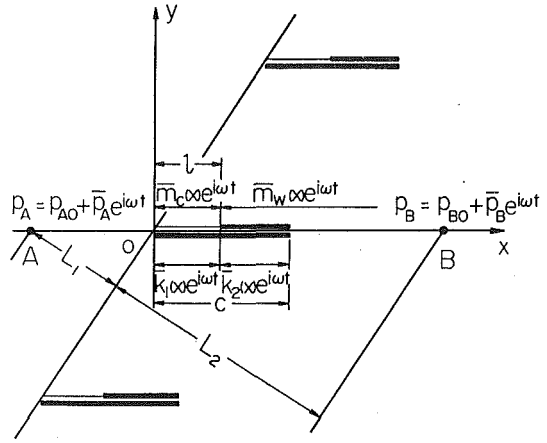

Fig. 2 Representation of flow by singularity distributions

in which C_w denotes a specific heat of the water and C_p, C_v a specific heat at constant pressure and volume of the air, respectively. Then the local acoustic velocity of bubbly water is given by, from equations (1) and (2)

$$a^2 = \frac{dp}{d\rho} = \frac{1+\epsilon}{1+\mu} \cdot \frac{p}{\rho_w} \cdot \frac{(1+\theta)^2}{\theta} \tag{3}$$

When taking x-axis parallely and y-axis normally to the reference velocity U_∞ in two dimensional bubbly water flows of static pressure p_∞ and air volume ratio θ_∞, and also denoting the perturbed steady and unsteady velocities, pressure and density by $(u, v; \tilde{u}, \tilde{v})$, $(p, \tilde{p})$, $(\rho, \tilde{\rho})$ respectively, the governing equation derived from the linearized continuity equation and Euler's equation of motion is, for the perturbed velocity potential

$$(1-M_\infty^2)\frac{\partial^2\tilde{\phi}}{\partial x^2} + \frac{\partial^2\tilde{\phi}}{\partial y^2} - \frac{1}{a_\infty^2}\frac{\partial^2\tilde{\phi}}{\partial t^2} - 2\frac{M_\infty}{a_\infty}\frac{\partial^2\tilde{\phi}}{\partial t \partial x} = 0 \tag{4}$$

in which

$$a_\infty^2 = \frac{1+\epsilon}{1+\mu}\frac{p_\infty}{\rho_\omega}\cdot\frac{(1+\theta_\infty)^2}{\theta_\infty}\ ,\ M_\infty = \frac{1}{1+\theta_\infty}\sqrt{\frac{\theta_\infty}{p_\infty/\rho_\omega U_\infty^2}} \tag{5}$$

And also the unsteady Bernoulli's equation is given by, for the bubbly water of small air volume ratio of practical interest

$$\frac{\partial\tilde{\phi}}{\partial t} + \frac{1}{2}[(U_\infty+u+\tilde{u})^2 + (V_\infty+v+\tilde{v})^2] + \frac{p_\infty+p+\tilde{p}}{(1+\mu)\rho_w} [1+(\theta_\infty+\theta+\tilde{\theta})ln(p_\infty+p+\tilde{p})] = \text{constant} \tag{6}$$

3 Unsteady Perturbed Velocities

A rectilinear cascade of pitch chord ratio d/c and stagger angle γ in partial cavitation of steady length l_0 is assumed to be of unsteady cavity length l in axial gust $\bar{w}_{1u}e^{i\omega t}$, as shown in Fig. 1. Since the unsteady perturbed flow quantities can be put

$$\tilde{u} = \bar{u}e^{i\omega t}, \tilde{v} = \bar{v}e^{i\omega t}, \tilde{p} = \bar{p}e^{i\omega t}, \tilde{\rho} = \bar{\rho}e^{i\omega t}, \tilde{\phi} = \bar{\phi}e^{i\omega t} \tag{7}$$

we hereafter omit $e^{i\omega t}$ in each terms for brevity.

Now we are here interested in the bubbly water flow in which the Mach number obtained by equation (5) from the air volume ratio and static pressure coefficient is smaller than one, that is, subsonic. Representing the perturbed flow field by singularities – pressure doublets $\bar{K}_1$, $\bar{K}_2$ and sources $\bar{m}_c$, $\bar{m}_w$ distributed over the range as shown in Fig. 2, then the unsteady perturbed velocity potential by the partially cavitated cascade can be obtained from equation (4)

$$\begin{aligned}\bar{\phi}(x,y) = {} & \frac{i}{4U_\infty\beta}\left\{\int_0^l \bar{K}_1(\xi) + \int_l^1 \bar{K}_2(\xi)\right\} \\ & \sum_{-\infty}^{\infty} e^{-ik(x-\xi-nB)} d\xi \int_{-\infty}^{x} e^{\frac{ik}{\beta^2}(X-\xi-nB)} \frac{\partial}{\partial y}\{H_0^{(2)}(w_n)\}dX \\ & + \frac{i}{4\beta}\left\{\int_0^l \bar{m}c(\xi) + \int_l^\infty \bar{m}_w(\xi)\right\} \\ & \sum_{-\infty}^{\infty} H_0^{(2)}(w_n) e^{\frac{ikM_\infty^2}{\beta^2}(x-\xi-nB)} d\xi\end{aligned} \tag{8}$$

in which k is a gust reduced frequency defined by $\omega c/U_\infty$ and the length is normalized by chord.

$$B = \frac{d}{c}\sin\gamma, H = \frac{d}{c}\cos\gamma; q_1 = \frac{\beta H}{B^2+\beta^2H^2}, q_2 = \frac{B}{B^2+\beta^2H^2}$$

$$w_n = \eta\sqrt{(n+\nu)^2+\lambda^2}; \nu = -\{q_2(x-\xi)+\beta q_1 y\},$$

$$\lambda = |q_1(x-\xi)-\beta q_2 y|,\ \eta = \frac{kM_\infty}{\beta^2}\sqrt{B^2+\beta^2H^2}$$

$$\beta = \sqrt{1-M_\infty^2}; H_0^{(2)} = \text{Hankel function}$$

Hence equation (8) yields the unsteady perturbed velocities on x-axis like

$$\left.\begin{aligned}\bar{u}(x,\pm 0) &= \pm\frac{\bar{K}_1(x)}{2U_\infty} \mp \frac{ik}{2}\int_0^x \frac{\bar{K}_1(\xi)}{U_\infty} e^{-ik(x-\xi)}d\xi + \bar{u}_0(x) \\ \bar{v}(x,\pm 0) &= \pm\frac{\bar{m}_c(x)}{2} + \bar{v}_0(x)\end{aligned}\right\}, 0 \le x \le l$$

$$\left.\begin{aligned}\bar{u}(x,\pm 0) &= \pm\frac{\bar{K}_2(x)}{2U_\infty} \mp \frac{ik}{2}\left\{\int_0^l \frac{\bar{K}_1(\xi)}{U_\infty} + \int_l^x \frac{\bar{K}_2(\xi)}{U_\infty}\right\} e^{-ik(x-\xi)}d\xi + \bar{u}_0(x) \\ \bar{v}(x,\pm 0) &= \pm\frac{\bar{m}_w(x)}{2} + \bar{v}_0(x)\end{aligned}\right\}, l \le x \le c \tag{9}$$

where

$$\begin{pmatrix}\bar{u}_0(x)\\ \bar{v}_0(x)\end{pmatrix} = \left\{\int_0^l \frac{\bar{K}_1(\xi)}{U_\infty} + \int_l^1 \frac{\bar{K}_2(\xi)}{U_\infty}\right\}\begin{pmatrix}E(x-\xi,0)\\ F(x-\xi,0)\end{pmatrix}d\xi$$

$$+\left\{\int_0^l \bar{m}_c(\xi) + \int_l^\infty m_w(\xi)\right\}\begin{pmatrix}L(x-\xi,0)\\ M(x-\xi,0)\end{pmatrix}d\xi \tag{10}$$

$$
\left.
\begin{aligned}
E(x-\xi,0) &= -\frac{i}{2}\left\{e^{\frac{ikM_\infty^2}{\beta^2}(x-\xi)}(q_1H_3-\mathrm{Sgn}\,|x-\xi|\,iq_2H_1)\right.\\
&\left.-ike^{-ik(x-\xi)}\int_{-\infty}^{x-\xi}e^{\frac{ikx}{\beta^2}}(g_1H_3-\mathrm{Sgn}\,|x|\,ig_2H_1)dX\right\}\\
F(x-\xi,0) &= -\frac{\beta}{2}\left\{e^{\frac{ikM_\infty^2}{\beta^2}(x-\xi)}(\mathrm{Sgn}\,|x-\xi|\,q_1H_1-iq_2H_3)\right.\\
&\quad+\frac{ikM_\infty^2}{\beta^2}e^{\frac{ikM_\infty^2}{\beta^2}(x-\xi)}H_2-ike^{ik(x-\xi)}\\
&\quad\left.\int_{-\infty}^{x-\xi}e^{\frac{ikx}{\beta^2}}(\mathrm{Sgn}\,|x|\,q_1H_1-iq_2H_3)dx\right\}\\
L(x-\xi,0) &= \frac{1}{2\beta}e^{\frac{ikM_\infty^2}{\beta^2}(x-\xi)}\left\{\mathrm{Sgn}\,|x-\xi|\,q_1H_1-iq_2H_3\right.\\
&\quad\left.-ik\frac{M_\infty^2}{\beta^2}H_2\right\}\\
M(x-\xi,0) &= -\frac{i}{2}e^{\frac{ikM_\infty^2}{\beta^2}(x-\xi)}\{q_1H_3-\mathrm{Sgn}\,|x-\xi|\,iq_2H_1\}
\end{aligned}
\right\} \tag{11}
$$

with

$$
H_1=\sum_{-\infty}^{\infty}h_m,\ H_2=\sum_{-\infty}^{\infty}\frac{h_m}{\sqrt{(g+2\pi m)^2-\eta^2}},
$$

$$
H_3=\sum_{-\infty}^{\infty}\frac{g+2\pi m}{\sqrt{(g+2\pi m)^2-\eta^2}}h_m:\ g=-\frac{kM_\infty^2B}{\beta^2}
$$

$$
h_m=\exp\{-i\nu(g+2\pi m)-\lambda\sqrt{(g+2\pi m)^2-\eta^2}\}
$$

As is clear from equation (9), the unsteady perturbed velocities depend strongly on the unsteady partial cavity model. Thus we hereafter decide analytically the unsteady cavity model so as to be capable of taking account of the unsteady part of cavity termination thickness, cavity area and cavity pressure.

4 Conservation Laws of Mass and Momentum

When denoting the ordinate of hydrofoil back, steady cavity and unsteady one by $y_b(x)$, $y_c(x)$ and $\bar{y}_c(x)e^{i\omega t}$ respectively, then the cavity area is given by

$$
S_{(t)}=S_0+\bar{S}e^{i\omega t};S_0=\int_0^{l_0}(y_c(x)-y_b(x))\,dx,\ \bar{S}=\int_0^{l}\bar{y}_c(x)\,dx \tag{12}
$$

Since the kinematical condition on the unsteady cavity streamline is given by

$$
ik\bar{y}_c(x)+\frac{d\bar{y}_c(x)}{dx}=\frac{\bar{v}_c}{U_\infty};0<x<l \tag{13}
$$

then we have the unsteady cavity thickness like

$$
\bar{y}_c(x)=e^{-ikx}\int_0^x\frac{\bar{v}_c}{U_\infty}e^{ik\xi}d\xi \tag{14}
$$

Thus the unsteady discharge through the cavity is, from equation (13)

$$
\frac{\bar{Q}}{U_\infty c}=\int_0^l\frac{\bar{v}_c}{U}d\xi=ik\bar{S}+\bar{y}_c(l) \tag{15}
$$

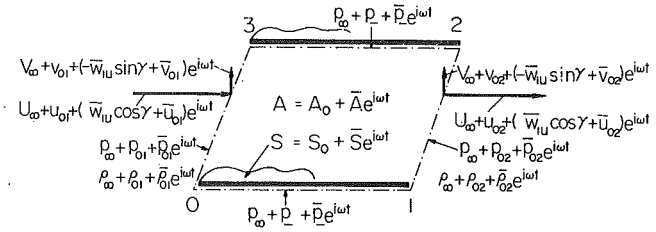

Fig. 3 Control surface

which shows an interrelation between the unsteady parts of the discharge, cavity area and cavity termination thickness.

Since the unsteady downstream velocity ($\bar{w}_{2n}$, $\bar{w}_{2t}$) as shown in Fig. 1 are of arbitrariness depending on the unsteady parts of cavity termination thickness and cavity area, we determine explicitly it so as to satisfy the conservation laws of mass and momentum. Thus, applications of the conservation laws of mass and momentum in y-direction to control surface as shown in Fig. 3 yield, respectively

$$
\begin{aligned}
&\int_1^2(\rho_\infty+\rho_{02}+\bar{\rho}_{02}e^{i\omega t})[\{U_\infty+u_{02}+(\bar{w}_{1u}\cos\gamma+\bar{u}_{02})e^{i\omega t}\}dy\\
&-\{V_\infty+v_{02}+(-\bar{w}_{1u}\sin\gamma+\bar{v}_{02})e^{i\omega t}\}dx]\\
&+\int_3^0(\rho_\infty+\rho_{01}+\bar{\rho}_{01}e^{i\omega t})[\{U_\infty+u_{01}+(\bar{w}_{1u}\cos\gamma+\bar{u}_{01})e^{i\omega t}\}dy\\
&-\{V_\infty+v_{01}+(-\bar{w}_{1u}\sin\gamma+\bar{v}_{01})e^{i\omega t}\}dx]\\
&+\frac{\partial}{\partial t}\int\int_A(\rho_\infty+\rho+\bar{\rho}e^{i\omega t})\,d(cd\cos\gamma-S_0-\bar{S}e^{i\omega t})=0
\end{aligned}
\tag{16}
$$

$$
\begin{aligned}
&\frac{\partial}{\partial t}\int\int_A(\rho_\infty+\rho+\bar{\rho}e^{i\omega t})\{V_\infty+v+(-\bar{w}_{1u}\sin\gamma+\bar{v})e^{i\omega t}\}\\
&d(cd\cos\gamma-S_0-\bar{S}e^{i\omega t})-\int_3^0(p_\infty+p_{01}+\bar{p}_{01}e^{i\omega t})\,dx\\
&-\int_0^1(p_\infty+p_-+\bar{p}_-e^{i\omega t})\,dx-\int_1^2(p_\infty+p_{02}+\bar{p}_{02}e^{i\omega t})\,dx\\
&-\int_2^3(p_\infty+p_-+\bar{p}_-e^{i\omega t})\,dx+\int_3^0(\rho_\infty+\rho_{01}+\bar{\rho}_{01}e^{i\omega t})\\
&\{V_\infty+v_{01}+(-\bar{w}_{1u}\sin\gamma+\bar{v}_{01})e^{i\omega t}\}[\{U_\infty+u_{01}\\
&+(\bar{w}_{1u}\cos\gamma+\bar{u}_{01})e^{i\omega t}\}dy-\{V_\infty+v_{01}+(-\bar{w}_{1u}\sin\gamma+\bar{v}_{01})e^{i\omega t}\}dx]\\
&+\int_1^2(\rho_\infty+\rho_{02}+\bar{\rho}_{02}e^{i\omega t})\{V_\infty+v_{02}+(-\bar{w}_{1u}\sin\gamma+\bar{v}_{02})e^{i\omega t}\}\\
&[\{U_\infty+u_{02}+(\bar{w}_{1u}\cos\gamma+\bar{u}_{02})e^{i\omega t}\}dy-\{V_\infty+v_{02}\\
&+(-\bar{w}_{1u}\sin\gamma+\bar{v}_{02})e^{i\omega t}\}dx]=-(L_0+\bar{L}_2e^{i\omega t})
\end{aligned}
\tag{17}
$$

Retaining the unsteady terms of the first order in equations (16) and (17), we have

$$
\frac{\bar{Q}}{U_\infty c}=\int_1^2\left(\frac{\bar{u}_{02}}{U_\infty}dy-\frac{\bar{v}_{02}}{U_\infty}dx\right)-\int_0^3\left(\frac{\bar{u}_{01}}{U_\infty}dy-\frac{\bar{v}_{01}}{U_\infty}dx\right) \tag{18}
$$

$$
\begin{aligned}
\frac{\bar{L}_2}{\frac{1}{2}\rho_\infty U_\infty^2c}&=\bar{C}_{L2}=-2ik\int\int_A\frac{(-\bar{w}_{1u}\sin\gamma+\bar{v})}{U_\infty}d(cd\cos\gamma\\
&-S_0-\bar{S}e^{i\omega t})+\left\{\int_1^{1+B}\frac{\bar{p}_{02}}{\frac{1}{2}\rho_\infty U_\infty^2}dx-\int_0^B\frac{\bar{p}_{01}}{\frac{1}{2}\rho_\infty U_\infty^2}dx\right\}\\
&+2\int_0^H\left(\frac{\bar{v}_{01}}{U_\infty}-\frac{\bar{v}_{02}}{U_\infty}\right)dy
\end{aligned}
\tag{19}
$$

which show the interrelations between the unsteady cavity area and perturbed velocities and also between the unsteady

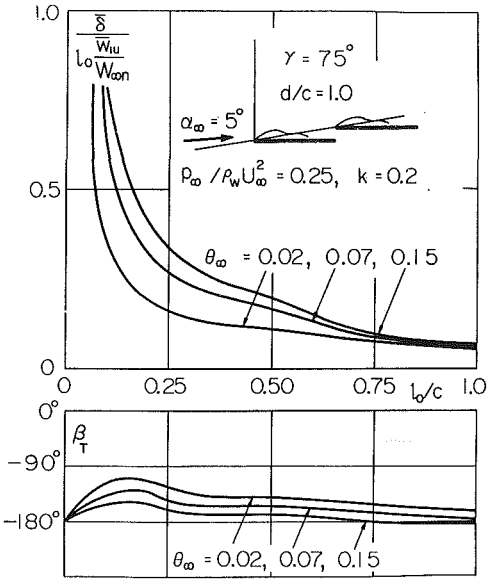

Fig. 4 Cavity termination thickness of optimum cavity model

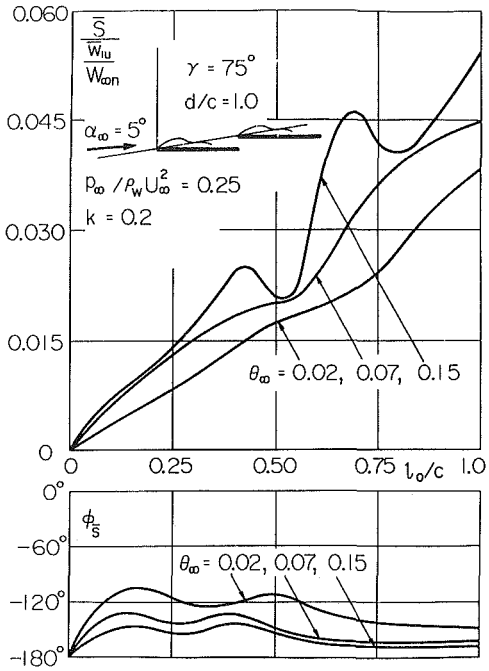

Fig. 5 Variations of unsteady cavity area with cavity length and air volume ratio

perturbed velocities, pressure at inlet and outlet and the unsteady lift respectively.

5 Method of Solutions

5.1 Tripled Integral Equation. The tangential flow conditions over the wetted portions of the hydrofoil are given by

$$\frac{\bar{w}_{1u}}{U_\infty}\sin\gamma = \frac{\bar{v}(x,-0)}{U_\infty} = -\frac{\bar{m}_c(x)}{2U_\infty} + \left\{\int_0^l \frac{\bar{K}_1(\xi)}{U_\infty^2} + \int_l^1 \frac{\bar{K}_2(\xi)}{U_\infty^2}\right\} F(x-\xi,0)d\xi + \left\{\int_0^l \frac{\bar{m}_c(\xi)}{U_\infty} + \int_l^\infty \frac{\bar{m}_w(\xi)}{U_\infty}\right\} M(x-\xi,0)d\xi; 0<x<l \tag{20}$$

$$\frac{\bar{w}_{1u}}{U_\infty}\sin\gamma = \frac{1}{2}\left\{\frac{\bar{v}(x,+0)}{U_\infty} + \frac{\bar{v}(x,-0)}{U_\infty}\right\} = \left\{\int_0^l \frac{\bar{K}_1(\xi)}{U_\infty^2} + \int_l^1 \frac{\bar{K}_2(\xi)}{U_\infty^2}\right\} F(x-\xi,0)d\xi + \left\{\int_0^l \frac{\bar{m}_c(\xi)}{U_\infty} + \int_l^\infty \frac{\bar{m}_w(\xi)}{U_\infty}\right\} M(x-\xi,0)d\xi; l<x<c \tag{21}$$

where

$$U_\infty = W_{\infty n}\cos\alpha_\infty/\cos(\alpha_\infty+\gamma) \tag{22}$$

Since the cavity pressure is assumed to consist of steady and unsteady ones denoted by p_c and $\bar{p}_c e^{i\omega t}$, respectively, application of equation (6) to the upstream point A shown in Fig. 2 and any point on cavity yields the boundary condition for the unsteady cavity

$$\frac{1+\theta_\infty(1+\ln p_\infty)}{1+\theta_\infty}\bar{\sigma}_A = 2ik\frac{\bar{\phi}_c(x,+0)}{U_\infty c} + 2\frac{\bar{u}_c(x,+0)}{U_\infty} = \frac{\bar{K}_1(x)}{U_\infty^2} + 2\left\{\int_0^l \frac{\bar{K}(\xi)}{U_\infty^2} + \int_l^1 \frac{\bar{K}_2(\xi)}{U_\infty^2}\right\} M(x-\xi,0)d\xi + \left\{\int_0^l \frac{\bar{m}_c(\xi)}{U_\infty} + \int_l^\infty \frac{\bar{m}_w(\xi)}{U_\infty}\right\} N(x-\xi,0)d\xi \tag{23}$$

where

$$\bar{\sigma}_A = (\bar{p}_A - \bar{p}_c)/\frac{1}{2}\rho_\infty U_\infty^2, N(x-\xi,0) = 2L(x-\xi,0) - \frac{ik}{\beta^2}e^{\frac{ikM_\infty^2}{\beta^2}(x-\xi)}H_2.$$

And also we put the unsteady cavity termination thickness obtained from equation (14) in a form

$$\bar{y}_c(l) = e^{-ikl}\int_0^l \frac{\bar{m}_c(\xi)}{U_\infty}e^{ik\xi}d\xi = \bar{\delta}e^{i\beta_T} \tag{24}$$

Equation (18) can be reduced to an alternate form by equation (9)

$$\frac{\bar{Q}}{U_\infty c} = \left\{\int_0^l \frac{\bar{K}_1(\xi)}{U_\infty^2} + \int_l^1 \frac{\bar{K}_2(\xi)}{U_\infty^2}\right\} d\xi \int_0^d \left[\left\{E_{02}(1-\xi,y') - E_{01}(-\xi,y')\right\}\cos\gamma - \left\{F_{02}(1-\xi,y') - F_{01}(-\xi,y')\right\}\sin\gamma\right] dy' + \left\{\int_0^l \frac{\bar{m}_c(\xi)}{U_\infty} + \int_l^\infty \frac{\bar{m}_w(\xi)}{U_\infty}\right\} d\xi \int_0^d \left[\left\{L_{02}(1-\xi,y') - L_{01}(-\xi,y')\right\}\cos\gamma - \left\{M_{02}(1-\xi,y') - M_{01}(-\xi,y')\right\}\sin\gamma\right] dy' \tag{25}$$

where

$$x = x' + y'\sin\gamma, y = y'\cos\gamma$$

Thus the boundary conditions (20), (21), (23) may be regarded as a tripled integral equation for determining the singularity distributions $\bar{K}_1(x)$, $\bar{K}_2(x)$, $\bar{m}_c(x)$ and unsteady cavitation coefficient $\bar{\sigma}_A$ under the additive conditions (24) and (25).

5.2 Series Expansions. Singularity distributions are expressed by power series including the inherent singularity to cavity flow like

$$\frac{\bar{K}_1}{U_\infty^2} = a_{-1}\frac{1-\cos\phi}{2} + a_0\sqrt{\frac{1-\sin(\phi/2)}{\sin(\phi/2)}} + \sum_1^\infty a_n \sin n\phi:$$

$$x = \frac{l}{2}(1-\cos\phi) \tag{26}$$

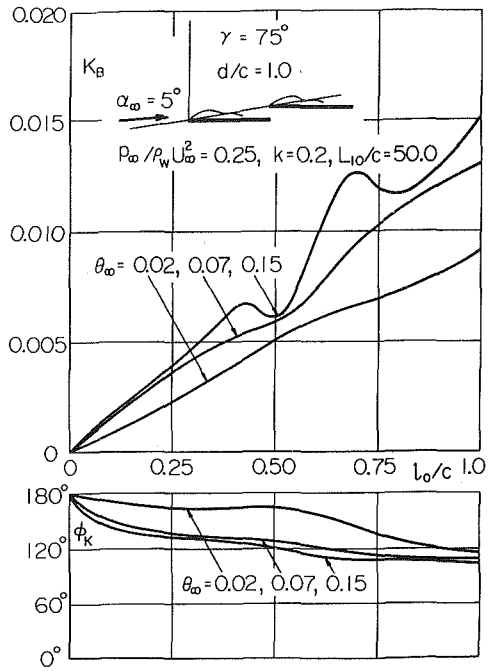

Fig. 6 Variations of cavitation compliance with cavity length and air volume ratio

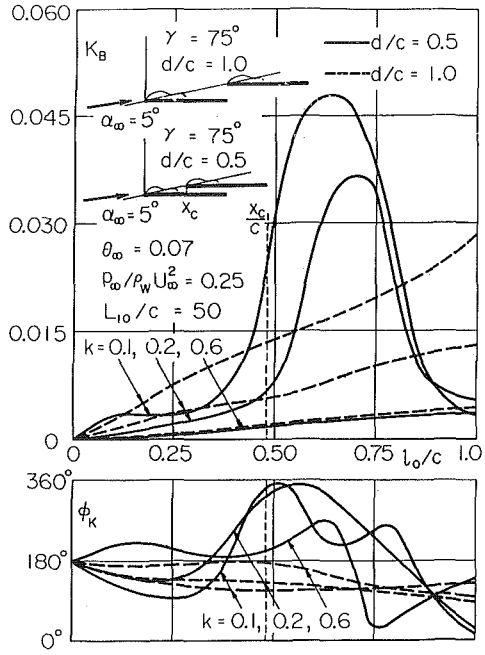

Fig. 7 Variations of cavitation compliance with cavity length and reduced frequency

$$\frac{\bar{K}_2}{U_\infty^2} = b_0 \frac{1+\cos\epsilon}{2} + \sum_1^\infty b_m \sin m\epsilon; x = \frac{1}{2}(1-l)(1-\cos\epsilon) + l \quad (27)$$

$$\frac{\bar{m}_c}{U_\infty} = c_{-1}\sqrt{\frac{1-\cos(\theta/2)}{\cos(\theta/2)}} + c_0 \frac{1+\cos\theta}{2} + \sum_1^\infty Cq \sin q\theta:$$

$$x = \frac{l}{2}(1+\cos\theta) \quad (28)$$

Thus, according to the conservation law of discharge, the free source corresponding to the unsteady part of cavity area is [6]

$$\frac{\bar{m}_w(x)}{U_\infty} = \frac{\bar{m}_c(l)}{U_\infty} e^{ik(l-x)} = c_0 e^{ik(l-x)} \quad (29)$$

Hence the tripled integral equation can be readily reduced to a set of simultaneous linear equation with respect to the unknowns a_n, b_m, c_q, and $\bar{\sigma}_A$.

5.3 Unsteady Characteristics. Once the unknowns are determined, the unsteady characteristics of the cavity and hydrofoil can be obtained from

$$\bar{p}_c = \bar{p}_A - \frac{1}{2}\rho_\infty U_\infty^2 \bar{\sigma}_A \quad (30)$$

$$\bar{S} = \frac{-il}{2k}\left[c_0 + \frac{\pi}{2}(c_{-1}+c_1) - \frac{2}{l}\bar{y}_c(l)\right] \quad (31)$$

$$\bar{c}_{L1} = l\left[a_{-1} + \frac{\pi}{2}(a_0+a_1)\right] + (1-l)\left(b_0 + \frac{\pi}{2}b_1\right) \quad (32)$$

5.4 Optimum Cavity Termination Thickness. We regard such amplitude $\bar{\delta}$ and phase β_T of the unsteady cavity termination thickness as optimum that the lift $\bar{c}_{L1}$ from pressure integration coincides exactly with one $\bar{c}_{L2}$ from conservation law of momentum, that is, from equations (17) (32)

$$\bar{c}_{L1} = \bar{c}_{L2} \quad (33)$$

Successive approximations are suitably adopted for determination of $\bar{\delta}$ and β_T.

6 Dynamic Responses

6.1 Mean Unsteady Pressure Rise. The mean unsteady pressure over one pitch at points A and B in Fig. 2 can be obtained from the linearized Euler's equation

$$\frac{1}{d}\int_0^d \bar{p}_A dy' = \bar{\bar{p}}_A = -i\omega\rho_\infty(\bar{\bar{w}}_{1n}\cos\gamma + \bar{\bar{w}}_{1t}\sin\gamma)(-L_1/\cos\gamma) + \bar{\bar{p}}_1 \quad (34)$$

$$\frac{1}{d}\int_0^d \bar{p}_B dy' = \bar{\bar{p}}_B = -i\omega\rho_\infty(\bar{\bar{w}}_{2n}\cos\gamma + \bar{\bar{w}}_{2t}\sin\gamma)(L_2/\cos\gamma) + \bar{\bar{p}}_2 \quad (35)$$

with

$$\bar{\bar{w}}_{jn} = \bar{\bar{u}}_j\cos\gamma - \bar{\bar{v}}_j\sin\gamma + \bar{w}_{1u}, \bar{\bar{w}}_{jt} = \bar{\bar{u}}_j\sin\gamma + \bar{\bar{v}}_j\cos\gamma$$

$$(\bar{\bar{u}}_j, \bar{\bar{v}}_j) = \frac{1}{d}\int_0^d (\bar{u}_j, \bar{v}_j)dy' : j = 1,2$$

in which the first and second terms in right-hand side may be interpreted as resulting from the flow inertia and dynamic responses respectively. Thus our interests are hereafter confined to the latter only. Hence the mean unsteady pressure rise can be obtained by applying the unsteady Bernoulli's equation (6) to points A and B

$$\frac{\bar{\bar{p}}_2 - \bar{\bar{p}}_1}{\rho_\infty U_\infty^2} = \frac{W_{1n}}{U_\infty}\frac{\bar{\bar{w}}_{1n}}{U_\infty} + \frac{W_{1t}}{U_\infty}\frac{\bar{\bar{w}}_{1t}}{U_\infty} - \frac{W_{2n}}{U_\infty}\frac{\bar{\bar{w}}_{2n}}{U_\infty} - \frac{W_{2t}}{U_\infty}\frac{\bar{\bar{w}}_{2t}}{U_\infty}$$
$$+ ik\left[\frac{\bar{w}_{1u}}{U_\infty}\left(\frac{L_{10}}{c} + \frac{L_{20}}{c}\right) + \left(\frac{\bar{\bar{w}}_{1n}}{U_\infty} + \frac{\bar{\bar{w}}_{1t}}{U_\infty}\tan\gamma\right)\frac{L_{10}}{c} + \left(\frac{\bar{\bar{w}}_{2n}}{U_\infty}\right.\right.$$
$$\left.\left. + \frac{\bar{\bar{w}}_{2t}}{U_\infty}\tan\gamma\right)\frac{L_{20}}{c}\right] \quad (36)$$

in which L_{10} and L_{20} may be interpreted as effective inertia length given by, respectively

$$i\omega\{(\bar{\bar{w}}_{1n}\cos\gamma + \bar{\bar{w}}_{1t}\sin\gamma)L_1/\cos\gamma + \bar{\bar{\phi}}_1\}$$
$$= i\omega(\bar{\bar{w}}_{1n}\cos\gamma + \bar{\bar{w}}_{1t}\sin\gamma)L_{10}/\cos\gamma \quad (37)$$

$$i\omega\{(\bar{\bar{w}}_{2n}\cos\gamma + \bar{\bar{w}}_{2t}\sin\gamma)L_2/\cos\gamma - \bar{\bar{\phi}}_2\}$$
$$= i\omega(\bar{\bar{w}}_{2n}\cos\gamma + \bar{\bar{w}}_{2t}\sin\gamma)L_{20}/\cos\gamma \quad (38)$$

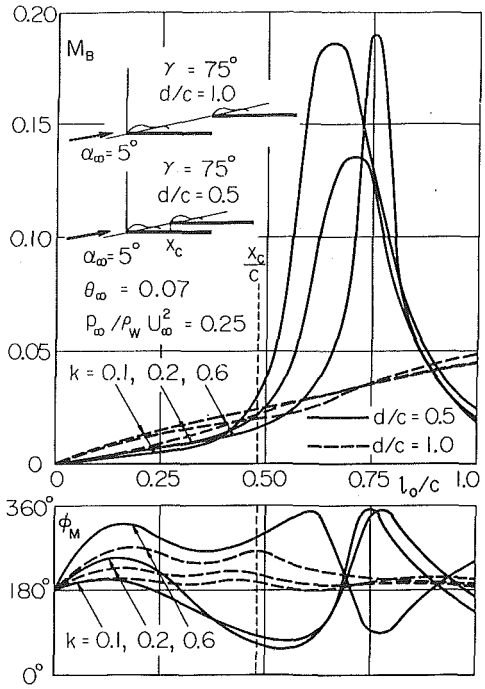

Fig. 8 Variation of mass flow gain factor with cavity length and reduced frequency

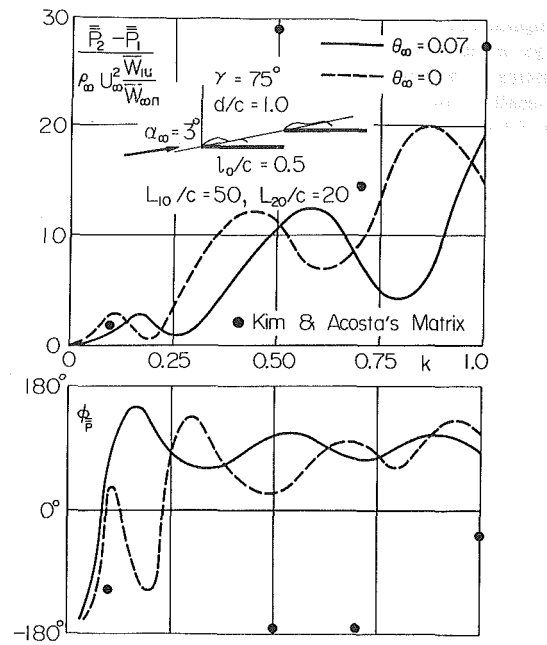

Fig. 9 Frequency responses of mean unsteady pressure rise

6.2 Cavitation Compliance and Mass Flow Gain Factor. We define the cavitation compliance and mass flow gain factor as measures of the variations of unsteady cavity area with the unsteady cavitation coefficient and the axial gust, respectively, that is

$$K_B = -\frac{\partial}{\partial t}(\bar{S}e^{i\omega t})/\frac{\partial}{\partial t}(\bar{\sigma}_1 e^{i\omega t}) = \bar{S}/\bar{\sigma}_1 \tag{39}$$

$$M_B = \frac{\partial}{\partial t}(\bar{S}e^{i\omega t})/\frac{\partial}{\partial t}\left(\frac{\bar{w}_{1u}}{W_{\infty n}}e^{i\omega t}\right) = \bar{S}/\bar{w}_{1u}/W_{\infty n} \tag{40}$$

where

$$\bar{\sigma}_1 = \bar{\sigma}_A - 2ik\frac{\bar{w}_{1u}}{U_\infty}\frac{L_{10}}{c}$$

Hence we can find readily K_B and M_B by substituting equations (30) and (31) to equations (39) and (40).

7 Numerical Examples

Numerical calculations are made for the partially cavitated flat plate cascade of stagger angle 75 deg and pitch-chord 0.5, 1.0 at mean attack angle 5 deg in bubbly water of air volume ratios 0.02, 0.07, 0.15 and static pressure coefficient 0.25 with gust reduced frequencies 0.1, 0.2, 0.6. And also μ, ϵ was neglected because of its extreme smallness. Details of numerical method of solutions are omitted here [7].

7.1 Optimum Cavity Flow Model. An example of the optimum cavity termination thickness obtained is shown in Fig. 4: The amplitude decreases considerably with the increase of cavity length but increases with the increase of air volume ratio. The phase lag is almost invariant with the cavity length but increases with the increase of air volume ratio.

The unsteady part of cavity area is shown in Fig. 5: The amplitude increases with the increase of cavity length and its oscillation, which results from the pressure wave in super-resonance condition of subsonic bubbly water, becomes significantly with the increase of air volume ratio.

7.2 Cavitation Compliance and Mass Flow Gain Factor. Variations of the cavitation compliances and mass flow gain factors with the cavity length are shown in Figs. 6, 7, and 8 for various air volume ratios and gust reduced frequencies respectively.

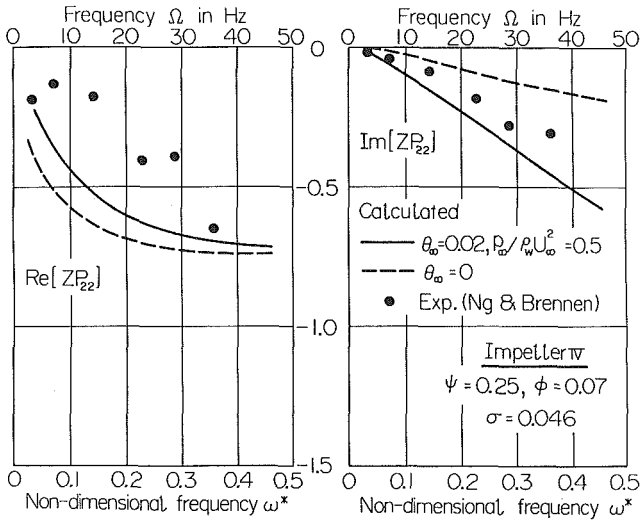

Fig. 10 Comparisons of predicted unsteady discharge difference between inlet and outlet with available data

As for the cavitation compliance, increases of air volume ratio make the amplitude increase in oscillatory manner and the phase ahead decrease. These trends become notable with the increase of cavity length as shown in Fig. 6. Further, decrease of gust reduced frequency makes the amplitude increase monotonically for pitch-chord ratio 1.0 but maximum at cavity length of about 0.6c for pitch-chord ratio 0.5 as shown in Fig. 7. This is because the cascade interference effects become notable immediately after the cavity termination enters into the downstream from the leading edge of the backside neighbouring hydrofoil for pitch-chord 0.5 as shown by x_c in Fig. 7. Corresponding to this, the phase ahead changes considerably for this region.

As is clear from equation (40), Fig. 5 can also be regarded as showing the effects of air volume ratio on mass flow gain factors. Although its tendencies are quite similar to ones in Fig. 6, its amplitude is significantly larger than the cavitation

compliances. This clearly shows the mass flow gain factor plays a more important role in dynamic transfer characteristics in bubbly water. And further, same notable features in small reduced frequency as in Fig. 7 can be clearly seen in Fig. 8 for pitch-chord ratio 0.5 from above stated reasons.

7.3 Mean Unsteady Pressure Rise. Frequency responses of the mean unsteady pressure rise to axial gust are shown in Fig. 9 with the corresponding ones [7] in pure water and Kim's result [1] for comparisons. Both of the amplitude and phase increase in fluctuatory manner with the increase of gust reduced frequency. This can be interpreted as resulting from the pressure waves in super-resonance condition of subsonic bubbly water in downstream from cascade. Further, considerable differences from Kim's result can be seen in amplitude and phase due to their neglections of free vortex and free source in downstream from cascade.

Comparisons of the difference between the unsteady discharge at inlet and outlet with the available data [8] are shown in Fig. 10 with one in pure water. Both of the real and imaginary parts by present method may be found to be more comparable than ones in pure water with the experimental data, though there remain to be further examined the present assumptions for the real bubbly water and also the order of some experimental uncertainties included.

8 Conclusions

A method of analysis is presented for the dynamic responses of the partially cavitated hydrofoil cascade to axial gust in bubbly water and then the unsteady compressibility effects are discussed through some numerical examples. Main contents are summarized as follows.

(1) The homogeneous bubbly water flows of axial gust is shown to be regarded as the unsteady subsonic one and then the unsteady perturbed flow by the partially cavitated hydrofoil cascade is described by singularity distributions based on governing equation.

(2) Conservation laws of mass and momentum are applied to take account of the unsteady parts of cavity area, cavity termination thickness and cavity pressure for unsteady partial cavity model. The optimum cavity model is determined explicitly in such manner that both unsteady lifts from conservation law of momentum and pressure integration are exactly same.

(3) A method of analysis based on the unsteady cavity model obtained is presented for dynamic responses of the partially cavitated hydrofoil cascade. Some notable features of the optimum cavity model, the cavitation compliance and mass flow gain factor are clarified in relation to air volume ratio and gust reduced frequency for various cavity length. Further, the unsteady pressure rise and unsteady discharge difference between inlet and outlet are compared with the former available results.

References

1 Kim, J. H., and Acosta, A. J., ASME JOURNAL OF FLUIDS ENGINEERING, Vol. 97, No. 4, Dec. 1975, pp. 412–418.

2 Brennen, C., and Acosta, A. J., ASME JOURNAL OF FLUIDS ENGINEERING, Vol. 98, No. 2, June 1976, pp. 182–191.

3 Brennen, C., *Journal of Fluid Mechanics*, Vol. 89, Part 2, 1978, pp. 223–240.

4 Kolesnikov, K. S., and Kinelev, V. G., *Izvestiya VUZ. Aviatsionnaya Tekhnika*, Vol. 16, No. 4, 1973, pp. 87–92.

5 Wieghardt, K., *Schiffstechnik*, Vol. 14, Part 70, 1967, pp. 24–28.

6 Nishiyama, T., *JSME Transaction*, Vol. 46, No. 408, 1980, pp. 1372–1382.

7 Nishiyama, T., and Nishiyama, H., *JSME Transaction*, Vol. 47, No. 415, 1981, pp. 412–422.

8 Ng, S. L., and Brennen, C., ASME JOURNAL OF FLUIDS ENGINEERING, Vol. 100, No. 2, June 1978, pp. 166–176.

Some Features of Water Flows With Ventilated Cavities[1]

J. M. Michel
Research Worker,
Institut de Mecanique de Grenoble,
Grenoble, France

A survey of the main mechanisms of air entrainment in largely developed cavity flow is given, with paticular attention being given to plane, almost horizontal flows. Specific characteristics of dimensional analysis in this case are exhibited. The evolution of flow configuration when the air flow rate changes is described. Special emphasis is placed on cavity pulsation and its physical characteristics. Some aspects of the pulsation mechanisms are discussed, from a qualitative point of view, with a more detailed examination of the phase relations between the quantities involved.

Introduction

The aim of this paper is to describe the main features of water flows in which cavities are created by air injection, and to give some general conclusions of experiments which were carried out in our Laboratory for about ten years. The ventilated cavities considered are largely developed by the large amount of air inflow. They are formed in the wake of forebodies such as hydrofoils or propeller blades, and in regions of deadwater following a step in a solid wall. Examples of the latter configuration can be found in the ventilation of flood spillways or hull bottoms. At all events, ventilation is used to reduce either the risk of erosion or the energy losses in high speed machinery.

Our experience in this field is partly derived from the fact that we have a hydrodynamic tunnel at our disposal in which very large amounts of air (up to 5.5 g/s) can be injected in the water flow the cross sectional area of which is about 0.05 m^2. To give an idea of the volumes involved, suffice it to say that in the second test section of the tunnel, in which the inlet water depth is 40 cm, and the water speed is between 2.5 and 13 m/s, the total height of the water-air mixture at the outlet can reach and even exceed 50 cm. This is obtained without any recirculation of the air injected, by means of an intermediate tank and a downstream tank which are placed between the test section and the recirculating pump of the tunnel (a sketch of the uper part of the tunnel is given in [24]). To our knowledge, only a few recirculating tunnels offer such a facility, and consequently research on this subject is poor and papers rather scarce.

The principal configurations under consideration were the following:

(*a*) Flows around a wedge (chord 6 cm, angle 16 deg, incidence zero) in a free surface channel of total height 28 cm with submersion depths of 7, 14 and 21 cm (test section N° 1 of our tunnel); tests were also made on wedges (chord 6 or 4 cm) placed in a solid wall tunnel of 30 cm total height (tunnel operated by the Neyrtec Company).

(*b*) Flows around 3-D wings of rectangular or trapezoidal planform with wedge-shaped cross sections, in the test sections 1 and 2 of our tunnnel.

(*c*) Plane, horizontal jet of water falling on a solid plate placed in its vicinity, the initial space between the plate and the jet being filled with air. This configuration will later be referred to as the half cavity. The following paper in the present issue is devoted to his case.

In addition, the following flows, which were studied especially from the standpoint of hydrodynamic characteristics of foils, gave valuable information on the mutual influence of the circulation around lifting foils and the flow of air at the rear of the cavity:

(*d*) Flows around 2-D hydrofoils with rounded nose, wetted upper side and vented base (test sections 1 and 2).

(*e*) Three-dimensional flows around base-vented wings in the largest of Neyrtec's hydrodynamic tunnels.

Here we want to give special attention to the physical aspects of the phenomena, especially to air entrainment. The following topics, common to the various flow configurations, will be discussed:

- air entrainment in ventilated cavities,
- dimensional analysis,
- flow behaviour when air flow rate varies
- pulsation of the cavities.

At this point, a preliminary remark may be useful: in laboratory conditions, the experimental procedure is such that the mass air flow rate Q_m which is injected in the water flow can be easily controlled. Thus, the conditions of artificial ventilation are simulated and the problem is to determine the relation between the air flow rate Q_m and the pressure p_c in the cavity; p_c determines the global flow geometry and, therefore, the forces on obstacles. However, another procedure would be possible consisting in allowing air to flow out of a constant pressure container into the cavity through a constant or varying head loss. In such a case, the conditions of natural ventilation would be simulated. The air flow rate would result from the main dynamic conditions: pressure in

[1] This paper was first given as a lecture at the Euromech Colloquium 146: "Flows of Liquids Past Bodies with Developed Cavities" which was held at Villard de Lans, near Grenoble, France in September 1981.

Contributed by the Fluids Engineering Division for publication in the JOURNAL OF FLUIDS ENGINEERING. Manuscript received by the Fluids Engineering Division, June 10, 1982.

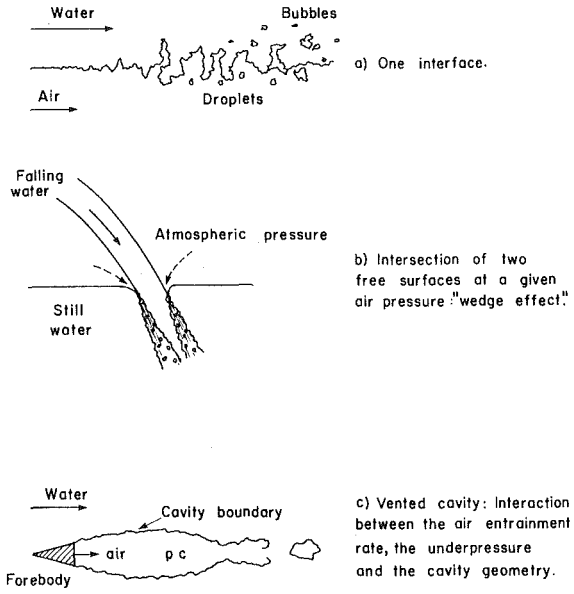

Fig. 1 Typical cases of air entrainment

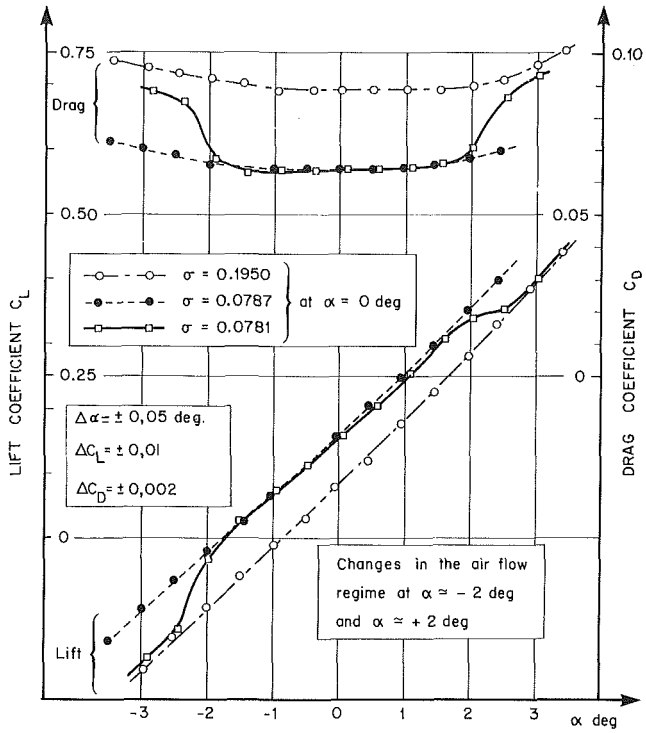

Fig. 2 C_D and C_L versus the incidence α at constant air flow rate Q_m for a base-vented, wedge-shaped hydrofoil under a free surface

the upstream container, speed of water, ambient pressure near the cavity. It is clear that this problem is related to the broad problem of air entrainment by a free surface of moving liquid. The two view points are not incompatible and this remark aims only to stress the fact that the study of the relationship between Q_m and p_c leads to the study of transfer mechanisms in the vicinity of one (or several) free surface(s).

I Air Entrainment in Ventilated Cavities

Taking the case of ventilated cavities behind lifting or nonlifting two-dimensional foils as a typical example, what are the transfer mechanisms to be considered?

Strictly speaking, there is a double mass transfer at the interface: firstly of water by evaporation and/or condensation, secondly of air because the air content of water does not generally correspond to the saturation value at the air pressure in the cavity. Air transfer is increased, with respect to the case of still water, by convection which renews the under-layer of the liquid and keeps the concentration gradient constant (Parkin and Kermeen [1]). This effect is greatly amplified by the water flow turbulence level, as established by Brennen [2] and by Billet and Weir [3]. In our case, however, these mass transfers are negligibly small due to the large amounts of air injected into the cavity.

The transfer of momentum at the interfaces is related to the shear stresses and consequently, to the viscosity of the fluids and to flow turbulence. This effect is increased by actual turbulent deformation of the interfaces: on a small scale, the interfaces have a fluctuating shape, also partly caused by the roughness of the upstream solid wall, the interfacial tension and the instabilities due either to gravity or to differences between air speed and water speed. As a result, a significant amount of air is entrapped in the interface irregularities and is carried away over a thickness approximately equal to their height. At their ultimate stage, the interface irregularities give rise to water drops in the cavity and to air bubbles in the liquid. When the air flow rate is very large, most of the air is evacuated through the upper surface of the cavity: then the cavity length cannot be increased and the relative underpressure σ in the cavity reaches an experimental minimum value σ_m which is greater than the minimum value given by hydrodynamic theory, Fig. 1(*a*).

When one free surface is at the boundary of two fluid flows, only the above-mentioned mechanisms need to be considered. However, another situation arises where two free surfaces coming into contact form a shear layer and draw the locally entrapped air into a sort of wedge. In current situations, for example, in the case of overspill waves [4] or hydraulic jumps [5], the entrainment zone is at the boundary of an infinite medium of air where the pressure is fixed (Fig. 1(*b*)). In our case, the wedge effect can be observed when the air flow rate is not large, so that the short cavity terminates by alternate vortices in which air is inserted. But in many circumstances, for larger air flow rates the cavity forms a geometrically limited volume in which air tends to be blocked. Then, the cavity pressure determines the global geometry of the flow, but depends on the dynamics of air entrainment, which is itself related to flow geometry (Fig 1(*c*)). A striking

Nomenclature

$C_D = D/\frac{1}{2}\rho V^2 S$, drag coefficient

$C_L = L/\frac{1}{2}\rho V^2 S$, lift coefficient

$C_{Qm} = Q_m/\rho VS$, mass air flow coefficient

$C_{Qv} = Q_m/\bar{\rho}_{air} VS$, volume air flow coefficient

Fr $= /\sqrt{gd}$, Froude number

Re $= \rho Vd/\mu$, Reynolds number

We $= \rho V^2 d/A$, Weber number

$\phi = f/\sqrt{P_{air}/\rho d\bar{l}}$, non-dimensional frequency

$\sigma_v = (p_r - p_v)/\frac{1}{2}\rho V^2)$, cavitation number

$\sigma = (p_r - p_v - \bar{P}_{air})/\frac{1}{2}\rho V^2$, relative cavity underpressure

$\sigma/\sigma_a = (p_r - p_v - \bar{P}_{air})/\bar{P}_{air}$, pressure parameter

example of this fact is the jump in the cavity pressure—and then cavity length, lift and drag—when the incidence of a 2-D foil is slightly modified, the other paramters being kept constant (Fig. 2). On Figure 2, the three curves $C_L(\alpha)$ or $C_D(\alpha)$ correspond to three values of the ambient pressure. The intermediate curve shows a jump from a running joint to another one near -2 and $+2$ degrees: the modification of circulation is sufficient to change the mode of air evacuation at the rear of the cavity and then the air pressure into the cavity. Thus, it is clear that there is a strong interaction between flow geometry, cavity pressure and air evacuation rate or, in other words, the phenomenon is very nonlinear. As a result it is not possible to split up this global mechanism into simpler fundamental mechanisms. Indeed, the above-mentioned interaction is the fundamental aspect of air entrainment in ventilated cavities, and the best we can do is to compare some typical situations so as to demonstrate the influence of various parameters such as gravity, ambient pressure and water flow speed.

Cavity flows are essentially controlled by the inertial forces of the liquid. In the 2-D case—plane or axisymmetrical—an overpressure zone and the reentrant jet are observed at the rear of the cavity in the proximity of the stagnation point which, according to hydrodynamic theory, occurs at any steady confluence region. The reentrant jet prevents air entrainment by the aforesaid "wedge effect." As a result, air is blocked in the cavity. When the other evacuation mechanisms, such as air evacuation by bubbles which rise through the upper free surface are inoperative, the only outlet for the air is by discontinuous gusts at the rear of the cavity, the flow then becoming unsteady. In addition, in most cases, the flow presents a periodical character which is complicated by the existence of different regimes, and hysteresis cycles appear, since the free surface unsteady flow memorizes its previous history. The characteristics have been studied by Silberman and Song [6], [7] and by Michel [8], [9] and will be discussed later. In 3-D flows, the air finds an outlet in the core of the vortex in which vorticity is concentrated. The circulation may be due to a gravity effect, as in the case of low speed horizontal flow around a vertical disk (Cox and Clayden [10], Campbell and Hilborne [11], Pernik [12] Ephstein [13]) in which a relationship can be found between the air flow rate, the relative underpressure of the cavity and the Froude number. This relationship is confirmed by experiment, at least when the turbulence level is small. Of course, circulation is also connected to the lift of a wing: a tip vortex cavity can then coexist with a 2-D-type middle cavity (Verron and Michel [14]). It is noteworthy that the characteristics of the 2-D flow are not significantly affected by the presence of the tip cavity: thus the pulsation subsists even for low values of wing aspect ratio and the evolution of the lift does not seem to be modified when the tip cavity appears (Verron [15]).

As a conclusion to this section, it can be said that various mechanisms are involved in the term "air entrainment," particularly as regards developed ventilated cavities. Experience shows that these mechanisms are superimposed and have successively predominating effects depending on the amount of injected air, thus determining several air flow regimes. The most difficult mechanism to clarify is the one in which, as was previously mentioned, strong interaction exists between cavity pressure, flow geometry and air entrainment. In order to sketch out at least an approach of the global phenomenon, it is useful to examine what can be obtained from the similarity rules.

II Similarities Analysis

In a particular situation, the relevant quantities which can be fixed and which determine the flow are the following:

- $g_i, i=1, \ldots, n$, : which are related to the geometry (foil chord, incidence, depth of submersion. . . .) and also the microgeometry (roughness of the wall);
- ρ, μ, A : specific mass, dynamic viscosity, and surface tension of water;
- $V, g, p_r - p_v$: speed of flow, gravity and difference between the reference pressure and the vapor pressure p_v;
- Q_m : mass flow rate of air injected into the cavity.

Let G be any quantity which results from the flow:

$$G = G[g_i, \rho, \mu, A, V, g, p_r - p_v, Q_m]$$

then we can write:

$$\frac{G}{G_0} = g\left[\frac{g_i}{d}, \mathrm{R_e}, \mathrm{W_e}, \mathrm{F_r}, \sigma_v, C_{Qm}, \text{ or } C_{Qv}\right]$$

in which:

G_0 is quantity analogous to G, built up with one or several primary quantities,

d is a primary reference length, chosen among the g_i values,

$\mathrm{Fr} = V/\sqrt{gd}$ is the Froude number,

$\mathrm{R_e} = \rho V d/\mu$ is the Reynolds number,

$\mathrm{W_e} = \rho V^2 d/A$ is the Weber number,

$C_{Qm} = Q_m/\rho V S$ is the mass air flow coefficient,

$C_{Qv} = Q_m/\rho_{\mathrm{air}} V S$ is the volume air flow coefficient,

$\sigma_v = (p_r - p_v)/\frac{1}{2}\rho V^2$ is the cavitation number.

Of course, if the scales of the phenomena are different, the use of several reference lengths may be necessary. The coefficient C_{Qv} is above all dependent on the flow geometry ([13], [14]) and its values are not very sensitive to the reference pressure p_r. If we write: $Q_m = \rho_{\mathrm{air}} V_{\mathrm{air}} S$, we see that $C_{Qv} \simeq V_{\mathrm{air}}/V$: C_{Qv} is also an index of the relative mean velocity of air in the cavity. Thus, it is more suitable than C_{Qm} for describing the flow geometry.

This analysis is applied to the three following quantities:

- the mean length of the cavity

$$\frac{\bar{l}}{d} = \frac{\bar{l}}{d}\left[\frac{g_i}{d}, \mathrm{R_e}, \mathrm{W_e}, \mathrm{Fr}, \sigma_v, C_{Qm} \text{ or } C_{Qv}\right] \tag{2}$$

- the mean air pressure in the cavity $\bar{P}_{\mathrm{air}}$

$$\sigma_a = \frac{\bar{P}_{\mathrm{air}}}{\frac{1}{2}\rho V^2} = \sigma_a\left[\frac{g_i}{d}, \ldots\ldots, \sigma_v, C_{Qm} \text{ or } C_{Qv}\right] \tag{3}$$

- the frequency of pulsation f, in the case of pulsating cavities

$$\phi = \frac{f}{\sqrt{\bar{P}_{\mathrm{air}}/\rho\, d\, \bar{l}}} = \phi\left[\frac{g_i}{d}, \ldots\ldots, \sigma_v, C_{Qm} \text{ or } C_{Qv}\right] \tag{4}$$

We deduce, for the relative underpressure of the cavity:

$$\sigma = \frac{p_r - \bar{p}_a}{\rho V^2/2} \simeq \frac{p_r - p_v - \bar{P}_{\mathrm{air}}}{\rho V^2/2} = \sigma_v - \sigma_a$$

$$\sigma = \sigma\left[\frac{g_i}{d}, \ldots\ldots, \sigma_v, C_{Qm} \text{ or } C_{Qv}\right] \tag{5}$$

The nondimensional frequency ϕ is the ratio of the frequency f to the natural small pulsation of a piston with a thickness d, a density ρ, which oscillates above an isothermal air cylinder with a height equal to $\bar{l}$, where the pressure is $\bar{P}_{\mathrm{air}}$. It was found [8], [9] that this parameter alone can bring

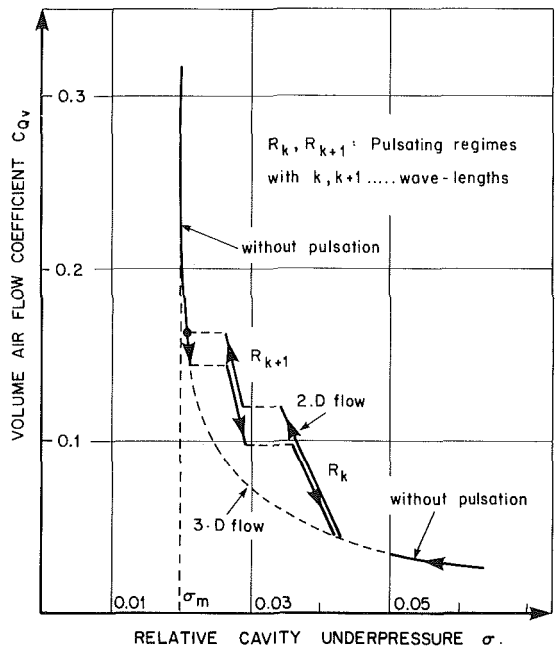

Fig. 3 L-shaped curve $C_{Qv}(\sigma)$

together the experimental points and thus is pertinent to describe the pulsation frequency of ventilated cavities. This fact makes obvious the importance of the cavity length as a reference length for the pulsation phenomenon.

We can eliminate C_{Qm} or C_{Qv} between σ and $\bar{l}/d$ using (2) and (5):

$$\frac{\bar{l}}{d} = \frac{\bar{l}}{d}\left[\frac{g_i}{d}, \mathrm{Fr}, \sigma_v, \sigma\right] \tag{6}$$

(in order to be brief, here and in the following sections, the dependence on the Reynolds and Weber number is not written).

Likewise, we can express ϕ as a function of σ. But from our experience we know that the phenomen are best represented if we substitute the parameter σ/σ_a ($\sigma/\sigma_a = \sigma_v/\sigma_a - 1$) for σ:

$$\phi = \phi\left[\frac{g_i}{d}, \mathrm{Fr}, \sigma_v, \sigma/\sigma_a\right] \tag{7}$$

The nondimensional σ/σ_a is the ratio of the mean underpressure of the cavity, responsible for the mean flow geometry, to the mean air pressure in the cavity $\bar{P}_{\mathrm{air}}$, to which the cavity pulsation is related. It determines the different cavity pulsation regimes.

At this point, it should be noted that the mean relative length $\bar{l}/d$, and some other parameters which depend essentially on the flow geometry, such as for example the lift coefficient C_L in the case of a lifting foil, do not actually depend on the parameter σ_v:

$$\left.\begin{matrix}\bar{l}/d \\ C_L\end{matrix}\right\} = \text{functions of}\left[\frac{g_i}{d}, Fr, \sigma\right] \tag{8}$$

Then, according to a theorem of the implicit functions theory, for such a quantity G/G_0, the simultaneous elimination of σ_v and C_{Qv} involves:

$$\frac{\partial(G/G_0)}{\partial\sigma_v} \Big/ \frac{\partial(G/G_0)}{\partial C_{Qv}} = \frac{\partial\sigma}{\partial\sigma_v} \Big/ \frac{\partial\sigma}{\partial C_{Qv}}$$

where the derivatives have to be calculated in the expression (1) of G/G_0. This relation is roughly verified in actual situations.

Finally, the initial problem is divided into two problems: the first, of hydrodynamic nature, is summarized by the relation (8), while the second, expressed by the relation (5), is related to the various mechanisms of air entrainment mentioned above. As to the relations (4) or (7), they concern both hydrodynamics and physical characteristics of the flow. A remark must be made here that, as a matter of fact, from the experiments, it is found that the cavitation number σ_v does not appear in the relation (7) which is written:

$$\phi = \phi\left[\frac{g_i}{d}, \mathrm{Fr}, \sigma/\sigma_a\right] \tag{9}$$

but, in such a case, the elimination of σ_v together with C_{Qv}, and in the same way the good correlation between the parameters ϕ and σ/σ_a are results derived directly from the experiments, but are not well understood.

III Description of the Air Flow Regimes

Keeping in mind the entrainment mechanisms indicated above, a qualitative description can be given of the phenomena which result from an increase in the amount of air injected into a flow of water. Consideration is given here to the typical situation where the wake of a slender 2-D body is ventilated in a horizontal flow.

At first, it is noted that the relation between the air flow coefficient C_{Qv} and the relative underpressure σ is expressed as an L-shaped curve whenever the air flow at the rear of the cavity is continuous (Fig. 3). The vertical branch corresponds to the large amount of air injected and its abscissa σ_m corresponds to the minimum value of σ. In this region, most of the air is evacuated in the form of large bubbles which rise through the upper free surface of the cavity. The almost horizontal branch of the L-curve corresponds to small values of air flow (σ fairly high, small cavity length). In this zone, a small variation in the amount of air injected entails a significant variation in σ, i.e., in the cavity pressure: then the entrainment mechanisms do not allow evacuation of a large amount of air. The matching zone of the horizontal and vertical branches can be either continuous or discontinuous. In 3-D situations, where the circulation can be carried away by the flow, a tip vortex cavity can evacuate the air injected and the matching can thus be smooth. But in the 2-D cases, for the middle values of air flow, there is no air evacuation mechanism other than by cavity pulsation. Discontinuities then appear in the L-curve due to different pulsation regimes. This point will be considered in more detail below. What then is the behavior of the flow when the amount of air increases from zero to the largest values that can be injected?

(a) Case of Small Values of Air Inflow. If no vapor cavity is present in the wake, the air is evacuated as small bubbles snatched by the liquid layers which roll in alternate vortices. This entrainment mechanism can be considered as a "wedge effect," the liquid layers intersecting alternately one inside the other. When the amount of air increases, an emulsion cavity and then a monophasic steady cavity form behind the body. These cavities are often followed by alternate vortices in which air is evacuated.

When σ_v is smaller than its value σ_{vc} corresponding to the onset of cavitation in the wake, a small amount of air does not significantly modify the appearance of the existing vapor cavity, apart from a slight lengthening. Indeed, the vapor cavity wake is characterized on the one hand by trains of alternate vortices broken off by the random emission of the reentrant jet, and on the other hand, by the presence of vapor bubbles which are carried away as they were uncondensable. The addition of the small amount of air does not modify these characteristics.

(b) Case of Middle Values of Air Inflow. For an increasing rate of air inflow, air evacuation either by diffusion or by small bubbles resulting from the "wedge effect" usually becomes insufficient. In such cases, the rear region of the

cavity tends to form a steady reentrant jet, so that it can sustain the increase in cavity pressure and air is blocked in the cavity. The size of the cavity increases until it attains the order of one or several "wavelengths" of the fluctuations conveyed by the free boundaries at the local mean velocity of the liquid. Then the pulsation phenomenon begins to take effect. The wavelength λ (kinematic wave) is equal to U_c/f, where $U_c = U(1 + \sigma)^{1/2}$ is the velocity at the cavity free boundary, and f, the frequency, is roughly proportional to the square root of the pressure $\tilde{P}_{air}$ in the cavity. Thus the variation in cavity length, when the pulsation phenomenon becomes established, is larger if the velocity is large or the ambient pressure is small (σ_v small). The number k of wave lengths is the initial regime R_k depends essentially on the value of the parameter σ/σ_a, the R_1 regime beginning when σ/σ_a becomes smaller than about 0.23, the other regimes corresponding to smaller ranges of values of that parameter. In each period, an air pocket detaches from the cavity. Its initial size is equal to the difference between the maximum and the minimum values (l_M and l_m, respectively) of the cavity length. Often it is broken into many smaller air bubbles before its detachment from the cavity. It is organized around two symmetrical vortices downstream and some alternate vortices upstream, the symetrical vortices being due to the reentrant jet. The symmetry can be destroyed by the transverse effect of gravity. The evolution of a R_1 cavity was experimentally studied by a special optical device and is given in [8] (p. 349–50). It is not reproduced here for brevity.

(c) Case of Large Amounts of Air Injected Into the Cavity. This case corresponds to the almost vertical branch of the $C_{Qv}(\sigma)$ curve. The increase in air flow rate does not modify the general geometry of the flow. Only the growth rate of air bubbles which rise through the upper free surface increases. At this stage, the 3-D fluctuations due to these bubbles tend to prevent the formation of the ordered structure at the rear of the cavity, so that the air is also evacuated at the rear part without cavity pulsation. The larger the amount of air injected, the larger the proportion of air evacuated by bubbles through the upper-free surface. Naturally this phase needs a large cavity so that the development of the turbulent fluctuations results in quite a lot of bubbles able to evacuate the air injected. Also, it is noted that all the factors promoting turbulent fluctuations of the upper cavity boundary—roughness of the forebody, turbulence of the flow, gravity, ambient pressure—also tend to diminish the maximum cavity length and to increase the minimum relative underpressure σ_m. In limit cases, if the fluctuation growth rates were large enough, it would be possible to avoid the pulsating regime transition at least for very slender forebodies.

To end this section, it is worth adding to most of the characteristics exhibited in the case of cavities formed behind a 2-D body are also found in the case of the half cavity or in 3-D flows around ventilated wings. In the latter case, the tip cavity which is formed in the tip vortex serves as a duct for the evacuation of air. But it is noteworthy that the middle cavity follows approximately the same evolution as a 2-D cavity and also has pulsations, contrary to what was expected.

IV Some Problems Related to Cavity Pulsation

It seems that in the past, scientific exchange on the pulsation of ventilated cavities has centered on somewhat controversial aspects. Indeed, some questions arise concerning this self-oscillating phenomenon, which can be roughly summarized in the following manner:

- Is it connected with some compliance of the recirculating tunnel in which it is produced?
- Does it require the proximity of an external free surface, or can we imagine its existence in an unbounded 2-D field of flow?
- What are the physical mechanisms in which periodical fluctuations originate, while the given quantities governing flow are kept constant?

It is not easy to give a balanced answer to these questions, the final aim of which is to determine whether the pulsation phenomenon has any fundamental interest—or at least some important technical interest. In fact, the three questions are not independent and thus a full answer to the first question can be obtained only after having dealt with the second and the third one. Some brief, although certainly incomplete, indications will be given here.

(a) Is There Any Connection With the Compliance of the Recirculating Tunnel? It is useful to remark that cavity pulsation was observed in facilities other than recirculating tunnels, for example in some turning-arm basins. But, from our experience, the pulsation phenomenon was obtained in the past although two modifications were made to our free surface tunnel:

- Firstly, the distance between the upper and lower levels of the tunnel was extended by about 2 m (on the occasion of its installation in the present laboratory buildings).
- Secondly, and more important, the addition of the intermediate tank placed between the test section and the original downstream tank [24]. This second tank is designed to separate the main flow of injected air from the water, while the first tank serves to fix the air content in the water.

It is certain that the compliance of the tunnel would have been considerably modified by these transformations and it seems unlikely that the cavity pulsation can be explained in such a way. Of course, the tunnel has to be suited to the introduction of a large amount of air for long periods. Moreover, for a complete view of the phenomenon, the air injection must be compatible with the large variations in ambient pressure and velocity which are customary in current facilities. If our information is correct, most of the existing tunnels do not meet with these conditions. It seems, therefore, that the rarity of observations concerning cavity pulsation is due more to the inadequacy of most the facilities rather than the compliance of a few of them.

(b) Is the Presence of an External Free Surface Necessary for Cavity Pulsation? From our experience, the answer to this question is negative, and we can imagine cavity pulsations in an infinite 2-D field of liquid. This assertion is supported by experimental observations and by theoretical considerations.

In many circumstances, the existence of strong cavity pulsations behind a wedge placed in our channel led to only small perturbations in the upper free surface of the flow. This result is supported by some simple calculations which show that the free surface subjected to a constant pressure, is not very sensitive to the effect of an internal source of pressure fluctuations. Then, it was conjectured that the channel free surface was not an essential element for the pulsation mechanism. This was verified when pulsations were obtained in the solid wall channel of the Neyrtec (formerly Sogréah) tunnel (see [8]). Of course, an objection may arise since, in this case as well, a free surface is present in the underpressurized tank downstream of the test section. In fact, the tank is connected to the test section by an almost cylindrical duct about eight meters long: the free surface is not near the pulsating cavity, but rather a long way from it. It is not therefore possible to give the same signification to the term "proximity of a free surface," in this case as with a free jet or a free surface channel, and the modeling procedure has to be carried out in a very different way when estimating the free surface effect. If we consider the pulsation as resulting

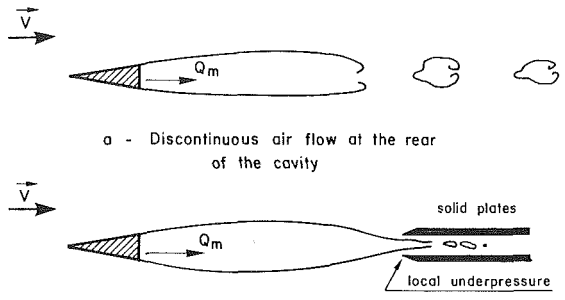

Fig. 4 Role of free streamlines curvature in air blocking

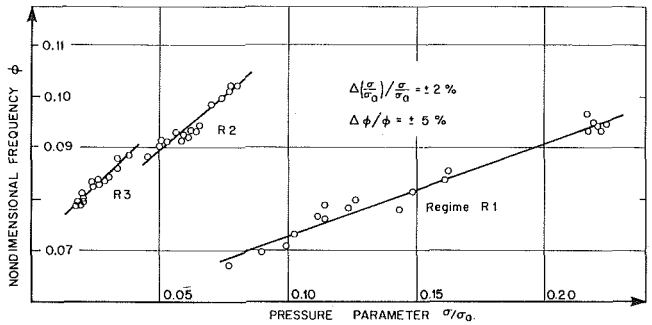

Fig. 5 Relation ϕ (σ/σ_a) - case of a rectangular wing - AR = 8. For smaller aspect ratios, the straight lines are nearly parallel, in each regime.

from the oscillation of the mass of the air-water mixture in the duct between the cavity in the test section and free surface in the tank, we obtain a normal mode of frequency at least of one order of magnitude less than the experimental pulsation frequency (thirty times in the best case).

On the theoretical side, the chief difficulty results from the pressure singularity at infinity in a 2-D unbounded flow: at infinity, the flow behaves as a fluctuating source, so that the potential is:

$$\varphi(r,t) \simeq \frac{q(t)}{2\pi} \log r$$

where $q(t)$ is the variable flow rate of the source. The general Bernoulli equation then shows that the pressure behaves as $\partial\varphi/\partial t$, and thus has a logarithmic singularity. In a 1-D flow, the singularity is stronger still, since $\partial\varphi/\partial t \simeq r$.

In order to avoid this difficulty, some models rely on stratagems such as: proximity of an external free surface [7] (Song), compressibility of water [16] (Hsu and Chen), three-dimensionality of the flow [7] (Benjamin). The three-dimensionality of the flow was also invoked by Wu [21], [22], and more recently by Furuya and Acosta [23]. Apart from the fact that the conclusions of such models are not confirmed by our experiments (for example, in the Song model, the parameter σ/σ_a is constant in each regime R_k, and in the Hsu-Chen model, the variation of the cavity length $\Delta l/l$ during a period is of the order $(\Delta\sigma/\sigma)^2$, while experiments give a σ/σ_a not constant and, for example, $\Delta l/l \simeq 0.5$, $\Delta\sigma/\sigma \simeq 0.1$), their main disadvantage is to prohibit the cavity pulsation in the 2-D, unbounded flow for an incompressible fluid. Moreover, they assume that the system is conservative and that pulsation is only a small perturbation around an equilibrium state. Actually, if such a hypothesis can be adopted in order to perform some calculations, it must be remembered that, on physical grounds, the mean and fluctuating aspects of the flow are both determined by the given flow parameters, in the absence of any given scale length. This aspect, which is closely related to the almost parallel geometry of the flow, should be taken in account in a complete theory of the phenomenon, just as the non-conservative character of the flow. Such a condition is undoubtedly difficult to fulfill, but the beginning of a solution is seen in the Woods model [18], in which it is assumed that the total volume of the cavity plus the wake is constant so that the pressure singularity at infinity disappears. Moreover, it allows momentum and energy exchanges between the cavity and its wake, thereby supporting the idea of a feed-back pulsation mechanism. It seems that among all the available theoretical models, the Woods model appears to be the most natural and the best suited to describe the pulsation of ventilated cavities.

(c) What Are the Mechanisms of cavity Pulsation? At the present time, it would seem that a full answer cannot be given to this question. Nevertheless, the outline of a future solution to the problem can be attempted.

Firstly, two problems need to be distinguished:

- the first concerns the discontinuities between the different pulsation regime R_k (with one, two, . . . wave lengths) and the hysteretic behavior of the flow, particularly in the $C_{Qv}(\sigma)$ diagrams, when the air flow rate is varied;

- the second is related to the pulsation mechanism itself. Here, the aim would be to describe the feedback mechanism, by which pulsation is possible, by one or possibly several chains of self-generating elementary mechanisms. Along a loop, the ratio of the amplitudes should be equal to one and the phase angle should be equal to 2π.

As far as the first problem is concerned, the following result was experimentally obtained in several flow configurations: the minimum value l_m of the cavity length is related to the wave length λ, in a regime R_k, by the relation:

$$\text{(A)} \qquad l_m = k\lambda$$

In other words, in the absence of any given reference length, the flow itself creates two lengths, the minimum length l_m (near enough to the mean length $\bar{l}$) and the wave length λ, both having to be compatible, in accordance with the relation (*A*). As the variation in l_m and λ, when C_{Qv} or σ varies, are different, it is understandable that the passage from one regime to the other is made by jumps in the values of σ and $\bar{l}$. But what is the physical quantity that triggers this passage? This remains unknown. Perhaps it would be correct to look in the direction of the overpressure at the rear of the cavity, but that is only a hypothesis.

Concerning the pulsation mechanism itself, here also a distinction can be made between the problem of the discontinuous release of air at the rear of the cavity and the periodicity problem. The formation of isolated air pockets is due to the blocking condition, resulting from the curvature of the streamlines which tends to close the cavity, as was easily proved by a simple experiment: by placing two plates in the wake of the cavity in order to create an underpressure zone in the liquid, the direction of the streamline curvature is reversed, the flow of air becomes continuous and the pulsation disappears (Fig. 4).

As regards the pulsation mechanism, it should be sufficiently complete not only to explain the periodicity of the phenomenon, but also to clear up the chief experimental results which can be summarized below, in addition to the relation (*A*):

(B) If the gravity effect is not important, and the circulation around the forebody is negligible, the fluctuations of both the free surfaces of the cavity are symmetrical.

(C) The fluctuating pressure is nearly the same throughout the cavity; its minimum value corresponds to about the instant when the minimum value l_m and the maximum value l_M of the cavity length are simultaneously reached. At that instant also, fluctuations of the free cavity boundaries, directed inwards, occur at the trailing edges of the forebody, according

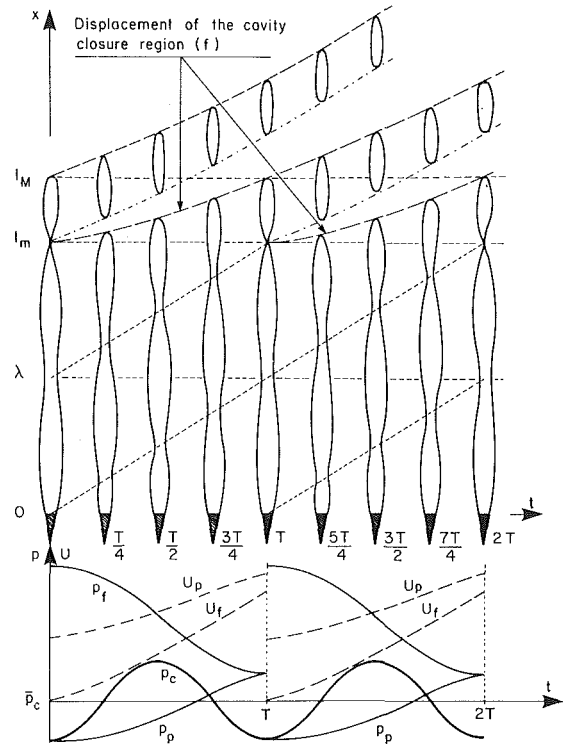

Fig. 6 Schematic Evolution of a R_2 cavity

to the relation (A). The amplitude of pressure fluctuations is between about 100 and 1000 Pa in the experiments.

(D) The adimensional frequency ϕ, previously defined in (4), is related to the parameter σ/σ_a. In each flow configuration, and for a pulsation regime R_k, we have:

$$\phi = a_k . \sigma/\sigma_a + b_k$$

where a_k is roughly proportional to k^2 (Fig. 5). Similar curves $\phi(\sigma/\sigma_a)$ were obtained in all configurations we tested, first in 2-D, then in 3-D flows.

(E) The pulsation regimes are determined by ranges of values of the parameter σ/σ_a. Thus we have, in most 2-D situations:

R_1 determined by $0.006 \lesssim \sigma/\sigma_a \lesssim 0.23$

R_2 determined by $0.022 \lesssim \sigma/\sigma_2 \lesssim 0.06$

the other regimes corresponding possibly to identical values of σ/σ_a in the narrow range lower than 0.022. In 3-D situations, these limits are slightly larger (Fig. 5).

It is tempting to compare the characteristics of the pulsating cavities to those of oscillating flows in which alternate vortices play a dominant role, for example the edgetone as described by Naudascher [19]. There, the relation (A) is replaced by: $L = (k + 1/4)\lambda$, where L is a given reference length, namely the distance between the jet orifice and the wedge which allows the sound production. The fluctuations of the velocity are antisymmetrical. The frequency is determined by a hysteretic diagram S (Re), where S is the Strouhal number, and Re, the Reynolds number, the values of which determine several different regimes of alternate vortices. In the case of ventilated cavities, it is not possible to correlate the experimental results on the basis of the Strouhal similarity. As the curve S (Re) can be considered to express the change in energy transfer between the mean flow and the fluctuating flow, the same can be said of the $\phi(\sigma/\sigma_a)$ curve. Thus the source of the fluctuating energy, in the case of ventilating cavities, must be looked for in the injected air flow. This straight-forward conclusion is in agreement with the non-conservative characteristics of the flow and with the very small values of the mean velocity gradients which could not allow any appreciable exchange of energy between the mean and the fluctuating aspects of the liquid flow.

We now attempt to examine the mechanisms which regulate the pulsation of the cavities and we begin by considering the rear of the cavity. The sketch (Fig. 6) retraces the qualitative history of some specific qantities over two periods of pulsation for a cavity with two wave lengths (Regime R_2). It is based on the assumption that the Woods condition of constant volume is restricted to the near wake of the cavity, i.e., to a distance of one or perhaps two wave lengths. It can be seen that the variations in the different quantities, from the initial instant at which an air pocket separates from the cavity, are coherent:

- the overpressure p_f in the cavity closure region, which is created at the initial instant from the juncture of the perturbations of both the cavity boundaries, and which is then at its maximum, diminishes when the air pocket moves away from the cavity;
- the pressure p_p in the air pocket, which is initially equal to the minimum value of the cavity pressure, subsequently grows and reaches the same values as p_f;
- the volume v_p of the air pocket decreases and it is therefore accelerated. The volume reduction is balanced by the growth of the cavity;
- the velocity U_f of the rear of the cavity, initially equal to zero, increases to reach a value close to the velocity U_p of the air pocket.

The complete treatment of these quantities should be based on the use of specific relations. Among these, we find:

- the air mass in an air pocket is equal to Q/f;
- the velocities U_f and U_p are related repectively to the variations of the cavity volume v_c and to the virtual mass of the air pocket;
- the variations in the volumes v_p and v_c are related by the Woods condition;
- the variations in v_c result from perturbations in the vertical component v of the velocity;
- in addition, they are related to the air flow rate Q_m by

$$\frac{d(p_c v_c)}{dt} = Q_m \times \text{constant}.$$

Let us turn our attention to the upstream part of the cavity. One may ask what is the exact source of the velocity fluctuations, particularly when the phase relation (A) is taken into account. Here the matter is not absolutely clear:

- On the one hand, experiments show that the pressure in the cavity is nearly uniform, in amplitude and phase, to within the accuracy of the pressure transducers, i.e., up to about 30 pascals (experimental result C mentioned above).
- On the other hand, from the theoretical viewpoint, it is possible to consider several a priori mechanisms, all dependent only on the hydrodynamic conditions:

1) Pressure waves traveling in the cavity at the speed of sound. However, for the experimental frequencies (between 5 and 45 Hz), the wave length would be in all cases longer than cavity length by an order of magnitude. This mechanism must therefore be excluded.

2) Spatially uniform pressure variations due to air compressibility and to variations in cavity volume v_c. For example, we can consider a plane jet subjected on one face to pressure fluctuation $p' . \exp[j\omega t]$. In the case of an infinite jet, the transverse velocity fluctuations are $jp' . \exp[j\omega t'/\rho\omega h$, whereas for a semi-infinite jet starting from $x = 0, y = 0$, the expression becomes $jp'/\rho\omega h\{\exp[j\omega(t - x/V) - \exp[j\omega t]\}$ (h is the jet thickness). Both models give the experimental order of magnitude of the cavity boundary fluctuations.

However, the phase relation between the free surface fluctuations and the pressure fluctuations does not agree with the phase relation given in (A) and (C) since the models give them in quadrature. Of course, the spatial uniform pressure fluctuations do not generate any velocity fluctuations when they act on the free surface of a channel or a semi-infinite medium.

3) Finally, consideration can also be given to an inertial effect of the air flowing in the deformable duct formed by the cavity, the air velocity being less than the water velocity. The pressure is at its minimum near the narrows and thus complies with the phase condition (A). Here the question to be dealt with is Helmholtz instability and it is possible to perform some classical calculations [20], considering for example two parallel flows, the first being limited by a solid wall and the second by a free surface. If the calculated amplification rate of the interface fluctuations is used to approximate the evolution of an elliptic cavity with mean length $\bar{l}$, the result is pressure fluctuations with variations in the right direction but amplitude about twenty times smaller than the experimental value. This does not contradict the experimental results which give uniform pressure fluctuations since the calculated values are of the same order of magnitude as the experimental errors. Moreover, it means that very small pressure fluctuations can produce finite interface fluctuations when Helmotz instability is in action.

Thus, as a conjecture, the latter mechanism can be considered as responsible for the trigger action of the cavity free surface perturbations and for part of their amplification. The phenomenon could be described as follows: on one side the largest part of the pressure fluctuations would be due to the uniform effect of the air inflow and air compressibility while the pressure fluctuations due to the inertial effect would come in addition to the former and would be responsible for the onset of the free surface fluctuations.

Consideration is not given here to the eventuality of an interaction between the cavity and the air feed duct. That is because, from experiments, it appeared that the pressure fluctuations in the duct, upstream of the cavity, were late with respect to the pressure fluctuations in the cavity. The ratio of amplitude was about 1/10 and the ratio of the volume was about 1/8: the fluctuating energies in the duct and in the cavity differed by at least an order of magnitude. Thus it seems doubtful that the mentioned interaction, although theoretically plausible, is a serious candidate for the pulsation mechanism.

Conclusions

In the present paper, a survey of the main mechanisms of air entrainment in largely developed cavity flows is given, with particular attention to plane, almost horizontal flows. These mechanisms differ according to the amount of air injected into the cavity. The most typical situation is found for moderate air inflow rates: there is a strong interaction between the flow geometry, the cavity pressure and the air entrainment. Then, in most circumstances, the air is entrained by the periodical emission of air pockets at the rear of the cavity. The characteristics of this pulsation mechanisms, which is believed independent of the compliance of the facilities where it is observed, are relieved. It should be stressed that, in the absence of any given reference length, both the mean flow and the fluctuating flows are simultaneously determined by the global flow parameters, and chiefly by the air flow rate. It does not therefore seem pertinent to consider the fluctuating periodical flow as a small perturbation of a stable configuration. It is more so necessary to look for one, or perhaps several, chains of elementary mechanisms involving natural instabilities, and connected by adequate phase relations. For the anticipated feed-back mechanism, by which the work of the injected air against the wake inertia is expressed, the Woods condition of constant volume for the total body: cavity plus wake, plays an essential role since it allows the pulsation in a 2-D space without any pressure singularity at infinity. Finally, it appears that the hysteretic behavior of the flow, when the air flow rate changes, on the one hand is allowed by the memory of the unsteady free surface flows [21] and, on the other hand is due to the existence of two reference lengths created by the flow itself, namely the cavity length and the wavelength of the cavity boundary fluctuations.

It is worth nothing that, while the picture sketched seems to be qualitatively correct, numerous aspects remain unaccounted for. In particular, considerable effort have to be made in order to explain, from a quantitative viewpoint, the main characteristics of the relations on the one hand between the adimensional frequency ϕ and the pressure parameter σ/σ_a and, on the other hand, between the volume of air flow coefficient C_{Qv} and the relative cavity underpressure σ.

Acknowledgments

This research was carried out with the support of the French "Direction des Recherches, Etudes et Techniques."

References

1 Parkin, B. R., and Kermeen, R. W., "The Roles of Convective Air Diffusion and Liquid Tensile Stresses During Cavitation Inception," *IAHR Symposium on Cavitation and Hydraulic Machinery*, Sendai, Sept. 1962.

2 Brennen, C., "The Dynamic Balances of Dissolved Air and Heat in Natural Cavity Flows," J. OF FLUID MECH., Vol. 37-1, 1969, pp. 115-127.

3 Billet, M. L., and Weir, D. S., "The Effects of Gas Diffusion on the Flow Coefficient for a Ventilated Cavity," ASME J. OF FLUID ENG., Vol. 97, No. 4, Dec. 1975, pp. 501-506.

4 Rogala, R., "Entraînement d'air par lame déversante," *La Houille Blanche*, No. 1, 1981, pp. 15-21.

5 Resch, F. J., Leutherusser, H. J., and Ward, C. A., "Entraînement d'air et réaération en écoulement hydraulique," *Symp. IAHR/SHF*, Grenoble, Mar. 1976, pp. 347-357.

6 Silberman, E., and Song, C. S., "Instability of Ventilated Cavities," *J. of Ship Res.*, Vol. 5, No. 1, June 1961, pp. 13-33.

7 Song, C. S., "Pulsation of Ventilated Cavities," *J. of Ship Res.*, Vol. 5, No. 4, Mar. 1962, pp. 1-20.

8 Michel, J. M., "Ventilated Cavities: A Contribution to the Study of Pulsation Mechanism," *Symp. IUTAM*, Leningrad, June 1971, pp. 343-360.

9 Michel, J. M., "Sillages plans supercavitants—Etude physique," Thesis, Grenoble, Mar. 1973.

10 Cox, R. N., and Clayden, W. A., "Air Entrainment at the Rear of a Steady Cavity," *Symp. on Cavitation in Hydrodynamcis*, Teddington, 1955.

11 Campbell, I. J., and Hilborne, D. V., "Air Entrainment Behind Artifically Inflated Cavities," *2nd ONR Symp. on Naval Hydrodynamics*, 1958, pp. 467-480.

12 Pernik, A. D., "Cavitation Problems," Leningrad, 1966, pp. 422-431.

13 Ephstein, L. A., "Characteristics of Ventilated Cavities and Some Scale Effects," *Symp. IUTAM*, Leningrad, June 1981, pp. 173-185.

14 Verron, J. and Michel, J. M., "Entraînement d'air dans les écoulements à cavités ventilees: modes d'évacuation observés à l'aval des cavitiés," *Symp. IAHR/SHF*, Grenoble, Mar. 1976, pp. 359-367.

15 Verron, J., "Ecoulements cavitants ou ventilés autour d'ailes d'envergure finie en presénce d'une surface libre," Thesis Dr. Ing. Grenoble, July 1977.

16 Hsu, C. C., and Chen, C. F., "On the Pulsation of Finite Ventilated Cavities," *Hydronautics*, Techn. Rept., 115-4, 1962.

17 Benjamin, T. B., "Note on the Interpretation of Two-Dimensional Theories of Growing Cavities," *J. of Fluid Mech*, Vol. 19-1, 1964, pp. 137-144.

18 Woods, L. C., "On the Instability of Ventilated Cavities," *J. of Fluid Mech.*, Vol. 26-3, 1966, pp. 437-457.

19 Naudascher, E., "From Flow Instability to Flow-Induced Excitation," ASCE, *J. of Hydraulics Division*, June 1967, pp. 15-40.

20 Lamb, *Hydrodynamics*, Dover Publ., pp. 373-374.

21 Wu, T. Y. T., "Unsteady Supercavitation Flows," *2nd Symp. on Naval Hydrodynamics*, 1958, pp. 293-313.

22 Wu, T. Y. T., "Cavity and Wake Flows," *Annual Reviews of Fluid Mechanics*, Vol. 4, 1970, pp. 243-284.

23 Acosta, A. J., and Furuya, O., "A Brief Note on Linearized, Unsteady, Supercavity Flows," *J. of Ship Research*, Vol. 23, No. 2, June 1979, pp 85-88.

24 Rowe, A., and Kueny, J. L., "Supercavitating Hydrofoils with Wetted Upper Sides," *J. de Mécanique*, Vol. 19, No. 2, June 1980, pp. 249-294.

Air Entrainment in Ventilated Cavities: Case of the Fully Developed "Half-Cavity"

A. R. Laali
Research Student.

J. M. Michel
Research Worker.

Institut de Mécanique de Grenoble, Grenoble, France

Experimental results are given concerning the behavior of the so called "half-cavity" which is formed by a plane water jet, initially horizontal, projected over a small step at the bottom of a channel. The relation between the air flow rate and the cavity pressure is given particular consideration: the influence of geometrical or dynamic parameters on this relation is studied and it is found that the dominant role is played by the Froude number and the cavitation number. Other results concern cavity pulsation frequency and cavity length. Some theoretical considerations concerning the flow geometry are necessary to identify the gravity effect for the case where the cavity is long compared to the height of the step.

Introduction

The formation of cavities by natural or artificial ventilation has been considered as a way of increasing the efficiency of hydraulic components for about twenty years. In some cases, for example flood spillways, the aim is to reduce the danger of cavitation erosion caused by the high-speed flow of water over a rough concrete surface. In the naval engineering field, the aim is to create a developed vented cavity in order to diminish the drag of hydrofoils, propeller blades or hull bottoms.

In ventilated flows, as in supercavitating flows, available methods can generally be used to obtain a relatively good approximation of the relation between flow geometry and pressure or force coefficients: a common example is the relationship between the cavity length l and the relative underpressure of the cavity σ, in which, however, coefficients as large as 2.4 may be necessary in order to compare theory and experiments [1], at least if simple models are used. But, in the case of artificial ventilation, the mass air flow rate Q_m is a quantity which is imposed. The problem is then to determine the pressure distribution, i.e. the parameter σ when Q_m is given. In the past, the $Q_m(\sigma)$ problem was approached by several experimentors on the occasion of tests on vented hydrofoils, for example Lang and Daybell [2], Schiebe and Wetzel [3], Silberman and Song [4], but it was not usually considered as a problem on its own, except in the axisymmetric configuration and for low Froude numbers ([5], [6]).

Then it was decided to study this problem in a geometrically simplified configuration and the choice was oriented to the configuration called here the "half-cavity": this is formed by an initially horizontal plane water jet, projected over a step, and which bends under the influence of both gravity and the pressure difference between its upper and lower free surfaces. The jet then comes into contact with a solid plane wall which has a small slope and forms the channel bottom (Fig. 1). Beside its own interest, this configuration approximately simulates the air flow in a "foil cavity," i.e., the cavity which is formed downstream of a base-vented hydrofoil under a free surface, all the effects related to the incidence variations, the limited span and the shear stresses at cavity closure being, of course, excluded. Such an assessment is supported by the observation of the major role of air pressure in the foil-cavity behavior, which results in symmetrical fluctuations of the pulsating cavity boundaries and which relegates the other effects to a second order. In particular, the half cavity has a reentrant jet for moderate values of air flow rate, and is characterized, as the "foil" cavity, by the strong interaction between the geometry, the cavity pressure and the air entrainment. It follows that the occurence of cavity pulsations and the hysteretic behavior when the air flow rate changes can be expected with reasonable probability. Experience corroborates this anticipation and it is hoped that the experimental results obtained here, especially those ones which concern the relation $Q_m(\sigma)$, the minimum value σ_m of σ and the critical value of the air flow rate when the pulsating regime begins, can be transposed to the case of the base-vented hydrofoil.

Experimental Setup

The experimental setup was installed in the first test section of the hydrodynamic tunnel of the Institut de Mécanique de Grenoble (see [24] in the previous paper by Michel [7]). In the following account of the experimental results, two series of

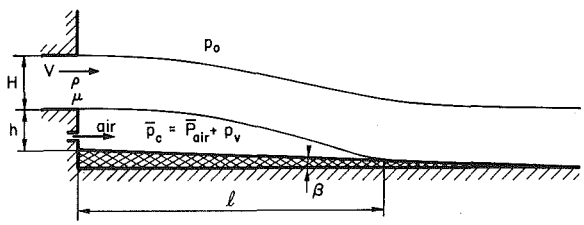

Fig. 1 Sketch of the flow

Contributed by the Fluids Engineering Division for publication in the JOURNAL OF FLUIDS ENGINEERING. Manuscript received by the Fluids Engineering Division, June 10, 1982.

tests are referred to: the second series was decided in order to increase the range of variation of several parameters, after the first series has confirmed the interest of the half-cavity configuration. Thus, while the first series was conducted through rather simple modifications of the existing device, the second series involved the construction of a new channel and a new converging nozzle. On the whole, it was possible to vary the following parameters (Fig. 1):

—the jet height H between 10 and 20 cm,
—the step height h between 2 and 6 cm,
— the slope β between 1.8 deg and 4 deg,
—the water speed V between 3 and 12 m/s,
—the absolute pressure p_0 over the upper free surface of the jet between 0.05 and 1.0 atm.

In addition, some experiments were made with artificial roughness added to the lower surface of the injector.

Similarity Parameters. According to the analysis presented in [7], it can be seen that the main given nondimensional parameters in the present configuration are the following:

—the cavitation number $\sigma_v = \dfrac{p_0 + \rho g H - p_v}{\frac{1}{2}\rho V^2}$

—the Froud number $F_r = \dfrac{V}{\sqrt{gH}}$

—the mass air flow coefficient $C_{Qm} = \dfrac{Q_m}{\rho V h b}$

where b is the width of the water jet. To those parameters, the Reynolds number and the Weber number must be added, if necessary.

The study of the resulting parameter is of interest:

—the relative underpressure in the cavity:

$$\sigma = \frac{p_0 + \rho g H - \bar{p}_c}{\frac{1}{2}\rho V^2} = \sigma_v - \sigma_a$$

with $\sigma_a = \bar{P}_{air}/1/2\rho V^2$, where $\bar{P}_{air}$ is the mean pressure of air in the cavity.

—the relative cavity length l/c. In the case of pulsating cavities whose length varies between a minimum value l_m and a maximum value l_M, the mean value $\bar{l} = 1/2(l_m + l_M)$ is taken,

—the nondimensional frequency of the pulsation:

$$\phi = f/\sqrt{\bar{P}_{air}/\rho h \bar{l}}$$

The experimental results will be presented in the form of curves $\bar{l}/c(\sigma)$, $\phi(\sigma/\sigma_a)$, $C_{Qv}(\sigma)$, (see [7]), where C_{Qv} is the volume air flow coefficient:

$$C_{Qv} = \frac{Q_m}{\bar{\rho}_{air} V h b}$$

and $\bar{\rho}_{air}$ is the main value of the specific mass of air in the cavity.

Experimental Procedure. The various parameters were measured by standard methods: water and mercury manometers, rotameters, stroboscope, etc. The expected precision of such methods is about one percent. In a few cases, the dispersion of points is not due to defective instrumention, but to the unsatisfactory definition of the phenomenon to be measured. For example, it is difficult to locate the rear part of the cavity exactly and therefore difficult to measure the length l. In addition, on occasion, the water level in the manometer giving the difference $p_0 - p_c$ oscillated between two extreme values thereby indicating an instability the characteristics of which were not examined in greater detail. In such cases, the two extreme values of $p_0 - p_c$, and thus σ where recorded: on the graphs $\bar{l}(\sigma)$ and $C_{Qv}(\sigma)$ the corresponding points thus have twin values; it is to be noted that the deviation in σ is not great.

The change in the phenomenon in the presence of pulsations is known not to be the same when the injected air flow rate is increased or decreased: the $C_{Qv}(\sigma)$ diagram has hysteris loops in this case. For simplicity's sake, the present study is limited to the change in the phenomena associated to a decrease in air flow rate variation. The test was therefore carried out in the following manner: with a given geometry, flow speed V and pressure p_0, the maximum air flow rate was injected and then the air flow rate was gradually reduced, in discontinuous steps, each time noting the change in the characteristic parameters of the phenomenon, especially the critical air flow rate at the instant when the pulsating regime became established.

Contrary to the case of a cavity forming behind a foil where the water injected by the reentrant jet is reentrained downstrean by the lower free surface, the presence of the solid wall limiting the half-cavity occasionally leads to the formation of layer of calm water which rises inside the cavity and which contributes to balancing the overpressure in the rear part of the cavity. Since the resultant head of this layer is typically of 1 or 2 cm of water, and should be compared with an overpressure which is, in the most adverse case, about one tenth of the dynamic pressure $\rho V^2/2$ [8], the disturbance cannot be very significant.

In the major part of the tests, air was injected in the opposite direction to the water flow, so as to avoid any effect of initial momentum on air evacuation at the rear of the cavity.

Hydrodynamic Modeling

In the view of the lack of experimental data available and the variety of mechanism involved in the air entrainment phenomenon, it does not seem possible to propose a suitable modeling system. However, hydrodynamic methods can be used to establish a relationship between flow geometry and the pressure or gravity forces in order to compare it with the experimentally established law $l(\sigma)$. This procedure, which is standard practice in studies of supercavitating flow, becomes particulary necessary in the case of vented flows since the cavity length plays the role of an intermediate parameter in the pulsation study, as can be seen by the shape of the admimensional frequency ϕ. In addition, it offers the opportunity of reflecting on the part played by gravity in this flow.

Two models were made. A survey of these models is given in Appendices A and B. In each model, the underpressure σ is given and the geometry is simplified by ignoring the slope β of the floor of the flume.

In the first approach, the effect of gravity is ignored. A linearized method is used, based on the fact that the parameter h/l is small and therefore that the slope of the current lines is small, except in the vicinity of the rear of the cavity. In this case, for large values of the parameter l/H, the relation $l(\sigma)$ is found to behave asymptotically as follows:

$$\frac{l}{H} \sim 2\sqrt{\frac{h}{H} \cdot \frac{1}{\sigma_p}} \qquad (1)$$

where $\sigma_p = (p_0 - p_c)/1/2\rho V^2$, under the condition $\sigma_p \lesssim 0.2\ h/H$ or $l/H \gtrsim 4.5$ (this condition was fulfilled fairly often in a good number of experimental situations). It is worth noting that the relation (1) can be found simply if it is assumed that the jet subjected to the uniform pressures p_0 and p_c behaves as a thin circular jet between the injector and the floor of the flume.

In the second approach, consideration is given to the

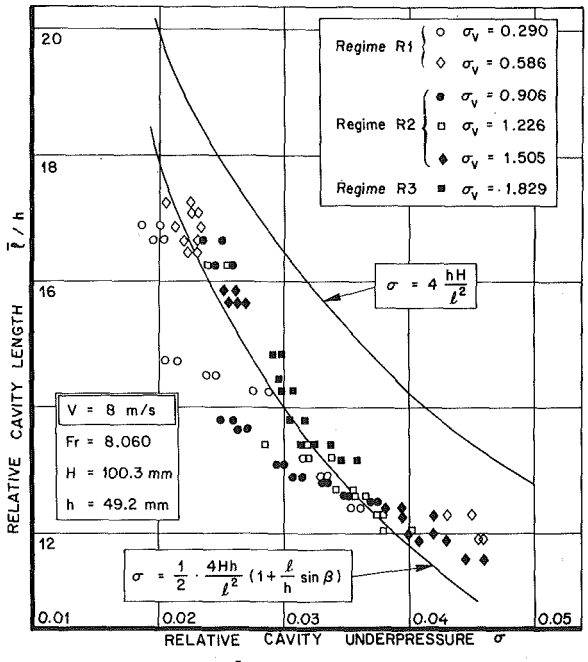

Fig. 2 Relation $\frac{\bar{l}}{h}(\sigma)$ $V = 8$ m/s

$$\Delta\sigma/\sigma = \pm 2 \text{ percent} - \Delta\left(\frac{\bar{l}}{h}\right)\Big|\frac{\bar{l}}{h} = \pm 5 \text{ percent}$$

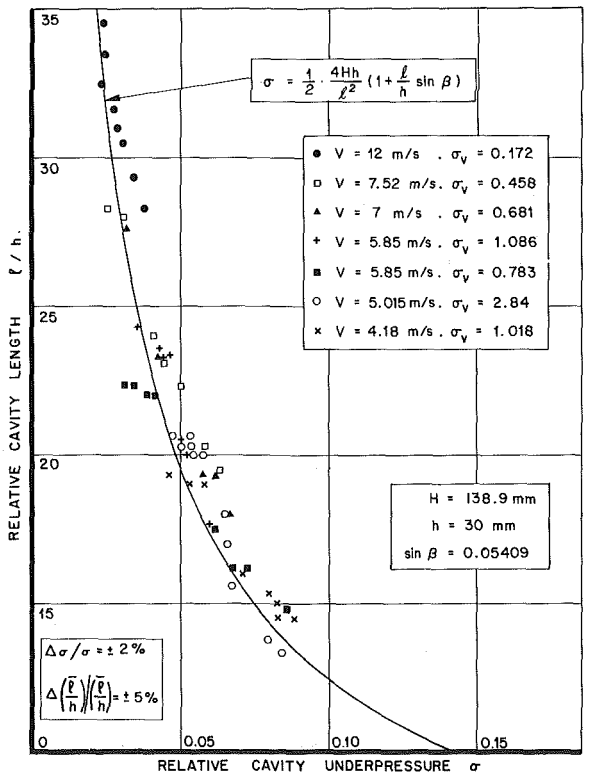

Fig. 3 Relation $\frac{\bar{l}}{h}(\sigma)$

evolution of a thin plane jet under the combined influence of gravity and the differential pressure $p_0 - p_c$. Depending on the value of the two parameters controlling the flow, quite complex geometries are obtained since the curves describing the average line of the jet are of the cycloid family. However, that part of the curve representative of the actual flow is restricted to the vicinity of the horizontal injector. In this region, the equation of the average jet line is reduced to the osculating parabola and becomes:

$$y = -\frac{\sigma}{4}\cdot\frac{x^2}{H} \tag{2}$$

where σ is defined as previously. The relation $l(\sigma)$ can be deduced for a thin jet if it is assumed that the jet impinges on the solid wall at a point $x = l$, $y = -h$. In such case, the relation (1) is found in which σ_p is replaced by σ. This result is remarkable since it means that the effect of gravity on the geometry is taken fully into account by the very definition of the number σ which can be written:

$$\sigma = \sigma_p + \frac{2gH}{V^2} \tag{3}$$

whereas, in the study of supercavitating flows around foils placed under a free surface, a direct gravity effect remains on the behavior of the cavity length and on the hydrodynamic forces [9]. The physical reason for this fact is that, in the present configuration, the pressure and gravity forces act almost throughout in the same direction since the flow is very elongated horizontally. The same result can be found by superimposing two deflections h' and h'': the first, due to the differential pressure $p_0 - p_c$ in the absence of gravity, is given according to (1) by: $h' = l^2\sigma_p/4H$ while the second, due to the action of gravity during the transit time $t \simeq l/V$ is given by $h'' = gt^2/2 = gl^2/2V^2$. Thus we obtain: $h = l^2/4H(\sigma_p + 2gH/V^2) = l^2\sigma/4H$ which is the relation announced for a thin jet.

For a closer expression of reality, allowance must be made for the thickness H of the jet and for the slope β of the floor of the flume. Thus, by simple geometeric considerations, the following relation is obtained:

$$\sigma = 4\frac{Hb}{l^2}\left(1+\frac{l}{h}\sin\beta\right) \tag{4}$$

which will be compared below with the experimental results.

Experimental Results

In this section, experimental results of both the previously mentioned test series are described.

It is worth recalling here that the cavity pulsation, when it exists, occurs for moderate values of C_{Qv} and that it is then characterized by regimes with one, two or three wave lengths [7].

In the half cavity configuration, each flow regime corresponds to a range of σ_v values for a geometry fixed by values of h and H. In the majority of the following figures, the regime and the corresponding value of σ_v have been indicated. Of the points having the same value of σ_v, only those which correspond to a moderate air flow rate thus describe a pulsating regime. They are more easily identifiable in the C_{Qv} (σ) diagrams where the changeover to pulsating regime, for a decreasing air flow rate, is marked by a horizontal arrow.

Cavity Length – Relation $l(\sigma)$. In the light of results (Figs. 2 and 3), the following comments can be made:

(*a*) As expected, the relation $l(\sigma)$ is influenced neither by σ_v, nor by the pulating regime: the general geometry depends only on the pressure difference $p_0 = \bar{p}_c$ and on the velocity v.

(*b*) Fairly good agreement with experimental results is found if the right-hand side of relation (4) is multiplied by the coefficient $K = 1/2$. The theoretical form (1) of the relation $l(\sigma)$ is shown on Fig. 2.

The other tests showed that all the cases are fairly well accounted for by the introduction of the same coefficient K. If the relation (4) is reversed in the form:

$$l_{th}(\sigma) = 2\sqrt{\frac{Hh}{\sigma}}\left(1+\sqrt{\frac{Hh}{\sigma}}\sin\beta\right)$$

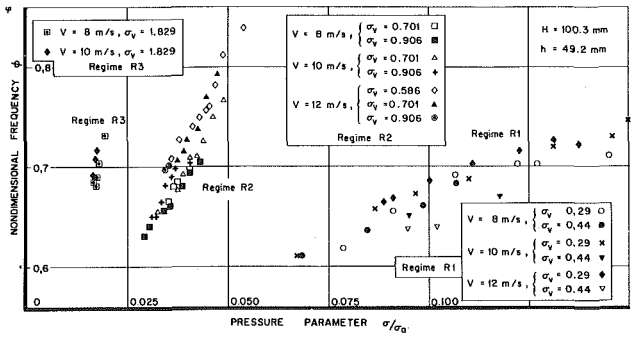

Fig. 4 Relation $\psi(\varphi/\sigma_a)$

$$\Delta\left(\frac{\sigma}{\sigma_a}\right)\Big/\frac{\sigma}{\sigma_a} = \pm 2 \text{ Percent} - \Delta\phi/\phi = \pm 5 \text{ percent}$$

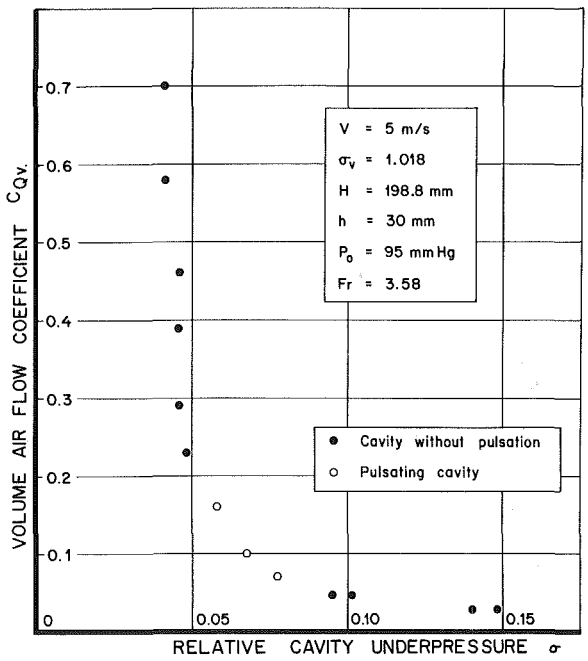

Fig. 5 Relation $C_{QV}(\sigma)$—Example of L-shaped curve for the half cavity configuration • $\Delta\sigma/\sigma = \pm$ 2 percent $\Delta C_{QV}/C_{QV} = \pm 2$ percent — Same incertitude in Figs. 6 to 11.

we obtain: $l_{exp} \simeq 2/3\ l_{th}$. The coefficient 2/3 is to be compared with the coefficient 2.4 already mentioned, obtained in the case of supercavitating flow: the geometry of flows with largely developed cavities, while dominated by pressure and inertial forces, still remains a difficult problem because of its almost one-dimensional character which associates large length variations with any variation, however small, in the wall geometry or the pressure.

(*c*) In the range of available velocities, the cavity length is independent of velocity (Fig. 3). As already mentioned, this means that the gravity influence is taken fully into account by the definition of the relative underpressure.

(*d*) Other tests show that vapor cavities agree with the same relation and with the same coefficient K. In such a case, $\sigma = \sigma_v$ is taken by neglecting air diffusion in the cavity.

Pulsation Regimes – Frequency. Figure 4 shows the experimental results concerning the dependence of the adimensional frequency ϕ on the parameter σ/σ_a. In each of the regimes R_k, where k is the number of wavelengths, the relation is roughly linear. It is remarkable that the presentation $\phi(\sigma/\sigma_a)$ enables plenty of experimental points to be grouped together, corresponding to very different values of both velocity and ambient pressure. The R_k regimes are established in the following ranges of values of σ/σ_a:

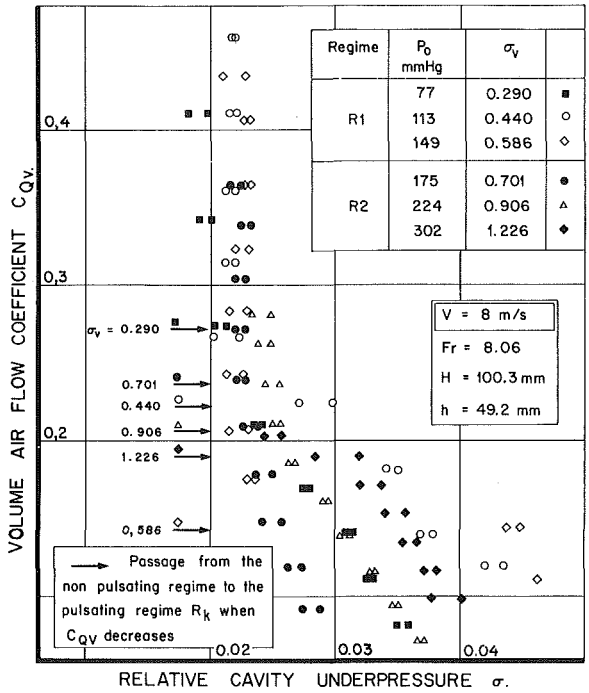

Fig. 6 Relation $C_{QV}(\sigma,\sigma_V)$, V fixed

$$\left.\begin{aligned} R_1&: 0.060 < \sigma/\sigma_a < 0.20 \\ R_2&: 0.020 < \sigma/\sigma_a < 0.06 \\ R_3&: 0.015 < \sigma/\sigma_a < 0.02 \end{aligned}\right\} \quad (5)$$

The parameters H and h have little effect on these limits. It is also found that the limits are almost the same as those obtained in the case of cavities formed downstream of hydrofoils in 2-D or 3-D flows [10], [11].

Moreover, for a constant jet height H, the pulsation regimes are found to correspond to separate ranges of values of the parameter σ_v. For instance, when $H = 100$ mm:

$$\left.\begin{aligned} R_1&: 0.029 \lesssim \sigma_v \lesssim 0.59 \\ R_2&: 0.059 \lesssim \sigma_v \lesssim 1.50 \\ R_3&: 1.8 \lesssim \sigma_v \end{aligned}\right\} \quad (6)$$

In general, the limit values increase with H and the upper values are the lowest velocities. The double conditions (5) and (6) are rather surprising at first glance. However, it will be shown that the inequalities (6) are the consequence of the inequalities (5) when the evolution of the minimum value σ_m of σ (see Fig. 12) is considered.

L-Shaped Curves $C_{Qv}(\sigma)$ in the Case of the Half-Cavity. The curve $C_{Qv}(\sigma)$ is generally L-shaped. The horizontal branch of this curve, which corresponds to short cavities with a small value of air flow rate, is difficult to obtain in our configuration. With the second experimental set-up, the velocity can be reduced to 4 m/s in order to obtain the full curve. Figure 5 shows such a curve ($V = 5\ m/s$, $p_0 = 95$ mm Hg or $\simeq 12.600$ Pa). The L-Shape and the three air flow regimes are clearly apparent. The curve is similar to the one which can be obtained for an ordinary cavity.

In most cases, it is not possible to obtain stable cavities for the small values of air injection. In such cases, the relation $C_{Qv}(\sigma)$ is expressed by curves such as those shown in Figs. 6 and 7, where either the velocity, or σ_v are kept constant. These figures express well the complexity of the phenomenon. Moreover, Fig. 6 shows that the concept of pulsation regime

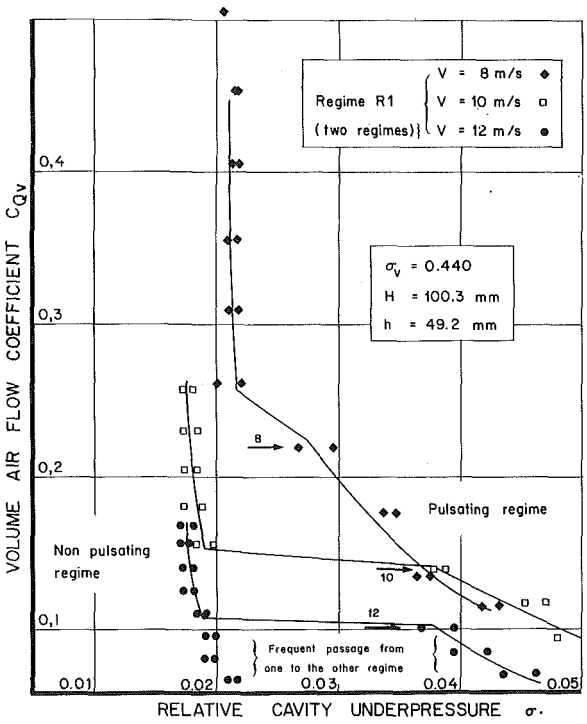

Fig. 7 Relation $C_{QV}(\sigma)$, σ_V fixed

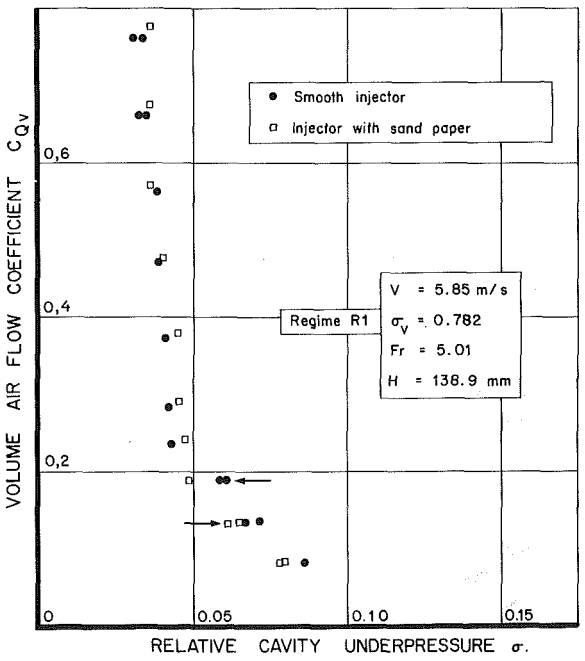

Fig. 8 Relation $C_{QV}(\sigma)$ – Influence of an artificial roughness of the injector.

starts to bring a semblance of order: in the same regime, the critical coefficient C_{Qv}—which marks the passage of nonpulsating to pulsating flow regime when reducing the air flow rate—diminishes when the value σ_v increases. However, it should be noted that the meaning of Fig. 6 and 7 is not the same: on Fig. 6, the change in σ_v at constant flow speed indicates the effect of the ambient pressure p_0 only, whereas in Fig. 7, the differences between the curves can be attributed either to the speed or to the ambient pressure.

Influence of Injector Roughness. The aim of the study of air entrainment by a flow from an injector provided with artifical roughness was to evaluate the effect of

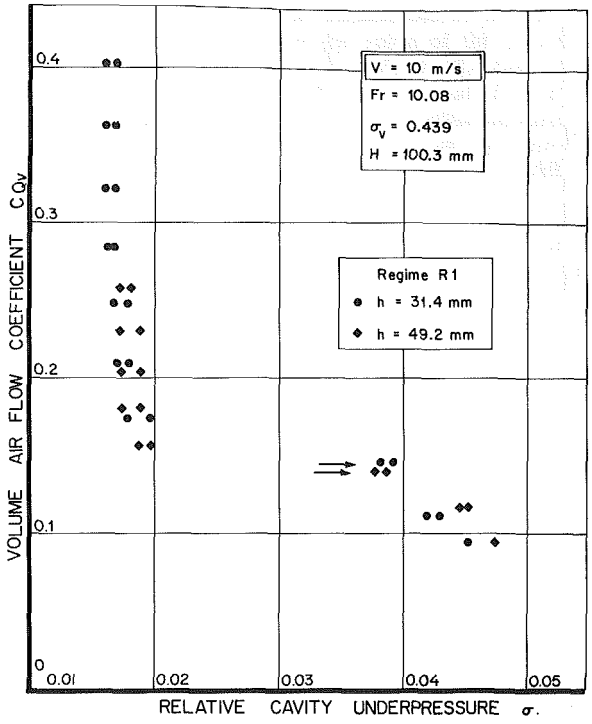

Fig. 9 Relation $C_{QV}(\sigma)$. Influence of the step height.

microgeometrical and microkinetic modifications of the free surface on air entrainment. This was based on a previous study made by Dodu and Heraud [12] in which these authors characterized the influence of nozzle roughness on the geometry of free surface asperities of a circular liquid jet. Their main conclusion is that for different roughness and velocity values, the increase in root-mean-square deviation, characteristics of the free surface transverse position, with respect to the deviation observed for a smooth nozzle, is considerable in that part of the jet close to the orifice, but that it decreases asymptotically with distance from the orifice and becomes zero after a certain distance. This distance is all greater, at equal speed, as the height of the asperities increases, and, at equal roughness, as the speed increases.

Since we do not posses an experimetnal means of controlling the height of the asperities of the nozzle and measuring the correlative fine fluctuations in cavity free surface, a single articial nozzle roughness was used, consisting of sand paper, and the resulting modifications in overall flow behavior were observed. The results obtained are qualitatively in agreement with the conclusions of Dodu and Heraud. An example is given on Fig. 8.

For nonpulsating cavities with a high air flow rate, the addition of an artifical roughness over the convergent section does not modify the air entrainment conditions or the relation $C_{Qv}(\sigma)$. In some cases, however, a small increase in the value of the minimum value σ_m is observed. In general, the free surface at the rear of the cavity is already sufficiently destabilized, particularly by the bubbles which ascend under the gravity effect, and an increase in agitation at the origin does not modify the air evacuation conditions or the gravity pressure, at least for the artificial roughness used in the tests. It can be seen also that the injector roughness reduces the critical value of C_{Qv} since it contributes to destroying the ordered structure of the rear part of the cavity and thus delays establishment of the blockage condition [7]. This effect is less important for larger speeds of water. On the whole, it appears that the influence of wall roughness on the relation $C_{Qv}(\sigma)$ is weak.

Effect of Step Height on Air Entrainment. The effect of step height on the relation $C_{Qv}(\sigma)$ was studied in the first and

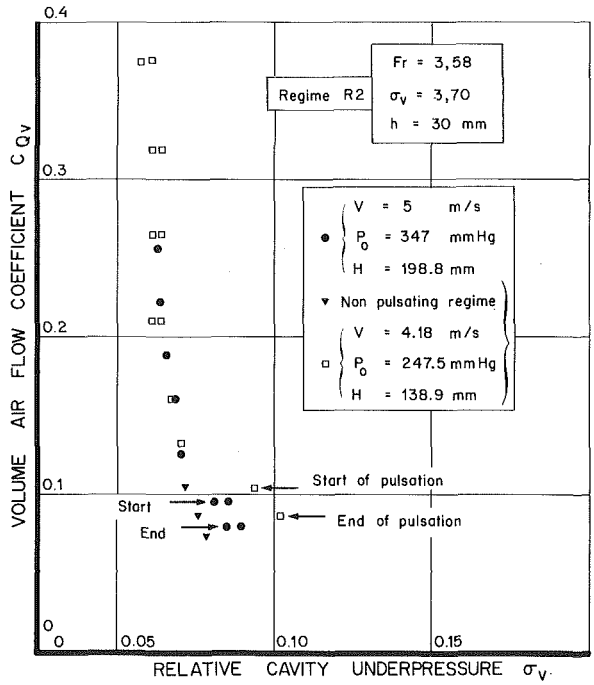

Fig. 10 Relation $C_{QV}(\sigma)$. Tests with identical σ_V and Froude numbers.

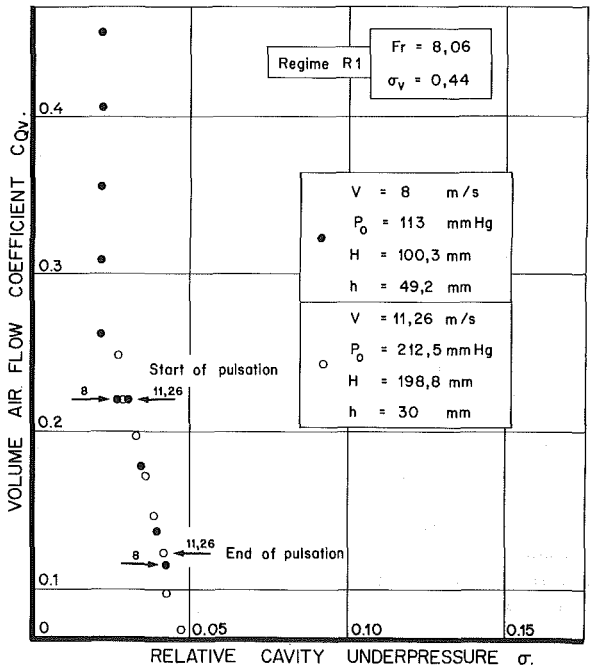

Fig. 11 Relation $C_{QV}(\sigma)$. Tests with identical σ_V and Froude numbers.

the second series of tests. Typical results are presented on Fig. 9. Generally speaking, step height has little effect on the relation $C_{Qv}(\sigma)$. The critical flow rate C_{Qv} seems to be totally independent of this height, as are the jumps in σ.

This independence is an important factor for analysis simplification. It means first of all the air flow rate is proportional to h. Secondly, in view of this independence, it can be affirmed with some safety that, in the analogous case of a ventilated cavity behind a foil, the thickness of the foil does not play an important part in air entrainment and in pulsating regime. This affirmation nevertheless needs to be moderated when the cavity thickness becomes approximately the same as the geometrical fluctuations of the cavity boundary [11].

Relation $C_{Qv}(\sigma)$: Significant Parameters. With a view to identifying the parameters governing the relationship between air flow and cavity pressure, an attempt was made to obtain the arrangement of representative experimental points on the basis of factors of theoretical and physical origin used in the formulation of similitude laws.

A number of particular results served as a guide for obtaining a less dispersed representation of the experimental points:

(*a*) The introduction of a fairly high artificial roughness on the lower part of the injector does not disturb the shape of the phenomenon very much. This result tends to show that, of the parameters initially considered, not only the relative roughness, but also Reynolds number (or at least the Reynolds number relative to the roughness dimensions) and the Weber number have little significance.

(*b*) When the pulsating regime occurs, it becomes established in one of the three regimes R_1, R_2, R_3, determined first of all by the value of the parameter σ/σ_a, and secondly by the value of the cavitation number σ_v, at least when the jet height is fixed and the variations in flow velocity V are not too great. The cavitation number, which also governs the direction of variations in the critical coefficient C_{Qv} in a regime, must be considered as an essential parameter.

(*c*) Since the flow related to turbulence can be temporarily ignored, consideration must be given to the part played by velocity with respect to gravity forces, i.e., consideration to Froude similitude.

It was therefore decided to compare the tests carried out with identical σ_v and Froude numbers. Examples are given in Figs. 10 and 11, which show that a suitable arrangement of experimental points is observed considering the dispersion of the measurements. The values of C_{Qv} critical are approximately equal. Figure 11 represents the more complete results obtained. The arrangement of points is very satisfactory; the start and end of pulsation correspond to the same value of C_{Qv} critical and for relatively different values of the jet height, velocity, and pressure at the free surface.

In conclusion to this section, it seems possible to affirm that within the limits of the experimental conditions, the cavitation number σ_v and the Froude number Fr are the major governing factors in the determination of the relationship between air flow and cavity pressure.

Dependence of the Minimum σ_m on σ_v and Fr. The characteristics curve of air entrainment, i.e., the L-shaped curve, can be roughly determined from five parameters, namely the minimum relative underpressure σ_m, the critical air flow coefficient C_{Qv}, the discontinuity $\Delta\sigma$ occuring on the establishment of a pulsating cavity regime, the minimum air flow rate C_{Qv} which corresponds to the limit case of developed cavity disappearance and corresponding relative underpressure σ maximum. Unfortunately, the last two parameters cannot be investigated systematically in the present case since they correspond to the almost horizontal part of the curve, i.e., to the case of small nonpulsating cavities at very low air flow rates which can be obtained only with great difficulty with the half-cavity configuration. As regards the discontinuity $\Delta\sigma$, it was found to reach a maximum value of the order to 0.01 to 0.02, tending to reach this maximum value in regime R_1, i.e., for the lower ambient pressure p_0 when the velocity V is fixed (Fig. 7).

Figure 12 demonstrates the dependence of σ_m on the Froude number and also shows an influence of the cavitation number σ_v. This influence is independent of the flow regime and pulsation regime. It is found that σ_m is a decreasing function of the Froude number, i.e., for an identical jet height, a decreasing function of the flow velocity. Consequently, σ_m is also an increasing function of σ_v at constant Froude number. This means that the gravity influence on the air evacuation by

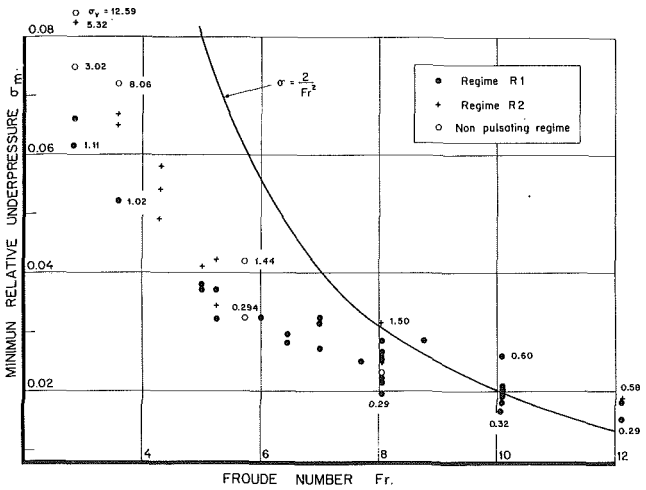

Fig. 12 Dependence of the minimum relative underpressure σ_m on the Froude number

bubbles is more efficient when the ambient pressure is high. On the contrary, the jet velocity, by reducing the time available for fluctuations to develop over a given distance, tends to increase the maximum length of the cavity and thus to decrease σ_m.

Figure 12 also shows, for comparison purposes, the curve $2/Fr^2$ which corresponds to $\sigma_p = 0$ in the relation (3) and thus to a jet subject to gravity only and not to a pressure gradient as well. When σ_m is smaller than $2/Fr^2$, which occurs for small values of the Froude number, the pressure in the cavity is greater than the ambient pressure p_0: the jet lies on a cushion of pressurized air and the pressure gradient promotes the rise of air bubbles. For example, with Fr = 3, a value of $\sigma_m \simeq 0.075$ is found for $\sigma_v \simeq 3$. The relation (3) gives $\sigma_p \simeq -0.147$ with $2/Fr^2 = 0.222$. Let $H = 10$ cm, then $V \simeq 3$ m/s, $p_c - p_0 \simeq 660$ Pa: this difference is of the same order as the pressure corresponding to the head H of water at rest (about 1000 Pa). For higher values of the Froude number, it is seen that σ_m is slightly greater than $2/Fr^2$: the situation is reversed, the pressure gradient tends to oppose the rise of bubbles. This effect is not very strong but would become significant if relatively high values of ambient pressure p_0 could be achieved in order to be able to increase the value of σ_v and thus the limit of σ_m. It is then probable that the internal turbulence, the shear forces at the interface and the surface tension all play an increasing part in the formation and growth of the disturbances allowing air to be evacuated.

Dependence of Critical C_{Qv} on σ_v and Fr. The tests demonstrate the dependence of critical C_{Qv} (whose value is between 0.1 and 0.4 approximately) on the Froude number Fr and on the cavitation number σ_v: for a constant Froude number, the C_{Qv} critical is a decreasing function of σ_v, i.e., of the ambient pressure p_0. This decrease is roughly linear. The pulsating regime R_k and the convergent roughness are factors also in this relationship. The results have a fairly wide dispersion, in particular for the low Froude number. This can be partly due to the experimental procedure, since the air flow rate was most varied continuously. The C_{Qv} critical is also a decreasing function of Fr at constant σ_v for a given pulsation regime and roughness. These results confirm that the domain of cavity pulsation is restricted by the high ambient pressure. Thus, in Fig. 7, the decrease of C_{Qv} critical when the velocity increases must be attributed firstly to the increasing values of the ambient pressure necessary to maintain the value of σ_v constant.

Remark on the Ranges of σ_v Values in Pulsating Regimes. The previously described results can explain [14] why the pulsating phenomen is subjected to the conditions (5) and (6). The most constant and best established fact in all the configurations is the restriction on the value of the parameter σ/σ_a analogous with the inequalities (5). In the case of the half-cavity, the variations in σ are too small for several regimes to be set up one after the other, for constant values of σ_v and Fr. Since the variations in σ in the pulsating regime R_k are themselves small, the following expression can be written:

$$\sigma \simeq \sigma_k = \sigma_m + \Delta\sigma_k$$

where σ_k is the average value of σ in R_k and $\Delta\sigma_k$ is the difference with respect to the minimum value σ_m established under nonpulsating conditions.

In the Regime R_1, the change of values of σ/σ_a is as follows:

$$0.06 < \sigma/\sigma_a < 0.20$$

With $\sigma_v = \sigma_1 + \sigma_a$, we can deduce:

$$6(\sigma_m + \Delta\sigma_1) \lesssim \sigma_v \lesssim 18(\sigma_m + \Delta\sigma_1)$$

The left-hand inequality expresses the fact that the pulsating conditions is not to set up when the values of σ_v is too small: this fact had already been observed [13]. The right-hand inequality is related to the boundary with the regime R_2. The presence of σ_m within the limits of the domain is indicative of the dependence on the Froude number. If the Froude number is assumed to be fairly high, according to Fig. 12 a value of $\sigma_m = 0.02$ can be taken. Therefore, $\Delta\sigma_1 \simeq 0.01$, and:

$$0.18 \lesssim \sigma_v \lesssim 0.54$$

These limits are of the same order as those obtained in the first inequality (6), due allowance being made for the rough approximations involved. Similar considerations can be made concerning the regime R_2 and R_3. It is possible to obtain limits which keep closer to experimental reality by taking into account the fact the value of σ_k, like that of the difference $\Delta\sigma$, increases with σ_v within a given regime. This simple example is sufficient to show the coherency of the experimental results that are obtained when the $C_{Qv}(\sigma)$ curve is reduced to its principal parameters.

Conclusion

The experimental results presented here demonstrate, within the limits of the values of the global parameters imposed, the importance of the part played by gravity, liquid inertia and pressure in air entrainment in quasi-horizontal flow. In particular, it has been noted that these parameters fix the limit value of the relative underpressure of the cavity when flow speeds are not too high; they therefore contribute to the determination not only of the local geometry of the cavity, but also the instabilities at the boundary of the half-cavity which allow air to be evacuated for high flow rates. At high water jet speeds, other mechanisms associated with the subscales of the flow take over from gravity in this limit situation. In particular, and subject to verification, such mechanisms could include the internal turbulence of the jet, the shear stresses at the water-air interface and the surface tension of the water. The study results confirm the presentation $C_{Qv}(\sigma)$ is more apt for describing overall air entrainment in a developed cavity. They show that the study of the effect of global parameters is an indispensable stage in the approach to the phenomenon since, despite raising numerous problems, it gives a preliminary idea as to the relative importance of the various mechanisms involved. Finally, the reduction of the $C_{Qv}(\sigma)$ curve to its essential parameters enables, on the one hand, the particular characteristics of the pulsating flow to be dissociated from the more general characteristics of ventilated flows, and, on the other hand, the coherency of different experimental results to be established.

Acknowledgments

This work was supported by the French "Direction des Recherches, Etudes et Techniques" (Contract 78-490).

References

1 Rowe, A., and Michel, J. M., "Two-Dimensional Base-Vented Hydrofoils Near a Free Surface: Influence of the Ventilated Number," JOURNAL OF FLUIDS ENGINEERING, Vol. 97, No. 4, Dec. 1975, pp. 465-474.

2 Lang, T. C., and Daybell, D. A., "Water Tunnel Tests of Three Vented Hydrofoils in Two-Dimensional Flow," *Journal of Ship Research*, Vol. 5, No. 3, Dec. 1961.

3 Schiebe, F. R., and Wetzel, J. M., "Ventilated Cavities on Submerged Three Dimensional Hydrofoils," St. Anthony Falls Hydraulic Laboratory, Tech. Paper No. 36, Dec. 1961.

4 Silberman, E., and Song, C. S., "Instability of Ventilated Cavities," *J. of Ship Research*, Vol. 5, No. 4, June 1962, pp. 1-20.

5 Cox, R. N., and Clayden, W. A., "Air Entrainment at the Rear of a Steady Cavity," Symp. on Cavitation in Hydrodynamics, Teddington (1955).

6 Ephstein, L. A., "Characteristics of Ventilated Cavities and Some Scale Effects," Symp. IUTAM, Leningrad, June 1971, pp. 173-185.

7 Michel, J. M., "Some Features of Water Flows With Ventilated Cavities," ASME JOURNAL OF FLUIDS ENGINEERING, present issue.

8 Michel, J. M., "Wakes of Developed Cavities," *Journal of Ship Research*, Vol. 21, No. 4, Dec. 1977, pp. 225-238.

9 Rowe, A., and Kueny, J. L., "Recent Research Results on Cavity Flows About Hydrofoils," 13th Internationl, Symposium on Naval Hydrodynamics, O.N.R., Tokyo, Oct. 1980.

10 Michel, J. M., "Profils minces supercavitants à arrière tronqué. III—Etude physique du sillage en écoulement plan," La Houille Blanche, Vol. 6, 1974, pp. 429-445.

11 Verron, J., "Ecoulements cavitants ou ventilés autour d'ailes d'envergure finie en présence d'une surface libre," Thesis, Grenoble, July 1977.

12 Dodu, J., and Heraud, D., "Dispersion des jets liquides. Influence de la rugosite d'injecteur," C.R.A.S. t 262, pp. 1329-1332. (13 juin 1966).

13 Michel, J. M., "Ventilated Cavities—A Contribution to the Study of Pulsation Mechanism," *Proceedings of the IUTAM Symposium*, Lennigrad, June 1971, pp. 343-360.

14 Laali, A. R., "Ecoulements ventilés, Etude de l'entrainment d'air. Gas d'une cavité formée entre un jet plan et une paroi solide," Thesis, Grenoble, September 1980.

APPENDIX A

The flow is represented on Fig. A.a, and the linearized physcial plane $z = x + iy$ is represented on Fig. A.b. The conformal transformation $z(t)$:

$$z = -\frac{1}{\pi}\left[\log\left(1-\frac{t}{b}\right)-\log\left(1-\frac{t}{d}\right)\right]$$

transforms the z-plane band into the upper half-plane of the auxiliary plane $t = r +$ is (Fig. A.c). The unit length is the width H of the jet. We thus obtain:

$$b = -d = \left[th\frac{\pi l}{2}\right]^{-1}$$

so that the transformation is determined solely by the length l of the cavity.

Let $U(x, y)$ and $V(x, y)$ be the velocity components and let U be the velocity modulus on the upper free line of the jet. The following equations can be written:

$$\frac{U(x,y)}{U} = 1 + \epsilon u_1 + \text{Ord}(\epsilon^2)$$

$$\frac{V(x,y)}{U} = \epsilon v_1 + \text{Ord}(\epsilon^2)$$

where $\epsilon = h/l$ is the small parameter of the flow. The complex function $w_1(t) = u_1 - iv_1$ (first order velocity perturbation) is then determined by the mixed boundary conditions presented in Fig. A.c and by the continuity conditions at the points A and O where the jet detaches from the injector. In addition, the number σ_p is determined by considering that the deviation of the lower free line OC is equal to h.

The function $w_1(t)$, selected as invariant in the transformation, which satisfies the previous conditions, is (according to classical results):

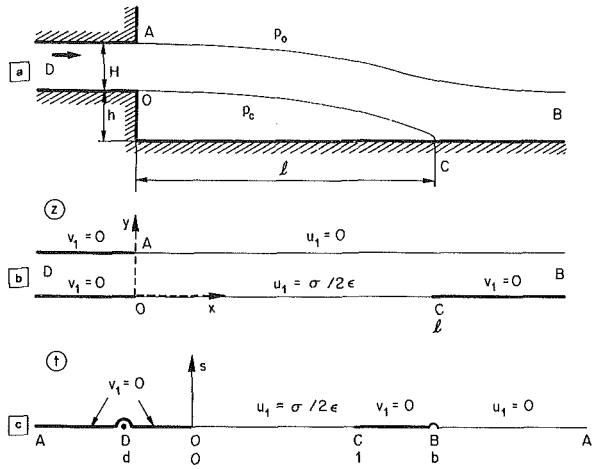

Fig. A $g = 0, \sigma_p = (p_0 - p_c)/\frac{1}{2}\rho V^2, \epsilon = h/l$

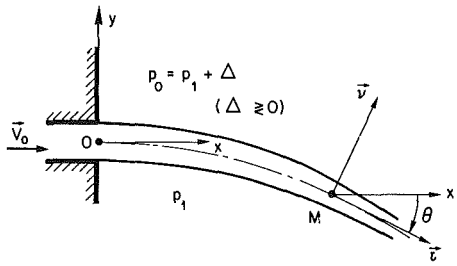

Fig. B

$$w_1(t) = \frac{i}{\pi}\frac{\sigma_p}{2\epsilon}\sqrt{\frac{t(t-b)}{t-1}}\int_0^1\sqrt{\frac{1-r'}{r'(b-r')}}\cdot\frac{dr'}{t-r'}$$

Consequently, for $t = r$ and $0 \leq r \leq 1$:

$$w_1(r) = -\frac{\sigma_p}{2\pi\epsilon}\sqrt{\frac{r(b-t)}{1-r}}\int_0^1\sqrt{\frac{1-r'}{r'(b-r')}}\cdot\frac{dr'}{t-r'}$$

where the integral must be taken in Cauchy's principal value. The condition giving h is:

$$y_C = y_{r=1} = \epsilon\int_0^1 v_1(r)\frac{dx}{dr}dr = -h$$

where

$$\frac{dx}{dr} = \frac{2b}{\pi(b^2-r^2)}$$

so that, ultimately, the relation $l(\sigma_p)$ is given by:

$$\frac{h}{\sigma_p} = \frac{b}{\pi^2}\int_0^1\frac{1}{b^2-r^2}\cdot\sqrt{\frac{r(b-r)}{1-r}}\int_0^1\sqrt{\frac{1-r'}{r'(b-r')}}\cdot\frac{dr'}{r-r'}\cdot dr$$

The variations of l as a function of σ/h (respectively l/H and $\sigma/h/H$ when physical parameters are used), is given in [14]. The asymptotic behavior of $l(\sigma)$ is as follows:

$$\frac{l}{H} \simeq 2\sqrt{\frac{h}{H\sigma_p}} \text{ for high values of } \frac{l}{H}$$

$$\frac{l}{H} \simeq \frac{4h}{\pi H}\cdot\frac{1}{\sigma_p} \text{ for small values of } \frac{l}{H}\left(\text{high values of } \frac{l}{h}\right)$$

APPENDIX B

A plane jet of nonviscous liquid discharging from a horizontal injector is subjected only to the action of gravity

and the difference between the pressures imposed on the two boundaries, this difference not necessarily being uniform (Fig. B). The jet is thin, or in other words, its thickness S is small compared with the radius of curvature of the mean line OM which is such that the flow rates on either side of the line are equal. Consequently, the pressure and velocity variations along a straight section can be considered to be linear. Let s be the length of arc OM, $\mathbf{t}$ and ν the unit vectors of the tangent and normal at M of the mean line. The problem consists in determining the function $S(s)$, $\theta(s)$ and $V(s)$ where V designate the velocity of a particle of the mean line, θ the slope of this line at M, given the following conditions at the origin: $S(0) = S_0$, $\theta(0) = 0$, $V(0) = V_0$.

The available equations are the equation of conservation of matter:

$$SV = S_0 V_0$$

and the dynamics equation:

$$\gamma = g - \frac{\Delta}{\rho s}\nu - \frac{1}{\rho}\frac{d\epsilon}{ds}\mathbf{t}$$

in which:

$$\Delta(s) = p_0 - p_1$$
$$\epsilon(s) = (p_0 + p_1)/2$$

In the following, $v = V/V_0$ and $\bar{s} = S/S_0$. The other geometrical parameters, $x, y, s \ldots$ are made dimensionless by reference to V_0^2/g. The following dimensionless numbers are then introduced:

$$\mathrm{Fr} = V_0/\sqrt{gS_0} \text{ (Froude number)}$$
$$\delta(s) = \frac{\Delta(s)}{\rho g S_0} + 1 = \frac{p_0 + \rho g S_0 - p_1}{\rho g S_0}$$
$$\gamma(s) = \frac{\epsilon(s)}{\rho g S_0}$$

It should be noted that the parameter $2\delta/\mathrm{Fr}^2$ represents the relative underpressure σ of a cavity.

Therefore, the equations become:

$$\bar{S}v = 1$$
$$v\frac{dv}{d\bar{s}} = -\sin\theta - \frac{1}{\mathrm{Fr}^2}\frac{d\gamma}{d\bar{s}}$$
$$\frac{V^2}{\bar{R}} = -\cos\theta - (\delta - 1)v$$

with the conditions: $v = 1$, $\bar{S} = 1$, $\theta = 0$ in $\bar{x} = \bar{y} = 0$; $\bar{R}$ is the dimensionless radius of curvature. The last two equations are the dynamic equations in projection on the directions τ and ν.

When the pressure p_0 and p_1 are uniform, δ is constant, $d\gamma/d\bar{s} = 0$. The solution is obtained analytically by two first integrals, one of which represents the law of conservation of energy:

$$\bar{y} = \frac{1 - v^2}{2}$$

The jet takes the form of curves belonging to the cycloid family: this characteristic can be deduced from the laws of conservation of energy and conservation of mass: when y decreases, v increases and the jet becomes thinner. Consequently, the pressure forces, which tend to become predominant, deviate the jet upwards. Near the origin, the only area of interest to us here, the solution reduces to:

$$\bar{y} = -\frac{\delta}{2}\bar{x}^2$$

or

$$y = \frac{-\delta}{2\,\mathrm{Fr}_2}x^2 = -\frac{\sigma}{4}\frac{x^2}{H}$$

in which we make $S_0 = H$ to return to the general notations of the paper.

It is worth noting that the jet thinness conditions is fully satisfied in the experimental cases.

R. E. Franklin

J. McMillan

Oxford University Engineering Laboratory, Oxford, England

Noise Generation in Cavitating Flows, the Submerged Jet

Measurements are reported of the pressure fluctuations in the near field of a submerged jet. The mechanisms by which the pressure fluctuations may be generated are discussed and estimates are presented of two of these, namely the transient oscillations of micro-bubbles of air excited by the pressure drop in the nozzle, and the cavitation of micro-bubbles by the turbulent pressure fluctuations in the jet mixing region.

Introduction

Problems in cavitation are generally complicated and difficult, and that of noise generation is no exception. Basically, the difficulties of cavitation problems arise from the fact that they involve the generation and development of a two-phase flow by pressure reductions in a liquid due to the motion of the liquid and, once the cavitation has started, the fluid dynamics of the two-phase flow. From a theoretical point of view, the problem is a daunting one, and over the years it has also proved to be difficult experimentally, mainly because of obscure scaling problems between one experiment and another, or between an experimental and prototype configuration.

In the experimental field, the situation has improved over the last decade or so, mainly because of progress on two fronts. The first is the realization and acceptance of the importance of detailed fluid mechanic effects, and particularly boundary layer mechanics, on cavitation inception and development [1, 2]. The second is the now rapidly-developing knowledge of the nature and importance of the constitution of the fluid, particularly in respect of free air content [3]. It now seems reasonably safe to say that progress in any cavitation problem can be expected with more confidence if these two effects are accounted for, or controlled.

When the present project on noise generation in cavitating flows was set up, careful thought was given to the experimental configuration to be used, and that chosen was the submerged jet. The reasons for this choice were that the turbulent jet is a flow problem which has been shown to be largely independent of Reynolds number, and one which has been extensively studied as a single-phase flow over the last thirty years in relation to jet noise. It is therefore a flow in which fluid dynamic scale effects between one setup and another are likely to be small, and the structure of which is well documented in great detail. This seemed to be a sound basis for comparison of experimental data with other workers, and for seeking progress along theoretical lines.

The general features of cavitation in submerged jets and the noise generated by this flow have been known for some time, [4, 5]. Nevertheless, in the following sections the problem is described and analyzed largely using experimental data from the present project, since the precise conditions under which these were obtained are familiar to the authors.

Experimental Work [6, 7]

The Apparatus. The rig consists of an open-topped tank 6096 mm long by 1519 mm wide, in which water normally stands at a depth of about 1450 mm, with provision at one end for the fitting of nozzles with diameters up to 50 mm at a depth of 750 mm. Water is supplied to the nozzles from a roof-tank through a main of diameter 250 mm which terminates at a bellows connecting it to the nozzle-mounting stub in the tank. The hydrostatic head is sufficient to give jet speeds up to 20 m/s. For speeds greater than this the supply may be diverted through a booster pump. The greatest speed currently possible is 36 m/s.

Near to the tank, the supply main is interrupted by a set of flexible polythene tubes, each fitted with a straight through on-off valve, which is used in several combinations to provide a primary flow control by pressure drop, and serve also to prevent the transmission of noise and vibration from the upstream pipework. Downstream of this system, a tank bypass is fitted to provide a secondary, fine flow control, together with a branch to a small pump which is used to extract air. Water is exhausted from the tank by a siphon through a second set of flexible tubes, the ends of which are submerged in a sump tank at a lower level from which it is returned to the roof tank by centrifugal pumps. Transmission of noise and vibration to the test tank is small, and the underwater ambient noise level is very low.

Pressure fluctuations are detected by a B and K Type 8101 PZT Hydrophone, measured and analyzed with a B and K Type 2112 1/3 octave Audio-frequency Spectrometer and recorded on a B and K Type 2305 Level Recorder.

Results and Typical Data. In early experiments, difficulty was experienced in securing repeatability of data. This was traced to variations in the free air content of the water and operational techniques were established to bring this under control. Repeatability is now good and although the actual free air content is not measured, it is possible to control the air content over a range extending from a very low to a very high

Contributed by the Fluids Engineering Division of THE AMERICAN SOCIETY OF MECHANICAL ENGINEERS and presented at the Winter Annual Meeting, Phoenix, Ariz., November 14-19, 1982. Manuscript received by the Fluids Engineering Division, March 23, 1983.

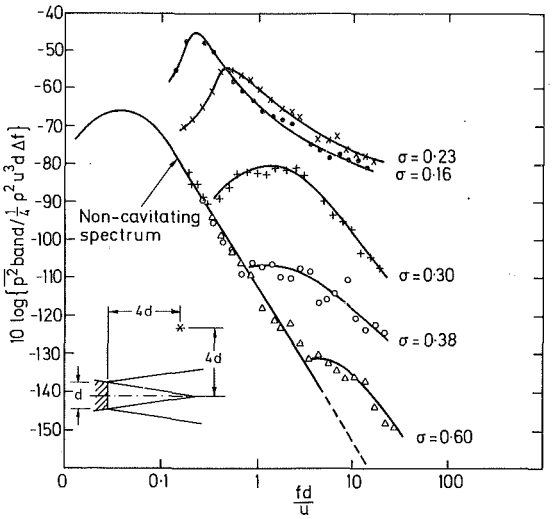

Fig. 1 Measured nondimensional power spectral densities for a 14.0 mm diameter jet

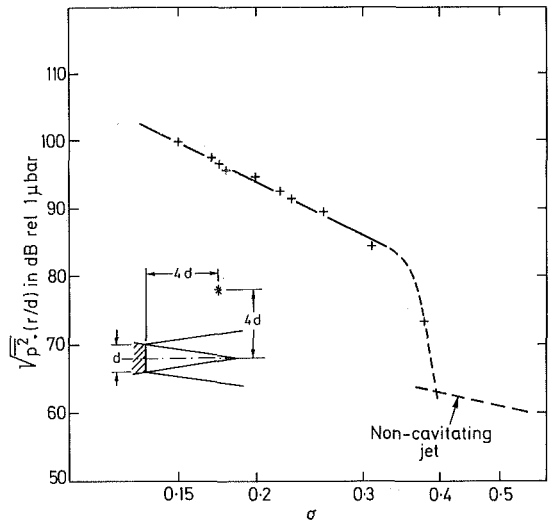

Fig. 2 Overall rms pressure fluctuations as a function of cavitation number, for a 14.0 mm diameter jet

value, to keep it constant at a low level during a series of runs and to check that it is the same in different series.

A considerable amount of data has now been collected, examples of which are shown in Figs. 1 and 2.

The first of these shows the power spectral density of the pressure fluctuations at the position $x = y = 4d$ (a point chosen to allow comparison with the data in [4]) for a jet of nozzle diameter 14.0 mm at cavitation numbers between 0.6 and 0.16 and a low free air content. In general, the spectra may be divided into two parts: (i) that due to the pressure fluctuations associated with a noncavitating, or single-phase jet, and (ii) a departure from the noncavitating spectrum having the form of a low, broad hump at high cavitation numbers which quickly rises as the cavitation number is lowered and develops into a sharply-peaked form at lower cavitation numbers. Other data show that for a given σ, an increase in the free air content has no effect on the first, noncavitating part of a spectrum. The same is true of the second part of a spectrum for those values of σ for which it shows a relatively sharp peak, ($\sigma < 0.25$), but at the higher cavitation numbers this part of the spectrum is sensitive to air content, the effect being that an increase in air content raises the level without materially affecting the shape.

The second figure shows the way in which the mean-square of the pressure fluctuations changes with σ. It is seen that at a value of about $\sigma = 0.4$, the level suddenly rises from that associated with noncavitating jets, and that below a value of about $\sigma = 0.3$, the level varies as $1/\sigma^{4.5}$.

Data from nozzles with diameters 25 and 50 mm exhibit the same general characteristics, and the data are similar to those of other investigators [4].

Preliminary photographic work has also been carried out. Still photography with short-duration flash has produced pictures similar to those published elsewhere, [5], and high-speed motion photography has resulted in clear records of the growth, collapse and rebound of bubbles in the flow, together with details of the bubble motions. For present purposes, however, the most important visual observation is that if jets are run for some time under cavitating conditions, small bubbles accumulate in the bulk water in the test tank. Clearly, these bubbles are bubbles of air and they emphasize the fact that a theoretical model of the problem must take account of the presence of free air in the jet fluid.

Nomenclature

a = radius of microbubble in the flow
a_0 = radius of microbubble in the reservoir
a_m = maximum radius of expanded microbubble
$\bar{a}$ = characteristic radius of microbubble concentration distribution
c_p = fluctuating pressure coefficient
c = velocity of sound in water
d = diameter of nozzle
e = energy spectral density
f = frequency
$\bar{f}$ = characteristic frequency of pressure fluctuations
n = number density of bubble radius concentration distribution
p = instantaneous pressure
p_0 = jet stagnation pressure
p_v = vapor pressure
p_t = threshold pressure
$\bar{p}$ = mean static pressure
p' = acoustic pressure
$\bar{p}^2$ = mean square pressure
r = radial distance from center of nozzle exit
t = time
$\bar{t}$ = average duration of a pressure minimum
t_c = collapse time of a cavitation bubble
u = jet exit velocity
w = power spectral density
x = axial distance from jet exit
y = radial distance from jet axis
z = standard variate
E = acoustic energy radiated from bubble collapse
R = radius of cavitation bubble
R_m = mode of distribution of cavitation bubble radii
W = radiated sound power
α = exponent in Rosin-Rammler distribution
β = volume concentration of free air in flow
β_0 = volume concentration of free air in reservoir
γ = isentropic index for air
δ = delta function
η = efficiency
ν = flux of microbubbles
ν_c = number of cavitation events per second
ω = angular frequency
ρ = density of water
σ = cavitation number
ζ = damping ratio
ξ = defined in text

Theoretical Work [8–10]

The Constitution Of the Fluid. It is usually the case that the tensile strengths of liquids are considerably less than their theoretical tensile strengths. The difference is attributed to the presence of nuclei, or points from which rupture of the liquid is relatively easily propagated. The nature of these nuclei has been, and to some extent is still, obscure, but evidence tends to support the idea that the nuclei are small bubbles of air in the bulk of the liquid and at the surfaces of contact between the liquid and its container. These micro-bubbles are not all of the same radius and the reasons why the smaller ones are not driven into solution and the larger ones do not rise to the surface, and whether or not in the bulk of the liquid they are all necessarily associated with small solid particles, are matters for conjecture. Nevertheless, their presence can be detected by several different sorts of measurement and it seems reasonable to take it as an experimental fact that nuclei may be modeled in this way.

Experimental data are usually presented in the form of a concentration density distribution on micro-bubble radius, and the number per unit volume of bubbles with radii in the range a, $a + da$ is written as $n(a) \cdot da$, [11]. Empirical analysis of data results in the representation

$$n(a) = \frac{A}{a^{\alpha}},$$

where the exponent α lies in the range $3 < \alpha < 4$, and A is a number which depends on the history of the water from which the sample was taken. This empirical result is not altogether satisfactory and a more sophisticated representation is to be preferred. A suitable one is the Rosin-Rammler distribution [12] which starts from the idea that the fraction by volume of bubbles with radii greater than a is given by

$$\int_a^{\infty} d\beta = \beta \cdot \exp\left\{-\left(\frac{a}{\bar{a}}\right)^{\alpha}\right\}$$

This may be differentiated to find

$$n(a) = \frac{3\beta\alpha}{4\pi\bar{a}^4} x^{\alpha-4} \exp(-x^{\alpha}), \tag{1}$$

where $x = a\sqrt{a}$, and $\bar{a}$ is a characteristic radius. A study of the data shows that a suitable value for α is 0.5, and typical values of a and β, the volume concentration of free air, are found to be:

(i) For low air concentration typical of water that has been standing for a few hours: $\beta = 10^{-9}$, $\bar{a} = 4.15.10^{-6}$ m,

(ii) For higher concentrations typical of water found in some cavitation experiments: $\beta = 10^{-5}$, $\bar{a} = 4.15.10^{-5}$ m.

Values of β considerably higher than these may well be encountered in some situations.

Mechanism Of Noise Generation. Given that a real liquid may be taken to contain a certain concentration of free air micro-bubbles, several different mechanisms of noise generation may be suggested.

A first listing of these includes the following, some of which have already received attention in the literature:

(i) Transient volume oscillations of the micro-bubbles excited by:

(a) their passage through the static pressure field of the flow,

(b) their splitting and coalescence,

(ii) Forced volume oscillations of the micro-bubbles excited by their passage through or motion with the turbulent pressure field of the flow,

(iii) Transformation of the turbulent kinetic energy of the flow into radiated sound by the corresponding volume motions of the micro-bubbles,

(iv) Fluctuations in the slip of micro-bubbles relative to the liquid,

(v) Sudden and large volume changes of the micro-bubbles in their role as nuclei of cavitation, the required excursion below the corresponding threshold pressure being caused either by passage through a low-pressure region of the static pressure field or by occasional large-amplitude fluctuations in the turbulent pressure field.

In the light of this list, two mechanisms seem most likely to dominate the noise generated in a submerged jet flow, namely the transient volume oscillations of the micro-bubbles excited by the pressure drop in the nozzle and the cavitation induced by the large-amplitude fluctuations of pressure in the highly-turbulent jet mixing region. These are studied in the following sections under the headings of bubble expansion noise and cavitation noise respectively.

Theoretical Results: Bubble Expansion Noise

In passing through the nozzle, the micro-bubbles in the flow are subjected to pressure changes the precise form of which depends upon the particular nozzle profile. The effect of the nozzle profile on the noise of a bubbly jet of water in air has been studied, [13], but for present purposes it is sufficient to model the pressure change as a sudden drop in pressure at the exit plane of the nozzle. On receiving this step change from the stagnation pressure to the static pressure of the jet, a bubble first expands to a radius a_m which may be estimated from the simple Rayleigh equation

$$a\ddot{a} + \frac{3}{2}\dot{a}^2 = (p_0 - \bar{p})/\rho.$$

For isentropic expansion, this yields the result

$$x^{1-\gamma} - 1 = (1-\gamma)\frac{\bar{p}}{p_0}(x-1),$$

where $x = a_m/a_0$, and a_0 is the radius of the bubble when in equilibrium with the stagnation pressure. The pressure within the bubble then being less than the local static pressure, it executes a damped volume oscillation which may be represented by

$$\Delta v = v_{\Omega} \cdot e^{-\zeta\Omega t} \cdot \cos\Omega t,$$

where $v_{\Omega} = 4/3\ \pi\ (a_m^3 - a^3)$, and Ω is approximately equal to the bubble resonant frequency $(1/a).\sqrt{3\gamma\bar{p}/\rho}$.

Provided that the damping ratio is small, the form of the associated radiated acoustic pressure pulse is given by

$$p' = \frac{p'_{\Omega}}{r} \cdot e^{-\zeta\Omega t}\cos\Omega t,$$

where

$$p'_{\Omega} = \gamma\bar{p}a\left\{\left(\frac{am}{a}\right)^3 - 1\right\}$$

The energy density spectrum of this pulse is easily found to be

$$e(\omega) = \frac{{p'_{\Omega}}^2}{2\pi r^2} \frac{\zeta^2\Omega^2 + \omega^2}{(\zeta^2\Omega^2 + \Omega^2 - \omega^2)^2 + 4\zeta^2\Omega^2\omega^2},$$

and if the total acoustic signal for bubbles of this size is taken to be a train of such pulses occurring randomly at an average frequency ν, the contribution to the power spectral density of the radiated noise will be given by

$$dw(\omega) = \nu \cdot e(\omega).$$

Now the average frequency of the pulses is equal to the flux of micro-bubbles through the nozzle. Thus:

$$\nu = (\pi/4) \cdot d^2 un(a) \cdot da,$$

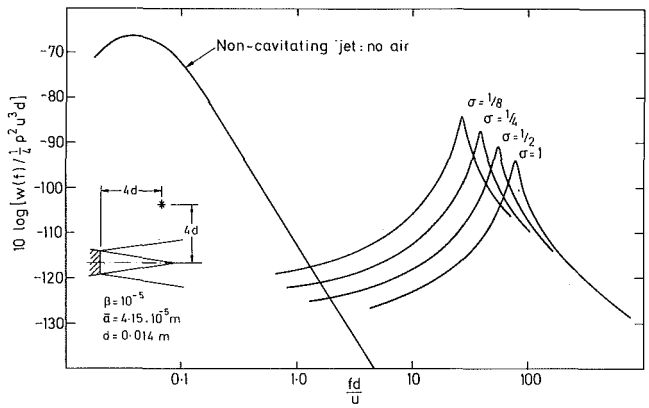

Fig. 3(*a*) Bubble expansion noise. Bubbles of a single size

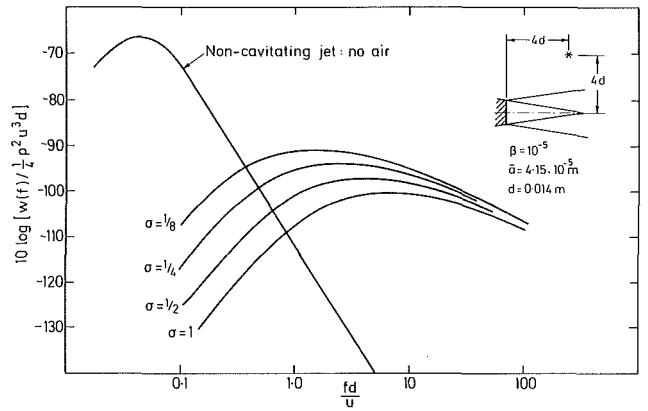

Fig. 3(*b*) Bubble expansion noise. Bubbles with radii distributed according to Rosin-Rammler distribution

and if the damping ratio is taken to be the same for bubbles of all radii, then by integrating over all bubble sizes it may be shown that the nondimensional power spectral density finally takes the form:

$$\frac{w(\omega)}{\tfrac{1}{4}\rho^2 u^3 d} = 0.23\gamma^{3.5}\zeta^3\left(\frac{d}{r}\right)^2\left(\frac{\bar{p}}{\tfrac{1}{2}\rho u^2}\right)^{3.5}$$
$$\left\{\left(\frac{a_m}{a}\right)^3 - 1\right\}^2 \cdot \left(\frac{u}{\omega d}\right)^5$$
$$\cdot d^4 \int_0^\infty f(\xi)\cdot\xi^4\cdot n(\xi)\,d\xi \qquad (2)$$

where:

$$f(\xi) = (1+\xi^2)/\{(1+\zeta^{-2}-\xi^2)^2 + 4\xi^2\},$$

and

$$\xi = \sqrt{\frac{2}{3\gamma\zeta^2}}\cdot\frac{\omega d}{u}\cdot\left(\frac{\tfrac{1}{2}\rho u^2}{\bar{p}}\right)^{1/2}\cdot\frac{a}{d}$$

Two micro-bubble concentration density distributions may usefully be studied. The first corresponds to bubbles of a single size and is written

$$n(a) = \frac{3\beta}{4\pi\bar{a}^3}\,\delta(\bar{a}),$$

and the second is the Rosin-Rammler distribution of equation (1). In both cases, if β_0, a_0 are taken to be constant values in the flow upstream of the nozzle and the expansion in the nozzle is taken to be isentropic, then for the jet flow

$$\beta\bar{a} = \beta_0\bar{a}_0\left\{1 + \frac{\tfrac{1}{2}\rho u^2}{\bar{p}}\right\}^{4/3\gamma}$$

The results of calculations for these two cases are shown in Figs. 3(*a*) and (*b*). It is seen that bubbles of a single size produce a peaked spectrum, but that bubbles with a distribution in size more in accordance with that found experimentally, give rise to a spectrum with a broad flat shape similar to that shown in the spectra of Fig. 1 at the higher cavitation numbers. The estimated level is reasonable, but the variation in level with cavitation number is small.

The general conclusions to be drawn seem to be that the departure from the noncavitating spectrum at higher cavitation numbers may reasonably be attributed to bubble expansion noise, and that as the cavitation number is lowered, the increased pressure drop in the nozzle causes substantial changes in the free air content.

Theoretical Results: Cavitation Noise

General. Cavitation occurs in a turbulent flow field because at any point the static pressure varies randomly with time and although the probability that at some instant the pressure falls below the threshold pressure is small, it is nevertheless finite.

The random pressure may be scaled into the standardized random variable $z = (p-\bar{p})/\sqrt{p^2}$, and for the case in which this variable has a Gaussian distribution, many theoretical results are available [14]. In particular, the probability that the pressure lies below the threshold pressure is

$$P(p<p_t) = \frac{1}{\sqrt{2\pi}}\cdot\int_{-\infty}^{z_t}\exp(-\tfrac{1}{2}x^2)dx, \qquad (3)$$

and the average time between two passages in the same direction of the line $p(t) = p_t$ is

$$\bar{T} = \frac{1}{\bar{f}}\cdot\exp\{+\tfrac{1}{2}z_t{}^2\}, \qquad (4)$$

the reciprocal of which is equal to the average frequency of pressure minima with values less than p_t,

$$\nu(p_{\min}<p_t) = \bar{f}\exp\{-\tfrac{1}{2}z_t{}^2\} \qquad (5)$$

The Radius Of the Most-Frequently Occurring Cavitation Bubbles. By combining equations (3) and (4) it is possible to show that the average duration of a pressure minimum with value less than p_t is given by

$$\bar{t} = \frac{1}{\sqrt{2\pi}}\cdot\frac{1}{\bar{f}}\cdot\left|\frac{\sqrt{\bar{p}^2}}{p_t-\bar{p}}\right|,$$

and this result may be used in the simple, constant-velocity bubble-growth formula to estimate the radius to which a nucleus with this threshold pressure will grow. If now equation (5) is differentiated, the resulting expression for the average frequency of pressure minima with values in the range p, $p + dp$ may be transformed into an expression for the average frequency of occurrence of cavitation bubbles with radii in the range R, $R + dR$ and by seeking the maximum value of this, the radius of the most frequently occurring cavitation bubble may be found. The result is

$$R_m = \frac{1}{\sqrt{6\pi}}\cdot\frac{1}{\bar{f}}\cdot\sqrt{\frac{\bar{p}-p_t}{\rho}}\cdot\left\{\frac{\bar{p}^2}{\bar{p}-p_t}\right\}^2,$$

which, on introducing a threshold cavitation number $\sigma_t = (\bar{p}-p_t)/\tfrac{1}{2}\rho u^2$ and a fluctuating pressure coefficient

$$c_P = \sqrt{\bar{p}^2}/\tfrac{1}{2}\rho u^2,$$

may be written:

$$\frac{R_m}{d} = \frac{c_p^2}{\sqrt{12\pi}}\cdot\frac{u}{\bar{f}d}\cdot\frac{1}{\sigma_t^{3/2}} \qquad (6)$$

The Peak Frequency of Cavitation Noise. After a nucleus has received a pressure minimum and the resulting cavitation bubble has grown to the size calculated in the previous sec-

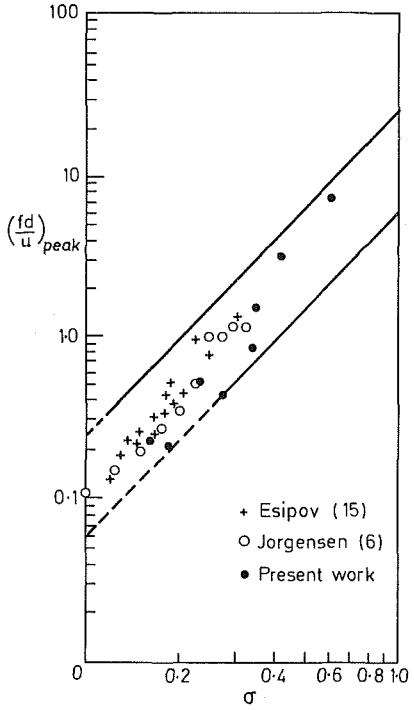

Fig. 4 Peak frequency of cavitation nose. Comparison of estimates with experimenta data

tion, the pressure rises again and the bubble collapses and rebounds several times. If it is assumed that the pressure causing collapse is the local mean static pressure, the collapse time is given approximately by:

$$t_c = R_m \cdot \sqrt{\frac{\rho}{\bar{p} - p_l}} \cdot$$

It is usually the case that the rebound time is shorter than the collapse time and because of this it may be argued that the frequency of the damped pressure pulse radiated away from the bubble is of the order $f = 1/2t_c$. The dominant frequency of the noise is therefore estimated by:

$$\left(\frac{fd}{u}\right)_{\text{peak}} = \sqrt{\frac{3\pi}{2}} \cdot \frac{1}{c_p^2} \cdot \frac{\bar{fd}}{u} \cdot \sigma_l^2 \tag{7}$$

An analysis of experimental data on the pressure fluctuations in the mixing region of a jet shows that $c_p = 0.06$, and $\bar{fd}/u$ (which must be measured in a frame of reference moving with the fluid) is in the range 0.01 - 0.04. On taking these data, the estimate for the dominant frequency becomes

$$6\sigma^2 < \left(\frac{fd}{u}\right)_{\text{peak}} < 24\sigma^2$$

This result is plotted in Fig. 4, together with data from several sources. It is seen that the estimate is a good one, which suggests that there is some substance to the present calculations.

The Event Rate. For a flow in which the characteristic length is d, the volume of the region in which cavitation can occur may be written as kd^3, where k is some geometrical factor. If the volume concentration of nuclei is β and all have the same radius $\bar{a}$, the number of nuclei in the zone is given by

$$N_c = kd^3 \cdot \frac{3}{4\pi} \cdot \frac{\beta}{\bar{a}^3} \cdot \tag{8}$$

The average frequency with which any nucleus receives a pressure minimum with level below its threshold pressure may be found from equation (5), and on combining this with (8), the average frequency of cavitation events is found to be

$$\nu_c = \frac{3k}{4\pi} \cdot \frac{d^2}{a^3} \sqrt{\frac{2(\bar{p} - p_l)}{\rho}} \cdot \beta \cdot \frac{1}{\sqrt{\sigma}} \frac{\bar{fd}}{u} \cdot \exp\{-\tfrac{1}{2}z_l^2\} \tag{9}$$

For a jet, the value of k might reasonably be estimated at 5, and for a nozzle of diameter 14 mm, $\bar{p} = 10^{-5}$ N/m^2, $\beta = 10^5$, $\bar{a} = 10^{-5}$ m, $\bar{fd}/u = 0.02$, calculations yield the figures shown in the second column of the following table. Experimental data to check these results are not yet available. Nevertheless, the values do not seem unreasonable.

σ	$\nu_c(s^{-1})$	$\bar{p}^2\left(\frac{r}{d}\right)^2 \frac{1}{\eta}$ dB rel 1 μbar
0.4	$1.86.10^{-3}$	53.1
0.35	$45.2.10^{-3}$	69.5
0.3	4.5	92.5
0.25	224.8	113.1
0.20	5,270	131.5
0.15	75,070	148.1

The Overall Level of the Cavitation Noise. The energy radiated away from the collapse of a single cavitation bubble may be expressed as some fraction η of the potential energy at maximum radius. Thus the energy may be written

$$E = \eta \cdot \frac{4\pi}{3} \cdot R_m^3 (\bar{p} - p_l)$$

where it is again assumed that the pressure causing collapse is the mean static pressure.

If there are ν_c such events per second on average, then the radiated power is, approximately,

$$W = \nu_c E,$$

and the mean square acoustic pressure at distances from the collapse zone large enough for the sound waves to be effectively plane will be given by

$$\bar{p}^2 = \frac{\rho c}{4\pi r^2} \cdot W \cdot$$

After some manipulation, and using the earlier result for R_m, this becomes

$$\bar{p}^2 = \frac{1.44}{10^3} \cdot \eta \nu_c (\bar{p} - p_l) \cdot \rho c d \left(\frac{d}{r}\right)^2 c_p^6 \left(\frac{u}{\bar{fd}}\right)^3 \frac{1}{\sigma_l^{4.5}} \tag{10}$$

Using the same data as in the previous section, this may be evaluated to give the results shown in the third column of the table.

These are plotted in Fig. 5 and compared with the results for both noncavitating and cavitating jets.

It is seen that the sudden rise in the overall pressure level at inception is satisfactorily modeled, and attention is drawn to to fundamental questions, namely:

(i) what are the factors which determine the value of σ at which the sudden rise in cavitation noise is first detected, i.e., the value of σ at inception?

(ii) for what reason does the variation in cavitation noise with σ change from the very rapid form associated with inception to that proportional to $1/\sigma^{4.5}$ at lower cavitation numbers?

If there is real substance to the present theoretical estimates, answers to these questions are not difficult to find. The principal factors seem to be the efficiency η, the event rate ν_c (which is primarily dependent on the volume concentration and size of the free-air microbubbles), and the effective collapsing pressure.

It seems quite likely that at incipience it is the event rate which is dominant and that this is determined by the statistical

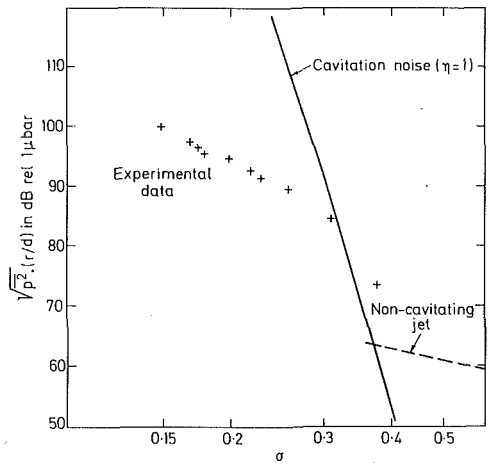

Fig. 5 Estimated form for overall level of cavitation noise

characteristics of the noncavitating flow, and the free air content of the fluid.

As the cavitation number is taken below the value at incipience, the event rate, and therefore the density of cavitating sites, increases very rapidly. It is then possible that at some critical density, interaction between cavitation sites begins to take place. Such an interaction has been noted in nucleate boiling, where observations have shown that a growing bubble has a particular sphere of influence in which the growth of other bubbles is inhibited, which gives rise to a limiting density of nucleating sites. On the other hand, it could be the case that as the density of cavitating sites increases, the efficiency of the conversion of potential energy into radiated sound falls, and in this connection one notes the wide variation between the values of efficiency measured for single bubbles, (which is reported as lying between 30 and 50 percent), and for clouds of bubbles, (which is reported possibly to be as low as 0.1 percent). The resolution of this question must await further work but in the meantime it is interesting to note that if, for whatever reason, the product $\eta\nu_c$ becomes constant, the theory predicts the correct variation of overall pressure level with cavitation number.

The Power Spectral Density Of Cavitation Noise. The broad agreement between the measured and estimated values of the dominant frequency of cavitation noise illustrated in Fig. 4 suggests that the size-distribution of cavitation bubbles has a relatively sharp peak at the value estimated as R_m. In this case, the power spectral density of radiated noise should be similar to that estimated for the oscillations of bubbles of a single size and a comparison of Figs. 1 and 3(*a*) show this to be so for cavitation numbers below that at inception. Preliminary calculations of the power spectral density have been carried out. Further work is in hand and will be reported later.

Conclusion

The work reported here seems to imply a clear and consistent explanation for the variation of the power spectral density of the pressure fluctuations near to a submerged jet as the cavitation number is lowered by raising the speed. At high cavitation numbers, the spectrum is the same at lower frequencies as that for a noncavitating jet, but at higher frequencies shows a broad flat peak which may be attributed to the free oscillations of micro-bubbles in the flow excited by the pressure drop in the nozzle. As the speed is raised, the level of the broad flat peak rises steadily, probably because the increasing pressure drop in the nozzle releases more and more dissolved gas from solution. At a certain value of σ, the occasional large-amplitude turbulent pressure fluctuations in the mixing region become sufficiently frequent for the noise radiated from the collapse of the associated cavitation bubbles to be detected and inception to be defined. Below inception, this component shows a sharp peak which first rises very rapidly and then in proportion to $1/\sigma^{4.5}$ after some interaction phenomenon comes into play.

References

1 Wykes, M. E. P., "Experimental Studies of Viscous Effects on Cavitation," D. Phil thesis, Oxford, 1978.

2 Mussared, M. R., "Cavitation on a Two-Dimensional Cylinder," M.Sc. thesis, Oxford, 1978.

3 Ripkin, J. F., Killen, J. M., "Gas Bubbles: Their Occurrence, Measurement, and Influence in Cavitation Testing," *Proc. I.A.H.R. Symposium on Cavitation in Hydraulic Machinery*, 1962.

4 Jorgensen, D. W., "Noise from Cavitating Submerged Water Jets," D.T.M.B. Report 1126, 1960.

5 Rouse, Hunter, "Cavitation in the Mixing Region of a Submerged Jet," *La Houille Blanche*, Vol. 8, 1950, p. 9.

6 Franklin, R. E., and McMillan J., "The AMTE/OUEL Underwater Jet Noise Rig, 1977/78" O.U.E.L. Report 1226/77, 1977.

7 Franklin, R. E., and McMillan, J., "The ATME/OUEL Underwater Jet Noise Rig, 1978/79," OUEL Report 1310/80, 1980.

8 Franklin, R. E., McMillan, J., "Noise Generation in Cavitating Flows. The Submerged Water Jet, I," OUEL Report 1312/80, 1980.

9 Franklin, R. E., and McMillan, J., "Noise Generation in Cavitating Flows. The Submerged Water Jet II," OUEL Report 1313/80, 1980.

10 Franklin, R. E., and McMillan, J., "Noise Generation in Cavitating Flows. The Submerged Water Jet III, OUEL Report 1326/80, 1980.

11 Gates, E. M., and Acosta, A. J., "Some Effects of Several Free-Stream Factors on Cavitation Inception of Axisymmetric Bodies," *12th Symp. Naval Hydrodynamics*, 1978, p. 86.

12 Rosin, P., and Rammler, E., "The Laws Governing the Fineness of Powdered Coal," *J. of the Institute of Fuel*, Vol. 7, 1933, p. 29.

13 Whitfield, O. J., and Howe, M. S., "The Generation of Sound by Two-Phase Nozzle Flows and its Relevance to Excess Noise of Jet Engines," *J. Fluid Mech.*, Vol. 75, 1976, p. 553.

14 Rice, S. O., *Noise and Stochastic Processes*, Ed. Wax, N., Dover Publications 1954, p. 133.

15 Esipov, I. B., and Naugol'nykh, K. A., "Cavitation Noise in Submerged Jets," *Sov. Physics Acoustics*, Vol. 21, 1976, p. 404.

16 Latorre, R., "TVC Noise Envelope — An Approach to Tip Vortex Cavitation Noise Scaling," *J. of Ship Research*, Vol. 26, 1982 p. 65.

17 Latorre, R., "Study of Tip Vortex Cavitation Noise From Foils," *Int. Shipbuilding Progress*, Vol. 27, 1980, p. 66.

C. Samuel Martin
Professor
School of Civil Engineering
Georgia Institute of Technology,
Atlanta, Ga.
Fellow ASME

P. Veerabhadra Rao
NRC-NASA Research Associate
NASA Lewis Research Center
Cleveland, Ohio

Application of Signal Analysis to Cavitation

The diagnostic facilities of the cross power spectrum and the coherence function have been employed to enhance the identification of not only the inception of cavitation, but also its level. Two piezoelectric pressure transducers placed in the downstream chamber of a model spool valve undergoing various levels of cavitation allowed for the use of both functions—the phase angle of the complex cross spectrum and the dimensionless coherence function—to sense clearly the difference between noise levels associated with a noncavitating jet from those once cavitation inception is attained. The cavitation noise within the chamber exhibited quite a regular character in terms of the phase difference between instruments for limited cavitation. Varying cavitation levels clearly illustrated the effect of bubble size on the attendant frequency range for which there was an extremely high coherence or nearly perfect causality.

Introduction

As reported by Arndt [1], a number of investigators have employed spectral analysis techniques to identify the onset and extent of cavitation in various flow configurations. Frequently, mean noise levels as monitored by a r.m.s. voltmeter, or the mean-square energy content over a specified frequency band on an energy spectrum, are related to the hydrodynamic parameters and the cavitation index. On occasion, as reported by Jorgensen [2] for cavitating water jets, by Deeprose et al. [3] for cavitating centrifugal pumps, by Ōba and Itō [4] for cavitation in a venturi and by Blake et al. [5] for cavitation noise on a hydrofoil, noise or pressure spectra as affected by cavitation are investigated in more detail. Moreover, Martin et al. [6] employed various analytical features of auto power spectra to identify cavitation inception in directional control valves. Outside of the employment of power spectra analysis there has been only limited, if any, application of other signal analysis techniques to the detection and identification of cavitation. It is the purpose of this paper to demonstrate the usefulness of other signal analysis features available to the experimentalist, namely, the employment of cross sepctral and coherence functions. It will be shown that these facilities enhance the commonly used power spectral analysis capability when investigating the onset and extent of cavitation.

Experimental Facility

Various levels of cavitation were investigated in the plexiglass spool valve described in detail by Martin et al. [6]. This valve, which is a model three times larger than a prototype metal valve, has a spool diameter of 57.2 mm (2.25 in). A longitudinal view of the body of the test valve and associated instrumentation are shown in Fig. 1. The annular opening could be controlled by the mechanism attached to the end of the spool. As described in [6] a petroleum based hydraulic oil (MIL-H-5606C) was supplied to the valve by a hydraulic test loop consisting of an axial piston pump, a high pressure supply line, a drag-type flow meter, a bypass system, the test valve, downstream valves for control of back pressure, and finally a return line to the pump at low pressure.

The instrumentation on the model valve shown in Fig. 2 consisted of the linear variable displacement transducer (LVDT) for precise determination of the valve opening, and pressure transducers for measuring such mean pressures as (1) the pressure differential $\Delta p = p_u - p_d$ across the annular

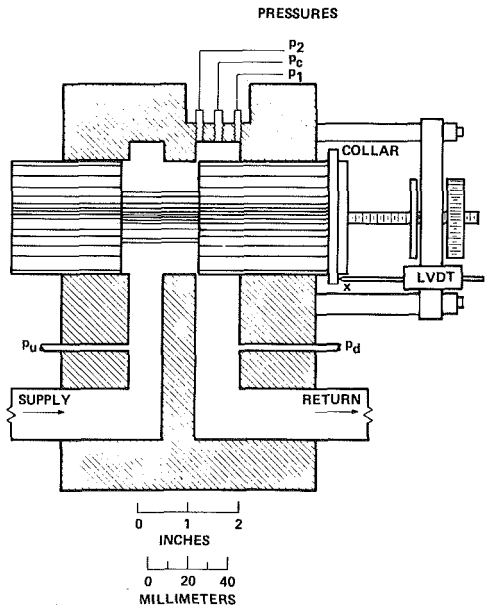

Fig. 1 Longitudinal section of model valve

Contributed by the Fluids Engineering Division of THE AMERICAN SOCIETY OF MECHANICAL ENGINEERS and presented at the Winter Annual Meeting, Phoenix, Ariz., November 14-19, 1982. Manuscript received by the Fluids Engineering Division, April 13, 1983.

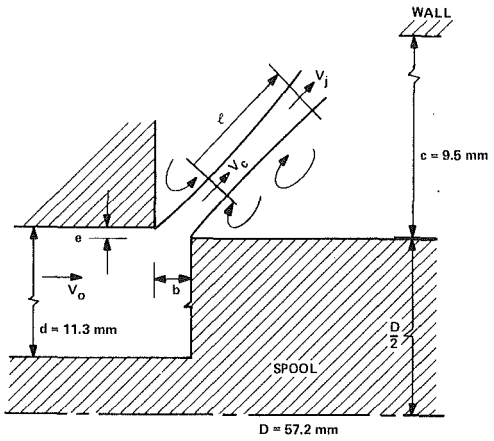

Fig. 2 Definition of valve and jet parameters

orifice, (2) the chamber pressure p_c and (3) the downstream or return line pressure p_R. Piezoelectric pressure transducers were mounted within the valve chamber to sense high-frequency fluctuations associated with cavitation noise. These latter two flush-mounted instruments, one ($P2$) located adjacent to the plane of the opening and the other ($P1$) positioned on the opposite extreme of the valve chamber constituted the input signals for the sophisticated signal analysis to be described later. Each transducer has a sensing diameter of 2.51 mm (0.099 in.) and a natural frequency in air of 250 kHz.

A Hewlett-Packard Model 5420A Digital Signal Analyzer was employed to process on a real-time basis the dynamic signals from the two piezoelectric pressure transducers. Simultaneous processing of both signals allowed for the following ensemble-averaged functions: the two power spectra, and the cross spectrum and coherence function between the two signals. The processor had a frequency resolution of 100Hz and a maximum bandwidth of 25.6 Hz, which was always utilized in this study. Preliminary investigations demonstrated that no more than 50 ensemble averages were required to achieve an essentially stationary result.

in accordance with Bendat and Piersol [7] the various digital signal analysis functions are in terms of time domain input $x(t)$ and $y(t)$ for pressure transducers $P1$ and $P2$, respectively. The two auto correlations are then defined by

$$R_{xx}(\tau)=\lim_{T\to\infty}\frac{1}{T}\int_0^T x(t)x(t+\tau)dt \tag{1}$$

and

$$R_{yy}(\tau)=\lim_{T\to\infty}\frac{1}{T}\int_0^T y(t)y(t+\tau)dt \tag{2}$$

These time-domain functions can be transformed into the frequency domain by applying the Fourier transform F, yielding the two real-valued auto spectra

$$G_{xx}(f) = F[R_{xx}(\tau)] \tag{3}$$

and

$$G_{yy}(f) = F[R_{yy}(\tau)] \tag{4}$$

Relationships (1-4) are clearly single-channel functions, and in *themselves reflect nothing regarding causality between input* and output or between two transducer signals. The similarity between two signals $x(t)$ and $y(t)$ may be measured by the cross correlation, which is defined by

$$R_{yx}(\tau)=\lim_{T\to\infty}\frac{1}{T}\int_0^T y(t)x(t+\tau)dt \tag{5}$$

The cross correlation function when transformed into the frequency domain yields the complex-valued cross spectrum

$$G_{yx}(f)=F[R_{yx}(\tau)] \tag{6}$$

a function that automatically contains both magnitude and phase information regarding the two input signals. Finally, the coherence function is defined as the ratio of the magnitude squared of the cross spectrum normalized by the two auto spectra

$$\gamma^2(f)=\frac{\overline{|G_{yx}(f)|^2}}{\overline{G_{xx}(f)}\ \overline{G_{yy}(f)}} \tag{7}$$

This function is a measure of causality between input and output, or in other words the strength of signal $y(t)$ due to the input signal $x(t)$. A value of $\gamma^2=1$ denotes perfect correlation; whereas, if $\gamma^2=0$ signal $x(t)$ has no influence on $y(t)$.

Experimental Uncertainty The drag-type flow meter, the displacement transducer, and the two pressure transducers used to measure mean pressures were all calibrated *in situ* using the data acquisition system. Least-square regression techniques were employed to fit empirical equations to sets of 8 to 20 data points, yielding coefficients of determination $r^2\geq 0.99$. The estimates of experimental uncertainty are as follows.

Nomenclature

b = opening of valve
c = radial distance between spool and wall
D = spool diameter
d = radial distance between spool neck and valve body
e = radial eccentricity between spool and valve body
f = frequency
$F[\ ]$ = Fourier transform
$G_{xx}(f)$ = auto spectral function for $x(t)$
$G_{yy}(f)$ = auto spectral function for $y(t)$
$G_{yx}(f)$ = cross spectral function for $x(t)$ and $y(t)$
l = axial distance along jet
p = pressure
p' = fluctuating pressure
p_c = mean pressure in valve chamber
p_u = upstream pressure
p_d = downstream pressure
p_v = vapor pressure
p_1 = pressure at transducer $P1$
p_2 = pressure at transducer $P2$
Q = volumetric flowrate
T = time of integration
t = time
$R_{xx}(\tau)$ = auto correlation function for $x(t)$
$R_{yy}(\tau)$ = auto correlation function for $y(t)$
$R_{yx}(\tau)$ = cross correlation function for $x(t)$ and $y(t)$
V_c = velocity in vena contracta
V_j = jet velocity
V_0 = approach velocity
$x(t)$ = input signal from transducer $P1$
$y(t)$ = input signal from transducer $P2$
Δf = width of frequency channel/band
$\Delta p=p_u-p_d$ = pressure differential across valve
$\gamma^2(f)$ = coherence function
σ = cavitation index
τ = time

Table 1 Estimates of experimental uncertainty

Quantity and units	Mean Value	Fluctuating Value
Flow rate (m^3/s)	$\pm 1 \times 10^{-5}$	- -
Valve position (m)	$\pm 5 \times 10^{-6}$	- -
Temperature (°C)	± 0.5	- -
Pressure (Pa)	$\pm 2 \times 10^{4}$	± 2

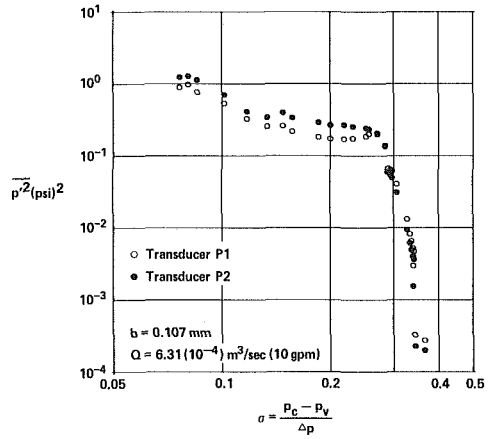

Fig. 3 Mean-square energy versus cavitation index for model valve at a fixed opening

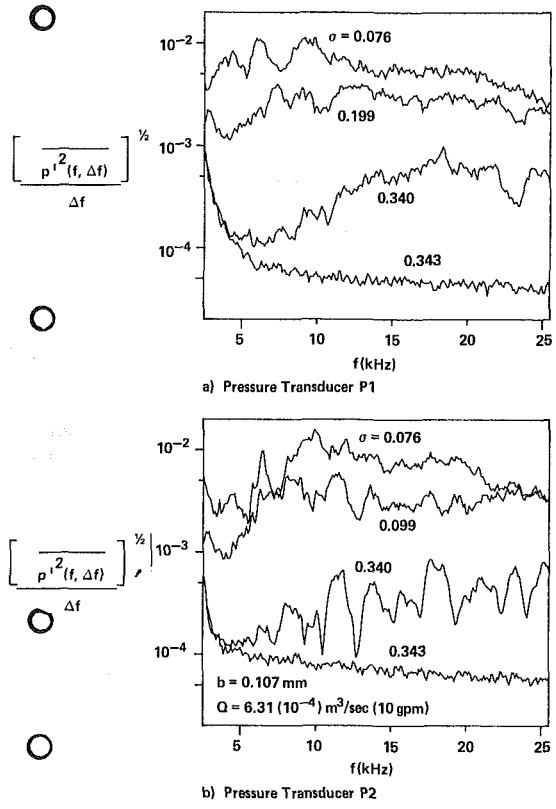

Fig. 4 Energy spectra for model valve at fixed opening

Results

The tests to be reported here were conducted with the valve held at the fixed opening b shown in Fig. 2, and the flowrate Q maintained virtually constant by careful and continuous monitoring of the output from the drag-type flow meter. As discussed thoroughly in Martin et al. [6] cavitation could be either completely suppressed, or allowed to develop extensively by control of downstream throttle valves, in conjunction with upstream valves to maintain constant flow. The cavitation index is defined in terms of the chamber pressure p_c by

$$\sigma = \frac{p_c - p_v}{\Delta p} \tag{8}$$

in which p_v is the vapor pressure of the oil, and Δp is the pressure drop across the valve.

Figure 3 demonstrates the sensitivity of mean square energy to the degree of cavitation as represented by the cavitation index, σ. The results plotted on this graph for a fixed opening b = 0.107 mm and a constant flowrate of Q = 6.31 (10^{-4})m^3/s (10 gpm) cover the range of maximum or fully-developed cavitation ($\sigma = 0.076$) to no cavitation ($\sigma = 0.364$). Note that the mean-square energy varies over a range of nearly five orders of magnitude, and is in particular a very sensitive indicator of cavitation intensity once cavitation commences. Indeed, the energy level increased by factors of 14.5 and 16.0 for transducers $P1$ and $P2$, respectively, from the lower noncavitating run ($\sigma = 0.343$) to the first cavitating test ($\sigma = 0.340$). The value of the cavitation index at inception can be assumed to be approximately 0.342. The individual auto spectra plotted in Figs. 4(a) and 4(b) for transducers $P1$ and $P2$, respectively, illustrate the effect of cavitation on noise levels over a frequency band 2.5 kHz$<f<$25.6 kHz. The lower limit is fixed by the desired intent to eliminate noise created by the downstream throttle valves, which was especially a nuisance for the larger values of σ. The auto spectra for the two lower values σ show that noise is fairly wide band once cavitation is quite developed. Clearly, the examination of auto spectra from either pressure transducer, or the simple use of r.m.s. energy, can be useful diagnostic tools in the detection of cavitation inception and its extent, once developed.

Two instruments can on occasion be used in conjunction with digital signal analysis to show causality of recordings. The cross spectrum between two signals, which is the Fourier transform of the cross correlation, as well as the coherence, can be employed to indicate correlation, if in fact it exists. Both of the functions will be demonstrated to be useful diagnostic tools in the identification of cavitation inception as well as rough indicators of the extent of developed cavitation.

The cross spectrum, being a complex function, can either be represented in terms of its real and imaginary parts, or perhaps more usefully in this instance, in terms of magnitude and phase. Inasmuch as the magnitude is simply the product of the magnitudes of the two auto spectra, which are only real-valued functions, a plot of mean-square energy in the cross spectrum would be no more revealing than the individual mean-square energies shown on Fig. 3 because of their similarity. The phase differences between the two signals tend to be quite revealing, as shown in Fig. 5 for the same runs discussed earlier. The nearly random phase angle variation for the noncavitating run ($\sigma = 0.343$) suggests that transducer $P1$ was apparently too far distant from transducer $P2$ to effect any correlation. Immediately following cavitation inception ($\sigma = 0.340$) the regularity in the phase angle variation with frequency becomes remarkable. Although not shown here, the regularity persists, as σ is lowered to the intermediate case plotted ($\sigma = 0.199$), finally becoming perhaps somewhat less regular as the cavitation develops more fully at $\sigma = 0.076$. Interestingly, the rather limited linear variation of phase angle versus frequency from $f = 2.5$ kHz to $f = 5.0$ kHz for $\sigma = 0.199$ suggests a pure time delay, or in other words a constant acoustic velocity for the noise created in this band by perhaps some of the larger bubbles. Selected curves of the coherence function are plotted in Fig. 6 for the same runs, again demonstrating virtually no correlation for the noncavitating run. This low level of coherence indicates that transducer $P2$ receives little or no related disturbances sensed by transducer $P1$, probably as a consequence of the

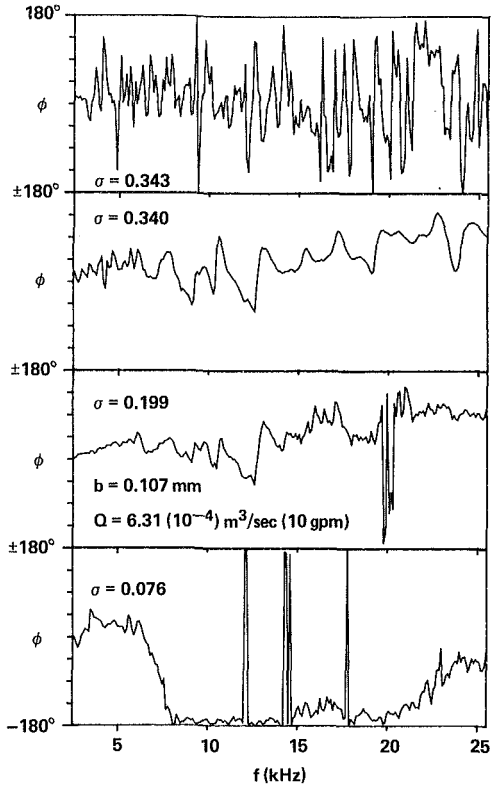

Fig. 5 Phase difference versus frequency for model valve at fixed opening

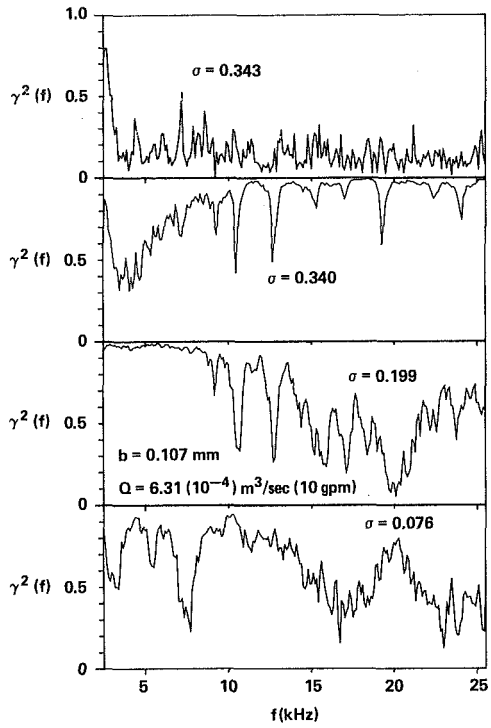

Fig. 6 Coherence function versus frequency for model valve at fixed opening

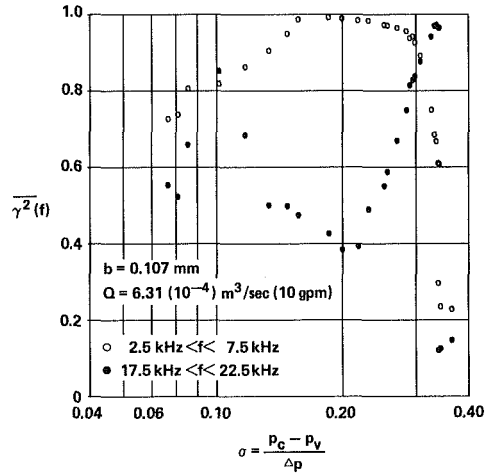

Fig. 7 Area under coherence function for model valve at fixed opening

large separation of the two instruments in terms of jet thickness. The remaining three curves suggest the probable influence of bubble size on the shifting range of very significant coherence values (>0.8) as the cavitation number changes. Clearly, the very high coherence for $\sigma=0.340$ should correspond to the expected existence of the smallest bubbles and lowest void fractions, while for $\sigma=0.199$ the domination of larger bubbles shifted the range of high coherence, which is in this instance indeed remarkably high (>0.95) over a 5 kHz range, to the lowest end of the frequency spectrum. Once the cavitation develops more fully ($\sigma=0.076$), resulting in a range of bubble sizes, not to mention interference and interaction during collapse, etc. the higher coherence values begin to diminish, but still contain some semblance of causality. The apparent effect of the cavitation index on bubble size and their resulting shifting influence on the coherence function for different frequencies can be clarified by the two plots in Fig. 7 for the same series of tests as shown in Fig. 3. Each point on Fig. 7 corresponds to the normalized area under the coherence function plotted in Fig. 6 over the specified frequency band of 5 kHz. The open circles, which represent the average coherence between 2.5 kHz to 7.5 kHz, show a lower coherence until the cavitation develops, a very high value for a wide range of cavitation index, and finally a continual dropoff as σ falls below 0.156. On the other hand, the darkened circles for 17.5 kHz$<f<$22.5 kHz show a peak in the average coherence near inception, followed by a gradual falling until σ approaches 0.199, after which there is an erratic increase as σ is lowered further. It is contended that the somewhat opposite trends shown by the two plots of Fig. 7 reflect the direct effect of the cavitation index on bubble size and the associated frequency range for which the coherence is evaluated.

Conclusions

It has been demonstrated that digital signal analysis can be expanded beyond the common use of auto power spectra to the application of such two-channel features as the cross spectrum and the coherence function. Both of the diagnostic facilities can be employed to enhance the identification of cavitation inception as well as to provide some measure of the level or extent of cavitation. The cross spectrum not only contains the usual mean-square energy available through individual auto spectra, but can also represent the extent of causality, or randomness, in terms of the phase difference between the two instruments. The coherence function, being a measure of causality, can be employed to detect the inception and, to a lesser extent, the degree of cavitation, because of the effect of the cavitation index on bubble size, and hence indirectly the associated frequency range for which there is a correlation between instruments. Although these results are for measurements conducted in an enclosed space for which reverberation effects may be present, some similarity would be expected for unconfined systems.

In summary, two dynamic instruments sensitive to pressure fluctuations emanating from cavitation can be utilized to enhance the identification of cavitation. These instruments could be two pressure transducers as reported here, two accelerometers properly placed, or perhaps a pressure transducer and an accelerometer. Indeed, limited testing with the latter pair on the prototype metal valve reported in Martin et al. [6] yielded similar conclusions.

Acknowledgments

The results reported in this paper originated from the investigation supported by the Air Force Aero Propulsion Laboratory through AFOSR Contract F33615-77-C-2036, under the direct administration by Project Engineer Paul D. Lindquist.

References

1 Arndt, R. E. A., "Cavitation in Fluid Machinery and Hydraulic Structures," *Annual Review of Fluid Mechanics*, Vol. 13, 1981, pp. 273–278.

2 Jorgensen, D. W., "Noise from Cavitating Submerged Water Jets," *Journal of the Acoustical Society* of America, Vol. 33, October 1961, pp. 1334–1338.

3 Deeprose, W. M., King, N. W., McNulty, P. J., and Pearsall, I. S., "Cavitation Noise, Flow Noise and Erosion," *Cavitation Conference*, Institution of Mechanical Engineers, September 3-5, 1974, Edinburgh, pp. 373–381.

4 Ōba, R., and Itō, Y., "Cavitation Shock Pressures in a Venturi," ASME *Cavitation and Polyphase Flow Forum*, 1975, pp. 2–6.

5 Blake, W. K., Wolpert, M. J., and Geib, F. E., "Cavitation Noise and Inception as Influenced by Boundary-Layer Development on a Hydrofoil," *Journal of Fluid Mechanics*, Vol. 80, 1977, pp. 617–640.

6 Martin, C. S., Medlarz, H., Wiggert, D. C., and Brennen, C., "Cavitation Inception in Spool Valves," Transactions, ASME JOURNAL OF FLUIDS ENGINEERING, Vol. 103, 1981, pp. 564–576.

7 Bendat, J. S. and Piersol, A. G., *Measurement and Analysis of Random Data*, Wiley, 1966.

Correlation of Cavitation Erosion and Sound Pressure Level

P. A. Lush
Thermo-Fluids Engineering
Research Centre,
The City University,
London, EC1V 0HB

B. Angell
Admiralty Marine Technology Establishment,[1]
Holton Heath,
Poole, Dorset, U.K.

The purpose of this paper is to investigate the existence of a correlation between the cavitation erosion rate of 99 percent pure aluminium and the sound pressure level of the cavitation noise. The data used were obtained recently for a variety of cavitation inducers and specimen locations at both the University of Southampton, Southampton, U.K. and the Admiralty Marine Technology Establishment, Holton Heath. A regression analysis of the logarithm of erosion rate on sound pressure level, expressed in decibels, shows that for each configuration there is a significant correlation, which is independent of fluid velocity and cavitation number, although the likely error is quite large. It is concluded that an absolute relation between erosion and sound pressure cannot be ruled out and that in any case it would be possible to define a relation for a given configuration provided that calibration could be done in advance.

Introduction

The aim of this work is to establish experimentally using recently obtained data whether or not there exists a relation between cavitaion erosion and noise. Such a relation would allow the determination of the amount of erosion of components subjected to cavitating flow by simply monitoring the sound pressure level. Since both cavitation erosion and noise are produced by collapsing bubbles, it would seem reasonable that some relation exists but it is likely that any such relation would be affected by the material of the component, the flow pattern and the cavitation conditions, i.e., fluid velocity and cavitation number. It has already been established [1] that the sound pressure level varies at about the fourth power of fluid velocity at constant cavitation number while erosion rate tends to vary at a somewhat higher power, nearer the sixth. On the other hand, at a constant velocity, the erosion rate tends to peak at a cavitation number just above the choking or blocking point and the sound pressure behaves similarly but the maximum is not as sharply defined. Therefore at first sight there appears to be a good case for investigating the direct correlation between erosion rate and sound pressure.

The purpose of this paper is to review the previous work on this topic at Southampton University, Southampton U.K., and at the Admiralty Marine Technology Establishment, Holton Heath, and to decide if the idea is feasible. Preliminary work [2] suggested that a correlation existed between erosion rate and sound pressure level independent of flow conditions at least for the erosion of 99 percent pure aluminium. The erosion was characterized by the steady state rate of weight loss of the material and the sound, measured using a flush mounted pressure transducer positioned downstream of the cavitation zone, was expressed as the mean square pressure over the audio-frequency range, i.e., 10 Hz - 40 kHz. Results were obtained at Southampton University for a convergent-divergent wedge inducer using a sidewall specimen of the material, i.e., 99 percent pure aluminium and at A.M.T.E. for a circular cylinder using the cylinder itself as specimen. It was found that an expression of the form:

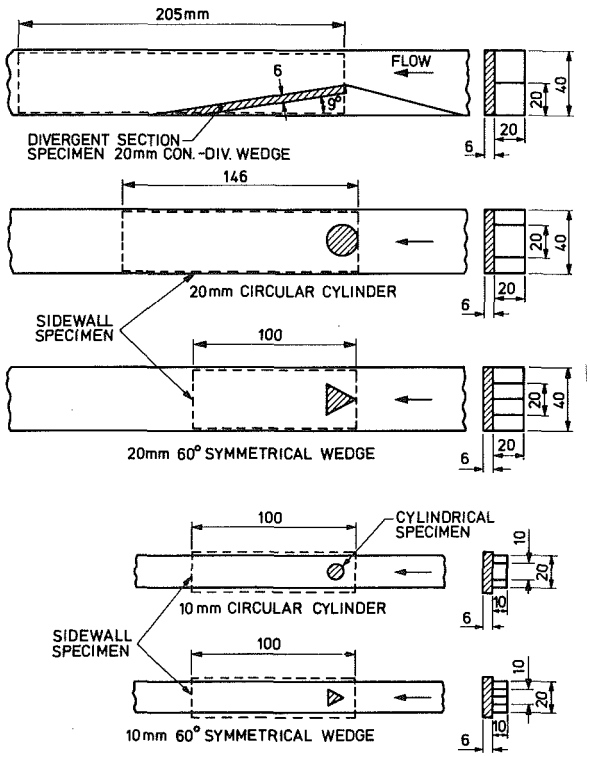

Fig. 1 Erosion test specimens and their position in the working section. (All dimensions in mm).

[1] Now Admiralty Research Establishment, Holton Heath.

Contributed by the Fluids Engineering Division of THE AMERICAN SOCIETY OF MECHANICAL ENGINEERS and presented at the International Symposium on Cavitation Noise. Manuscript received by the Fluids Engineering Division, March 30, 1983.

$$\text{Erosion rate} \propto (\text{Mean square pressure})^n \quad (1)$$

was applicable and that this expression was apparently independent of cavitation conditions, i.e., throat velocity and cavitation number. It appeared that the index n was different for the two configurations, being about 0.4 for the convergent-divergent wedge and 0.6 for the cylinder. The actual erosion rate at a particular sound pressure level was about a factor of 10 higher for the cylinder compared with the convergent-divergent wedge.

. Subsequently, the tests were repeated using the same configuration at A.M.T.E. [3] and at Southampton University, Selim [4] extended his tests to cover additional configurations, in particular the circular cylinder and the 60 deg symmetrical wedge. The main purpose of these tests was to explore the difference between operating at constant cavitation number and at constant velocity and the changes in erosion rate for the different configurations.

Because of the large amount of scatter and the relatively small number of points, the data from all these tests has been analyzed by the method of least squares to find the best fit to the power law expression, equation (1), and the fit has been checked for significance and the 95 percent confidence limits calculated. Some 20 percent of results were found not to be significant at the 5 percent level and have been excluded from any further consideration. This analysis should allow an assessment to be made of the usefulness of the above expression for 99 percent pure aluminium over a range of different configurations.

Experimental Work

For the experiments at the Department of Mechanical Engineering, Southampton University, Selim used a cavitation tunnel with a parallel-sided working section of either 40 × 20 mm or 20 × 10 mm cross-section. The flow rate and pressure in the working section could be varied independently and therefore operation at either constant throat velocity or constant cavitation number was possible. The flow rate through the working section could be controlled by a bypass valve and the pressure by a regulator valve connected to an external compressed air supply. The cavitation was produced by various inserts fitted into the upstream portion of each working section; they were a convergent-divergent wedge, a circular cylinder and a 60 deg symmetrical wedge, all having a geometrical blockage of 50 percent in their respective working sections (see Fig. 1).

The cavitation number upstream of the throat is defined as follows:

$$\sigma_0 = \frac{p_0 - p_v}{\frac{1}{2}\rho U_0^2} \quad (2)$$

where p_0 and U_0 are, respectively, the static pressure and fluid velocity in the working section upstream of the throat, p_v is the vapor pressure at bulk liquid temperature and ρ is fluid density. Although the geometrical blockage of each inducer is similar, the actual blockage varies considerably. An allowance has been made for this by redefining a cavitation number as follows:

$$\sigma = \frac{\sigma_0 - \sigma_{0b}}{1 + \sigma_{0b}} \quad (3)$$

where σ_{0b} is the value of σ_0 at choking or blocking and is approximately independent of fluid velocity. Furthermore the throat velocity U can be obtained from:

$$U = U_0\sqrt{1 + \sigma_{0b}} \quad (4)$$

The results were obtained by running the tunnel in two ways: one at a constant cavitation number σ of 0.035, corresponding roughly to the maximum noise at a given velocity, while the throat velocity U was varied between 24 and 40 m/s, and the other at a constant throat velocity of 37 m/s while cavitation number σ was varied between zero, corresponding to choking or blocking, and about 0.1. The air content in the tunnel remained constant at about 75 percent of the value at saturation.

The sound pressure was measured using a quartz piezoelectric transducer, Vibrometer type 6QP500, which was flush-mounted in the tunnel wall at a distance of 215 mm and 130 mm downstream from the throat in the larger and smaller working sections respectively. The transducer was connected to a charge amplifier, Vibrometer type TA-3/C and the voltage output analyzed in the audio-frequency range, i.e., 10 Hz to 40 kHz using a Bruel and Kjaer sound level meter type 2203 as a true RMS meter. The sound pressure level (SPL) was expressed in decibels relative to 1 μbar, i.e., $20 \log_{10} p_{rms}/p_{ref}$, where $p_{ref} = 1$ μbar.

The erosion was determined using a specimen of the material mounted on the sidewall of the tunnel downstream of the inducer. For the convergent-divergent wedge, a specimen was also mounted on the divergent wall of the inducer and the circular cylinder was also itself a test specimen. The material used for all specimens in these tests was 99 percent pure aluminium (S1C, B.S. 1470: 1969) in the form of either plate 6 mm thick or rod of 20 mm or 10 mm diameter. This material was chosen because it is easily eroded. The weight loss was determined by weighing the specimen at, typically, 1½ hour intervals and comparing its weight with the initial value. A precision electronic balance (Oertling, Model R42) was used, which allowed the weight to be determined to the nearest 0.1 mg. It was found that there was an incubation period during which no material was lost and after a short acceleration period, which was virtually undetectable, the erosion proceeded at a constant rate. This was the value of weight loss rate (WLR) measured in these tests and the most convenient unit was found to be mg/hr. Further details of the apparatus and test procedures can be found in Selim's thesis [4].

The experiments at A.M.T.E. (Holton Heath) were made in a seawater cavitation tunnel with a working section of 47 × 47 mm which is somewhat larger than that at Southampton University. Using control valves positioned upstream and downstream of the working section, it was possible to operate the tunnel at either constant velocity or constant cavitation number. While this arrangement was not as convenient as on the other tunnel, it was nevertheless satisfactory. The cavitation was produced by a 25 mm diameter cylinder of the same material as used in the other experiments. The specimen was mounted centrally in the working section and produced nearly the same blockage as the other configurations, i.e., 53 percent. Because the rig uses seawater from an open sump, the gas content will be approximately constant at the saturation value.

The tunnel was run at a constant cavitation number

Nomenclature

n	= power law index	U	= fluid velocity in throat	σ	= throat cavitation number
p_0	= static pressure in working section	U_0	= fluid velocity in working section	σ_0	= working section cavitation number
p_v	= saturated vapor pressure	WLR	= weight loss rate in mg/hr	σ_{0b}	= value of σ_0 at choking
SPL	= sound pressure level in dB	ρ	= fluid density		

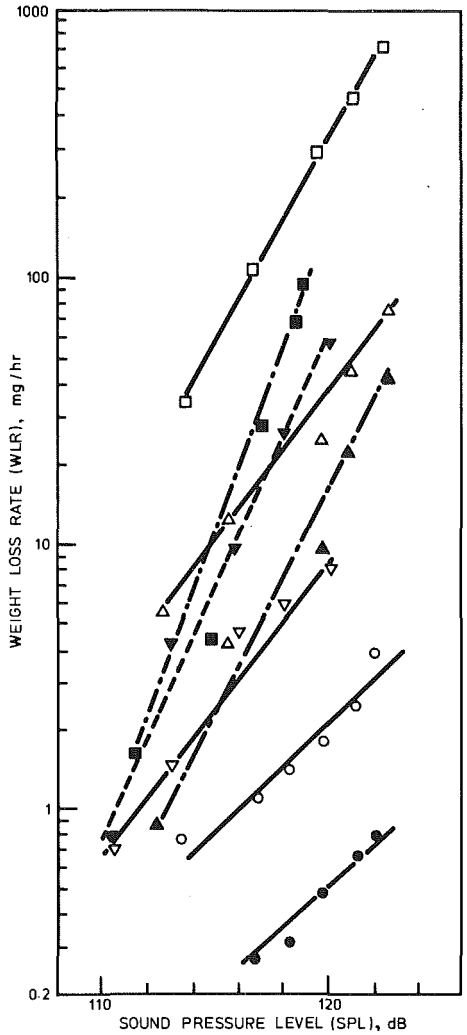

Fig. 2(*a*) Variation of WLR with sound pressure level at constant cavitation number of 0.035 with varying throat velocity for various configurations.

○, 20 mm CON. DIV. (SIDEWALL EROSION);
△, 20 mm CYLINDER (CYLINDRICAL EROSION);
□, 20 mm 60 deg SYMMETRICAL WEDGE;
▽, 10 mm CYLINDER (CYLINDRICAL EROSION).

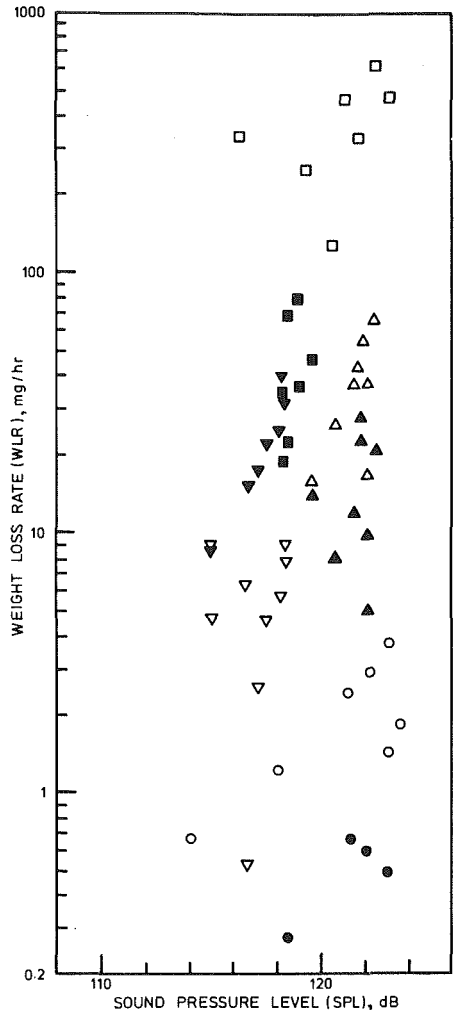

Fig. 2(*b*) Variation of WLR with SPL at constant throat velocity of 37 m/s with varying σ for various configurations:

●, 20 mm CON.-DIV. (DIVERGENT-SECTION EROSION);
▲, 20 mm CYLINDER (SIDEWALL EROSION);
■, 10 mm 60 deg SYMMETRICAL WEDGE;
▼, 10 mm CYLINDER (SIDEWALL EROSION).

corresponding to the maximum noise at a given velocity and the throat velocity varied over a range from 19 to 32 m/s. The velocity was also fixed at two values, i.e., 21.6 and 32.4 m/s, and the cavitation number varied over a range similar to that used in the Southampton tunnel.

The cavitation noise was measured with the same type of equipment as that used at Southampton and the transducer was located 240 mm downstream of the cavitation inducer. Because it was difficult to relocate the cylinder in precisely the same orientation, the weight loss was determined by weighing the specimen at the end of the exposure time and comparing it with the initial weight. The exposure time was adjusted to suit the severity of attack and varied between 1 and 10 hours. To determine the weight loss rate, the incubation period was neglected on the grounds that it would be a small fraction of the total time and the loss in weight was simply divided by the exposure time. As a check on this assumption, four separate tests were made at the same conditions, i.e., $U=25$ m/s at maximum noise but with exposure times varying between 1 and 7 hours. It was found that the incubation time was about 1 hour in this case, giving an error in weight loss rate of about 15 percent, which is considerably smaller than the scatter in the results produced by other causes. It was considered that the tests were so short and the erosion so rapid that electrochemical corrosion was negligible in all the results analyzed.

Analysis of Results

In order to make an objective assessment of the data, regression analysis was used and the results tested for significance. The variation between weight loss rate and mean square pressure was assumed to have the form given by equation (1), in which the index n and the constant of proportionality have to be determined. Since the sound pressure level is essentially the logarithm of the mean square pressure, this equation can be re-written as:

$$\log_{10}\mathrm{WLR} = \frac{n}{10} \times \mathrm{SPL} + \mathrm{const.} \tag{5}$$

The regression line of log WLR on SPL is then found in order to determine the slope and hence the index n. At the same time the correlation coefficient is calculated and compared with the value required for a significant correlation at the 5 percent level, i.e., a 95 percent probability that the correlation is not due to chance variation alone. The results from the groups of data that did not pass this test were excluded and the index

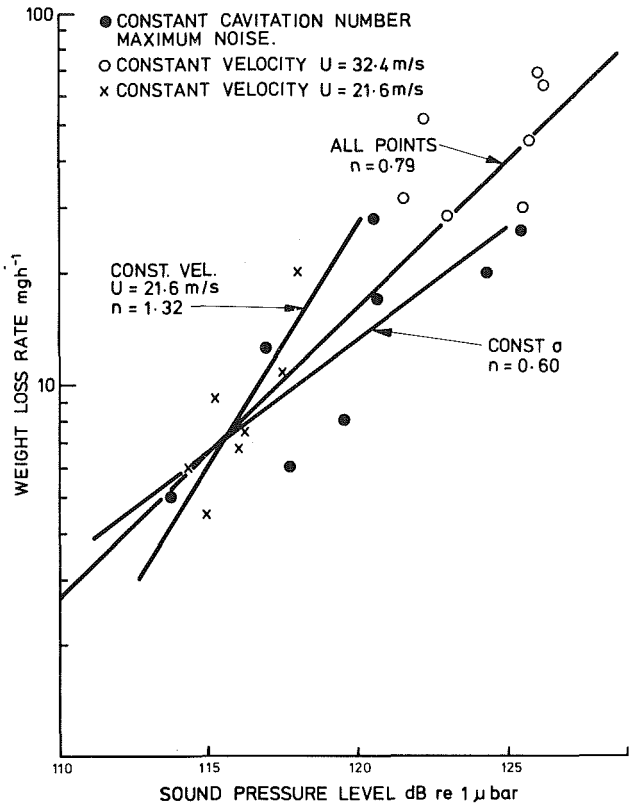

Fig. 3 Variation of weight loss rate as a function of sound pressure level.

was not calculated. In addition to the index, the weight loss rate at the arbitrary reference sound pressure level of 120 dB and the corresponding 95 percent confidence limits were determined.

Initially the data corresponding to a particular configuration, i.e., cavitation inducer and specimen location, was analyzed in two separate groups, one at constant cavitation number and the other at constant velocity. Then, since in practical cases both velocity and cavitation number would vary, all the data points for a particular configuration were analyzed together without regard to cavitation conditions. For the A.M.T.E. data, although there was only one configuration, there were two sets of data at constant velocities, one at 21.6 and the other 32.4 m/s, although the latter failed the significance test.

Selim's data are shown graphically in Figs. 2(*a*), 2(*b*) and the A.M.T.E. data in Fig. 3. The results of the regression analysis are shown in the tables; Table 1 gives the values of index n and Table 2 the values of WLR at 120 dB sound pressure level. The earlier A.M.T.E. data are excluded from the latter because the sound pressure measurements were uncalibrated.

Discussion of the Results

The first attempt [2] to correlate weight loss rate with sound pressure was made using results obtained in the Southampton University cavitation tunnel for the 20 mm convergent-divergent wedge with the erosion measured on the sidewall. It was found that the index n, taking all the data together, was 0.4 and the weight loss rate at 120 dB was 2.8 mg/hr. The results of erosion of cylindrical specimens obtained from the A.M.T.E. tunnel showed that the index was 0.63 with an estimated erosion rate of 40 mg/hr at 120 dB. If two data points which did not lie close to the trend line are included, these values must be modified to 0.85 and 49 mg/hr,

Table 1 Index (n) of power law

Cavitation inducer	Specimen location	Constant σ = 0.035	Constant U = 37 m/s	All Points
20mm con-div wedge	self sidewall	0.91 ±0.14 0.76 ±0.22	- 0.57 ±0.38	0.71 ±0.31 0.60 ±0.23
20 mm cylinder	self sidewall	1.07 ±0.19 1.54 ±0.32	- -	0.94 ±0.33 1.20 ±0.49
10 mm cylinder	self sidewall	1.14 ±0.27 1.83 ±0.29	- 2.17 ±0.84	1.01 ±0.74 1.88 ±0.19
20mm symmetric wedge	sidewall	1.48 ±0.08	-	1.05 ±0.47
10mm symmetric wedge	sidewall	2.43 ±0.56	-	2.10 ±0.57
AMTE cylinder	self "	0.60 ±0.36 0.56 ±0.27*	1.32 ±0.75† 1.08 ±0.74*	0.79 ±0.18 0.85 ±0.49*

Table 2 Weight loss rate at 120 dB (mg/hr) (giving upper 95 percent confidence limit)

Cavitation inducer	Specimen location	Constant σ = 0.035	Constant U = 37 m/s	All Points
20mm con-div wedge	self sidewall	0.50 +0.03 2.1 +0.4	- 1.6 +0.6	0.45 +0.07 1.8 +0.3
20mm cylinder	self sidewall	34 +7 15 +5	- -	27 +6 10 +4
10mm cylinder	self sidewall	9.2 +3.9 58 +27	- 78 +47	8.6 +9.1 64 +13
20mm symmetric wedge	sidewall	330 +21	-	280 +100
10mm symmetric wedge	sidewall	140 +120	-	86 +46
AMTE cylinder	self	13 +5	28 +29†	17 +3

* Earlier result

† U = 21.6 m/s.

respectively. These results did not show a marked change in index when operation of the tunnel was altered from constant cavitation number to constant velocity; however, the subsequent work at both Southampton [4] and at A.M.T.E. [3] did show marked differences between these two modes of operation. This change is possibly due to the rather small number of data points used in the original paper [2].

In general, the correlation of the data for operation at constant cavitation number with variation in velocity is highly significant, i.e., better than 0.1 percent level. On the other hand, data obtained at constant velocity with variation in cavitation number show very little correlation. When all the results, for a given configuration, are taken together without regard to cavitation conditions, the correlation coefficients are reduced but the significance is much the same as the case of constant cavitation number because of the increase in the number of data points. However, the 95 percent confidence limits for the regression lines are markedly increased in most cases.

The value of the index n varies quite widely between configurations and between test method, i.e., constant cavitation number or constant fluid velocity. The index also varies between the same configuration in different tunnels, i.e., circular cylinder (see Table 1). The average value of the

index for all configurations at constant cavitation number is 1.23; the average value at constant velocity for those sets of data which are significantly correlated is 1.29 and the average value for the combined sets of data is 1.11. These values are all very similar; it seems quite likely that the variations are statistical and that there is an underlying common value of just greater than 1.0. This conclusion is supported by recent results obtained by Grant [5] at City University, in which the noise measurements were made more carefully.

The value of weight loss rate at the arbitrary reference sound level of 120 dB also varies widely between configurations; as already noted by Selim [4] and Selim and Hutton [1], the values may vary by a factor of as much as about 600 (see Table 2). However, Grant's [5] more recent measurements indicate that the discrepancy between convergent-divergent wedge and symmetric wedge at the same sound level is very much less, rather a factor of about 3. This difference is attributed to the more careful measurement of the noise levels, which are strongly influenced by transducer positioning. The possibility of an absolute relation between weight loss rate and sound pressure level cannot be ruled out entirely. In any case, the highly significant value of correlation coefficient, particularly for the data obtained at constant cavitation number, does allow the possibility of defining a relation between erosion rate and sound level provided that the configuration can be calibrated by prior experiment.

Some idea of the likely error in weight loss rate can be obtained from the 95 percent confidence limits, i.e., the error which will not be exceeded in 95 percent of the cases considered (see Table 2). At constant cavitation number, the error ranges from 6 percent up to 84 percent with an average value of around 32 percent; if all points are considered, the likely error ranges more widely from about 15 percent up to 105 percent with an average in the region of 37 percent. It should be noted that, because the regression analysis has been done using the logarithm of the weight loss rate, the percentage values, unless small, apply only to errors in excess of the regression line; errors below the line will be somewhat smaller, e.g., 100 percent above implies 50 percent below. Only the upper 95 percent confidence limit is given in Table 2.

Therefore, the error involved in about 95 percent of all estimates would not on average exceed about 32 percent for operation at constant cavitation number and about 37 percent for operation under any conditions. While the average likely error in both these cases is probably acceptable in practice, the maximum likely error may not be; however an error of 105 percent amounts to slightly more than a factor of 2, and it is likely that this is within the usual uncertainty encountered in erosion testing. Moreover, operation under conditions which vary at random would tend to produce an average erosion rate much closer to the regression line. Therefore it should be feasible to monitor erosion with an acceptable accuracy for a given configuration provided that the regression line can be established by prior testing. Whether or not this can be done to an acceptable accuracy for more realistic engineering materials remains a matter for speculation until further experimental work can be done.

Conclusions

These experiments have shown that there is a good correlation between erosion of 99 percent pure aluminium and sound pressure level for a given configuration, i.e., inducer and specimen location, provided that the cavitation number remains constant; on the other hand at constant velocity the correlation is very poor. For the more practical case when both velocity and cavitation number may vary, the correlation is still good but the expected errors are slightly larger.

The results indicated that the relation between erosion rate and mean square sound pressure could be interpreted as a power law with an index, which although varying considerably from configuration to configuration, had a value on average just greater than unity. The erosion rate at a particular value of sound pressure level ranged over about three orders of magnitude but improvements in noise measurements may reduce this discrepancy thus allowing an absolute relation between erosion and sound. The good correlation observed at least for a given configuration does allow the possibility of defining a relation between erosion rate and sound pressure for 99 percent pure aluminium, provided that the configuration can be calibrated by prior testing to obtain a regression line and confidence limits. The errors involved may be fairly large but it is likely that these may be acceptable in practice.

Acknowledgments

The authors are grateful to S.M.A. Selim for access to his original data and for supplying Figures 1, 2(a) and 2(b). One of the authors (P.A.L.) gratefully acknowledges the financial support of Procurement Executive, Ministry of Defence.

References

1 Selim, S. M. A., and Hutton, S. P., "Hydrodynamic Similitude for Cavitation Erosion," *Symposium on Cavitation Erosion in Fluid Systems*, ASME Spring Annual Meeting, Boulder, Colo. 1981.

2 Lush, P. A., Selim, S. M. A., Studd, L. W., and Angell, B., "The Relation Between Cavitation Noise and Erosion," *Proc. 5th Int. Conf. on Erosion by Liquid and Solid Impact*, Cambridge, 1979.

3 Silvester, R. A., "Correlation of Cavitation Noise and Erosion for Soft Aluminium Cylinders," A.M.T.E., unpublished internal memorandum.

4 Selim, S. M. A., "Cavitation Erosion in Fluid Flow," University of Southampton, Ph.D. thesis, 1981.

5 Grant, M. McD., "The Prediction of Cavitation Erosion," unpublished Ph.D. thesis, The City University, London, 1984.

The Hydrodynamic Stability of Rapidly Evaporating Liquids With Time Dependent Base States

J. W. Jacobs

I. Catton

M. S. Plesset

School of Engineering and Applied Science,
University of California,
Los Angeles, Calif. 90024

The hydrodynamic stability of a rapidly evaporating liquid surface is examined. The problem is modeled to mimic the case of a superheated liquid in equilibrium with its vapor in which, the pressure above the liquid surface is dropped suddenly. Both the liquid and its vapor are assumed to be inviscid, incompressible and semi-infinite in extent. In addition, the temperature dependence of fluid properties is neglected. A linear stability analysis is applied to this model. This study differs from previous work in that time dependent base states are used. As a result, a system of linear homogeneous differential equations must be integrated in time. This system consists of a partial differential equation for the liquid temperature field and two other linked ordinary differential equations in time. Various types of thermal boundary conditions yielding different base state temperature profiles are considered. The results of this experimentation are contrasted. An attempt is made to compare results of the transient method to experimental data.

Introduction

The behavior of rapidly evaporating liquid surfaces has been a subject of considerable interest over the past 10 years. This attention is due to their importance in applications as well as to an interest in the physical processes involved. It has been found that under certain conditions, the disruption of an originally flat rapidly evaporating liquid surface occurs resulting in large increases in the net evaporation rate. One such circumstance in which this phenomena may be important is the vacuum distallation process. There is also interest in this subject in the field of nuclear safety. The primary loop of a pressurized water reactor is filled with superheated water. If a pipe were to break in this loop, the superheated water would flash to steam and escape through the broken pipe. In turn the vapor-liquid interface would recede into the system. In order to design for such an accident, the evaporation rate of the interface must be known; accurate calculations require an understanding of the behavior of the evaporating liquid surface.

Early researchers suggested that the disruption of the liquid surface resulted from the instability of the initially flat surface. One of the mechanisms for this instability can be explained as follows. Consider an infinite liquid-vapor system separated by a flat interface. The liquid is undergoing rapid evaporation so that there is a large negative temperature gradient near the surface of the liquid. Because there is a large difference in density between the liquid and vapor phases, a fluid particle passing through the interface from the liquid to the vapor via the evaporation process will undergo an acceleration. This causes the vapor to push down on the liquid due to Newton's second law of motion. Suppose then that the interface is perturbed slightly so that part of the surface is pushed into the liquid. Because of the large negative temperature gradient, this part of the interface will be pushed into a region of higher temperature. The net effect of this process is to locally increase the mass flux in the troughs of the disturbance wave while decreasing the mass flux on the peaks. These perturbations in mass flux cause local perturbations in the downward force exerted by the vapor on the liquid. In the troughs where the mass flux is locally increased, the downward force is increased. Likewise on the peaks where the mass flux is decreased, the force is decreased. This pressure differential causes the perturbed liquid surface to be displaced even further thus causing an auto-amplification leading to instability. Other authors have suggested instability mechanisms which involve the shearing effect between the liquid and vapor phases. In these cases the processes which lead to instability are much more complicated and are not immediately obvious. In this investigation we are interested in modeling the process described above. Thus, the model will be highly idealized however, we feel more can be gained by isolating particular mechanisms and analyzing simple models than by attacking the entire problem by solving the complex system of equations that completely describe the phenomena.

Hickman [1, 2] first presented experimental results in which surface waves were observed while performing experiments involving vacuum distillation. He was primarily interested in the effects of surface contaminants on a liquid undergoing evaporation in a vacuum. He explained the wave phenomena as being the result of a hydrodynamic mechanism. Much

Contributed by the Fluids Engineering Division of THE AMERICAN SOCIETY OF MECHANICAL ENGINEERS and presented at the Winter Annual Meeting, Phoenix, Ariz., November 14-19, 1982. Manuscript received by the Fluids Engineering Division, April 4, 1983. Paper No. 82-WA/HT-44.

later, Grolmes and Fauske [3] performed experiments in which they rapidly depressurized superheated liquids. Their experimental apparatus consisted of a glass tube containing a liquid at approximately room temperature and atmospheric pressure. Above the liquid a diaphragm separated this test section from a vacuum tank. The tank was evacuated and the diaphragm was broken to start the experiment. The process was photographed with a high speed movie camera. The investigators observed two distinct behaviors. For low superheat, the liquid vapor interface would remain intact and would recede slowly into the liquid. However, for high superheat the liquid surface would break apart and a mixture of vapor and liquid drops would be carried out the mouth of the tube. What appeared to be a two-phase wave traveled into the liquid at a constant speed.

Several authors [4–7] have presented studies in which the stability of an evaporating liquid surface was analyzed. However, these analyses were for systems with basic states that did not vary with time. If the physical system of interest varied slowly with time one could do a quasi-static stability analysis on the problem. This amounts to freezing the basic state at a point in time and performing the stability analysis as though the unperturbed problem was steady. Time would then be treated as an added parameter in the problem. The use of this method for the case of the Bénard problem with a density gradient which is a function of time, is discussed in detail by Mahler et al. [8], and by Gresho and Sani [9]. The general consensus is that the frozen time assumption is a good one if the base state evolves slowly enough; that is, if the rate of change of the base state is much less than the rate of growth or decay of the disturbance. In any case, the results of the quasi-static analysis would probably not differ significantly from the results mentioned above.

The physical systems which we are interested in this work are ones in which the basic state evolves very quickly. In particular, we are interested in modeling a configuration similar to the experimental set-up of Grolmes and Fauske. For this case it is clear that the time scale for the base state will not be much greater than the time scale of the disturbances. Therefore, a quasi-static analysis cannot be justified and a full transient analysis is necessary. We will look at the stability of two systems. The first one is the case where the pressure above a saturated liquid is suddenly decreased at $t=0$. This corresponds to the experiments of Grolmes and Fauske [3]. The second is the transient case where the evaporation rate is stepped at $t = 0$ to some constant value. We will show that the problem can be simplified by investigating an asymptotic solution of the cases mentioned above. A linear stability analysis will be employed.

Mathematical Formulation

In analyzing the system consisting of an infinite region containing a liquid and its vapor, both fluids are assumed to be inviscid, incompressible, and irrotational. In addition, we will assume constant fluid properties in this development. We realize that these restrictions eliminate many processes (including cellular convection and the Marangoni effect), however, as we mentioned earlier we are primarily interested in isolating the process described in the previous section. Further, the elimination of these phenomena aids us in that we solve a much simpler and more tenable set of equations. The equations governing the conservation of mass, momentum and energy in each fluid are:

$$\nabla^2\phi=0 \tag{1}$$

$$\frac{\partial\phi}{\partial t}+\frac{P}{\rho}+\frac{1}{2}(\nabla\phi)^2+gy=\text{constant} \tag{2}$$

$$\frac{\partial T}{\partial t}+\nabla\phi\cdot\nabla T=\alpha\nabla^2 T \tag{3}$$

where

$$\mathbf{v}=\nabla\phi$$

Auxiliary conditions at the interface are needed to solve equations (1, 2, 3). These are the jump conditions of the conservation of mass, normal momentum and energy across the free surface

$$\rho_l(\mathbf{v}_l-\mathbf{w})\cdot\mathbf{n}=\rho_v(\mathbf{v}_v-\mathbf{w})\cdot\mathbf{n}=J \tag{4}$$

$$\rho_v[(\mathbf{v}_v-\mathbf{w})\cdot\mathbf{n}](\mathbf{v}_v-\mathbf{v}_l)\cdot\mathbf{n}+P_v-P_l=\sigma\nabla\cdot\mathbf{n} \tag{5}$$

$$\rho_v[(\mathbf{v}_v-\mathbf{w})\cdot\mathbf{n}]L+(k\nabla T)\cdot\mathbf{n}=0 \tag{6}$$

Because in the case of a liquid-vapor system the latent heat of vaporization is usually very large we have neglected the transfer of sensible heat in the vapor phase. This is equivalent

Nomenclature

a = wave number
Bo = Bond number
c = heat capacity
c_1 = sound speed in the vapor before depressurization
c_2 = sound speed in the vapor after depressurization
f = periodic function which is a solution to equation (11)
g = gravitational acceleration
h = constant defined by equation (9)
J = mass flux
Ja = Jakob number
k = thermal conductivity of the liquid
L = latent heat of vaporization
M = molecular weight
$\mathbf{n}$ = unit normal vector to the free surface
N_ρ = density ratio
P = pressure
Q = dimensionless group defined by equation (27)
R = gas constant
t = time
t_c = critical time
t_0 = ramping time interval
T = temperature
T_i = uniform initial liquid temperature
T_∞ = vapor temperature at $y = +\infty$
T_s = temperature at the free surface
U = unit step function
$\mathbf{v}$ = velocity vector
V = base state liquid velocity
$\mathbf{w}$ = free surface velocity vector
W = variable defined by equation (21)
x,y,z = spatial coordinates
α = thermal diffusivity of the liquid
β = dimensionless growth rate
ΔT = T_i-T_∞
∇ = gradient operator
∇^2 = Laplace operator
η = surface height
$\eta_{\max}$ = maximum surface height attained
ρ = density
σ = surface tension
τ = temperature scale defined by equations (17) and (18)
ϕ = velocity potential
ψ = function of time used in the velocity potential solutions
ω_0 = natural frequency

Superscripts/Subscripts

$'$ = superscript denoting perturbation quantity
$*$ = superscript denoting base state quantity
l = subscript denoting a liquid property or variable
v = subscript denoting a vapor property or variable
sat = subscript denoting saturation value

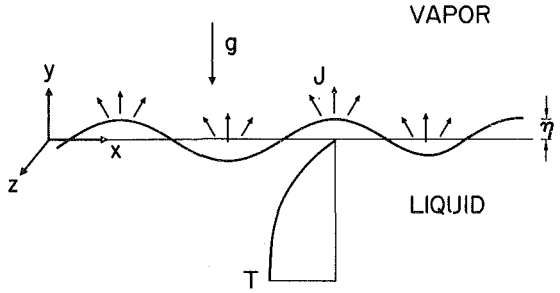

Fig. 1 Schematic of the physical system

to assuming that all the thermal energy transferred from the liquid phase to the surface is consumed in the latent heat. Except for the case of very high speed flows, the kinetic energy transferred across the interface is negligible so we will not consider it in our analysis. In addition we need another condition at the interface dealing with the kinetics of the process of evaporation. The following expression from Plesset [10] can be used

$$J=\left(\frac{RT_s}{2\pi M}\right)^{1/2}(\rho_{\text{sat}}-\rho_\infty) \tag{7}$$

At the present time there exists some debate as to whether this expression should be multiplied by a factor of two. This factor would have little effect on the results presented here and will therefore be omitted. The relation above can be linearized,

$$J=h(T_s-T_\infty) \tag{8}$$

where

$$h=\left(\frac{M}{2\pi RT_s}\right)^{1/2}\left(\frac{dP_{\text{sat}}}{dT}\right) \tag{9}$$

Figure 1 is a schematic of the system we wish to model. We shall specify that for $t<0$, the liquid and the vapor are in thermodynamic equilibrium and that the liquid is contained in the region $-\infty<y<0$ and the vapor in the region $0<y<\infty$. At $t=0$, the pressure of the vapor is reduced so that the system is no longer in equilibrium. The result will be a net mass flux from the liquid region to the vapor via the evaporating liquid surface. If the system is not perturbed, the surface will remain flat. We shall fix the plane $y=0$ to this free surface location. As a result $y=0$ will always be the location of the unperturbed free surface. This means that our frame of reference may be an accelerating one, however, the effects of this acceleration are small and for simplicity will be neglected in this analysis.

The base state we will look at is one with a flat interface located on the plane $y=0$. There will be a uniform upward velocity V in the liquid due to vaporization and the coordinate system chosen. We must then solve

$$\frac{\partial T^*}{\partial t}+V\frac{\partial T^*}{\partial y}=\alpha\frac{\partial^2 T^*}{\partial y^2} \tag{10}$$

where

$$V=-\frac{k}{\rho_l L}\frac{\partial T^*}{\partial y}\bigg|_{y=0}$$

to obtain the base state temperature profile. We will take the fluid temperature to be initially at a uniform value of T_i. We will look at two different cases which will determine the boundary condition at $y=0$ of equation (10). In the first T_∞ will be reduced at $t=0$ by a constant amount (call it ΔT) and held at that point. This represents the physical situation where the pressure is stepped down at $y=\infty$, thus in this case we are trying to duplicate the conditions of Grolmes and Fauske's experiments. In the second case, the net mass flux will be held constant starting at $t=0$. This configuration can, at least in principle, be physically duplicated by turning on a vacuum pump at $t=0$ which will draw the vapor out of the system at a constant rate. The implementation of this boundary condition in the solution of equation (10) requires the surface temperature to continuously drop. This may not be physically realistic, however, if we constrain ourselves to analyzing the system for a relatively short period of time the results should be physically meaningful. In implementing this constant flux condition we are by no means requiring that the total mass flux at each point on the surface be constant. We are only requiring that the net or average over the surface is constant. We are still allowing for perturbations in this flux to exist.

If now the initially flat interface located at $y=0$ is given a small perturbation to the position $y=\eta(t)f(x,z)$, where f is a periodic function satisfying

$$\frac{\partial^2 f}{\partial x^2}+\frac{\partial^2 f}{\partial z^2}+a^2 f=0 \tag{11}$$

and, in addition, if the other variables are given similar infinitesimal perturbations

$$\phi'=\phi'(y,t)f(x,z) \tag{12}$$

$$T'=T'(y,t)f(x,z) \tag{13}$$

$$P'=P'(y,t)f(x,z) \tag{14}$$

$$J'=J'(t)f(x,z)$$

Then equation (1) has the following solutions

$$\phi_l'=\psi_l e^{ay} \tag{15}$$

$$\phi_v'=\psi_v e^{-ay} \tag{16}$$

We will make the equations dimensionless by

$$T\to(\tau)\,T \qquad (\eta,x,y,z)\to\left(\frac{\alpha^2}{g}\right)^{1/3}(\eta,x,y,z)$$

$$(V,W)\to(\alpha g)^{1/3}(V,W) \qquad t\to\left(\frac{\alpha}{g^2}\right)^{1/3}t$$

$$a\to\left(\frac{g}{\alpha^2}\right)^{1/3}a \qquad J\to(\rho_l(\alpha g)^{1/3})J$$

where

$$\tau=T_i-T_\infty=\Delta T \tag{17}$$

for the first base state configuration mentioned above (constant ΔT) and

$$\tau=-\left(\frac{\alpha^2}{g}\right)\frac{\partial T^*}{\partial y}\bigg|_{y=0} \tag{18}$$

for the second (constant flux). Note that we have made no distinction between dimensionless and dimensional variables since from this point on we will be dealing only with dimensionless quantities. The dimensionless perturbation equations are then,

$$\frac{\partial T'}{\partial t}+V\frac{\partial T'}{\partial y}+\left[\left(1-\frac{2N_\rho}{N_\rho+1}\right)J+W\right]e^{ay}\frac{\partial T^*}{\partial y}=\frac{\partial^2 T'}{\partial y^2}-a^2T' \tag{19}$$

$$\frac{d\eta}{d\tau}=W-2\frac{N_\rho}{N_\rho+1}J \tag{20}$$

$$\frac{dW}{dt}=-\left(\frac{N_\rho-1}{N_\rho+1}\right)a\left[N_\rho VJ+\left\{1+\frac{a^2}{\text{Bo}}\right\}\eta\right] \tag{21}$$

with the boundary condition for the perturbation liquid temperature at $y=0$

$$\frac{\partial T'}{\partial y} = -\frac{J}{\mathrm{Ja}} - \eta \frac{\partial^2 T^*}{\partial y^2}\bigg|_{y=0} \tag{22}$$

where

$$J = \mathrm{Ja} Q\left(T' + \eta \frac{\partial T^*}{\partial y}\right)\bigg|_{y=0} \tag{23}$$

and the dimensionless groups are

$$\mathrm{Ja} = \frac{\tau c}{L} \tag{24}$$

$$N_\rho = \frac{\rho_l}{\rho_v} \tag{25}$$

$$\mathrm{Bo} = \frac{(\rho_l - \rho_v) g \left(\frac{\alpha^2}{g}\right)^{2/3}}{\sigma} \tag{26}$$

$$Q = h\left(\frac{\alpha^2}{g}\right)^{1/3} \frac{L}{k} \tag{27}$$

The dimensionless wave number a is also a parameter in this problem giving us a total of five dimensionless parameters.

Solution Procedure

The dimensionless problem for the base state temperature profile is

$$\frac{\partial T^*}{\partial t} - \left(\mathrm{Ja} \frac{\partial T^*}{\partial y}\bigg|_{y=0}\right) \frac{\partial T^*}{\partial y} = \alpha \frac{\partial^2 T^*}{\partial y^2} \tag{28}$$

with initial condition

$$T^* = T_i \qquad t = 0$$

and boundary condition at infinity

$$T^* = T_i \qquad y \to -\infty$$

The boundary condition at $y = 0$ for the constant ΔT case is

$$\frac{\partial T^*}{\partial y} + Q(T^* - T_\infty) = 0 \quad y = 0$$

and for the constant flux case it is

$$\frac{\partial T^*}{\partial y} = -1 \quad y = 0$$

An interesting result occurs when examining the equations in the asymptotic limit of the parameter Q equalling infinity. For the constant ΔT case the only place this parameter appears in the equations for the base state is in the Robin type boundary condition

$$\frac{\partial T^*}{\partial y} + Q(T^* - T_\infty) = 0$$

If the limit of this equation is taken as $Q \to \infty$, the resulting boundary condition is

$$T^* - T_\infty = 0$$

Similarly, in the perturbation equations, the only place Q appears is in the boundary condition for the perturbation temperature

$$\frac{\partial T'}{\partial y} + QT' = -Q\eta \frac{\partial T^*}{\partial y}\bigg|_{y=0} - \eta \frac{\partial^2 T^*}{\partial y^2}\bigg|_{y=0}.$$

Again if the limit is taken as $Q \to \infty$, the resulting boundary condition is

$$T' = -\eta \frac{\partial T^*}{\partial y}\bigg|_{y=0}.$$

These new boundary conditions represent the case where the surface temperature is set identically equal to the temperature at infinity:

$$T|_{\text{Free Surface}} = T_\infty$$

In this case T_∞ is the saturation temperature associated with the pressure of the vapor. So what these new boundary conditions imply is that the liquid is in thermodynamic equilibrium with the vapor at the free surface. In fact, these conditions could have been derived from the beginning if we would have used an equilibrium condition in place of equation (7). In applying the same asymptotic limit to the equations describing the constant flux case we find that since the parameter Q does not appear in the base state equations the basic state is unaffected by this limit. However, Q does appear in the perturbation equations in the same form as in the constant ΔT case so that taking the limit imposes, in this situation, the same thermodynamic equilibrium condition as mentioned above. For most real fluids, Q is large ($10 \le Q \le 100$) so that this asymptotic result may be a very good approximation to the real case of a finite Q. In addition, using the approximation would simplify the analysis by eliminating the parameter Q, thus reducing the number of parameters in the problem.

In order to obtain simple solutions we will take the convective term in equation (28) to be equal to zero. This results in solutions which are good approximations to the true solutions so long as Ja is small. In fact, equation (28) can be solved in the constant ΔT case with $Q \to \infty$ (see Carslaw and Jaegar [11]). In this situation neglecting the convective term in equation (28) results in negligible error for the values of Jakob number we used in this analysis.

The boundary conditions as they are given above produce singularities in the solutions at $t = 0$. These singularities create problems for the numerical method which is used to solve the perturbation equations. A way of eliminating this problem is to ramp the boundary conditions from some value that is consistent with the initial condition to the desired form over a period of t_0. For the cases where T_∞ is stepped down at $t = 0$ we would instead say that T_∞ satisfies

$$T_\infty = T_i - \Delta T \frac{t}{t_0} + \Delta T \frac{(t - t_0)}{t_0} U(t - t_0)$$

where $U(t - t_0)$ is the unit step function applied at $t = t_0$. For the constant flux case we will specify

$$\frac{dT^*}{dt}\bigg|_{y=0} = \frac{t}{t_0} + \frac{(t - t_0)}{t_0} U(t - t_0)$$

In an experiment it is impossible to reduce the pressure above the superheated liquid instantaneously so we are not unreasonable in specifying these new conditions. The length of the ramping interval t_0 can be estimated as follows. Suppose the experiment which we are modeling is started by the breaking of a diaphragm a distance l above the liquid surface. If we then assume that his diaphragm can be broken infinitely fast, an estimate of t_0 is

$$t_0 = l\left[\frac{1}{c_2} - \frac{1}{c_1}\right]$$

where c_1 and c_2 are the speeds of sound in the vapor before and after the depressurization.

Once the base state temperature profile is known, the initial value problem for the perturbations can be solved. This problem consists of a partial differential equation for the perturbation temperature which must be solved simultaneously with two other ordinary differential equations for η and W. The equations are linear with non-constant coefficients. The method of lines is very well suited for solving this type of problem. In this method the space domain of the partial differential equation is discretized (i.e., the y direction is divided up into intervals) and the space derivatives (the derivatives taken with respect to y) are approximated by finite differences. This results in turning the partial differential

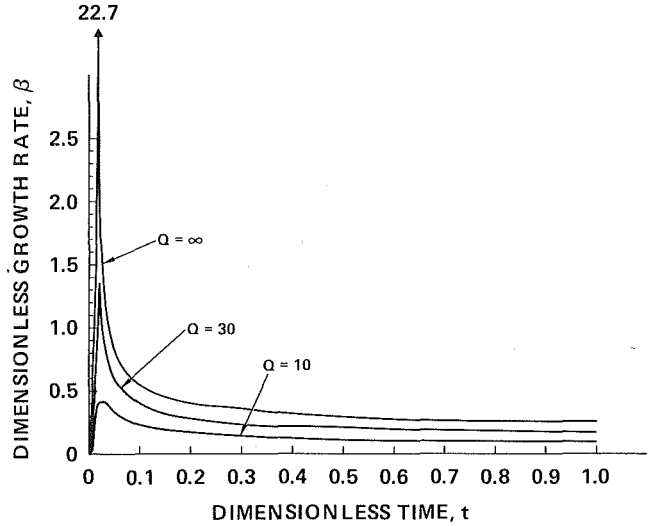

Fig. 2 Dimensionless growth rate versus dimensionless time for the constant ΔT case

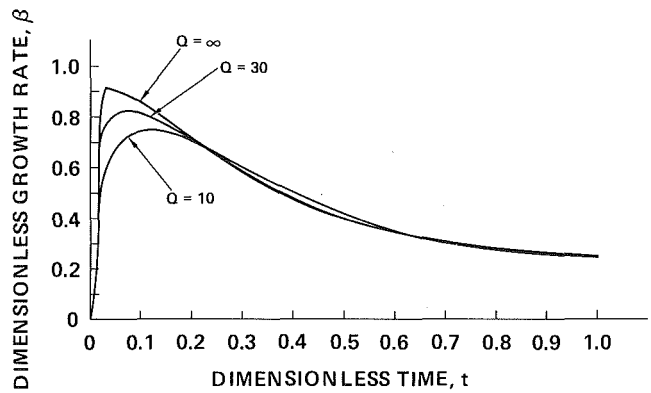

Fig. 3 Dimensionless growth rate versus dimensionless time for the constant flux case

equation into a system of ordinary differential equations (one for the perturbation temperature at each grid point in the y direction). After this is done the two ordinary differential equations for η and W can be collected with the ones resulting from the application of the method of lines and the whole system can be solved using a standard ordinary differential equation solver. In this case we used a packaged routine which implemented Gear's [12] stiffly stable method.

In order to solve the resulting system of ordinary differential equations, initial conditions must be supplied for the perturbation variables. This presents a problem because the initial conditions in a real physical system are not usually known. The fact that initial conditions are needed is one of the disadvantages of using a transient stability analysis. Gresho and Sani [8] have discussed this problem in detail in their work. Because the system of ordinary differential equations is linear and homogeneous, the initial conditions appear as constants multiplying the solution vector. Therefore, if all the elements of the initial condition vector are zero except for one, the ratio of any solution component to the nonzero initial value is invariant. In other words, the relative magnitude of the solution is not important. What is important is the ratio of the solution to the initial condition. In this study, the initial conditions we used were $\eta = 1$ with all other variables set equal to zero.

Discussion of Results

Figure 2 is a plot of the dimensionless growth rate of the surface height

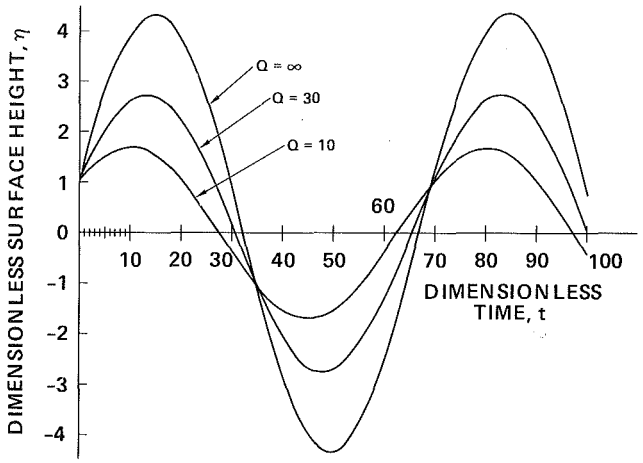

Fig. 4 Dimensionless surface height versus dimensionless time for the constant ΔT case

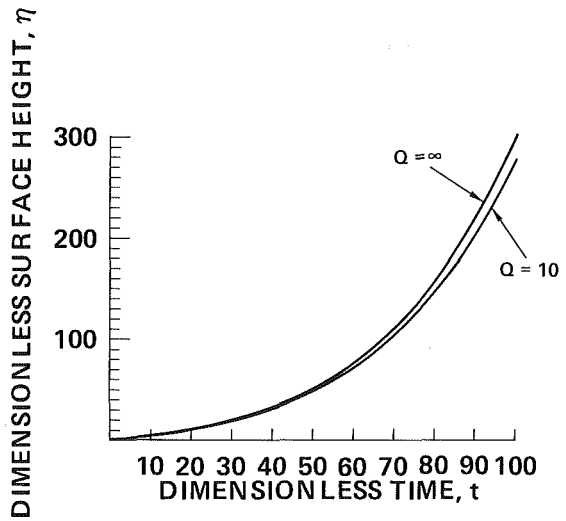

Fig. 5 Dimensionless surface height versus dimensionless time for the constant flux case

$$\beta = \frac{\frac{d\eta}{dt}}{\eta}$$

versus dimensionless time for the case where ΔT is constant. Shown in this plot are the results for Q equal to 10, 30 and infinity. The other parameter values used were

$$B_0 = 4 \times 10^{-5}$$
$$a = 1 \times 10^{-3}$$
$$N_\rho = 1500$$
$$\mathrm{Ja} = .2$$
$$t_0 = 2 \times 10^{-2}.$$

These values were chosen as being representative for an experiment similar to the ones done by Grolmes and Fauske [3]. Figure 3 is a similar plot of the solutions of the constant flux case. The same parameter values were used except for Ja which is equal to 1 in this example. The effect of ramping the free surface boundary condition over the interval $0 \le t \le t_0$ can be observed in these plots. In Fig. 2 the curve which corresponds to $Q = \infty$ has a very predominant spike at time t_0. This spike is a result of the fact that, for the situation where $t_0 = 0$ and $Q = \infty$, the base state mass flux is infinite at the initial time. This singularity is passed on to the perturbation

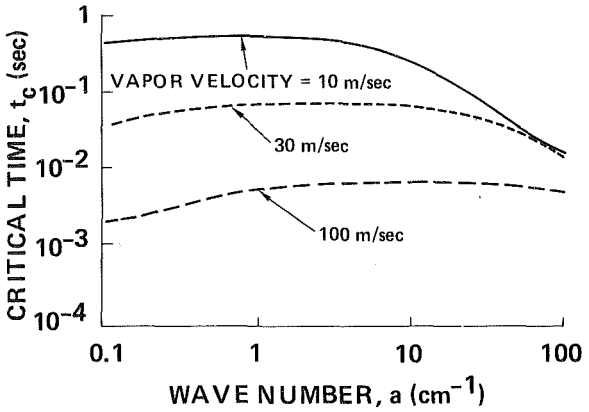

Fig. 6 Dimensional critical time versus dimensional wave number for the constant flux case using water at 100°C

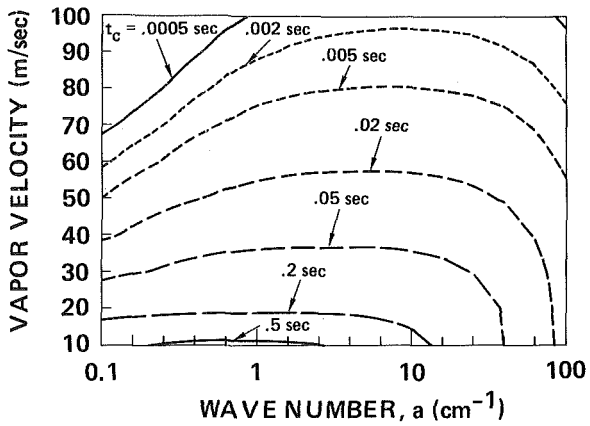

Fig. 7 Contour plot of the dimensional critical time t_c as function of dimensional vapor velocity and dimensional wave number for the constant flux case using water at 100°C

solutions resulting in an infinite growth rate at $t=0$. Ramping the boundary data removes this singularity; however, it leaves a remnant in the form of a spike in the growth rate curve.

Figure 4 is a plot of dimensionless surface height versus dimensionless time for the same cases as in Fig. 2. Figure 5 is a similar plot for the cases in Fig. 3. Figures 4 and 5, however, cover a greater duration of time than do Figs. 2 and 3. It is immediately evident from these plots that the constant flux cases exhibit the exponential growth that is so often seen in stability problems, however the constant ΔT solutions do not in any sense have this behavior. Instead, what we see in the latter is strictly oscillatory behavior. It is as if, in this case, the system received an impulse at $t=0$. This impulse can be seen in the form of a spike in the growth rate curves of Fig. 2. Because the system we are analyzing has no viscous dissipation, its response to this impulse is a sinusoidal oscillation of the surface height that lasts indefinitely. Furthermore, the frequency of these oscillations is

$$\omega_0 = \sqrt{a\left(\frac{N_\rho - 1}{N_\rho + 1}\right)\left(1 + \frac{a^2}{B_0}\right)}$$

which is the natural frequency of surface waves in the absence of mass transfer. These facts are verified by the computed results in Fig. 4. The general behavior described here for both the case of constant flux and the case of constant ΔT was observed for all the parameter combinations tried. Thus, it would appear that for constant Δt the driving force, particularly the base state temperature gradient at $y=0$, dies off much too quickly to cause unstable behavior in the traditional sense. On the other hand, in the constant flux case, the driving force is held constant by the imposition of the constant flux boundary condition. Thus, we observe the classical exponential-like growth.

In examining Figs. 3 and 5 we can see that for the constant flux case, the results with finite Q converge very quickly to the infinite Q solution. Figure 5 shows that for Q greater than 10 the surface height solution with finite Q is very close to the asymptotic result. Since in most practical applications Q is greater than 10, the asymptotic solution in this case would be a good approximation to the true solution. On the other hand, the constant ΔT surface height solutions do not converge as quickly to the asymptotic result. Since the motion of the surface height with time in this case is determined by an impulse near the initial time, it is anticipated that the convergence of the solution is strongly related to how well the growth rates for the finite Q cases converge to the infinite Q solution in the spike region. Figure 2 shows that although the growth rate for $Q=30$ appears to be very close to the infinite Q result, there is a large discrepancy in the heights of the spikes in these two curves. In looking at Fig. 4 we can see that for $Q=30$ the solution for surface height is not very close to the $Q=\infty$ solution. Thus, it may not be a good approximation to assume $Q=\infty$ in this case. It should be noted that in all the results the asymptotic solution of $Q=\infty$ is the upper bound for the cases where Q is finite. In other words, the asymptotic solution always represents the most unstable result. Because of this fact and also because the asymptotic solution is generally a very good approximation to the true solution, we will look only at the behavior of the asymptotic results from here on.

Constant Flux Results. The desired result of a steady base state or quasi-steady analysis is to obtain the growth rate of the disturbances as a function of the parameters of the problem. With this knowledge in hand we can then find the stability boundary as well as other important results such as the fastest growing wave number. We can also obtain growth rates using the transient analysis, however, as we have seen these growth rates are functions of time. This fact makes it difficult to compare the relative degree of instability of two different runs. To get around the difficulty we can define the critical time, t_c, as the time it takes the perturbation in surface height to grow to 1000 times its initial value; or

$$t = t_c \text{ when } \frac{\eta(t)}{\eta(0)} = 1000$$

Using the critical time as our desired stability result we can then make comparisons between runs of different parameter values.

Because of the many parameters involved in this problem we will simplify the presentation of the results by choosing specific fluids and states to compare results. In comparing constant flux results we will use water at 100°C to evaluate the fluid properties. Then

$$N_\rho = 1605$$
$$B_0 = 3.118 \times 10^{-5}$$
$$t_0 = 2 \times 10^{-2}.$$

Figure 6 is a plot of dimensional critical time versus dimensional wave number found using the transient analysis on the case of constant flux and for vapor velocities of 10, 30, and 100 meters per second. Figure 7 is a contour plot of this data showing lines of equal t_c.

Constant ΔT Results. We have seen that using the transient analysis with constant ΔT the solutions for surface height do not exhibit the usual exponential growth associated with unstable behavior. In a sense all the solutions are stable because they all eventually stop growing. Still we would like to

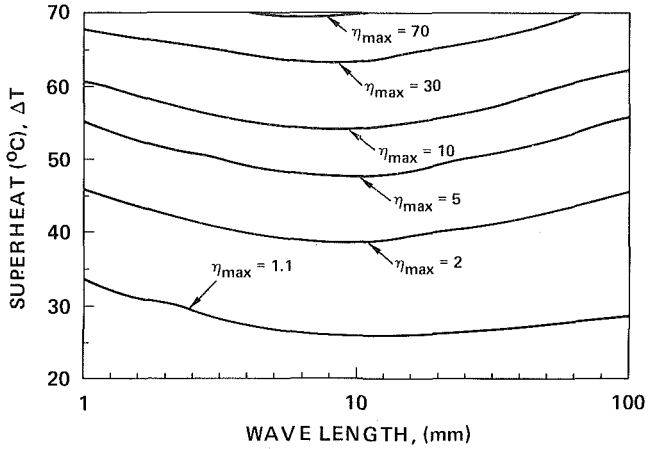

Fig. 8 Contour plot mimicking the experiments of Grolmes and Fauske using Freon 11

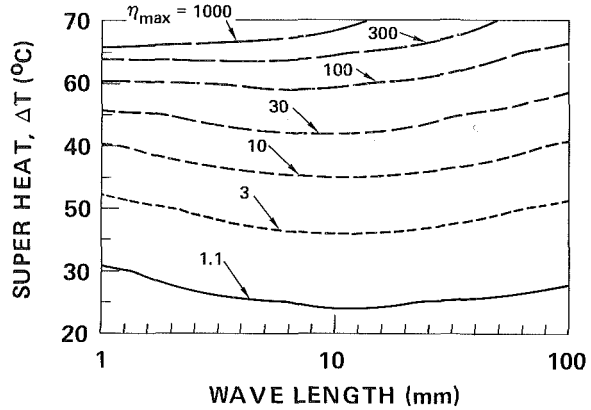

Fig. 9 Contour plot mimicking the experiments of Grolmes and Fauske using methanol

be able to predict the break-up of the fluid interface. We know that at the time when the surface is about to break apart the assumptions used in implementing the linear stability analysis are not valid. However, if we could find a number (such as t_c) for each set of parameter values which would be a good measure of the tendency towards instability, we could then compare our results with the experimental results of Grolmes and Fauske. The critical time is not a good choice since for most of the parameter combinations tried $\eta(t)/\eta(0)$ never reaches 1000. A good choice and the one that will be used here is the ratio of the largest value of surface height achieved to the initial surface height. Since the initial surface height in this case is 1, the stability parameter we will use is η_{max}, or the largest value of η attained in the run.

Figure 8 is a contour plot showing lines of constant η_{max} as functions of superheat (ΔT) and wavelength. The parameter values used in generating the data for this plot were chosen to best represent the experiments of Grolmes and Fauske [3] in which they used Freon 11 as their fluid. Figure 9 is a similar plot except that methanol is the fluid used. In their experiments Grolmes and Fauske took liquids at 30°C and atmospheric pressure and expanded them into different values of low pressure in order to achieve the desired ΔT. Because of this all the fluid properties were evaluated at 260°K except for the vapor density which was evaluated at 303°K minus ΔT.

The region where Grolmes and Fauske reported their stability boundary to be corresponds to an η_{max} varying from 1.1 to 10. A magnification of an initial perturbation by a factor of 10 does not seem to be enough to lead to the breakup of the liquid vapor interface. Thus, it appears that the analysis here does not contribute much to the understanding of the behavior observed by Grolmes and Fauske [3].

Conclusion

Although the transient analysis presented here exhibits some interesting results, it falls short of presenting a suitable theory which could be used to predict the experimental results of Grolmes and Fauske. Our work here is based on a linear hydrodynamic stability analysis which is subject to many limitations. In addition, because the model which we used was highly simplified we could have eliminated an important mechanism which would have caused the desired behavior. It is clear that more work is needed in both the analytical and experimental aspects of this problem. In particular, more experimental work is necessary in which careful observation is made of the liquid-vapor interface in order to gain further insight into the mechanism that causes the surface to break apart.

References

1 Hickman, K. C. D., "Surface Behavior in the Pot Still," *Ind. Eng. Chem.*, Vol. 44, 1952, pp. 1892–1902.

2 Hickman, K., "Torpid Phenomena and Pump Oils," *J. Vac. Sci. Tech.*, Vol. 9, 1972, pp. 960–976.

3 Grolmes, M. S., and H. K. Fauske, "Axial Propagation of Free Surface Boiling Into Superheated Liquids in Vertical Tubes," *Proceedings of the Fifth International Heat Transfer Conference*, Tokyo, Vol. 4, 1972, pp. 30–34.

4 Miller, C. A., "Stability of Moving Surfaces in Fluid Systems with Heat and Mass Transport," *A.I.Ch.E.J.*, Vol. 19, 1973, pp. 909–915.

5 Palmer, H. J., "The Hydrodynamic Stability of Rapidly Evaporating Liquids at Reduced Pressure," *J. Fluid Mech.*, Vol. 75, 1976, pp. 487–511.

6 Maheshri, J. C., and H. J. Palmer, "The Influence of Lateral Pressure Variations on the Stability of Rapidly Evaporating Liquids at Reduced Pressure," *A.I.Ch.E.J.*, Vol. 25, 1979, pp. 183–185.

7 Prosperetti, A., and M. S. Plesset, "The Stability of an Evaporating Liquid Surface," (to appear in *Physics of Fluids*).

8 Mahler, E. G., R. S. Schecter, and E. H. Wissler, "Stability of a Fluid Layer with Time Dependent Density Gradients," *Phys. Fluids*, Vol. 11, 1968, pp. 1901–1912.

9 Gresho, P. M., and R. L. Sani, "The Stability of a Fluid Layer Subjected to a Step Change in Temperature: Transient vs. Frozen Time Analyses," *Int. J. Heat Mass Transfer*, Vol. 14, 1971, pp. 207–221.

10 Plesset, M. S., "Note on the Flow of Vapor Between Liquid Surfaces," *J. Chem. Phy.*, Vol. 20, 1952, pp. 790–793.

11 Carslaw, H. S., and J. C. Jaeger, *Conduction of Heat in Solids*, 2nd edition, Oxford University Press, New York, 1959.

12 Gear, C. W., *Numerical Initial Value Problems in Ordinary Differential Equations*, Prentice-Hall, Englewood Cliffs, New Jersey, 1971.

Journal of Fluids Engineering

Discussion

Laser Velocimeter Measurements in Highly Turbulent and Recirculating Flows[1]

Eric Adams.[2] The paper "Laser Velocimeter Measurements in Highly Turbulent and Recirculating Flows" presents a study of several important aspects of separated flow research. Though the paper presents many ideas worthy of attention, only a few will be commented on.

(1) The method of bias elimination used in the paper has great promise because of its simplicity. The method is similar to that used by Tropea and Durst (1980), but the hardware and data processing used in the study by Stevenson et al. is significantly less complex. As the authors point out, Erdmann and Tropea (1981) shows that three frequency scales are important parameters in such a bias-elimination scheme. The frequencies are: f_{dr}, the rate of particles arriving at the measuring volume, f_s, the rate these particles are sampled; and f_t, a typical turbulence frequency scale (Erdmann and Tropea use the integral scale). Studies in our lab with the backward-facing-step configuration at about the same location and turbulence level (Adams, Eaton, and Johnston, 1984) indicate that when $f_{dr}/f_s > 10$–20, the velocity bias is eliminated (Fig. A). This value is in agreement with the value of 10–12 found in the study of Stevenson et al. (Fig. 3). Despite this agreement, the effect of second ratio, f_{dr}/f_t, on the velocity bias has not received sufficient study. Our data were taken at much lower particle rates ($f_{dr} \sim 500$ versus $f_{dr} \sim 20{,}000$), which could lead one to conclude that f_{dr}/f_t is less important than f_{dr}/f_s. However, in both cases the particle rate was several times f_t (f_t) estimated as U/δ_{SL}, where δ_{SL} is the shear layer width.) Without further information, it is recommended that the technique of bias elimination suggested by the paper be validated in the flow field where it will be used, so that any effect of f_{dr}/f_t on the velocity bias can be eliminated.

(2) To match the measured reattachment length of the experiment, the shear-layer growth rate of the numerical computation is about two times that observed experimentally (Fig. 7). This probably results as much from the fully three-dimensional nature of the backward-facing-step flow at an aspect ratio of 1 as from any inadequacy of the computations. The strong three-dimensionality of the flow field at small aspect ratio is interesting of itself (de Brederode and Bradshaw, 1972); however, it does mean that the numerical values of mean velocity and Reynolds stress presented in the study of Stevenson et al. are best used only qualitatively.

(3) Comparing the near-wall $\overline{u'v'}$ results in the recirculation zone of the study of Stevenson et al. with the measurements of Simpson et al. (1981), Driver and Seegmiller (1983), and Pronchick (1983) show that no experiment has

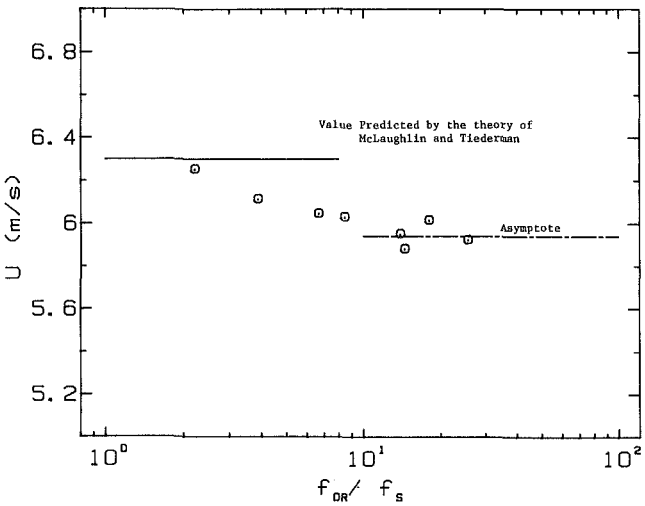

Fig. A The effect of the parameter f_{dr}/f_s on the measured mean velocity ($X/H = 3.0$, $u'/U = 0.25$)

measured a value of $-\overline{u'v'}$ more negative than the uncertainty of the data. If this near-wall region is a normal turbulent boundary layer, large negative ($-\overline{u'v'}$) would be expected.

A Reynolds number of the near-wall flow in the recirculation zone may be estimated based on the maximum backflow velocity, U_N, and the height to the maximum backlflow velocity, N (Westphal et al., 1984). This Reynolds number, Re_N, roughly corresponds to the boundary-layer-thickness Reynolds number of a normal boundary layer. Estimating the value of the Re_N for the experiment of Stevenson et al. based on previous backstep data ($N = 0.1$, H, $U = 0.2\ U_N$) gives a value of 3,500, a rather low value for a turbulent boundary layer. However, this value is the highest Re_N of any experiment to date which has measured $\overline{u'v'}$ in the near-wall zone beneath the separation bubble. For this reason, it is significant that Stevenson et al. did not measure negative ($-\overline{u'v'}$) in the near-wall region of the recirculation zone.

This point is important for k-ϵ models of turbulence using the law of the wall as a boundary condition. Without negative ($-\overline{u'v'}$) in the near-wall region of the recirculating flow, it seems unreasonable to expect the turbulent log-law to be valid. It would also seem unreasonable to expect k-ϵ models to predict the correct turbulence levels if they are using the wrong boundary condition in a region of the flow.

Additional References

Adams, E. W., Eaton, J. K., and Johnston, J. P. (1984), "An Examination of Velocity Bias in a Highly Turbulent Separated and Reattaching Flow," *Proceedings of the Second International Symposium on Applications of Laser Anemometry to Fluid Mechanics*, Lisbon, Portugal, July 2–4.

[1] By W. H. Stevenson, H. D. Thompson, and R. R. Craig published in the June 1984 issue of the JOURNAL OF FLUIDS ENGINEERING, Vol. 106, No. 2, pp. 173–180.

[2] Department of Mechanical Engineering, Stanford University, Stanford, Calif. 94305.

de Brederode, V., and Bradshaw, P. (1972), "Three-Dimensional Flow in Nominally Two-Dimensional Separation Bubbles. I. Flow Behind a Rearward-Facing Step," I.C. Aero Report 72-19, Imperial College of Science and Technology, Department of Aeronautics, London, England.

Driver, D. M., and Seegmiller, H. J. (1982), "Features of a Reattaching Turbulent Shear Layer," AIAA #82-1029.

Durst, F., and Tropea, C. (1980), "Digital Processing of LDA Signals by Means of a Transient Recorder and a Computer," *Proceedings, ISL Symposium on Long- and Short-Range Anemometry*, Sept. 15-19.

Erdmann, J. C., and Tropea, C. (1981), "Statistical Bias in Laser Anemometry," SFB 80/ET/198, Universitat Karlsruhe, August.

McLaughlin, D. K., and Tiederman, W. G. (1973), "Biasing Correction for Individual Realization of Laser-Anemometer Measurements in Turbulent Flows," *Physics of Fluids*, Vol. 16, No. 12, Dec. 1973, pp. 2082-2088.

Pronchick, S. W., and Kline, S. J. (1983), "An Experimental Investigation of the Structure of a Turbulent Reattaching Flow behind a Backward-Facing Step," Rept. MD-42, Thermosciences Division, Department of Mechanical Engineering, Stanford University, June.

Simpson, R. L., Chew, Y-T, and Shivaprasad, B. G. (1981), "The Structure of a Separating Turbulent Boundary Layer, Part 1. Mean Flow and Reynolds Stresses," *Journal of Fluid Mechanics*, 113, pp. 23-51.

Westphal, R. V., Johnston, J. P., and Eaton, J. K. (1984), "Experimental Study of Flow Reattachment in a Single-Sided Sudden Expansion," NASA CR 3765, January.

Authors' Closure

The perceptive comments of Adams draw attention to a number of interesting issues and are appreciated.

The question of the relative influence of f_{dr}/f_t and f_{dr}/f_s on the velocity bias magnitude is still unresolved and we certainly concur that until further information is available one cannot assume that $f_{dr}/f_s > 10$–20 is a suitable minimum arrival rate/sampling rate ratio in all flow situations. This has been emphasized in a paper summarizing our earlier work on the bias error problem [A1]. The important point is that velocity bias will always be eliminated if the samples are taken at essentially equal time intervals, provided the data is taken over a time long compared to $1/f_t$. Obviously a relatively high seeding density, corresponding to "large" f_{dr}/f_t, is needed to obtain an adequate set of such equal interval samples in a reasonable period of time. This will usually mean that artificial rather than natural seeding is required. It is possible to monitor the approach to equal time sampling in most systems by simply observing on an oscilloscope the pulses produced each time a sample is validated by the processor. An alternate method of verifying when correct sampling conditions have been achieved is described by Craig, et al. [A2].

The discrepancy between predicted and measured shear layer growth as reflected in the turbulent kinetic energy profiles may indeed result from three-dimensional effects as suggested by Adams. Certainly we would not expect the 2-D numerical computation to accurately describe behavior at the low aspect ratio used in this experiment. It is interesting to note, however, that rather large discrepancies between predicted and measured kinetic energies were also found in a recent axisymmetric sudden expansion flow study [A3]. In this case the computations under-predicted the TKE by as much as a factor of four even though mean velocity discrepancies were very small.

Adam's observation regarding the value of $\overline{u'v'}$ in the recirculation region near the wall is quite interesting. In the as yet unpublished investigation referred to above we were able to make more precise Reynolds stress measurements, but again found the value close to the wall to be near zero in the recirculation zone at $X/H = 2$. The largest deviation between predicted and measured mean velocity also occurred in this area. It is apparent that the boundary condition used in the k-ϵ model in this region should be re-examined if further experiments confirm these results.

Additional References

A1 Stevenson, W. H., Thompson, H. D., and Roesler, T. C., "Direct Measurement of Laser Velocimeter Bias Errors in a Turbulent Flow," *AIAA Journal*, Vol. 20, 1982, pp. 1720-1723.

A2 Craig, R. R., Nejad, A. S., Hahn, E. Y., and Schwartzkopf, K. G., "A General Approach for Obtaining Unbiased LDV Data in Highly Turbulent Non-Reacting and Reacting Flows" AIAA Paper No. 84-0366, 1984.

A3 Durrett, R. P., "Laser Velocimeter Measurements in an Axisymmetric Sudden Expansion with a Correction for Tube Wall Aberrations," M.S. thesis, Purdue University, May 1984.

Flow Field Due to Free Convection in Dead-End Channels

T. R. Sundaram.[2] One of the principal difficulties in the theoretical analysis of the thermal structure of waterbodies such as the oceans, lakes, and cooling reservoirs is that the eddy transport processes that control the downward transport of heat and momentum in such waterbodies are inherently coupled to each other. That is, the eddy diffusivity for downward transfer of heat not only controls the evolution of the temperature profile, but also is itself influenced by both the temperature and current distributions, with a similar state of affairs also being true for downward momentum transfer. Because the foregoing complexity makes theoretical analyses of the problem very difficult, most of the analyses described in the literature are based only on an approximate, and often implicit, accounting for the coupling between heat and momentum transfer. For example, many analyses of the thermal structure of the upper ocean are based on the assumption that the effects of wind-induced mixing on the thermal structure can be specified in terms of the friction velocity of the ocean surface, this approach being similar to that of the well-known Monin-Obukhov formulation for the atmospheric surface layer. In another type of approach the waterbody is divided into two or more horizontal layers, with the values of the eddy diffusivites being known "a priori"; this approach has been especially useful in analyzing the current structures of large waterbodies of complex geometry, such as the Great Lakes.,

The paper by Yildirim and Jain presents a very interesting approach to the problem of predicting the temperature and current distributions in the "side arms" of large cooling reservoirs. Detailed solutions to the temperature and current distributions have been obtained by assuming that the vertical profiles of temperature and velocity evolve in a self-similar fashion. Although the dependence of the eddy-transport coefficients on the temperature and current distributions has not been included, and although detailed solutions have been given by the authors only for the simple cases in which eddy diffusivities are assumed to be constant in the upper and lower layers (of forward and return flows, respectively), the formulation itself appears to be more general than conventional two-layer models.

The solutions display several important features, and at the same time place certain constraints on the applicable phenomenology; these are not discussed by the authors. For example, the similarity conditions represented by equations (18) and (29) require that the eddy diffusivities cannot vary horizontally, a requirement which is in fundamental contradiction with the phenomenology involved! Thus if the values of the diffusivities are governed by shear-produced turbulence (as can be expected to be the case in the lower layers), then even a simple theory such as the Prandtl-mixing-length theory would require that the value of the eddy diffusivity at any level vary as the velocity (and thus linearly with x). On the other hand, if the value of the eddy diffusivity is governed by convective turbulence (as may be the case in the upper layers), then it must necessarily be dependent on the

[1] By N. Yildirim and S. C. Jain, published in the June 1984 issue of the JOURNAL OF FLUIDS ENGINEERING, Vol. 106, No. 2, pp. 217-222.

[2] T. S. Associates, Inc., Columbia, Md. 21044.

de Brederode, V., and Bradshaw, P. (1972), "Three-Dimensional Flow in Nominally Two-Dimensional Separation Bubbles. I. Flow Behind a Rearward-Facing Step," I.C. Aero Report 72-19, Imperial College of Science and Technology, Department of Aeronautics, London, England.

Driver, D. M., and Seegmiller, H. J. (1982), "Features of a Reattaching Turbulent Shear Layer," AIAA #82-1029.

Durst, F., and Tropea, C. (1980), "Digital Processing of LDA Signals by Means of a Transient Recorder and a Computer," *Proceedings, ISL Symposium on Long- and Short-Range Anemometry*, Sept. 15-19.

Erdmann, J. C., and Tropea, C. (1981), "Statistical Bias in Laser Anemometry," SFB 80/ET/198, Universitat Karlsruhe, August.

McLaughlin, D. K., and Tiederman, W. G. (1973), "Biasing Correction for Individual Realization of Laser-Anemometer Measurements in Turbulent Flows," *Physics of Fluids*, Vol. 16, No. 12, Dec. 1973, pp. 2082-2088.

Pronchick, S. W., and Kline, S. J. (1983), "An Experimental Investigation of the Structure of a Turbulent Reattaching Flow behind a Backward-Facing Step," Rept. MD-42, Thermosciences Division, Department of Mechanical Engineering, Stanford University, June.

Simpson, R. L., Chew, Y-T, and Shivaprasad, B. G. (1981), "The Structure of a Separating Turbulent Boundary Layer, Part 1. Mean Flow and Reynolds Stresses," *Journal of Fluid Mechanics*, 113, pp. 23-51.

Westphal, R. V., Johnston, J. P., and Eaton, J. K. (1984), "Experimental Study of Flow Reattachment in a Single-Sided Sudden Expansion," NASA CR 3765, January.

Authors' Closure

The perceptive comments of Adams draw attention to a number of interesting issues and are appreciated.

The question of the relative influence of f_{dr}/f_t and f_{dr}/f_s on the velocity bias magnitude is still unresolved and we certainly concur that until further information is available one cannot assume that $f_{dr}/f_s > 10$–20 is a suitable minimum arrival rate/sampling rate ratio in all flow situations. This has been emphasized in a paper summarizing our earlier work on the bias error problem [A1]. The important point is that velocity bias will always be eliminated if the samples are taken at essentially equal time intervals, provided the data is taken over a time long compared to $1/f_t$. Obviously a relatively high seeding density, corresponding to "large" f_{dr}/f_t, is needed to obtain an adequate set of such equal interval samples in a reasonable period of time. This will usually mean that artificial rather than natural seeding is required. It is possible to monitor the approach to equal time sampling in most systems by simply observing on an oscilloscope the pulses produced each time a sample is validated by the processor. An alternate method of verifying when correct sampling conditions have been achieved is described by Craig, et al. [A2].

The discrepancy between predicted and measured shear layer growth as reflected in the turbulent kinetic energy profiles may indeed result from three-dimensional effects as suggested by Adams. Certainly we would not expect the 2-D numerical computation to accurately describe behavior at the low aspect ratio used in this experiment. It is interesting to note, however, that rather large discrepancies between predicted and measured kinetic energies were also found in a recent axisymmetric sudden expansion flow study [A3]. In this case the computations under-predicted the TKE by as much as a factor of four even though mean velocity discrepancies were very small.

Adam's observation regarding the value of $\overline{u'v'}$ in the recirculation region near the wall is quite interesting. In the as yet unpublished investigation referred to above we were able to make more precise Reynolds stress measurements, but again found the value close to the wall to be near zero in the recirculation zone at $X/H = 2$. The largest deviation between predicted and measured mean velocity also occurred in this area. It is apparent that the boundary condition used in the k-ϵ model in this region should be re-examined if further experiments confirm these results.

Additional References

A1 Stevenson, W. H., Thompson, H. D., and Roesler, T. C., "Direct Measurement of Laser Velocimeter Bias Errors in a Turbulent Flow," *AIAA Journal*, Vol. 20, 1982, pp. 1720-1723.

A2 Craig, R. R., Nejad, A. S., Hahn, E. Y., and Schwartzkopf, K. G., "A General Approach for Obtaining Unbiased LDV Data in Highly Turbulent Non-Reacting and Reacting Flows" AIAA Paper No. 84-0366, 1984.

A3 Durrett, R. P., "Laser Velocimeter Measurements in an Axisymmetric Sudden Expansion with a Correction for Tube Wall Aberrations," M.S. thesis, Purdue University, May 1984.

Flow Field Due to Free Convection in Dead-End Channels

T. R. Sundaram.[2] One of the principal difficulties in the theoretical analysis of the thermal structure of waterbodies such as the oceans, lakes, and cooling reservoirs is that the eddy transport processes that control the downward transport of heat and momentum in such waterbodies are inherently coupled to each other. That is, the eddy diffusivity for downward transfer of heat not only controls the evolution of the temperature profile, but also is itself influenced by both the temperature and current distributions, with a similar state of affairs also being true for downward momentum transfer. Because the foregoing complexity makes theoretical analyses of the problem very difficult, most of the analyses described in the literature are based only on an approximate, and often implicit, accounting for the coupling between heat and momentum transfer. For example, many analyses of the thermal structure of the upper ocean are based on the assumption that the effects of wind-induced mixing on the thermal structure can be specified in terms of the friction velocity of the ocean surface, this approach being similar to that of the well-known Monin-Obukhov formulation for the atmospheric surface layer. In another type of approach the waterbody is divided into two or more horizontal layers, with the values of the eddy diffusivites being known "a priori"; this approach has been especially useful in analyzing the current structures of large waterbodies of complex geometry, such as the Great Lakes.,

The paper by Yildirim and Jain presents a very interesting approach to the problem of predicting the temperature and current distributions in the "side arms" of large cooling reservoirs. Detailed solutions to the temperature and current distributions have been obtained by assuming that the vertical profiles of temperature and velocity evolve in a self-similar fashion. Although the dependence of the eddy-transport coefficients on the temperature and current distributions has not been included, and although detailed solutions have been given by the authors only for the simple cases in which eddy diffusivities are assumed to be constant in the upper and lower layers (of forward and return flows, respectively), the formulation itself appears to be more general than conventional two-layer models.

The solutions display several important features, and at the same time place certain constraints on the applicable phenomenology; these are not discussed by the authors. For example, the similarity conditions represented by equations (18) and (29) require that the eddy diffusivities cannot vary horizontally, a requirement which is in fundamental contradiction with the phenomenology involved! Thus if the values of the diffusivities are governed by shear-produced turbulence (as can be expected to be the case in the lower layers), then even a simple theory such as the Prandtl-mixing-length theory would require that the value of the eddy diffusivity at any level vary as the velocity (and thus linearly with x). On the other hand, if the value of the eddy diffusivity is governed by convective turbulence (as may be the case in the upper layers), then it must necessarily be dependent on the

[1] By N. Yildirim and S. C. Jain, published in the June 1984 issue of the JOURNAL OF FLUIDS ENGINEERING, Vol. 106, No. 2, pp. 217-222.

[2] T. S. Associates, Inc., Columbia, Md. 21044.

temperature and thus also vary with x. Thus the requirements for the validity of the similarity solutions appear to be in fundamental contradiction with well-understood concepts of eddy diffusion!

Despite the aforementioned shortcomings, the paper is a very useful contribution to the literature.

Additional Comments

The authors have also left unanswered some important questions. For example, what are the ranges of values of the relevant physical parameters over which the specific similarity solutions can be expected to be valid? In particular, are the solutions valid for all values of the depth, D? Are they valid regardless of the inlet temperature difference ΔT_{si}? In the specific formulation given by the authors, the relevant "external parameters" are K_m, K_h, ν, k, g, and D. (In a two-layer model, two separate values for both K_m and K_h have to be included. Also, the kinematic viscosity ν is an extraneous parameter, and appears to have been included only for the sake of convenience). The four independent nondimensional groupings that can be formed from the foregoing quantities are P, P_m, (K_m/ν) and (k^2/gD). (Since only the dimensions of length and time are involved in the aforementioned external parameters, there are four independent groupings). While the authors have discussed the implications of changing the values of the first three groupings, the relevance of the last grouping (a Froude-number-like quantity) is unclear.

The foregoing questions are closely related to the conditions under which the boundary-layer approximations made by the authors become valid. The "ordering" procedure used in the boundary-layer approximations are based on the assumption that the vertical velocity, v, is small compared to the horizontal velocity, u. However, in the present case, v is independent of horizontal position, while u decreases continuously, at *all* vertical locations, with increasing downstream distance (that is, as the y-axis is approached). Therefore, the quantity (v/u) will become quite large at small values of x. In the y-momentum equation, the authors have neglected terms such as $v\ (\sigma v/\sigma y)$ and $(\sigma/\sigma y)\quad (K_m\ (\sigma v/\sigma y))$ compared to the gravitational term. The similarity solutions can be used to estimate the order of magnitude of the aforementioned terms relative to the gravitational term, g; although this is difficult owing to the awkward nondimensionalization procedure used by the authors, it appears that the relative magnitudes will depend, among other things, on the value of the parameter (k^2/gD). Thus this parameter appears to be an important one.

The foregoing comments also have a bearing on the rather misleading representation of the flow field that is given in Fig. 1. Since v is independent of x, while u depends linearly on it, the streamlines cannot remain horizontal and parallel as depicted. Indeed, a particle on the free surface will travel towards the y-axis and then turn discontinuously downward along the y-axis; near-surface streamlines cannot overshoot the y-axis as shown!

The boundary conditions used by the authors also appear to be incomplete. Since the problem involved is the steady flow in a dead-end channel, the total horizontal transport across any vertical cross section must be zero. Indeed, integration of the continuity equation yields

$$\frac{d}{dx}\int_0^D u\,dy = 0.$$

It is unclear as to whether the authors have used this condition in the solution of equations (30) and (31).

Finally, contrary to the statement made by the authors, the approach that was used in reference [10] by Sundaram, et al. to study the thermal structure of temperate lakes does *not* assume that K_m is constant! Rather, the approach involves the uncoupling of the current and thermal structures by assuming that the effects of wind-induced mixing on the latter can be described in terms of the surface friction velocity alone. This approach is similar to that used in the oceanic and atmospheric theories already mentioned.

Authors' Closure

The authors wish to thank Sundaram for his comments on the limitations of the model. The relevant independent variables are K_{m1}, K_{h1}, K_{m2}, K_{h2}, k, D, αg, and ΔT_{si}. Since the flow in the lower layer was assumed to be laminar, K_{m1} was replaced by kinematic viscosity ν. The five independent nondimensional groups are $P_2 = \nu/K_{h2}$, $P_1 = \nu/K_{h1}$, $P_m = \nu/(kD)$, K_{m2}/ν, and $k^2/(\alpha g D \Delta T_{si})$. The first four groups appear in equations (30) and (31) and the last group arises in equation (29) on normalizing it by ΔT_{si}.

The simplification of y-momentum equation to equation (3) implies that the pressure distribution is assumed to be hydrostatic, which is believed to be applicable throughout the flow region.

The flow field was shown *schematically* in Fig. 1. The authors agree with Sundaram's observation relative to the streamlines. The introduction of stream function satisfied the continuity equation.

There is no limit on the values of depth and initial temperature difference as long as the flow field is primarily generated by buoyancy-driven currents. Phillips [15] used a similar similarity solution to describe the flow field in Red Sea.

Additional Reference

15 Phillips, O. M., "On Turbulent Convection Currents and the Circulation of the Red Sea," *Deep Sea Research*, Vol. 13, 1966.